MICROCOPY RESOLUTION TEST CHART
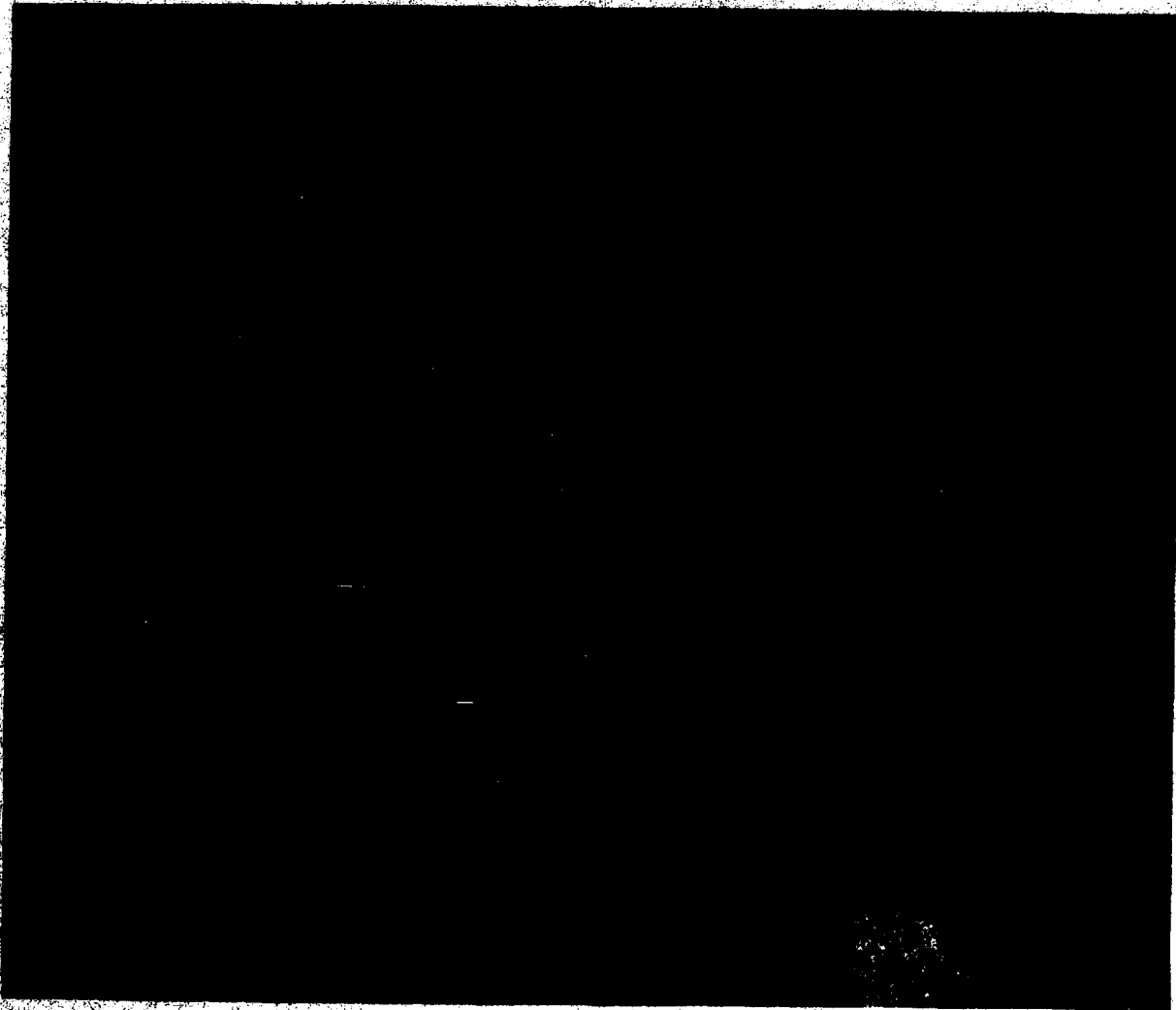
NATIONAL BUREAU OF STANDARDS-1963-A

12

CSL COORDINATED SCIENCE LABORATORY

ENCAPSULATION
AND IMPLANTATION
STUDIES OF InP

UNIVERSITY OF ILLINOIS AT URBANA-CHAMPAIGN

02 014 030

SECURITY CLASSIFICATION OF THIS PAGE *(When Data Entered)*

REPORT DOCUMENTATION PAGE		READ INSTRUCTIONS BEFORE COMPLETING FORM
1. REPORT NUMBER	2. GOVT ACCESSION NO. AD-A124388	3. RECIPIENT'S CATALOG NUMBER
4. TITLE *(and Subtitle)* ENCAPSULATION AND IMPLANTATION STUDIES OF InP		5. TYPE OF REPORT & PERIOD COVERED Technical Report
		6. PERFORMING ORG. REPORT NUMBER R-958; UILU-ENG 82-2224
7. AUTHOR(*s*) John David Oberstar		8. CONTRACT OR GRANT NUMBER(*s*)
9. PERFORMING ORGANIZATION NAME AND ADDRESS Coordinated Science Laboratory University of Illinois 1101 W. Springfield Ave. Urbana, IL 61801		10. PROGRAM ELEMENT, PROJECT, TASK AREA & WORK UNIT NUMBERS
11. CONTROLLING OFFICE NAME AND ADDRESS Joint Services Electronics Program		12. REPORT DATE July, 1982
		13. NUMBER OF PAGES 204
14. MONITORING AGENCY NAME & ADDRESS*(If different from Controlling Office)*		15. SECURITY CLASS. *(of this report)* Unclassified
		15a. DECLASSIFICATION/DOWNGRADING SCHEDULE

16. DISTRIBUTION STATEMENT *(of this Report)*

Approved for public release; distribution unlimited.

17. DISTRIBUTION STATEMENT *(of the abstract entered in Block 20, If different from Report)*

18. SUPPLEMENTARY NOTES

19. KEY WORDS *(Continue on reverse side if necessary and identify by block number)*

Semiconductors
Ion Implantation
Indium Phosphide

20. ABSTRACT *(Continue on reverse side if necessary and identify by block number)*

Successful ion implantation of InP will depend on detailed information regarding the protective qualities of prospective encapsulants and also the thermal annealing parameters (i.e., time and temperature) required to reorder the implant damaged lattice and to activate the implanted impurity. Using Auger electron spectroscopy (AES), secondary ion mass spectrometry (SIMS), and low temperature photoluminescence (PL) the InP encapsulation properties of CVD SiO_2, CVD PSG (phosphosilicate glass), and rf plasma-deposited Si_3N_4 have been examined. In addition, the annealing/implantation characteristics of semi-insulating (SI) InP

DD ᶠᴼᴿᴹ 1473
DD FORM 1 JAN 73 1473

SECURITY CLASSIFICATION OF THIS PAGE *(When Data Entered)*

20.

implanted with ^{4}He and ^{9}Be have been studied using PL and SIMS.

Following 60 min, 750°C anneals, indium is detected on the surfaces of Si_3N_4 encapsulant layers by both AES and SIMS. SIMS results also suggest that indium may outdiffuse through PSG caps during similar anneals. Indiffusion of Si from the cap to the underlying InP is found to be significant in annealed SiO_2 and Si_3N_4 capped samples. Little such Si contamination is observed after annealing InP with PSG encapsulants. PL measurements indicate that the spectral features and luminosity levels of capped and annealed InP are least altered by PSG encapsulants. From these results it is concluded that PSG encapsulation best preserves the initial characteristics of encapsulated InP during furnace anneals.
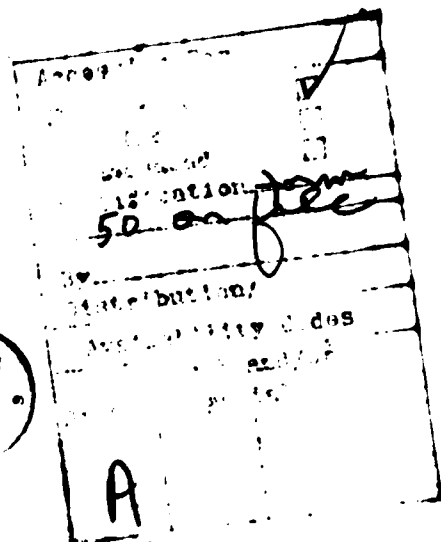
PL measurements indicate that following 51 keV, 10^{13}-10^{15} cm^{-2} implants of ^{4}He, thirty minute anneals at 750°C appear sufficient to restore the lattice to approximately pre-implant levels of quality. For 30 min anneals of 100 keV, ^{9}Be implanted InP, maximum Be activation appears to occur for all doses (10^{13}-10^{15}cm^{-2}) at ~ 750°C, 10^{15} cm^{-2} ^{9}Be implanted InP exhibits saturation of Be activation between 30-60 min with decreasing Be associated luminscence resulting from longer anneals. The Be acceptor ionization energy is estimated to be 41.3 ± 3 meV with characteristic emission at 1.382 eV (5°K).

Depletion zones of the compensating impurity, Cr or Fe, are observed with SIMS in SI InP capped with Si_3N_4 and annealed at 800°C for 30 min. Cr exhibits larger concentration gradients in these zones than does Fe.

Under typical annealing conditions for InP (T > 700°C, t = 15-30 min) it is observed using SIMS that implanted ^{9}Be is a rapid diffusant in SI InP. High dose (10^{15} cm^{-2}), 100 keV implants of ^{9}Be into SI InP result in structured and correlated Be and Cr or Fe atomic profiles. In addition, flat tails of ^{9}Be extending over distances on the order of a micron are observed in high dose implanted InP. Such constant-concentration tails of ^{9}Be are not observed in comparably processed, undoped vapor phase epitaxial (VPE) InP.

Drastic redistribution of Mg and Fe occurs during 30 min anneals of SI InP implanted with 10^{15} cm^{-2}, 250 keV ^{26}Mg. As in the previous Be studies using SIMS, constant-concentration tails of Mg extending over distances of 1 μm or more are observed in the bulk following annealing and the redistribution of Fe is again correlated to the diffusion profile of the implanted acceptor.

With SIMS, little redistribution of ^{28}Si occurs for 30 min, 750°C anneals of 5 x 10^{14} cm^{-2}, 240 keV ^{28}Si implants of SI InP. This behavior of the implanted donor Si differs significantly from the rapid redistribution behavior of the implanted Be and Mg acceptors studied here.

ENCAPSULATION AND IMPLANTATION STUDIES

OF INDIUM PHOSPHIDE

BY

JOHN DAVID OBERSTAR

B.S., University of Illinois, 1975
M.S., University of Illinois, 1977

THESIS

Submitted in partial fulfillment of the requirements
for the degree of Doctor of Philosophy in Electrical Engineering
in the Graduate College of the
University of Illinois at Urbana-Champaign, 1982

Thesis Advisor: B. G. Streetman

Urbana, Illinois

ENCAPSULATION AND IMPLANTATION STUDIES
OF INDIUM PHOSPHIDE

John David Oberstar, Ph.D.
Coordinated Science Laboratory and
Department of Electrical Engineering
University of Illinois at Urbana-Champaign, 1982

Successful ion implantation of InP will depend on detailed information regarding the protective qualities of prospective encapsulants and also the thermal annealing parameters (i.e., time and temperature) required to reorder the implant damaged lattice and to activate the implanted impurity. Using Auger electron spectroscopy (AES), secondary ion mass spectrometry (SIMS), and low temperature photoluminescence (PL) the InP encapsulation properties of CVD SiO_2, CVD PSG (phosphosilicate glass), and rf plasma-deposited Si_3N_4 have been examined. In addition, the annealing/implantation characteristics of semi-insulating (SI) InP implanted with ^{4}He and ^{9}Be have been studied using PL and SIMS.

Following 60 min, 750°C anneals, indium is detected on the surfaces of Si_3N_4 encapsulant layers by both AES and SIMS. SIMS results also suggest that indium may outdiffuse through PSG caps during similar anneals. Indiffusion of Si from the cap to the underlying InP is found to be significant in annealed SiO_2 and Si_3N_4 capped samples. Little such Si contamination is observed after annealing InP with PSG encapsulants. PL measurements indicate that the spectral features and luminosity levels of capped and annealed InP are least altered by PSG encapsulants. From these results it is concluded that PSG encapsulation best preserves the initial characteristics of encapsulated InP during furnace anneals.

PL measurements indicate that following 51 keV, 10^{13}-10^{15} cm^{-2} implants of ^{4}He, thirty minute anneals at 750°C appear sufficient to restore the lattice to approximately pre-implant levels of quality. For 30 min anneals of 100 keV, ^{9}Be implanted InP, maximum Be activation appears to occur for all doses (10^{13}-10^{15} cm^{-2}) at ~ 750°C. At 750°C, 10^{15}cm^{-2} ^{9}Be implanted InP exhibits saturation of Be activation between 30-60 min with decreasing Be associated luminscence resulting from longer anneals. The Be acceptor ionization energy is estimated to be 41.3 ± 3 meV with characteristic emission at 1.382 eV (5°K).

Depletion zones of the compensating impurity, Cr or Fe, are observed with SIMS in SI InP capped with Si_3N_4 and annealed at 800°C for 30 min. Cr exhibits larger concentration gradients in these zones than does Fe.

Under typical annealing conditions for InP (T ⩾ 700°C, t = 15-30 min) it is observed using SIMS that implanted ^{9}Be is a rapid diffusant in SI InP. High dose (10^{15} cm^{-2}), 100 keV implants of ^{9}Be into SI InP result in structured and correlated Be and Cr or Fe atomic profiles. In addition, flat tails of ^{9}Be extending over distances on the order of a micron are observed in high dose implanted InP. Such constant-concentration tails of ^{9}Be are not observed in comparably processed, undoped vapor phase epitaxial (VPE) InP.

Drastic redistribution of Mg and Fe occurs during 30 min anneals of SI InP implanted with 10^{15} cm^{-2}, 250 keV ^{26}Mg. As in the previous Be studies using SIMS, constant-concentration tails of Mg extending over distances of a 1 μm or more are observed in the bulk following annealing and the redistribution of Fe is again correlated to the diffusion profile

of the implanted acceptor.

With SIMS, little redistribution of ^{28}Si occurs for 30 min, 750°C anneals of 5 x 10^{14} cm^{-2}, 240 keV ^{28}Si implants of SI InP. This behavior of the implanted donor Si differs significantly from the rapid redistribution behavior of the implanted Be and Mg acceptors studied here.

ACKNOWLEDGEMENTS

TABLE OF CONTENTS

1. INTRODUCTION

In the last several years the semiconductor community has witnessed the emergence of InP (and its related alloys) into the position of the third most significant semiconductor after Si and GaAs. This has occured because of potential device performance benefits offered by InP over either Si or GaAs in several areas.

One area in which InP devices are expected to have major impact and also find their earliest application is in the field of microwave and millimeter wave solid state components [1-4]. Much of the motivation of the current research in InP originated with a theoretical proposal in 1970 by Hilsum and Rees [5] of a "three-level" electron transfer effect in InP leading to superior microwave characteristics in InP Gunn diodes in comparison to similar GaAs devices. Subsequent experimental results refuted the existence of a "three-level" effect in InP [6,7]; however, the predictions by Hilsum and Rees were an important catalyst in initiating serious research efforts examining the device potentials of InP. As a result of such efforts it is now known that because of several transport and material properties (i.e., energy relaxation time, peak-to-valley ratio, electron diffusion coefficient at fields above threshold, and thermal conductivity) that InP microwave and millimeter wave devices should operate at higher frequencies, with higher efficiency, and with lower noise than comparable GaAs devices [1,4].

Another area in which InP is expected to make significant contributions is in the field of electro-optics [8]. Large efforts are underway at several laboratories to develop sources, detectors, and even integrated optoelectronic circuits for the $1.1 - 1.6$ μm wavelength region where state-of-

the-art optical fibers exhibit their lowest attenuation and dispersion
[9,10]. In contrast to Si or GaAs/AlGaAs based electro-optical devices,
InP/InGaAsP based devices easily span the wavelength region from 0.9 - 1.7
µm. Besides microwave and electro-optical applications there is also
speculation that InP may become important in the fabrication of high speed
integrated logic circuits [11,12]. InP is an attractive material for such
circuits because the interface state density in InP metal-insulator-semi-
conductor (MIS) devices is intermediate between that of Si and GaAs [13-15].
This property means that while retaining the high speed characteristics of
InP or GaAs, InP integrated logic circuits could employ normally-off de-
vices, in marked contrast to the present limitations of metal-gate active
devices in GaAs IC technology.

Despite such research interest in the technological potentials of
InP, the material and devices currently fabricated from it are in a primi-
tive stage of development even in comparison to the still-evolving GaAs
technology. The main factors inhibiting larger research efforts into InP
devices are the availability and quality of single crystal InP and the lack
of a processing technology appropriate to the requirements of InP device
fabrication. The availability of commercial, single crystal InP is presently
confined to a small number of vendors with the majority of high quality,
high purity InP still grown by government or corporate research labs for
"in-house" use. Since the early reports of liquid encapsulated Czochralski
(LEC) growth of InP by Mullin et al. [16,17] major improvements in the
quality of bulk, single crystal InP have occured. In comparison to ordinary,
single crystal Si even the best currently available InP is poor in terms of
purity and crystalline defects. Further refinement in InP growth techniques

and a lowering of the material costs await the economic impetus provided by a wider acceptance of InP by the device community. The present inertia in developing InP devices is primarily due to the fact that only a limited body of work exists concerning the processing characteristics of this semiconductor.

Studies presented in this dissertation address issues associated with one specific area of InP material processing, that of ion implantation. It is envisioned that ion implantation, due to its control and reproducibility, will be used in the manufacture of InP devices such as it is now routinely employed in Si or GaAs fabrication. Compared to other aspects of the newly emerging InP technology, research concerning InP ion implantation is a recent development. The first general surveys of ion implantation in InP were published by Davies et al. [18] and Donnelley et al. [19] in 1977. In the years since these first reports a large number of questions have arisen. Specifically, a few such questions are: Which encapsulant best protects and preserves the characteristics of encapsulated InP during furnace anneals? What are the annealing parameters (i.e., time and temperature) most effective in reordering the implant-damaged lattice and in activating implanted impurities? What is the nature of atomic redistribution, if any, exhibited by implanted or other intentionally present impurities during furnace anneals? Study of these questions forms the core of this thesis. As might be expected in experimental research, during the span of this work additional issues and questions have unexpectedly been encountered and are also described here. The results presented in this work should contribute to the current understanding of ion implantation in InP, and thereby encourage a broader utilization of this material.

2. IMPLANTATION AND ANNEALING PROCEDURES

2.1 Material Characteristics

The bulk InP (100) substrates used in this work were grown by the liquid-encapsulation Czochralski (LEC) method at the Naval Research Laboratory (NRL) [20]. Sn-doped (100) InP (NRL #2-13-H) was used during Auger electron spectroscopy (AES) and secondary ion mass spectrometry (SIMS) studies of the annealing encapsulants to minimize charging effects during analysis of these dielectrics. The Sn concentration in this n-type material was determined by NRL to be approximately 2×10^{17} cm^{-3}. The photoluminescence measurements were made on semi-insulating (SI), Fe-doped (100) InP (NRL #2-10-H). This material had a resistivity of $\sim 8 \times 10^{16}$ cm^{-3} as determined by SIMS [21]. The SIMS studies of atomic redistribution during anneals were performed with both Fe- and Cr-doped InP (100). The Fe-doped material for these redistribution studies was the same as that employed in the photoluminescence measurements. The SI, Cr-doped (100) InP (NRL #1-48-H) had a resistivity of $\sim 5 \times 10^{3}$ Ωcm and a ^{52}Cr atomic concentration of $\sim 6.5 \times 10^{16}$ cm^{-3}, as determined with SIMS [21].

A detailed discussion of the LEC growth procedure, together with an examination of boron contamination in these crystals, is presented in Chapter 10.

2.2 Implantation

Ion implantation is now a standard technique for doping Si and GaAs, and the general properties of the method have been extensively reviewed in the literature [22-27]. Therefore, the remarks in this section will be confined to experimental details most relevant to this work.

The implantation process originates with a plasma containing a number of ionized impurities. These ions are then accelerated to high energy and the desired impurity is selected from the others using mass separation (post-acceleration analysis). This desired ion beam is then raster scanned across the target. The total impurity dose is obtained by monitoring the current flowing from the target or surrounding Faraday cups to ground. Upon penetration of the target the ions lose their energy via three processes: (i) collisions between the ions and the screened nuclei of the target atoms (nuclear); (ii) interactions with the bound electrons of the target (electronic); (iii) charge exchange between ions and host atoms (exchange) [28, 29]. It is the nuclear collision process which, by displacing the target atoms from their lattice sites, produces various forms of radiation defects that must be removed by annealing. Following implantation, the "as-implanted" impurity distribution is a function of the ion's mass, the implantation energy, target orientation, and the material characteristics of the target. The basic features of the implanted profile such as mean range and standard deviation can be fairly accurately predicted from the theory of atomic stopping developed by Lindhard, Scharff, and Schiott (hereafter referred to as LSS)[30-33]. Usually the implant profile can be adequately described by a gaussian distribution using the mean range and standard deviation obtained from LSS [22,24]. It should be noted, however, that certain combinations of projectile, target, and implant energy can result in skewed implant profiles which can be accurately represented only by using higher moments of the distribution. Techniques based on LSS theory for calculating these higher moments are described in the literature [34-37]. The use of such higher moments as it pertains to this work will be discussed in Chapter 8.
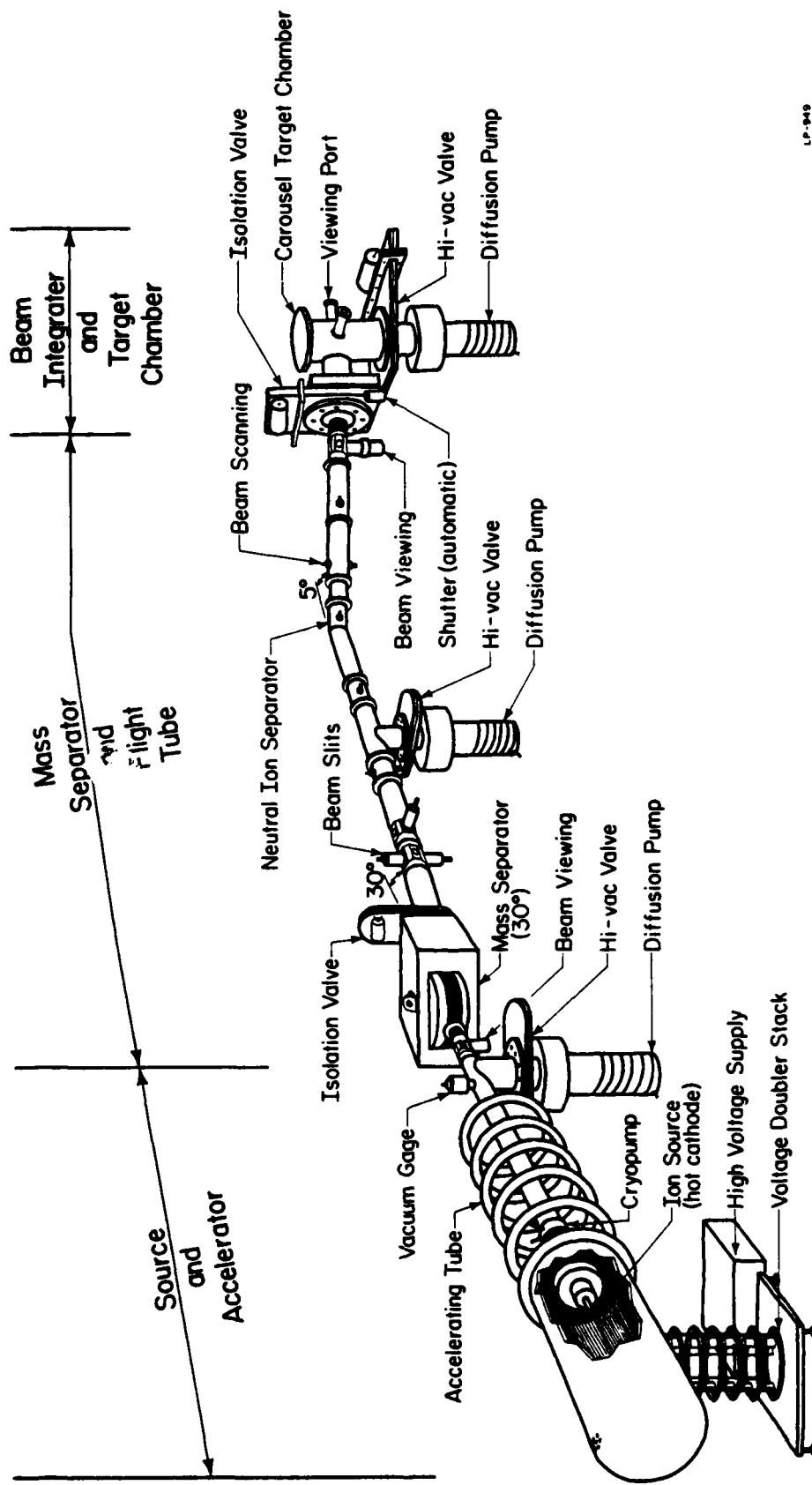
Figure 2.1: Schematic diagram of the 300 keV, A.I. 300-MP ion implanter.

Table 2.1

Implant Schedules and Statistics

Ion	Energy (keV)	Dose (cm^{-2})	Current Density ($\mu A\ cm^{-2}$)	Projected Range[37] (Å)	Standard Deviation[37] (Å)	Peak of Energy Deposition[35] (Å)	Energy Deposition Density ($keV\ cm^{-3}$)
^{4}He	51	10^{13}–10^{15}	0.02	3641	1517	3202	4.6×10^{17}–4.6×10^{19}
^{9}Be	100	10^{13}–10^{15}	0.02	3643	1429	2962	2.0×10^{18}–2.0×10^{20}
^{10}B	126	6.8×10^{14}	0.02	3643	1382	2887	2.0×10^{20}
^{26}Mg	250	10^{15}	0.10	2994	1081	1630	1.7×10^{21}
^{28}Si	240	5×10^{14}	0.04	2464	921	1563	1.1×10^{21}
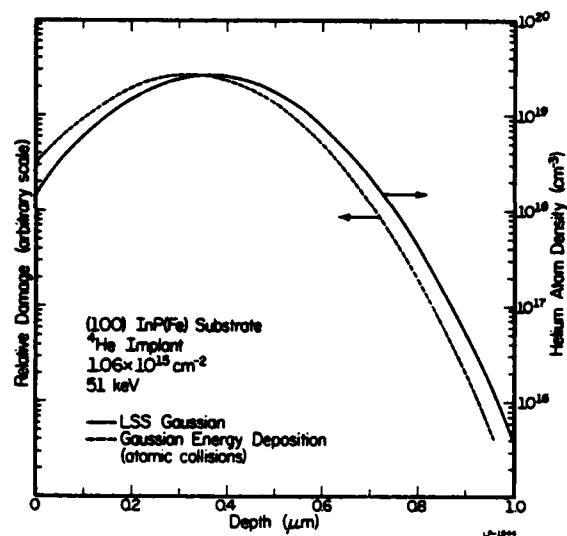
(a)
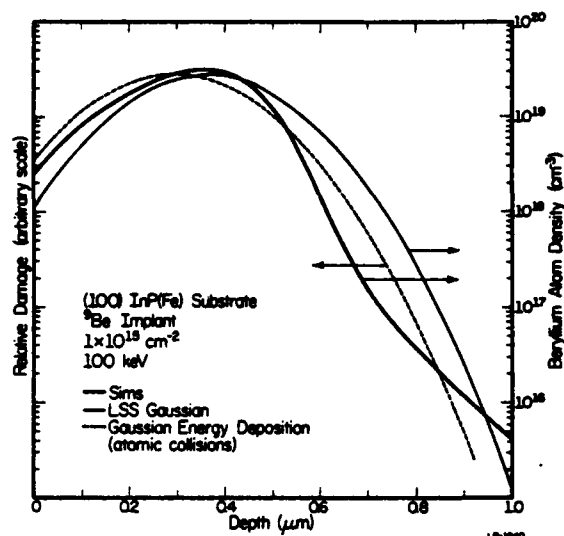
(b)
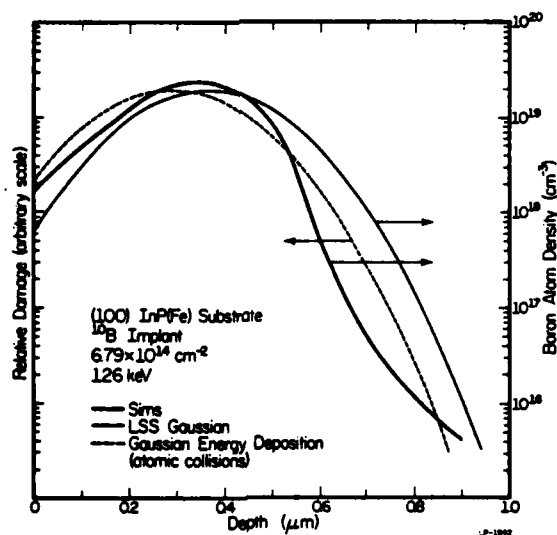
(c)

Figure 2.2: Theoretical and SIMS atomic profiles for: (a) 51 keV, 1.06 x 10^{15} cm^{-2} ^{4}He; (b) 100 keV, 10^{15} cm^{-2} ^{9}Be; (c) 126 keV, 6.79 x 10^{14} cm^{-2} ^{10}B.

(a)   (b)
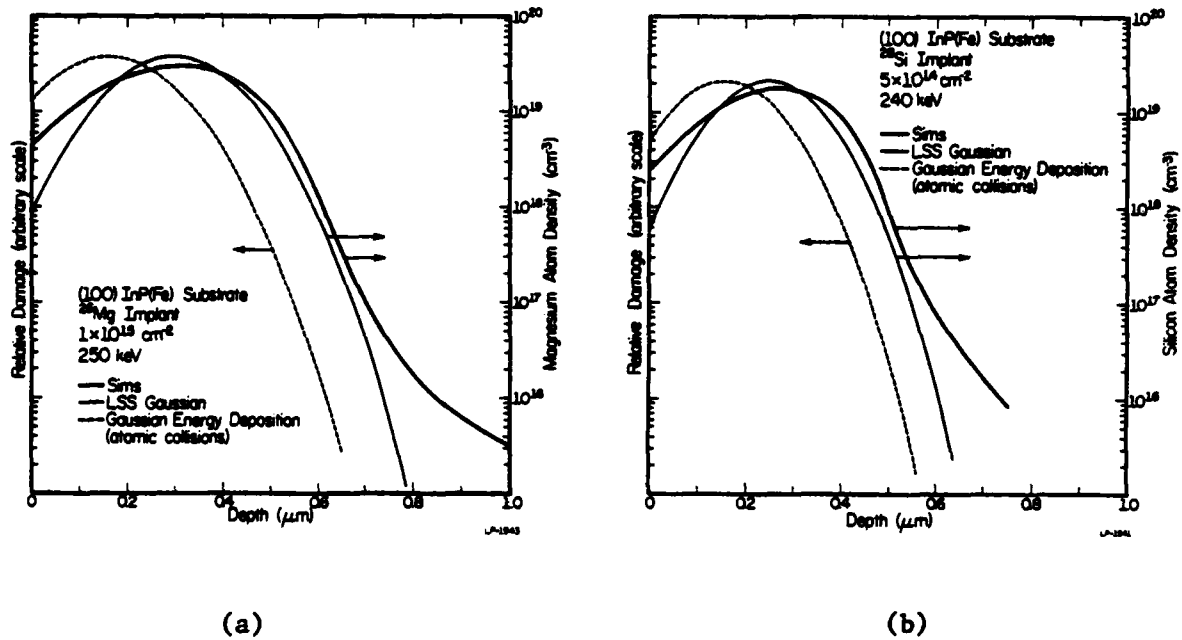
Figure 2.3: Theoretical and SIMS atomic profiles for: (a) 250 keV,
10^{15} cm^{-2} ^{26}Mg; (b) 240 keV, 5 x 10^{14} cm^{-2} ^{28}Si.

Implantations for this work were performed with a 300 keV Accelerators Inc., 300-MP ion implanter shown schematically in Figure 2.1. All implantations were done at room temperature with the sample normal inclined 7° from the incident beam to minimize channelling effects. The schedules for these implants are given in Table 2.1 together with relevant range and damage statistics. Values for the theoretical atomic profiles were obtained from a computer program utilizing the Gibbons, Johnson, and Mylroie formulation [37] of LSS theory (full program output for these implants is given in Appendix 1). The statistics for the damage profiles have been obtained from Winterbon's tables of data [35]. It is assumed that the profile of energy deposited into atomic collisions is directly proportional to the amount of damage (i.e., Frenkel defects, vacancies, and divacancies) produced. The values for the energy deposition density listed in Table 2.1 are approximations based on the product of the dose and the nuclear energy loss per unit length [37]. Shown in Figures 2.2 and 2.3 are the SIMS profiles of the unannealed implants together with the LSS Gaussian and the Gaussian damage profiles constructed from the statistical values of Table 2.1. Gaussian approximations are used for the damage profiles because the detailed distributions are not known.

2.3 Encapsulation Procedures

To protect the surface of InP from thermal degradation during the necessary high temperature anneal following implantation, various thin films were studied as encapsulants. A detailed study of the protective qualities of these caps is given in Chapter 4; only the experimental details of the film depositions are discussed in this section.

Prior to thin film deposition, the samples were rinsed in ultrasonic baths of trichloroethylene, acetone, and isopropyl alcohol. The unimplanted samples used in the encapsulant studies of Chapter 4 were additionally etched in 0.1% bromine-methanol and rinsed prior to encapsulation.

2.3.1 Silicon Dioxide (SiO_2) and Phosphosilicate Glass (PSG) Films

The chemical vapor deposited (CVD) SiO_2 layers (more correctly, SiO_x) were deposited by oxidation of silane (SiH_4). In this system the gases were pre-mixed for 10 min in a nitrogen-flushed cold wall reactor. The InP was then heated rapidly (< 15 sec) by a graphite heater strip to a temperature of 400°C to initiate deposition. The deposition rate for the SiO_2 films used in this work was $\sim 1500 \; Å \; min^{-1}$. Both sides of these samples were encapsulated with $\sim 3500 \; Å$ of SiO_2.

The CVD phosphosilicate glass (PSG) layers were deposited in the same reactor as the SiO_2, by the addition of phosphine (PH_3) to the reactant gases. The deposition temperature for the PSG layers was 300°C and the deposition rate was $\sim 2500 \; Å \; min^{-1}$. Estimates based on AES data indicate that these PSG layers contained 4 - 6 at. % P (6.2 - 9.3 wt. % P). Both sides of these samples were encapsulated with $\sim 4000 \; Å$ of PSG.

The average pinhole density in the SiO_2 films was determined by Cu-decoration [38] to be 130 cm^{-2}. Although corresponding measurements of the PSG film pinhole density were not made, it is expected that this value should be comparable to that of the SiO_2 films as the same deposition system was used for both films.
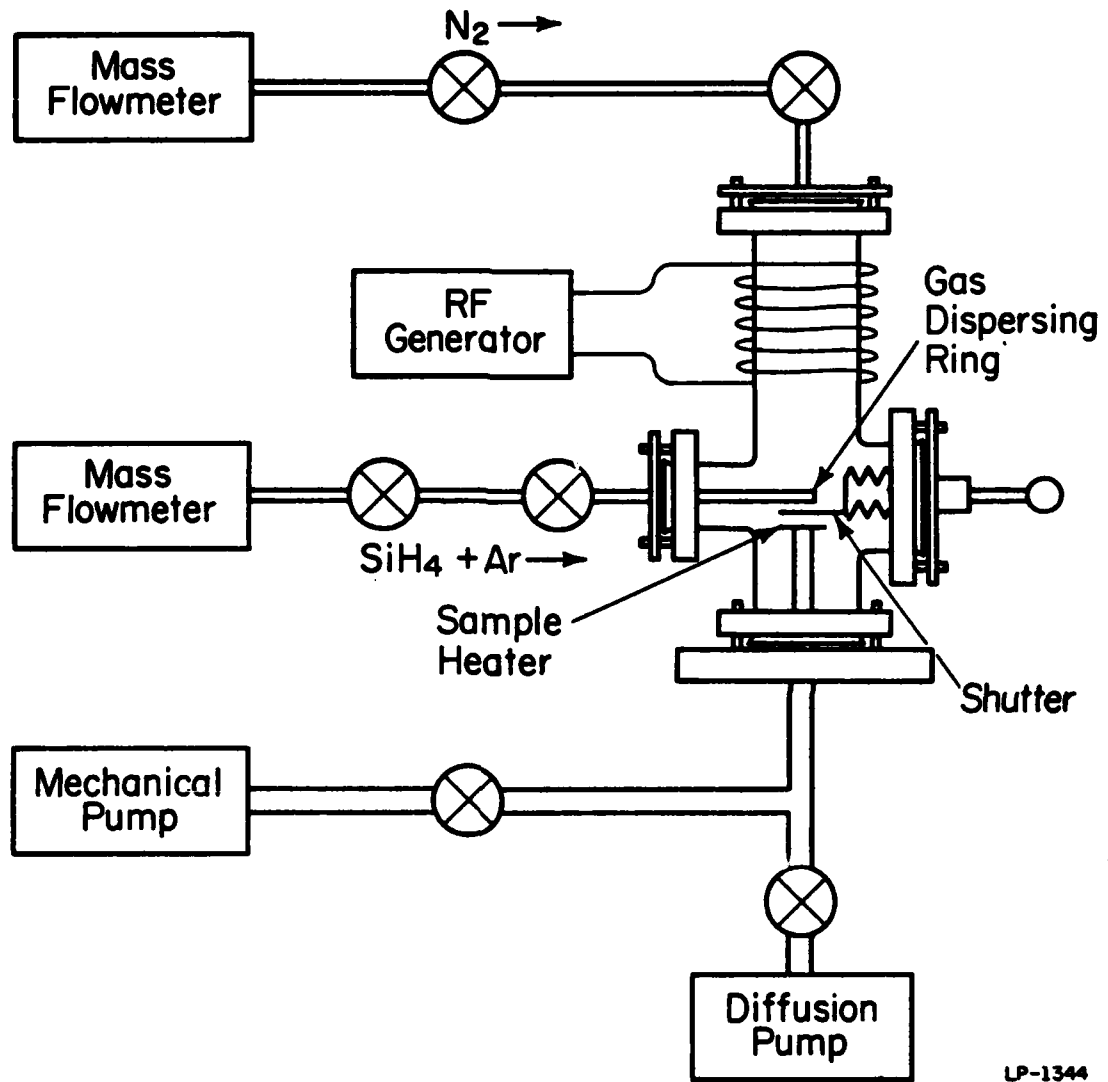
Figure 2.4: Schematic diagram of rf plasma silicon nitride deposition system [39].

2.3.2 *Silicon Nitride (Si_3N_4) Films*

The rf plasma-deposited Si_3N_4 layers used in this work were deposited in the system shown schematically in Figure 2.4. The details of this system have already been extensively discussed in other publications [39,40]. Measurements based on Rutherford backscattering and AES have shown that Si_3N_4 films deposited in this system contain oxygen levels on the order of 1 at. % or less, which has been shown to be important in GaAs encapsulation [39,41]. These Si_3N_4 layers were deposited by heating the samples quickly (< 20 sec) to a temperature of 350°C using a low mass carbon strip and simultaneously initiating the rf discharge. The deposition rate was ~ 110 Å min^{-1}. All Si_3N_4 samples were encapsulated with ~ 2500 Å of Si_3N_4 on both sides.

Using Cu-decoration techniques, the average pinhole density in these Si_3N_4 films was found to be 15 cm^{-2}.

2.4 Annealing Procedures

Thermal anneals were performed in a Trans-Temp silica furnace tube with 320 cm^{-3} volume and a flow of 200 cm^{-3} min^{-1} of desiccated forming gas (4% H_2 in N_2). The annealing temperature was monitored by a chromel-alumel thermocouple directly beneath the sample holder. To minimize thermal shock effects, samples were allowed to slowly (~ 2 min) reach 250°C in a cool furnace zone before insertion into the equilibrated temperature zone. Timing of the anneals was started when the sample temperature was within 5% of the stated anneal temperature. The anneals were terminated by rapidly removing samples to the cold end of the furnace and quenching them with a high velocity flow of forming gas.

The special procedures used for annealing samples in evacuated, silica ampoules will be discussed in Section 4.4.1.

3. CHARACTERIZATION TECHNIQUES

3.1 Auger Electron Spectroscopy (AES)

Auger Electron Spectroscopy (AES) was used in this work to analyze the encapsulants discussed in Chapter 2 for traces of indium or phosphorus which might have diffused through the cap layer during the annealing process. During AES a sample is held in high vacuum and is irradiated by a 1-10 keV electron beam of a few μA. This excitation produces a number of secondary processes of which the most relevant is the ionization of atoms within the irradiated sample volume. In such atoms, the primary beam causes the excitation of inner shell (K,L, and M) electrons. Within a short time ($\sim 10^{-15}$s) an outer shell electron decays to fill this inner shell vacancy. The recombination energy in this decay is either carried away be a photon (X-ray emission) or by another outer shell electron which is ejected from the atom (Auger electon). The energy of the Auger electron is determined by the atomic energy levels involved in the process and is therefore characteristic of the emitting atom. For atoms within 3-20 $\overset{\circ}{A}$ of the surface there is a high probability that the Auger electron will not suffer an inelastic collision, thereby maintaining its characteristic energy. Since the Auger peaks are small compared to the broad background in the electron energy spectrum (arising from inelastically scattered electrons from deep atoms) the energy density curve $N(E)$ is differentiated, $dN(E)/dE$, to improve detection. Most elements have several Auger transitions over a wide energy range, which allows one to identify the element after consulting a table of characteristic Auger electron energies. Depth profiling is accomplished by combining Auger electron spectroscopy with ion beam (Ar^+, Xe^+) sputtering of the surface.

A schematic diagram of a typical AES system is shown in Figure 3.1. A cylindrical mirror analyzer is the most commonly used dispersing element. Detection and amplification are provided by an electron multiplier. A lock-in amplifier or a pulse counter is used to discriminate the low-level Auger peaks from the background continuum. To monitor the intensity of several Auger transitions during depth profiling a multiplexer is employed. More detailed reviews of the Auger process, AES elemental sensitivity, and other AES system capabilities may be found in the literature [28, 43-45].

In the course of the encapsulant studies Auger electron spectra were acquired with either a Model 545 or a Model 595 Physical Electronics Industries, Inc. (PHI) scanning Auger microprobe (SAM). With the PHI 545, derivative mode spectra and conventional multiplexer depth profiles were obtained using primary electron beam energies of 5 keV, primary currents of 0.4-1.0 μA, and typical beam diameters of 5-10 μm. The same information was procured with the PHI 595 using primary electron beam energies of 10 keV, primary currents of 0.09 μA, and typical beam diameters of 1 μm. A 1 keV Xe^+ sputtering beam was used in the PHI 545 and a 1.3 keV Ar^+ beam in the PHI 595. Derivative mode spectra were taken from each surface and at several points in the film bulk by interrupting the ion sputtering beam. To prevent the loss of information from the surfaces, no "ion dusting" of the surface was performed. Wherever possible surface spectra were recorded from areas which had been minimally exposed to the primary electron beam so as to avoid desorption effects. Depth profiles were obtained by monitoring the Si KLL, N KLL, O KLL, P LVV, and In MNN Auger transitions. By using the standard imaging capabilities of the
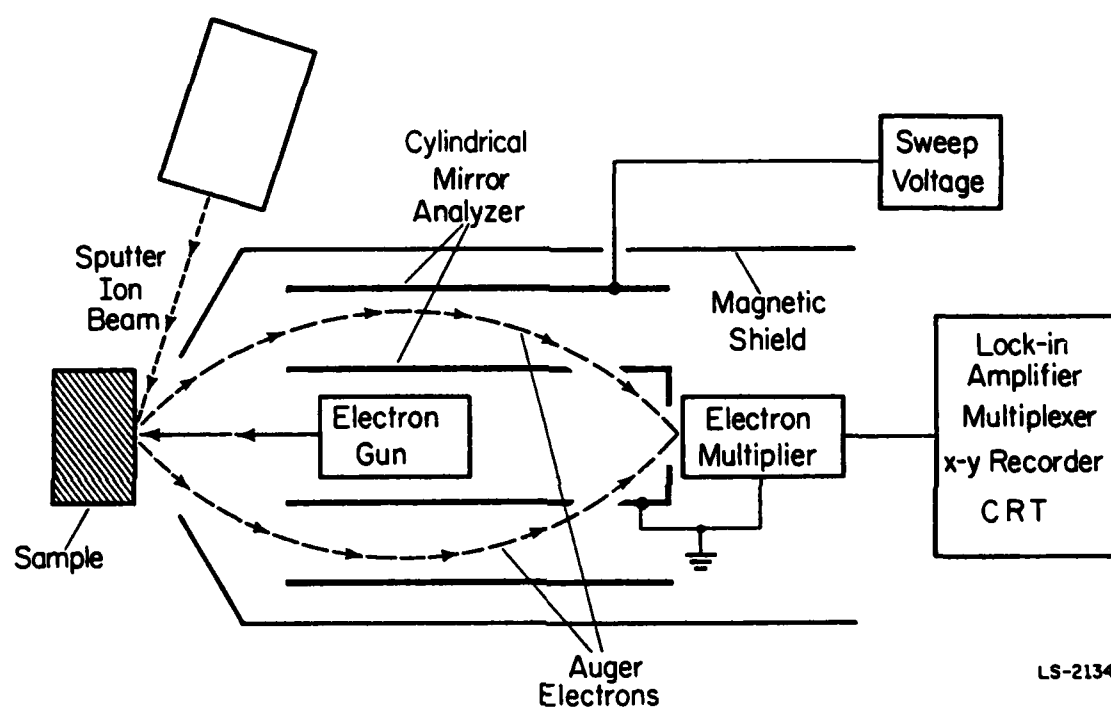
Figure 3.1: Schematic diagram of an AES system (after PHI [42]).

systems, every effort was made to obtain spectra and depth profiles from areas free of pinholes. Images of an element's distribution across a sample surface were obtained by scanning the primary beam across the surface and intensity-modulating the z-axis of a cathode ray tube display with the signal from the element's Auger transition.

3.2 Secondary Ion Mass Spectrometry (SIMS)

A natural distinction can be made between depth profiling techniques, based upon the function of the sputtering process. Some techniques (such as AES) use ion beam sputtering to expose underlying material to a second probing beam which generates the analytical signal. Other depth profiling techniques use ion beam sputtering to generate sputter-ejected material to analyzed. Secondary ion mass spectrometry (SIMS) is an example of the latter technique. SIMS was used in this work predominantly to examine the atomic redistribution of intentionally present impurities such as Cr or Fe and of implanted impurities in InP during thermal anneals. SIMS was also used as a complementary method to AES for characterizing the thin film encapsulants.

In SIMS a sample is bombarded by a 1-30 keV ion beam (Ar^+, $^{16}O_2^+$, $^{16}O^-$, Cs^+) at low (nA-μA) current. Within a depth of 5-50 Å this bombardment produces sputtered material in a number of forms: neutral atoms; molecules; negative and positive secondary ions; multiply charged secondary ions; and dimers. In standard depth profiling one is most often concerned with the first three forms. The yield of secondary ions can vary from 0.1-10% of the total sputtered material [45]. Ion bombardment of a solid produces secondary ions by kinetic [46] and chemical [47,48] processes.

The kinetic process results from the kinetic energy transfer from the bombarding ion to the sample atom. Sample atoms near the surface are then either ejected from the surface or are excited to ionized and metastable states. Unbound electrons near the excitation volume neutralize most atoms before they can escape the surface. Most secondary ions used for mass analysis result from an uncharged, metastable particle escaping from the surface and emitting an electron in vacuum. The chemical process relies on the reduction of the unbound electrons which neutralize the ionized atoms in the bulk by the introduction or presence of a chemically reactive species in the analyzed material. It is assumed that both the kinetic and chemical processes occur concurrently. Published work[47-49] has established that secondary ion yields are enhanced by the presence of an oxide layer on the analyzed surface. In order to utilize this chemical effect oxygen is either introduced into the sample chamber or, more commonly, oxygen ion bombardment is used which results in the formation of a surface oxide by the shallow implantation of oxygen atoms into the sample. Enhanced negative secondary ion yields have been observed with the use of cesium ion bombardment and are believed to result from a reduction in the surface work function by the chemical effect [50,51]. More detailed reviews of the physical processes associated with SIMS analysis may be found in the literature [44,45,50,52].

A schematic diagram of the CAMECA IMS-3f used during the SIMS studies is shown in Figure 3.2. This model is a direct imaging (ion microscope) mass analyzer as originally proposed by Castaing and Slodzian[54]. By feeding the appropriate gas into a high intensity duoplasmatron ion source, primary ions such as Ar^+ or O_2^+ can be produced. Cesium (Cs^+)
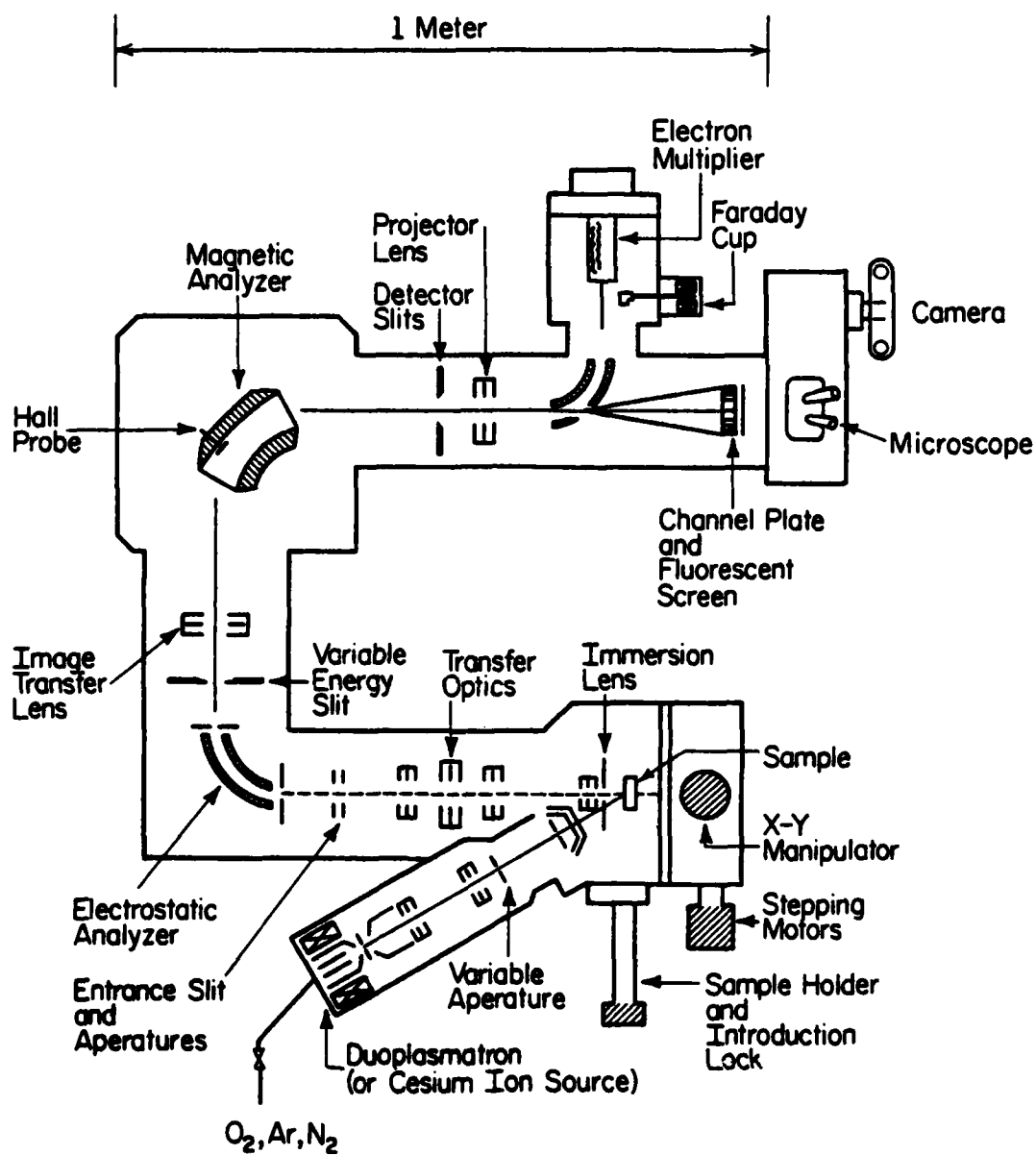
Figure 3.2: Schematic representation of a CAMECA IMS-3f direct imaging secondary ion mass spectrometer (after CAMECA [53]).

ions are produced in a separate ion source which vaporizes solid cesium and ionizes the gaseous atoms. Such primary ions are then extracted from the ion source and accelerated into the keV energy range. Scanning plates then raster the primary ion beam across the sample surface. Usually the primary ion beam is scanned over a much larger area than that used for analysis, with typical crater dimensions varying from 50-500 μm on a side. By proper mechanical or electronic aperturing only those ions originating from the flat-bottomed center of the sputtered crater give rise to the detected signal. Ions from the sloping crater walls are thereby rejected as these would adversely degrade depth resolution[50]. The sample itself is maintained at a repulsive polarity to the desired secondary ions for analysis. These secondary ions are extracted by an electrostatic im-mersion lens which maintains a point-to-point location image of the origin of each secondary ion. A special set of lenses referred to as transfer optics transport the extracted secondary ions to a double-focusing mass spectrometer. Sputtered secondary ions have an energy distribution which peaks in the range of ~ 5-10 eV, but can have low-level tails extending up to several hundred eV[52]. The double-focusing mass spectrometer is advantageous since it can accommodate both the directional spread and energy distribution of ions, resulting in a high transmission efficiency. It accomplishes this by combining ion optical elements which focus the divergent beams in such a way that the velocity dispersions cancel[55,56]. Ion detection can be recorded photographically or observed on a flourescent screen. Quantization of the ion signal is accomplished by either a Faraday cup or electron multiplier. The entire apparatus is interfaced to a small desk-top microcomputer.

In the studies discussed here, the 0_2^+ primary beam (5.0-7.7 keV impact energy) was rastered over areas of $\sim 250~\mu m^2$ and standard precautions were taken to reject spurious signals arising from the crater walls. A Sloan Dektak stylus instrument was used to measure the resultant crater depths. Our experience and that of others[57,58] has shown the uncertainty in such measurements to be $\pm$ 5-6%. These depth measurements together with the assumption of a constant sputtering rate were used to convert the sputtering time scale to a depth scale. The SIMS ion count data were calibrated in terms of concentration by integrating the area under the unannealed profile (corrected for background effects) and setting it equal to the implanted dose. The ^{31}P matrix ion signal was used to calibrate the concentrations in the annealed sample to the concentration scale of the unannealed implant. The concentration scales for ^{56}Fe and ^{52}Cr were obtained from a standard prepared by implanting Fe and Cr into semi-insulating InP. The conversion factors relating ion intensity to concentration were corrected for background effects.

3.3 Photoluminescence (PL)

Low temperature photoluminescence (PL) is a versatile, non-destructive characterization technique. Because radiative recombination processes depend critically on the degree of lattice perfection, PL is an extremely sensitive technique for studying either native or processing-related defects at levels which other characterization methods would fail to detect. Furthermore, the typical binding energies of shallow acceptors and the chemical shifts between them are large enough in GaAs and InP that PL can be readily applied to the characterization of shallow acceptors in

these materials (the characterization of shallow donors requires more
exacting techniques using far infrared spectroscopy). As examples of such
work, PL has been used extensively by members of this laboratory to
characterize implant damage, annealing defects, and implanted impurities
in Si[59], ZnSe[60], GaAsP [61,62], GaP[62], AlGaAs [62], and GaAs[63].
In this work PL has been applied to various InP studies. It has been used
here to characterize the effectiveness of the thin film encapsulants. In
addition, it has been used to determine the annealing parameters of temper-
ature and time required for InP lattice recovery from implant damage and
for optical activation of implanted impurities.

In general, photoluminescence is the recombinative luminescence
emitted from a crystal excited to a nonequilibrium state by irradiation
from light with an energy greater than the crystal's band gap. Because
the absorption coefficient for such light is large, the excitation is
confined to a region very near the irradiated surface. A large non-
equilibrium population of electrons and holes is created within this excited
region by the absorption of energy. Since this population of excess
carriers is nonuniformly distributed near the surface, the photo-generated
carriers diffuse away from the excitation region. While diffusing the
excess carriers are depleted by radiative and nonradiative recombination
processes such that the sample volume probed is confined to roughly a
diffusion length from the irradiated surface. By appropriate choice of
excitation wavelength, the absorption profile and generated carrier
population profile can be chosen to yield recombination luminescence from
near-surface regions of particular interest. As the excess photo-generated
electrons and holes diffuse through the sample, a variety of radiative

decay processes can occur, including free exciton, exciton bound to neutral

donor or acceptor, donor to free hole, acceptor to free electron, donor

to acceptor, or impurity to defect transitions. These transitions are

useful in implantation studies because by carefully monitoring them it

is possible to characterize the optical activation of implanted dopants

and also to determine the extent of defects created by post-implantation

processing. In addition, nonradiative processes indirectly have a role in

in implantation/photoluminescence studies by decreasing the total integrated

sample luminescence and thereby indicating the degree of residual lattice

damage following implantation and annealing. Due to self-absorption effects

it is usually most useful to collect the recombination luminescence emitted

from the irradiated, front surface of the sample.

Figure 3.3 is a schematic illustration of the photoluminescence

system employed in these studies. PL spectra were obtained from samples

mounted in a strain-free manner in a gas-exchange liquid helium cryostat

(Janis "Super Varitemp"). The temperature of the sample mount during photo-

excitation was maintained at 5°K, as monitored by a Ge resistance thermometer

embedded in the copper sample holder. Excitation was provided by the

5145 Å line of a Coherent Radiation Ar-ion laser with an incident power

density of $\sim 10^3$ W/cm^2 and a focused beam diameter of $\sim$ 40 μm. At this

wavelength the 1/e point for the penetration depth of the excitation beam

is 939 Å [64]. The front surface luminescence signal was collected and

focused onto the entrance slit of a 0.5 m Spex Model 1302 double-grating

spectrometer. The optical output was detected by a cooled (77°K) photo-

multiplier with S-1 response using conventional lock-in amplifier
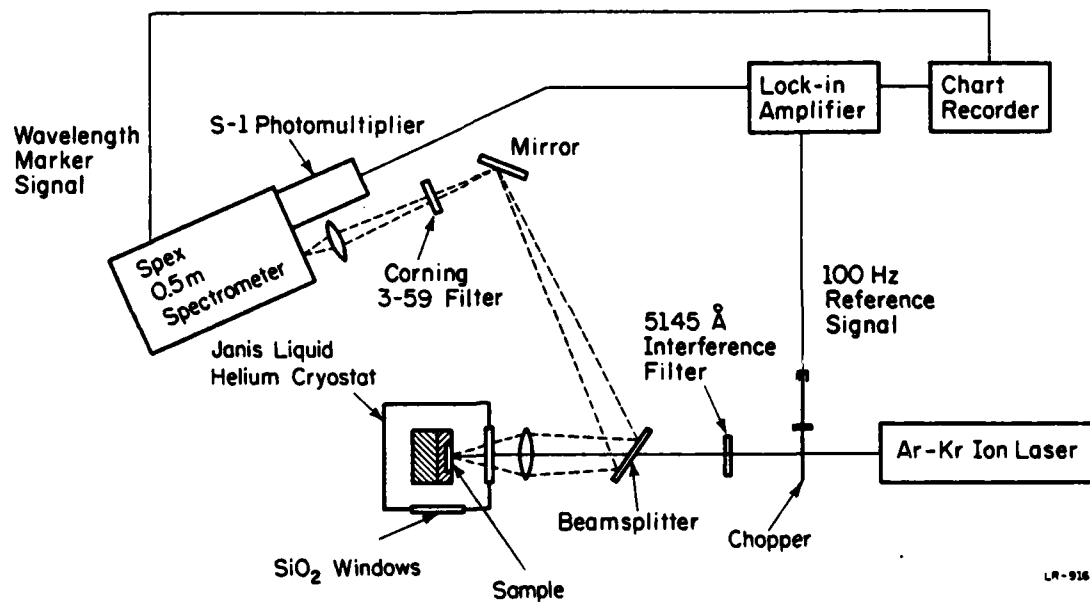
Figure 3.3:   Schematic diagram of the photoluminescence system.

techniques. The spectral resolution used in this work was 6.5 $\overset{\circ}{A}$ (or

1.1 meV). The (near-bandedge) spectral range examined was from 1.44 to

1.30 eV (or 8608 to 9535 $\overset{\circ}{A}$). The emission spectra presented here are

uncorrected for system response.

Throughout the entire series of spectral examinations a single

control sample was maintained to calibrate for possible differences in

system response between runs. All samples were indivudally examined

prior to processing to determine their optical characteristics. Using

this data, the integrated intensity values of the processed samples were

normalized to minimize differences in the spectral characteristics that

would result from sample variations. Each data point in the semi-log

plots represents the average value from at least two samples that were

processed under identical conditions.

3.4 Electron Channelling Patterns (ECP)

In scanning electron microscopy, patterns very similar to the

standard Kikuchi electron diffraction patterns seen in transmission electron

microscopy can be obtained by rocking a collimated electron beam about

a point on a crystal and monitoring the backscattered electron intensity.

Such patterns were first observed by D.G. Coates[65] and are usually

referred to as Coates-Kikuchi lines or electron channelling patterns(ECP).

The ECP are a function of the electron beam orientation with respect to

the crystal lattice symmetry planes. Due to this dependence on lattice

planes, the ECP are useful for a determination of crystalline perfection

because any change or loss in lattice periodicity will result in an

altered or degraded channelling pattern. The technique is particularly

useful for qualitative assessments of lattice perfection in implantation

work, where the process greatly disorders and sometimes even amorphizes
the implanted crystals.

Briefly, the physics of electron channelling patterns may be
explained as follows. When an electron beam is incident on a solid a
variety of energy loss events occur, some of which result in the back-
scattering of the incident electrons. As the angle of incidence from
sample normal increases, the fraction of backscattered electrons also in-
creases. Besides this usual backscattering phenomena there occurs in
crystalline solids an interaction between the incident electrons and the
periodic atomic lattice planes. In the diffraction theory of low energy
electrons (below 100 keV) the Schrödinger equation for the electron
probability distribution in a periodic lattice yields a solution which is
a superposition of two types of Bloch waves[66,67]. One set, say type 1
Bloch waves, have maxima at atomic sites, implying strong atomic interactions
with resultant high backscattering probabilities. The other set, type 2
Bloch waves, have maxima between atomic planes, connoting weak atomic inter-
actions with high transmission, low backscattering probabilities. The
changes in backscattered electron intensity observed when the incident beam
is rocked through various angles from normal occur because, except at certain
angles, either type 1 Bloch waves (high backscattering) or type 2 Bloch
waves (low backscattering) are predominantly excited. The particular angles
at which type 1 and type 2 Bloch waves are equally excited are the Bragg
angles θ_B satisfying the classical Bragg diffraction relation

$$n\lambda = 2d \sin \theta_B$$

For angles less than θ_B type 1 Bloch waves are preferentially stimulated,

resulting in high intensity because of the large backscattering. For angles greater than θ_B type 2 Bloch waves predominate, resulting in lower backscattering intensity. Therefore, as the incident electron beam sweeps through the Bragg angle for each order of crystalline lattice planes there is a discernible change in backscattered electron intensity. It is this periodic variation in backscattered intensity which defines the electron channelling pattern.

In the work discussed here, electron channeling patterns (ECP) were obtained using a JEOL model JSM-35 scanning electron microscope equipped with components (JEOL 35-SDC) which permit selected area channeling patterns to be observed. Beam voltages of 35 kV were used to analyze areas with ~ 20 μm diameters. The backscattered electron signals were usually differentiated to enhance the sharpness of the normal channeling pattern. To examine the electron channeling patterns at various depths, some samples were chemically etched in bromine-methanol. The depths of these etched surfaces were measured with a Sloan Dektak stylus.

4. ENCAPSULANT STUDIES

4.1 Introduction

If implantation is to become a standard doping technique in InP, it will be necessary to develop reliable annealing methods. Annealing is required to activate the implanted impurity and also to reorder the damaged crystalline lattice. Either beamed-energy (laser or electron beam) anneals or thermal (furnace) anneals can be employed, but furnace annealing is the most prevalent method. Thermal anneals of III-V compounds such as GaAs and InP require care to prevent surface deterioration at the common annealing temperatures.

The thermal degradation of unprotected InP surfaces has been described in articles by Bayliss and Kirk [68,69] and by Lum and Clawson[70]. This surface damage results from the preferential evaporation of the column V component at elevated temperatures. At 800°C the P vapor pressure over InP is $\sim 10^{-3}$ atm. and is generally orders of magnitude greater than that of As over GaAs for the temperature range considered here [71]. Therefore, InP surface degradation during anneals can be much more severe than in GaAs. Mass spectroscopic studies [72] indicate that the (001) InP surface evaporates congruently up to $362 \pm 5^{\circ}$C, with higher temperatures resulting in a disproportionate loss of P. In addition, electrical measurements of unprotected, n-type InP annealed for 15 min at 450°C show that a 2 μm surface depletion zone is formed, presumably by P vacancies [73]. These temperatures are comparatively low to the thermal anneal temperatures of $700-800^{\circ}$C which photoluminescence [74,75] and electrical measurements[19,76,77] indicate are needed to successfully reorder the damaged lattice and to activate the implanted impurity.

To prevent thermal damage at elevated temperatures it is necessary to anneal InP in a carefully controlled environment [70,78-81] or to encapsulate the surface with a thin dielectric layer having suitable mechanical and chemical properties to suppress evaporation and yet not interact significantly with the material [74-77, 82-84]. Several recent reviews of ion implantation III-V compounds have discussed the major role encapsulants can have in determining the electrical characteristics of these materials [25-27]. In this work Auger electron spectroscopy (AES), secondary ion mass spectrometry (SIMS), and low temperature photoluminescence (PL) were used to characterize the annealing properties of the most commonly employed InP encapsulants – chemical vapor deposited (CVD) SiO_2, rf plasma-deposited Si_3N_4, and CVD phosphosilicate glass (PSG).

Before discussing the results of these studies, it is necessary to point out that the anneal temperature limits for the SiO_2, PSG, and Si_3N_4 layers described here were approximately 650°C, 800°C, and 840°C respectively. Detailed analysis of the high temperature failure of these caps is presented in Chapter 5.

4.2 AES Results

AES examination of as-deposited and annealed (600°C, 60 min) SiO_2 caps did not indicate the presence of P o In either on the surface or in the film bulk. It has been reported [85] that 15 min anneals of CVD SiO_2 caps in InP similarly showed no AES P or In within the films for temperatures in the range from 500 - 750°C. Wilmsen et al. [86] have reported, however, that based on ESCA (electron spectroscopy for chemical analysis) measurements In was detected throughout as-deposited CVD SiO_2 layers on InP when the deposition temperature is 340°C or greater. ESCA analysis by Wilmsen's

group of one of our annealed (600°C, 30 min) CVD SiO_2 layers suggested

that small amounts of In and P were distributed throughout the film.

Because of the large area analyzed by ESCA and because of the pinhole

density in our CVD SiO_2 films, it is unclear if these In and P signals

represent actual outdiffusion or a loss through pinholes. AES examination

of as-deposited and annealed (750°C, 60 min) PSG caps did not reveal the

presence of In or P (above the initially deposited level) either on the

film surface or in the bulk. Auger spectra from as-deposited Si_3N_4 caps

also did not show any levels of P or In, nor was P detected anywhere in

annealed (750°C, 60 and 30 min) Si_3N_4 caps of InP. However, In was found

on the surfaces of annealed (750°C, 60 and 30 min) Si_3N_4 caps. This In

was confined exclusively to the near surface region and quickly dropped

to background levels within the film bulk. These results agree with

AES measurements by Kasahara et al. [82] who found In outdiffusion and

no indication of P outdiffusion from Si_3N_4 caps of InP annealed for 20

min at 900°C. It appears on the basis of AES measurements, therefore, that

In loss from InP surfaces does occur with Si_3N_4 encapsulation.

Figure 4.1 shows the Auger derivative mode spectra of the In MNN

transitions from several Si_3N_4 caps annealed for 30 min at 750°C. Comparison

of Figures 4.1(a) and 4.1(b) indicates that "thick" ($\sim$ 2000 $\AA$) Si_3N_4 caps

are superior to thinner layers in their ability to suppress In loss from

InP surfaces. The captions "exposed" and "unexposed" in Figure 4.1 refer

to whether the Si_3N_4 cap was in contact with the forming gas during the anneal

("exposed") or whether, in the same forming gas-flushed furnace, the cap

was covered with a thin, demetallized silica slide ("unexposed"). Suppressed

(a)
Si$_3$N$_4$ Cap
1000 Å
750°C, 30 min
Exposed

(b)
Si$_3$N$_4$ Cap
2300 Å
750°C, 30 min
Exposed

(c)
Si$_3$N$_4$ Cap
2300 Å
750°C, 30 min
Unexposed

Auger Intensity dN/dE (arbitrary units)

404 eV

397 eV

404 eV

397 eV

404 eV

397 eV
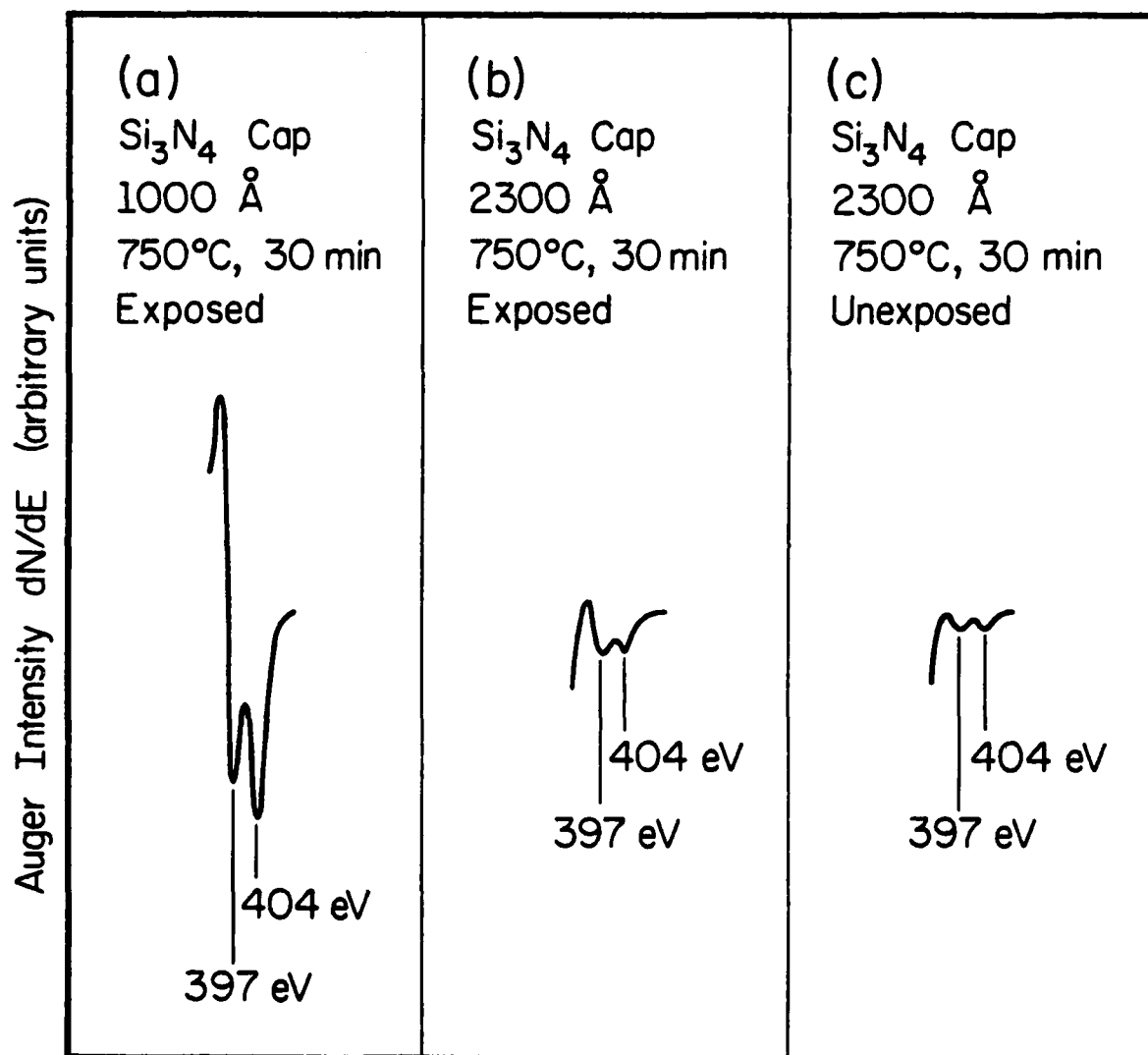
LP-2088

Figure 4.1: Indium MNN peaks in various Si$_3$N$_4$ caps annealed at 750°C for 30 min. "Exposed" means the cap was in contact with forming gas during the anneal. "Unexposed" means the cap was covered by a demetallized silica slide during the anneal [87].

In loss has consitently been observed in such covered Si_3N_4 films annealed at temperatures above 700°C, as Figure 4.1(c) indicates. Others have reported using this covering technique [74], and it has even been used to successfully anneal bare InP surfaces up to 760°C [81].

AES examination of the encapsulants on InP has several limitations. These include: (1) overall atomic sensitivity of only ~ 0.5 at. %; (2) phosphorus desorption by both electron and ion beam irradiation [88]; and (3) indium desorption stimulated by electron beam irradiation [89]. As a result of these sensitivity limitations, In and P must be present in relatively large concentrations in the film to be detected by AES, allowing only gross characterization of the encapsulants. For these reasons, SIMS was used in addition to AES to characterize the encapsulants.

4.3 SIMS Results

To supplement the information obtained with AES, the annealing characteristics of the InP caps were examined using secondary ion mass spectrometry (SIMS). The primary advantage of SIMS over AES is its much higher elemental detection sensitivity. Because of this, over the last several years there has been a growing acceptance and use of SIMS in the analysis of dielectric thin films [90-92]. The technique is not without its problems, however, and before discussing the results it would be worthwhile to point out some difficulties in the use of SIMS for dielectric thin film analysis.

The major problem which occurs during SIMS depth profiling of dielectric films is surface charging. This can promote field enhanced migration of the profiled ions [93]. More importantly, by affecting the energy distribution of secondary ion currents, such charging effectively degrades the

the technique's ultimate sensitivity [94-96]. To minimize this sensitivity degradation, several methods of reducing charging effects have been used with varying degrees of success. These methods include deposition of a conducting film onto the surface [93,97]; use of conducting grids in contact with the surface [91,92,94]; and flooding of the surface with an electron beam [95,96]. None of these methods has been generally adopted as a standard procedure. Also, since surface charging is seldom totally absent from SIMS depth profiles of dielectric films, another problem lies in finding a valid and convenient method of reprocessing data to correct for the sputter yield variations caused by charging. The prevalent technique is to normalize the profiles of interest to the profile of a host element or another element within the film of known constant concentration [91,92,96]. To our knowledge, however, it has not been demonstrated that the secondary ion yields of all impurities in a given matrix will respond uniformly to charging.

For the profiles presented here no special procedures were performed to reduce surface charging. Several areas were analyzed from each film and the results were averaged to construct representative impurity profiles. After constructing such profiles the data was re-processed by normalizing all signals levels to the ^{28}Si profile.

Examination of the annealed caps revealed that none of these films contained ^{31}P at levels above those observed in as-deposited films (where the ^{31}P level may be real or an instrumental background level). It seems likely that molecular interference from silicon hydrides such as $(^{30}SiH)^+$ may account for the difficulties in detecting low ^{31}P levels. The hydrogen for these hydrides may originate within the film itself or from residual

water vapor contamination in the analysis chamber. The [115]In profiles

from as-deposited and annealed (600°C, 60 min) SiO_2 caps also did not differ

significantly. The [115]In "real time" (unnormalized) profiles of PSG and

Si_3N_4 caps before and after anneals (750°C, 60 min) are shown in Figures

4.2 and 4.3, along with the normalized profiles. It is important to note

the charging effects observed during these sputter profiles before con-

sidering the [115]In profiles. Based on AES measurements described in

section 4.3 it is known that the Si levels in these layers are fairly

uniform. Therefore, the large variations in the [28]Si signals evident in

the unnormalized profiles of Figures 4.2(a) and 4.3(a) are presumably

the result of charging effects during sputtering (comparable charging

effects have been reported for [30]Si in SIMS profiles of SiO_2 films) [91,92].

Of significance here are the observed differences between unannealed and

annealed films in their response to charging. The [28]Si levels before

and after annealing in Figures 4.2(a) and 4.3(a) suggest that our as-

deposited and annealed Si_3N_4 caps charge similarly, whereas our PSG caps

showed considerable variation in their charging behavior depending on whether

or not they were annealed. Such variation in charging behavior was also

observed between unannealed and annealed SiO_2 films. These variations in

charging did not affect our interpretation of SiO_2 results, as identical

conclusions were drawn from both real time and normalized profiles; but

they do affect our interpretation of the [115]In profiles from PSG caps.

The unnormalized [115]In profiles in Figure 4.2(a) suggest that there is

a large accumulation of [115]In near the surface of the annealed PSG cap.

The normalized [115]In profiles of Figure 4.2(b) show a similar surface

accumulation of In but contain a confusing depressed [115]In level in the

PSG Cap – 750°C, 60 min Anneal

(a) Unnormalized

Unannealed ^{28}Si
Annealed ^{28}Si
Unannealed ^{115}In
Annealed ^{115}In

(b) Normalized

Relative Intensity

Sputtering Time (min)

LP-2091
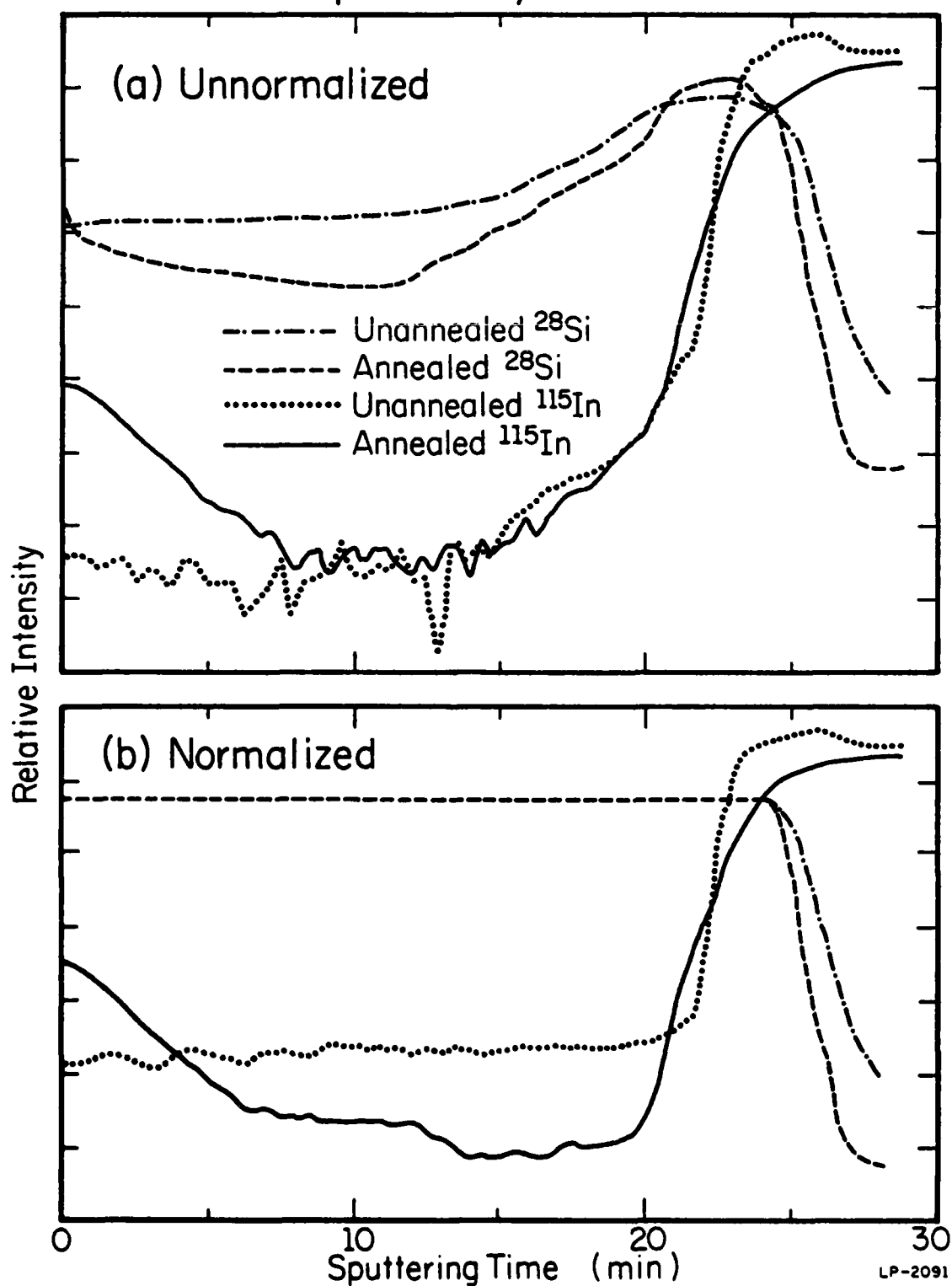
Figure 4.2: SIMS profiles of ^{115}In in annealed (750°C, 60 min) PSG films on InP: (a) unnormalized ("real-time") data and (b) normalized to ^{28}Si [87].

Si₃N₄ Cap – 750°C, 60 min Anneal
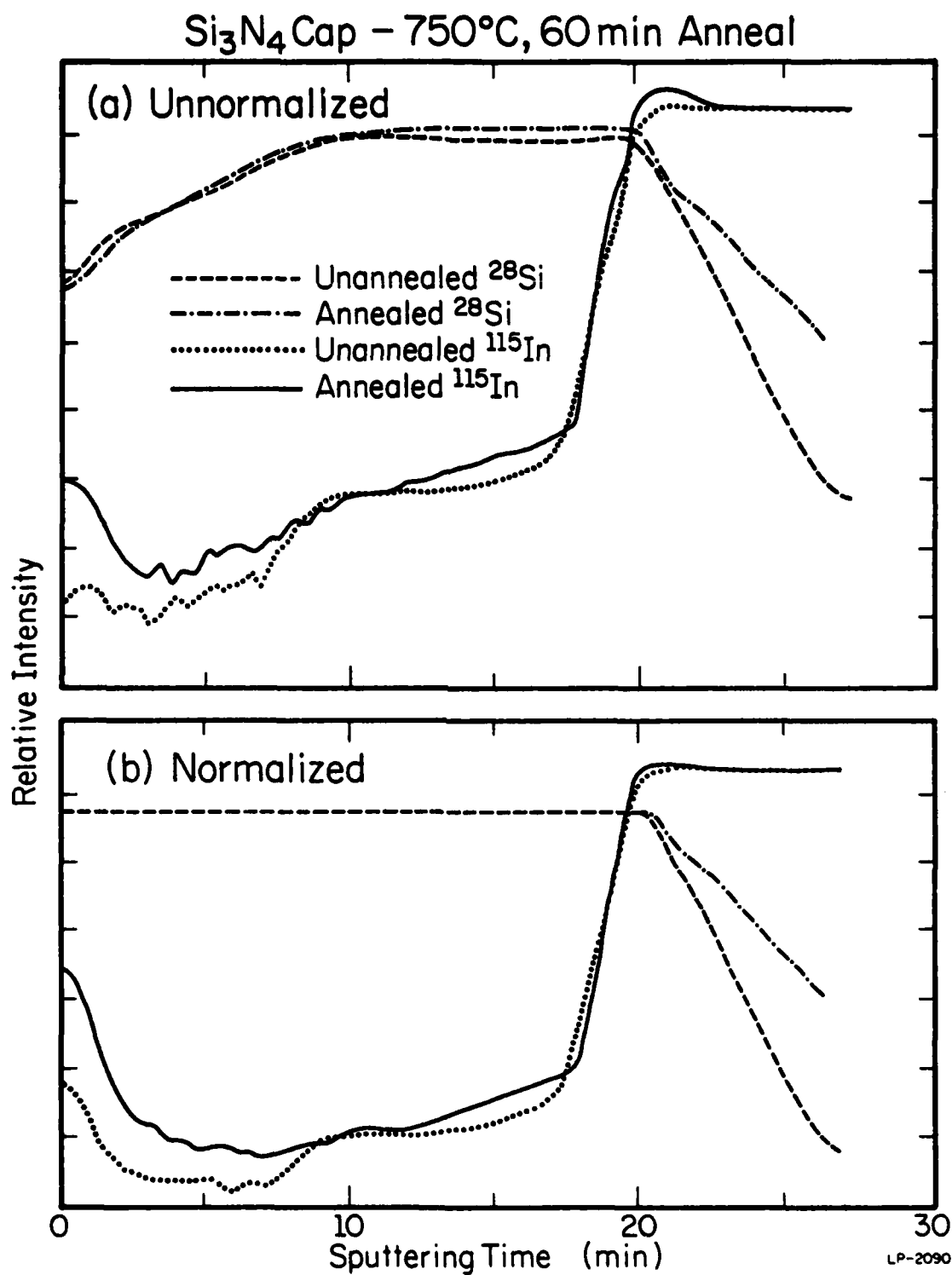
Figure 4.3: SIMS profiles of ^{115}In in annealed (750°C, 60 min) Si₃N₄ films on InP: (a) unnormalized ("real-time") data and (b) normalized to ^{28}Si [87].

bulk compared to the unannealed PSG film. It appears that at levels detectable with SIMS, In outdiffusion through PSG caps of InP is possible; however, more work will be needed to clearly resolve this issue. In comparison to the PSG ^{115}In profiles, the ^{115}In profiles from annealed Si_3N_4 caps shown in Figure 4.3 are not ambiguous. Both unnormalized and normalized profiles show an outdiffusion of In in annealed Si_3N_4 caps of InP, in agreement with our Auger results.

In a more conventional application, SIMS was used to analyze the InP surfaces beneath the caps of annealed samples. This was done to determine the extent of Si contamination, if any, originating from the cap. Si indiffusion into InP from the encapsulants is of significance since Si is a donor in InP [98] and will therefore influence the near surface electrical characteristics of such contaminated InP. To avoid sputter knock-in of ^{28}Si from the caps into the analyzed region, the caps were removed from the sample surfaces prior to SIMS analysis with buffered hydroflouric acid. The resulting SIMS ^{28}Si profiles are shown in Figure 4.4. Despite the low annealing temperature, Si indiffusion into InP from our SiO_2 cap is the most pervasive of the three caps examined, with levels above background extending to ~ 1.0 µm for 60 min anneals at 600°C. Si_3N_4 caps annealed for 60 min at 750°C show higher than normal ^{28}Si levels extending into the bulk a distance of ~ 0.7 µm. Of the three films analyzed here, only our PSG caps indicated no significant ^{28}Si indiffusion into the underlying InP during annealing. Besides ordinary diffusion, it is possible that the driving mechanism for the Si contamination arises from strain at the interface between the cap and the InP substrate. This would be consistent with the observation of less

Figure 4.4: SIMS profiles of ^{28}Si after annealing InP at the indicated temperatures and times with: (a) a SiO_2 cap, (b) a Si_3N_4 cap, and (c) a PSG cap. For comparison, the ^{28}Si SIMS level from unprocessed material is superimposed on each figure [87].
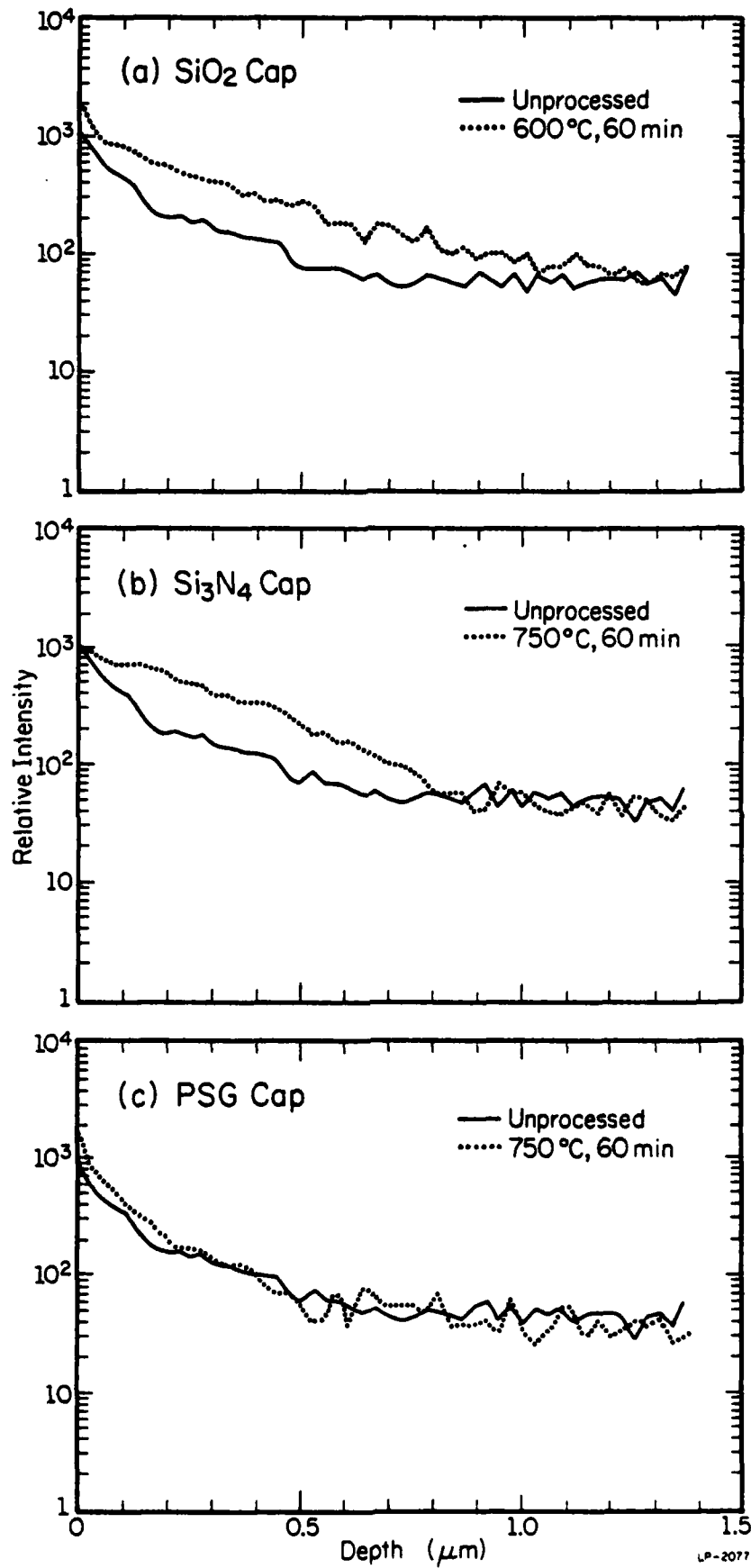
Figure 4.4

Si contamination from the PSG cap because a PSG cap with 5 at. % P is better matched to InP in terms of thermal expansion coefficient than the other two caps [19].

4.4 Photoluminescence Results

From the AES and SIMS results already discussed, no information was obtained concerning possible P outdiffusion through the caps. To examine this effect, low temperature photoluminescence measurements were made of InP samples annealed in controlled atmospheres and InP samples annealed with the three caps. A previous study of GaAs encapsulants by our group has demonstrated the usefulness of PL in characterizing the effectiveness of encapsulants [41].

Figure 4.5 shows the PL spectra from virgin samples of the semi-insulating, Fe-doped InP (100) used in these studies. This material exhibits three luminescence bands at 1.414, 1.384, and 1.341 eV. These are attribured respectively to bandedge luminescence (BE), band to acceptor and donor to acceptor (BA/DA) luminescence, and luminescence from the 1-LO phonon replica of the BA/DA band. A fuller discussion of these features and their origins appears in Chapter 6.

4.4.1 *Controlled Atmosphere Anneals*

In order to interpret the PL spectra of InP annealed with our caps, it was first necessary to examine and characterize the spectra from bare InP annealed in controlled environments (vacuum, In-source, and P-source). Such heat treatments should favor the creation of annealing defects which might subsequently lead to defect related luminescence peaks in the PL spectra.
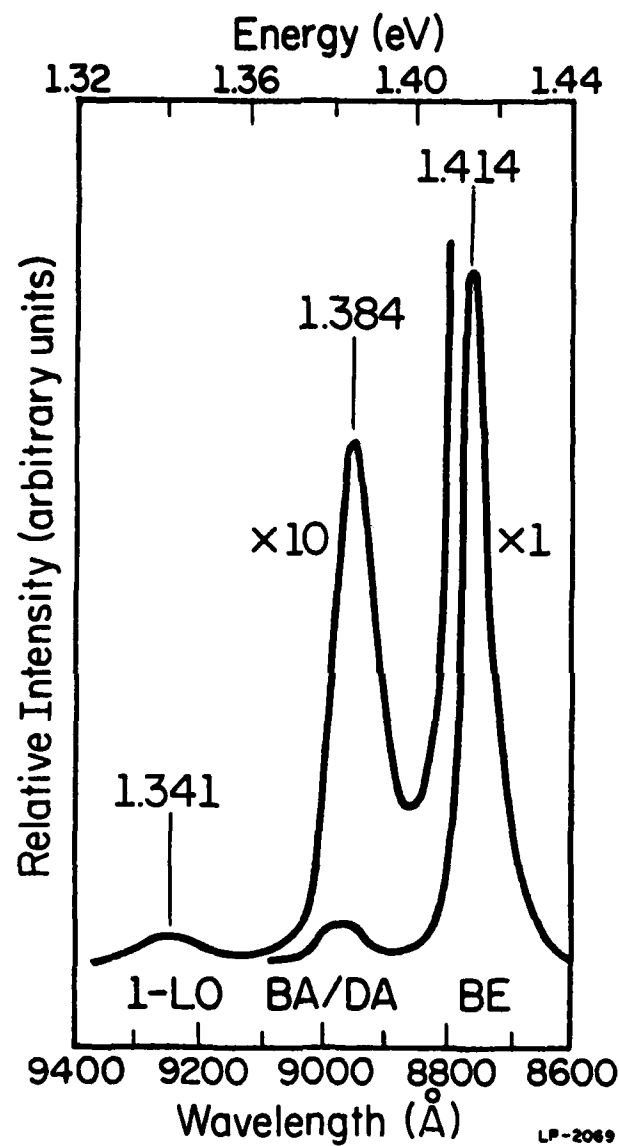
Figure 4.5: Photoluminescence spectra of virgin Fe-doped, semi-insulating InP (100). Numerical factors are amplification relative to that used for the bandedge luminescence [75].

Annealing ampoules were fabricated from silica tubing. A small dimple was formed in each ampoule to prevent contact between the samples and source materials during the anneals. The silica tubes were cleaned in standard organic solvents and placed in aqua regia for 24 hrs. The ampoules were then rinsed in deionized water and electronic grade isopropyl alcohol. Immediately prior to insertion of the sample and source materials, the tubes were outgassed by heating them with an oxyhydrogen flame while being evacuated with a diffusion pump. The source materials were five-nines pure In and six-nines pure, red P purchased from Alfa Ventron. After insertion of the samples and source material the ampoules were evacuated to 10^{-5} Torr and sealed off to a volume of about 5 cm^3. The amount of red phosphorus used in these anneals was calculated to create a P vapor pressure of 0.5 atm. at 750°C, sufficient, according to published vapor pressure curves of P over InP [77,99], to insure an overpressure of P. For In-source anneals, excess amounts of In were inserted in the ampoules to yield saturation overpressure during the anneals. After annealing, the ampoules were quenched by inserting the tube end furthest from the sample in cold water. Two-point probe electrical tests of sample surfaces following anneals at 750°C in any of the three environments revealed that in all cases the originally semi-insulating InP had formed a conductive layer.

Figure 4.6 exhibits the BA/DA bands from samples annealed in the three environments for the temperature range from 450-750°C. Within the limits of resolution used in this work, no shifts were observed in the peak positions of the BE bands. Changes were noted in the relative intensities of the BE bands but these changes generally varied in accordance with the decreases or increases shown by the BA/DA bands. Because of this and for simplicity, only emission in the region of the BA/DA band is shown in

Figure 4.6: Photoluminescence spectra of the BA/DA band after annealing SI
InP at the indicated temperatures and times in the following sealed ampoule
environments: (a) to (d), vacuum; (e) to (h), In vapor; and (i) to (l), P
vapor. Numerical factors are amplification relative to the bandedge
luminescence of Figure 4.5 [101].

44
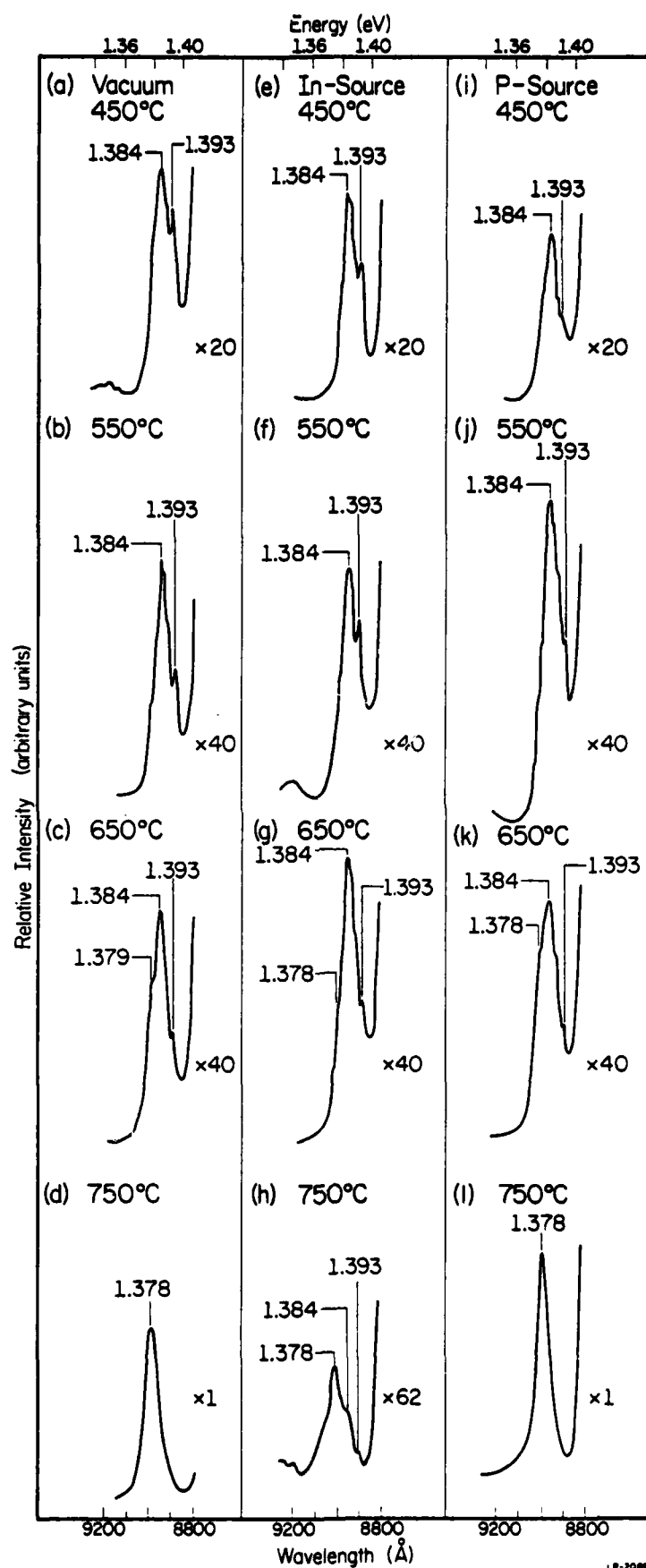
Figure 4.6

Figure 4.6. Three significant features of these spectra are: (1) variations in the BA/DA band intensities with annealing temperature; (2) a new emission peak at 1.378 eV which becomes the dominant emission of the BA/DA band for $T > 650^\circ C$; and (3) the appearance of a new, small emission peak at 1.393 eV in $450^\circ C$ and $550^\circ C$ vacuum and In-source anneals.

Comparing the amplification factors of the various BA/DA bands from samples annealed between $450^\circ C$-$650^\circ C$ to that of the BA/DA band from virgin material, it is clear that the annealed samples suffer a loss in luminosity. Presumably these intensity losses result from competition between the usual radiative processes operative in virgin material and new, non-radiative processes involving defects created by the anneals. This luminosity loss continues and worsens for samples annealed in In-source ampoules at least up to anneal temperatures of $750^\circ C$ (Figure 4.6(h)). The general trend is reversed, however, in $750^\circ C$ vacuum and P-source anneals (Figures 4.6(d) and 4.6(ℓ)). The BA/DA band intensity in these samples is now greater than that observed in the virgin spectra of Figure 4.5. The increase of BA/DA band integrated intensities above virgin levels is correlated to the increasing dominance of the 1.378 eV transition. This is certainly the case when one compares the featureless BA/DA bands of Figures 4.6(d) and 4.6(ℓ) to the structured BA/DA emission band of Figure 4.6(h). We will discuss possible causes for these increases in intensities when the spectra from capped samples are shown in the following section.

It is perhaps surprising that the vacuum and P-source anneals behave similarly at the high anneal temperature of $750^\circ C$. This result is understandable, however, in view of the physical surface deterioration of the samples. As expected, the samples annealed in the P-source ampoules

showed no visible deterioration and retained their mirror-like finish.
Samples annealed in the In-source ampoules had the most thermally damaged
surfaces of the three sets. This may be attributable to the In-source
acting as a large sink for the phosphorus which evaporates from the sample
surfaces. Surprisingly, the samples annealed in vacuum exhibited much
better surfaces than did the corresponding In-source annealed samples. With-
out excess In present in the ampoule to absorb the evaporated phosphorus,
it appears that the sample surface is eventually capable of achieving P
vapor phase equilibrium within the sealed environment, preventing further
surface deterioration.

In the 650°C anneals of Figure 4.6, a weak shoulder appears on
the BA/DA band at 1.378 eV which at 750°C becomes the new, dominant emission,
peak of the band. This new spectral peak at 1.378 eV may originate from
several sources, including Si contamination from the silica ampoule walls
(Si is a known contaminant of liquid phase epitaxial InP grown between
550°C-715°C) [100], annealing-induced radiative defects, or near-surface
gettering of impurities from the bulk. At present the specific origin of
this spectral feature at 1.378 eV cannot be identified.

The new feature of particular interest here is the small emission
peak at 1.393 eV, which is most pronounced in the 450°C and 550°C vacuum
and In-source anneals. In comparable P-source anneals, this 1.393 eV
feature appears only as a weak shoulder on the BA/DA band. Only a few of
the many published studies of InP photoluminescence have mentioned emission
peaks in this energy region [102-104]. To our knowledge Williams
et al. [102] were the first to report a feature at 1.39 eV. Although they
did not speculate on the origin of this emission, they noted that their

1.39 eV line increased in intensity when the samples were annealed for 5 min in H_2 at 500°C. They also found that the intensity of the 1.39 eV line increased as the epitaxial layer from vapor phase epitaxial InP was etched off and became strongest near the layer-substrate interface (where thermal damage to the substrate surface occurs prior to growth of the epitaxial layer). More recently, Yamazoe et al. [103], have reported observing a small emission line at 1.39 eV in 1 hr anneals of InP. On the basis of these reports and from the near suppression of the 1.393 eV line in 450°C and 550°C P-source anneals, we believe the 1.393 eV emission line results from P-related defect luminescence. Some loss of P can be exptected in the P-source anneals as the atmosphere is equilibrated. To minimize such transients of the phosphorus vapor pressure in the ampoule, others have reported converting red phosphorus to white phosphorus by heating the ampoule prior to annealing [105].

The annealing behavior of the 1.393 eV line is of interest, since for T > 550°C the intensity of this emission line decreases dramatically. This reduction could result from radiative recombination competition with the newly emerging line at 1.378 eV. It is also possible, however, that the decreased intensity may result from a reduction in the concentration of the P-related defects responsible for the 1.393 eV emission at anneal temperatures greater than 550°C. This would imply that the associated defect is a vacancy complex rather than isolated P vacancies, since the latter's concentration would be expected to increase with temperature instead of decreasing. Yamazoe et al. [103] have reported similar decreases in the PL intensities of other InP annealing related defects for T > 550°C. In addition, their deep level transient spectroscopy (DLTS)

measurements of four annealing related deep level traps indicate that all four traps achieve their maximum concentrations at $500^{\circ}C$ anneal temperatures.

4.4.2 Encapsulant Anneals

The BA/DA bands from samples encapsulated and annealed with our three encapsulants are shown in Figure 4.7. All encapsulant layers were removed from the annealed samples with hydroflouric acid prior to PL measurements. Two-point probe electrical tests of sample surfaces following $750^{\circ}C$ anneals with PSG or Si_3N_4 caps indicated that conductive surface layers had formed during the anneal. Similar effects following anneals with PSG and Si_3N_4 caps have also been reported by others [19,82].

On the basis of the appearance of the 1.393 eV line in Figures 4.7(a) to 4.7(d) it is clear that P-vacancy related defects are created in all our SiO_2 capped samples. It may also be observed that at temperatures between $600-650^{\circ}C$, the 1.378 eV emission is of comparable intensity to the 1.384 line present in virgin material. (The spectra of Figure 4.7(d) was obtained by analyzing regions away from the cracks which normally develop in our SiO_2 caps at this temperature.) Although not evident in Figure 4.7, for samples annealed at T < $650^{\circ}C$, we often observe the BA/DA band peak at 1.381 eV instead of at the usual location of 1.384 eV. Local variations in the single crystal or in the cap may account for the inconsistent position of the BA/DA band peak. We believe that this 1.381 eV peak is related to the 1.384 eV line and that the shift in energy results from the overlap of the 1.384 eV peak with the emerging 1.378 eV peak.

Figure 4.7: Photoluminescence spectra of the BA/DA band after annealing SI InP at the indicated temperatures and times with the following encapsulants: (a) to (d), SiO_2; (e) to (h), Si_3N_4; and (i) to (1), PSG. Numerical factors are amplification relative to the bandedge luminescenc of Figure 4.5 [101].

Figure 4.7

By examing the spectra of our PSG capped and annealed samples shown in Figures 4.7(i) to 4.7(ℓ) it appears, because of the presence of shoulders at 1.393 eV, that P-vacancy defects are also created to some extent in these samples. This could be due to pinholes or to insufficient phosphorus content in our PSG to totally suppress phosphorus outdiffusion. Further work with various types of PSG films will be required to clarify this issue. Comparing Figure 4.7(ℓ) to Figures 4.7(d) and 4.7(h) it can be concluded that these PSG caps are much more effective than SiO_2 or Si_3N_4 in preventing the formation of the 1.378 eV emission feature.

Judging by the intensity of the 1.393 eV emission, our Si_3N_4 caps seem comparable to the PSG caps in their ability to prevent substantial phosphorus outdiffusion (Figures 4.7(e) to 4.7(h)). Note that for anneal temperatures $T > 650^{\circ}C$ the 1.378 eV emission comes to dominate the BA/DA band of our Si_3N_4 capped and annealed samples. Furthermore, the luminosity of the BA/DA band in the $750^{\circ}C$ anneal (Figure 4.7(h)) is now significantly greater than that found in virgin samples. Also, as previously discussed with the SiO_2 spectra, we sometimes find the BA/DA band peak in Si_3N_4 capped samples annealed at $T < 650^{\circ}C$ at 1.381 eV rather than at 1.384 eV.

It was mentioned in the previous section that the emission at 1.378 eV may originate with Si indiffusion, annealing-induced radiative defects, or near surface gettering of impurities from the bulk. A comparable downward energy shift of 6 meV by the BA/DA band peak has also been recently reported by Shanabrook et al. [106] for Si_3N_4 capped and annealed SI InP(Fe). From temperature dependent PL measurements they attribute the new emission to donor-acceptor pair recombination, with the implication that the donor concentration has increased. They conclude

that such donors could be provided by Si indiffusion from the Si_3N_4 cap or from accumulation and redistribution of donors from the bulk to the surface. From the appearance of the spectra in Figures 4.7(h) and 4.7(ℓ) and from the SIMS ^{28}Si profiles shown in Figures 4.7(b) and 4.7(c) of the preceding article it certainly appears likely that Si could play a role in the 1.378 eV peak. It is not clear at this point, however, why the 1.378 eV peak does not similarly dominate the BA/DA band of SiO_2 capped and annealed samples when the SIMS ^{28}Si profiles from these samples showed the deepest indiffusion.

In our high temperature ampoule anneals (Figures 4.6(d) and 4.6(ℓ)) and again in our 750°C, Si_3N_4 anneal (Figure 4.7(h)) we have observed BA/DA band and BE band intensities greater than those found in virgin material. Such increases in bandedge luminosity have been reported in the past for annealed, semi-insulating GaAs(Cr) [107]. Recent reports have also described increases in the bandedge emission of InP samples capped with Si_3N_4 and annealed [74,106]. It has been noted here and elsewhere [101] that these increases in luminosity are correlated to the emergence of the 1.378 eV feature. Such increases in luminosity may result from the annealing out of native defects in bulk InP, surface accumulation of impurities with greater radiative efficiency than those normally present, or from a reduction of the surface space charge layer due to the presence of the impurity and/or defect involved in the 1.378 eV emission.

Figures 4.8(a) and 4.8(b) plot the integrated intensities of the BE and BA/DA bands for Si_3N_4 and PSG capped and annealed samples. Before pointing out the significance of these curves we must comment on a feature not discussed in this article which affects our Si_3N_4 data. We have
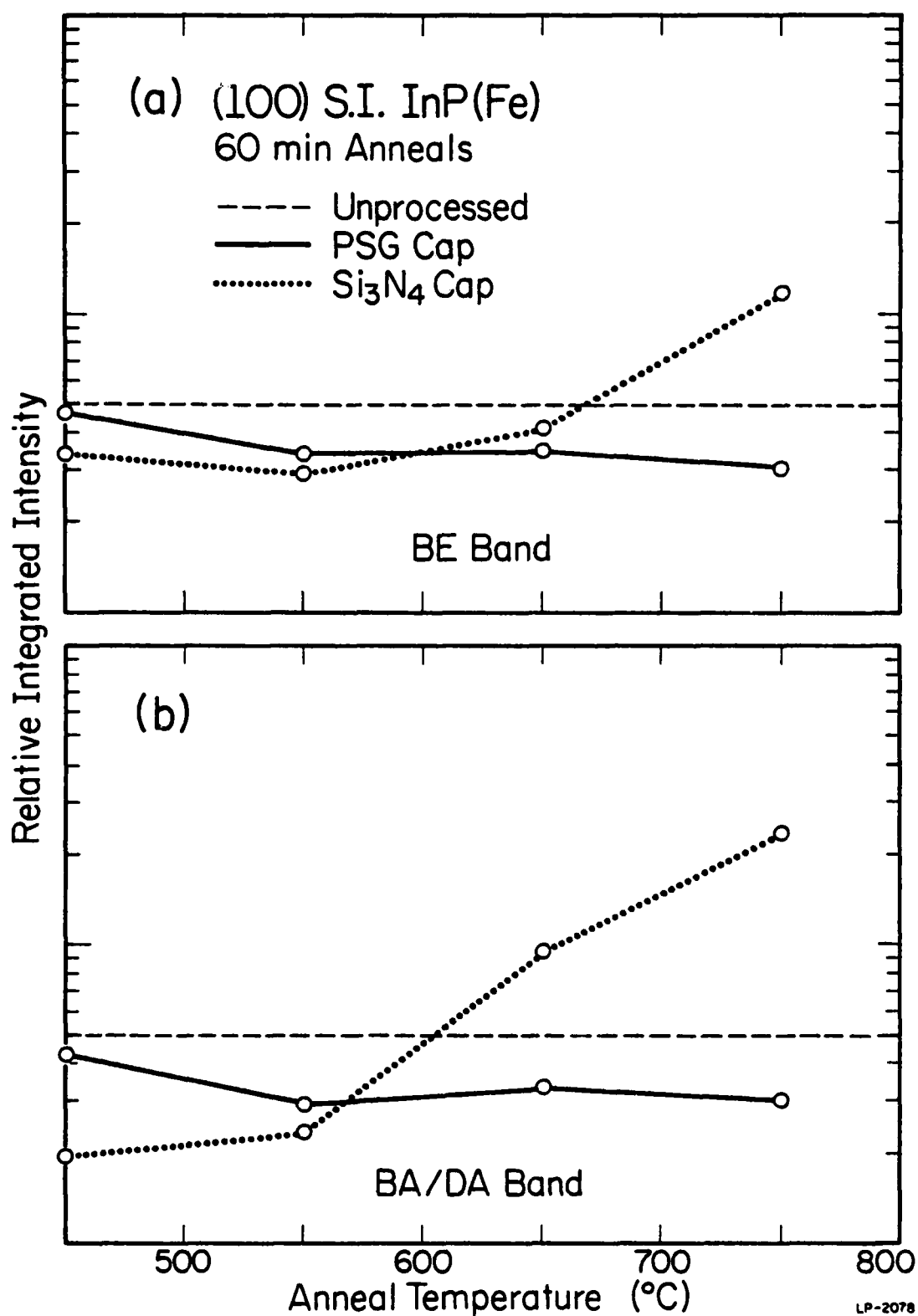
Figure 4.8: Integrated intensities of (a) the BE band and (b) the BA/DA band from SI InP capped with either Si_3N_4 or PSG and annealed for 60 min at the indicated temperatures [101].

observed that the spectra from samples annealed with Si_3N_4 at T > 650°C (and also from some high temperature P-source anneal spectra) contain a discernible tail of luminescence on the low energy side of the BA/DA band (Figures 4.6(ℓ), 4.7(g), and 4.7(h)). This broad tail extends from approximately the low energy side of the BA/DA band to the position of the 1-LO phonon band, with weak structures sometimes appearing at 1.363 eV and 1.355 eV. In this spectral range, Heim [108] has reported a band centered at 1.358 eV which is associated with long radiative decay times, and he attributes it to a DA transition involving a slightly deeper acceptor than the one responsible for the peak of the BA/DA band. White et al. [109] have observed a transition in this region at 1.367 eV, which they identify as a DA transition to Cd acceptors. It is feasible that the luminescence we observe in this region originates with an acceptor gettered to the surface from the bulk, but at present our data does not support specific indentification. Whatever the origin, the effect of this luminescence tail has not been included in the measurements of the Si_3N_4 BA/DA integrated band intensities plotted in Figure 4.8. Considering the Si_3N_4 spectra of Figure 4.7 together with the results of Figure 4.8 it becomes clear that the BE and BA/DA intensities in the Si_3N_4 capped and annealed samples exceed virgin levels when the 1.378 eV emission dominates the BA/DA band. More importantly, it can be concluded from Figure 4.8 that our PSG caps maintain the PL properties of the underlying InP samples with much higher integrity than do our Si_3N_4 caps.

4.5 Summary

The results of these studies of InP annealing encapsulants can be summarized as follows:

(1) Both AES and SIMS indicate that In diffuses through our Si_3N_4 caps when annealed at $750^\circ C$ for 60 min. Few conclusions could be drawn concerning outdiffusion in either SiO_2 or PSG caps. Some SIMS results suggest that In outdiffuses through PSG caps for 60 min, $750^\circ C$ anneals, but more work will be required to substantiate this.

(2) It is found from AES that thick ($\sim$ 2000 Å) Si_3N_4 caps are superior to thinner layers in their ability to suppress In loss from InP surfaces. Additionally, AES measurements consistently indicate that In loss from Si_3N_4 encapsulated samples can be reduced by covering the Si_3N_4 layer with a thin silica slide during the anneal.

(3) On the basis of SIMS results, Si indiffusion is found to be significant in our SiO_2 and Si_3N_4 capped and annealed samples. The PSG caps examined here showed little Si contamination of the underlying InP after annealing.

(4) PL spectra from samples annealed in controlled environments (vacuum, In-source, and P-source) indicate that a spectral line at 1.393 eV results from P vacancy-related defect luminescence.

(5) The presence of the 1.393 eV line suggest that at least up to anneal temperatures of $650^\circ C$, our SiO_2 caps allow P loss from the sample surface. A weak feature at 1.393 eV is also evident in the spectra of PSG capped and annealed samples, suggesting some P loss. This may occur due to pinholes or to inadequate phosphorus in these PSG films. Our Si_3N_4 caps seem comparable to the PSG layers in their ability to prevent substantial P outdiffusion.

(6) High temperature anneals ($T \sim 750^{\circ}C$) with Si_3N_4 result in the emergence of a new peak at 1.378 eV which dominates the BA/DA emission. This emission at 1.378 eV may originate with Si indiffusion, annealing-induced radiative defects, or near surface gettering of impurities from the bulk. Associated with this are BA/DA band and BE band integrated intensities greater than those found in virgin material.

(7) In comparison to SiO_2 or Si_3N_4, PL measurements indicate that PSG caps best preserve the spectral features and the luminosity levels of InP after annealing.

5. HIGH TEMPERATURE LIMITS ON ENCAPSULATION

5.1 Introduction

Perhaps the most prevalent problem with thin film encapsulants is their tendency to fail at high anneal temperatures by cracking, peeling, or blistering [19,110]. Such film failure is usually attributable to thermal expansion mismatch with the underlying material, but other factors such as chemical interactions can play a role [110]. In addition, there is considerable variation in the properties of thin films deposited by the same method at various laboratories. The anneal temperature limits for the SiO_2, PSG, and Si_3N_4 layers discussed here were approximately $650^{o}C$, $800^{o}C$, and $840^{o}C$ respectively. Our CVD SiO_2 films fail by cracking at temperatures in excess of $650^{o}C$ whereas CVD SiO_2 films on InP prepared at other labs have been reported to survive temperatures up to $700^{o}C$ before cracking. Our CVD PSG films also fail by cracking in a fashion similar to our SiO_2 layers. Contrary to other reports [84] cracking of Si_3N_4 caps on InP is not a universal phenomena for $T > 750^{o}C$. We routinely observe Si_3N_4 layers surviving 60 min anneals at $800^{o}C$ without cracking. The causes of the high temperature limits on the SiO_2 and Si_3N_4 caps are discussed in this chapter.

5.2 SiO_2 Cracking

5.2.1 Experimental Observations

The major difference observed in this work between SiO_2 encapsulated InP annealed below $650^{o}C$ and that annealed above $650^{o}C$ is the cracking phenomena shown in Figure 5.1. This cracking behavior was seen in all our samples annealed above $650^{o}C$. Other results indicate that the temperature for cracking of SiO_2 films is not unique but can vary in the
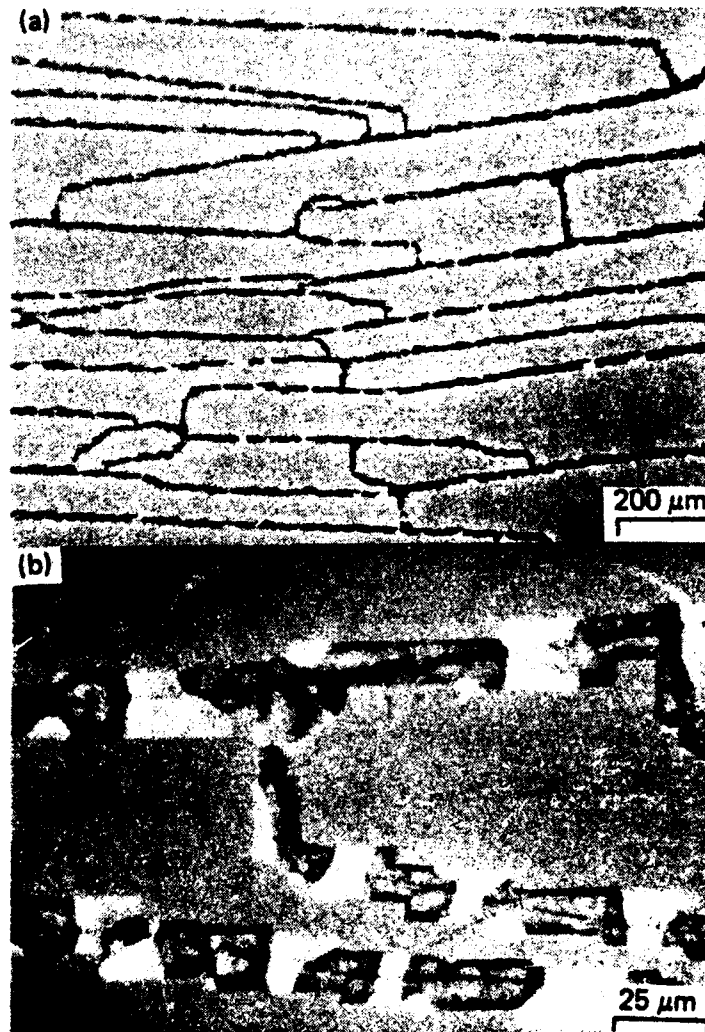
Figure 5.1: Optical micrographs of InP encapsulated with ~ 2500 Å of CVD SiO$_2$ and annealed at 700°C for 30 min [110].

range from 650 to 750°C [19,111]. To determine the role of film thickness, samples were prepared with SiO_2 layers of ~ 1000 Å, 1500 Å, 2300 Å, and 3000 Å on both sides and annealed at 750°C for 30 minutes. Each of these samples showed cracking of the SiO_2 encapsulant similar to that shown in Figure 5.1.

It was possible to observe the evolution of these cracks through the semi-transparent liner of the furnace. Following insertion into the equilibrated temperature zone, small cracks appear at the edges of the samples within 5 minutes. Generally, samples are cleaved into a rectangular shape. The cracking begins at the long edges of such samples and propagates essentially parallel to the short edges. Within this time period no cracks originate in the central portions of the samples unless a gross pinhole develops there. As time progresses these cracks increase in number and propagate from the edges toward the center. Cracks running parallel to the long axes of the samples generally develop after the major cracks meet near the center of the sample.

Figure 5.1(b) shows three distinct regions in the neighborhood of a crack network. The region which comprises the majority of this photograph is the uncracked SiO_2 encapsulant. We shall label the dark areas within the cracks region I and the light, metallic-appearing areas in these cracks region II. In addition, close examination of the uncracked SiO_2 in Figure 5.1(b) reveals the presence of small, hairline features between the major cracks. It is assumed that with further heat treatment these would develop into major cracks also.

A JEOL scanning electron microscope (SEM) was used to examine the cracks in greater detail. Figure 5.2 is a SEM micrograph showing the three regions mentioned above. The central portion of this figure corresponds to region II and the darkened edges to region I.

Two other features can also be seen with improved clarity in Figure 5.2. One of these features, seen as a line in Figure 5.1(b), is a clearly visible track running through the large crack structure. The width of this small track is $\sim$ 1.5 μm, while that of the larger crack is $\sim$ 25 μm. The path of this 1.5 μm feature does not appear to be associated with any major crystalline axes, in contrast to the 25 μm feature which is oriented piecewise in (100) directions as seen more clearly in Figures 5.1(b) and 5.3(a). It is also clear from Figures 5.1(b) and 5.2 that the 25 μm feature is not symmetrically centered about the 1.5 μm track.

The other feature revealed in Figure 5.2 is the apparent shearing of the SiO_2 layer. What appears to be a tearing of the SiO_2 film can be seen in the vicinity of the 1.5 μm track. Examination of the 1.5 μm feature in areas corresponding to region I show this same shearing of the SiO_2 layer.

A series of photographs were taken after the SiO_2 layer was removed with buffered HF. Two photographs from this series are shown in Figure 5.3. Figure 5.3(a) is a photograph taken with the microscope focused on the surface plane of the sample. The features visible in this photograph correspond to region II in Figure 5.1(b). The speckled surface of these regions closely resembles the surface of bare InP after annealing for 30 minutes at $650^{\circ}C$ in an In overpressure. This suggests that these regions are P-depleted InP islands. The dark regions in Figure 5.3(a)
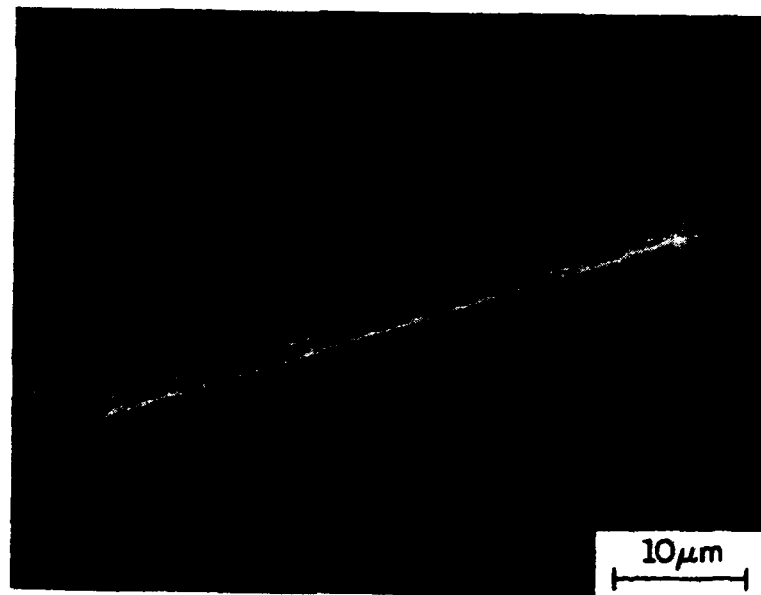
Figure 5.2: SEM micrograph of a cracked region in SiO_2 encapsulated InP annealed at $750^{\circ}C$ for 30 min. The central region is a P-depleted, In-rich material buildup in a thermal etch trough [110].
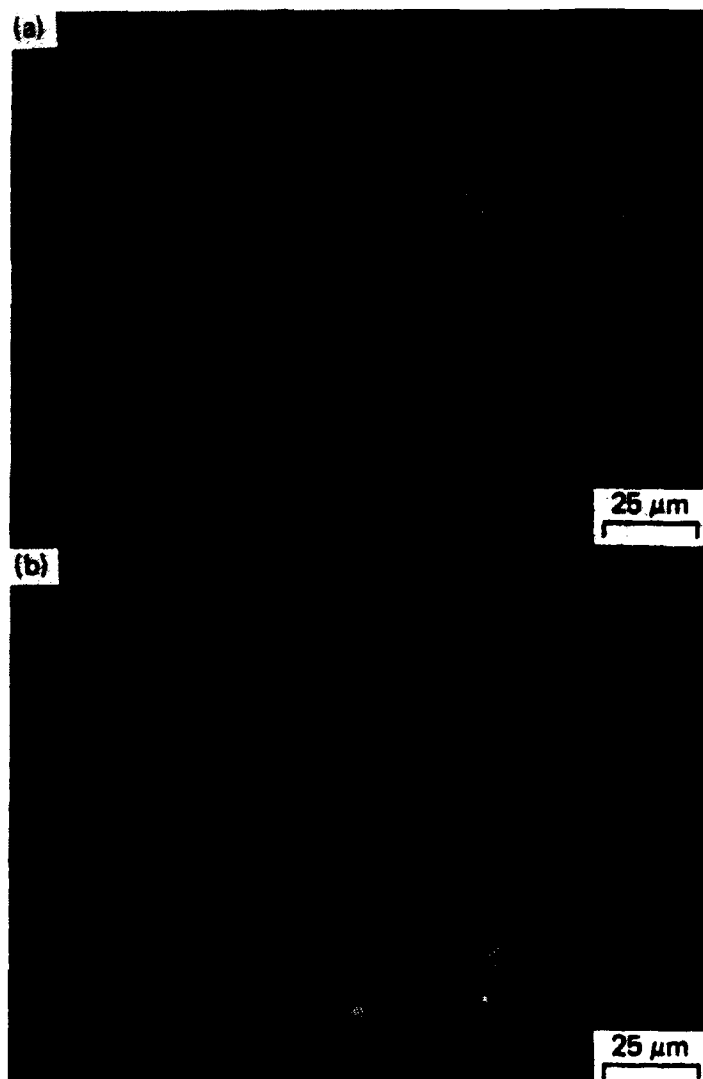
Figure 5.5: Auger spectra from the sample analyzed in Figure 5.4 but with the SiO_2 layer removed. [110].

correspond to the areas labeled region I in Figure 5.1(b). With the SiO_2 layer now removed, we can observe that these areas are actually troughs in the sample surface. Focusing the microscope into these troughs yields the image of Figure 5.3(b). It can be seen that the bottoms of these troughs (corresponding to region I) are populated by In droplets. Such droplets arise when phosphorus evaporates from the InP substrate. In this situation In is left on the surface and this In melt continues to etch the InP substrate in order to maintain equilibrium saturation with phosphorus at the substrate temperature [70,99]. The rectangular shapes of these droplets is characteristic of thermal etching of (100) InP.

Figure 5.4 exhibits Auger spectra taken from a sample annealed for 30 minutes at $750^{\circ}C$. The ~ 2300 Å SiO_2 layer was left on this sample to permit analysis of the three previously mentioned areas using a stationary electron beam. Spectra taken from the uncracked regions of the SiO_2 revealed the presence of In peaks at 298, 344, 404, and 410 eV. We also observed P peaks at 120 and 1859 eV. These peaks do not appear in the spectra of either as-deposited SiO_2 or SiO_2 annealed at $600^{\circ}C$ for 30 minutes, unless the analyzed region includes pinholes [87]. It is unclear whether these signals originate from In and P which has diffused through the film, or from material deposited on the SiO_2 surface from nearby cracks. Examination of the Auger spectra from region II (mottled, metallic colored areas in figure 5.3(a)) reveals several differences from the spectra of the uncracked SiO_2. The Si and O signals from region II are the weakest obtained from the three regions. Very little Si is actually detected within this region, as can be seen in Figure 5.4. The weakened O signal may arise from an oxide on the In-like surface of region
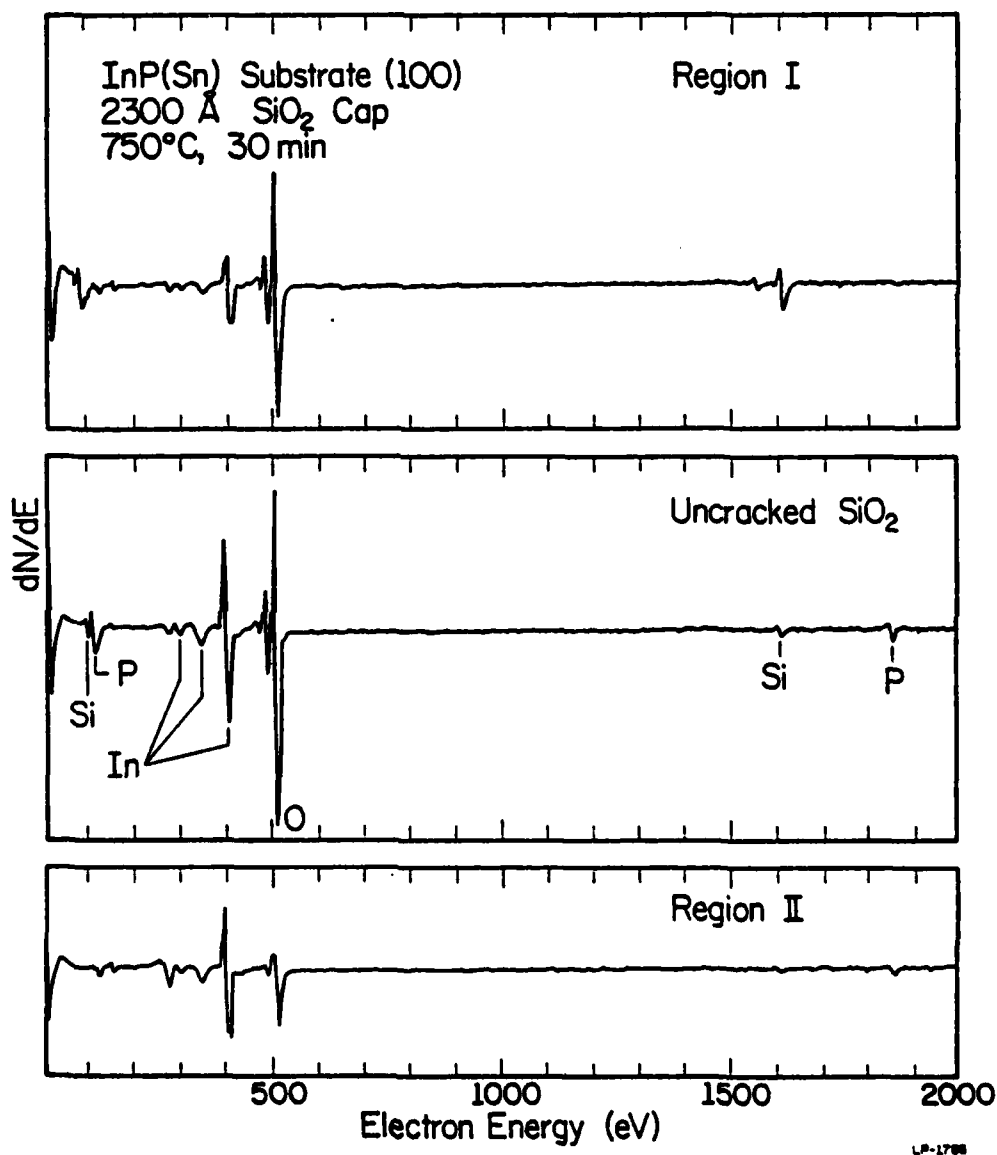
Figure 5.3: Auger spectra from InP annealed at 750°C for 30 min with ~ 2500 Å of CVD SiO_2. This series was taken with the cracked SiO_2 still on the InP surface [110].
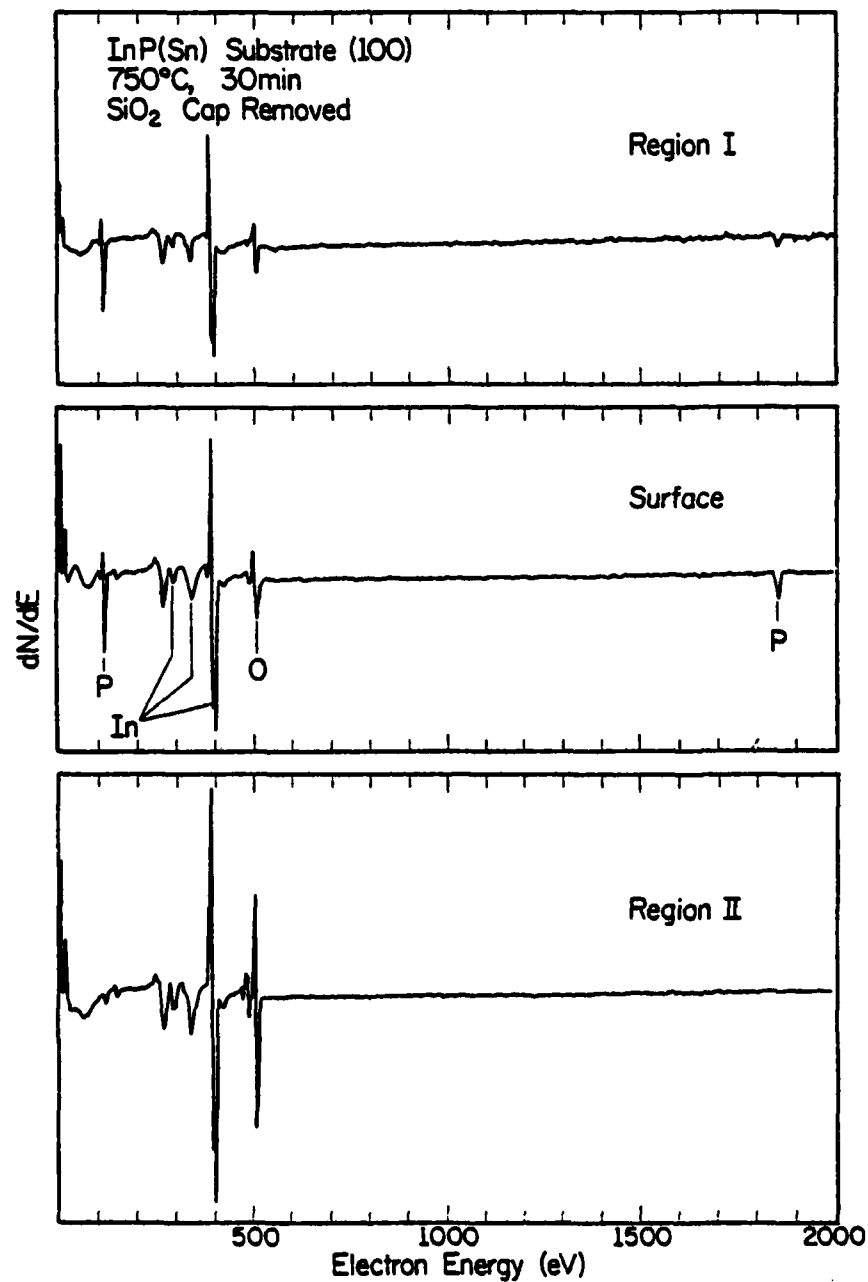
Figure 5.4: InP annealed at 750°C for 30 min with a ~ 2500 Å SiO_2 layer. This layer was then removed in buffered HF. (a) Microscope focused on the sample surface plane. (b) Microscope focused into the bottom of the thermal etch troughs. [110]

II. Additionally, the ratio of the P to In signals is much smaller than
that found in either the spectra of the uncracked SiO_2 of Figure 5.4 or
the spectra of the bare InP surface of Figure 5.5. Auger spectra from
region I (the region populated by In droplets seen in Figure 5.3(b))
show In and P signals essentially comparable to region II spectra. Region
I can be clearly distinguished from region II, however, on the basis of
the Si and O Auger signals. Whereas region II exhibited no Auger Si
signal, region I has Si signals at 76 - 92 eV and at 1620 eV comparable
in intensity to the Si signals from the uncracked SiO_2. Although the Si
signals of region I and the SiO_2 layer are comparable, the Auger O signal
from region I is consistently weaker than that obtained from uncracked
SiO_2.

Following this analysis we removed the SiO_2 layer from the
cracked sample using buffered HF. Auger spectra were taken again in the
three regions and are shown in Figure 5.5. Essentially no Si is now
detected in regions I and II, indicating that these regions were covered
by a thin SiO_x layer in the previous Auger analysis. This is consistent
with the appearance of these regions in Figure 5.1(b), 5.2, and 5.3. Also,
the differences in spectra between the uncracked InP surface and region II
indicate that the latter region is a P-depleted/In-rich region.

5.2.2 *Film Stress*

Cracks will occur in deposited thin films from stress which
exceeds the film strength or adhesive interface strength. Such stress has
two components: (1) an intrinsic stress, which is independent of the
substrate but dependent on system parameters such as deposition technique
and deposition rate; (2) thermal stress which arises from the mismatch
in thermal expansion coefficient between the film and substrate at

TABLE 5.1

PROPERTIES OF CVD SiO_2 FILMS AND

EXPANSION COEFFICIENTS OF InP AND GaAs

(Young's Modulus)/(1-Poisson's Ratio)	$E/(1-\nu)$	1×10^{12} dyne cm^{-2}
SiO_2 Thermal Expansion Coefficient	$\alpha_f(SiO_2)$	5.5×10^{-7} $^{\circ}C^{-1}$
GaAs Thermal Expansion Coefficient	$\alpha_s(GaAs)$	6.6×10^{-6} $^{\circ}C^{-1}$
InP Thermal Expansion Coefficient	$\alpha_s(InP)$	5.0×10^{-6} $^{\circ}C^{-1}$
Calculated GaAs Thermal Stress $(T_D = 400^{\circ}C, T_A = 750^{\circ}C)$	$\|\sigma_t(GaAs)\|$	2.1×10^{9} dyne cm^{-2}
Calculated InP Thermal Stress $(T_D = 400^{\circ}C, T_A = 750^{\circ}C)$	$\|\sigma_t(InP)\|$	1.6×10^{9} dyne cm^{-2}

temperatures differing from the film deposition temperature. The total stress in the film is given by:

$$\sigma_{total} = \sigma_i + \left(\frac{E}{1-\nu}\right)\int_{T_{DEP}}^{T} \left(\alpha_f(T) - \alpha_s(T)\right) \, dT$$

where σ_s is the intrinsic stress, E is the Young's modulus of the film, ν is the film's Poisson ratio, α_f and α_s are the thermal expansion coefficients of the film and substrate respectively [112]. As is commonly done, we will use constant values for the α's in our calculations. Values are reported in the literature for E and ν, although the ratio $E/(1-\nu)$ is more commonly extracted from data. For purposes of comparison we have calculated the thermal stress in SiO_2 encapsulated InP and GaAs annealed at 750°C using average values from the literature as shown in Table 5.1 [112-120]. For films deposited at 400°C and annealed at 750°C the thermal stress in the SiO_2/GaAs system is ~ 30% greater than that in the SiO_2/InP system.

To check the quality of our CVD SiO_2 we encapsulated Cr-doped GaAs along with Fe-doped InP and annealed the samples at 750°C for 30 min. Semi-insulating bulk crystals were chosen to minimize differences in crystal quality. The back surfaces of these samples were lapped to yield a uniform thickness in all samples, and the samples were cleaved to identical dimensions to minimize differences in stress that might result from sample size. Depositions were performed simultaneously on the GaAs and InP to insure identical intrinsic stress. In addition to the deposition system described in Section 2.3.1, a second CVD system with a deposition temperature of 500°C and a deposition rate of ~ 200 Å/min was employed. Following anneals at 750°C for 30 min, the SiO_2 layers on InP
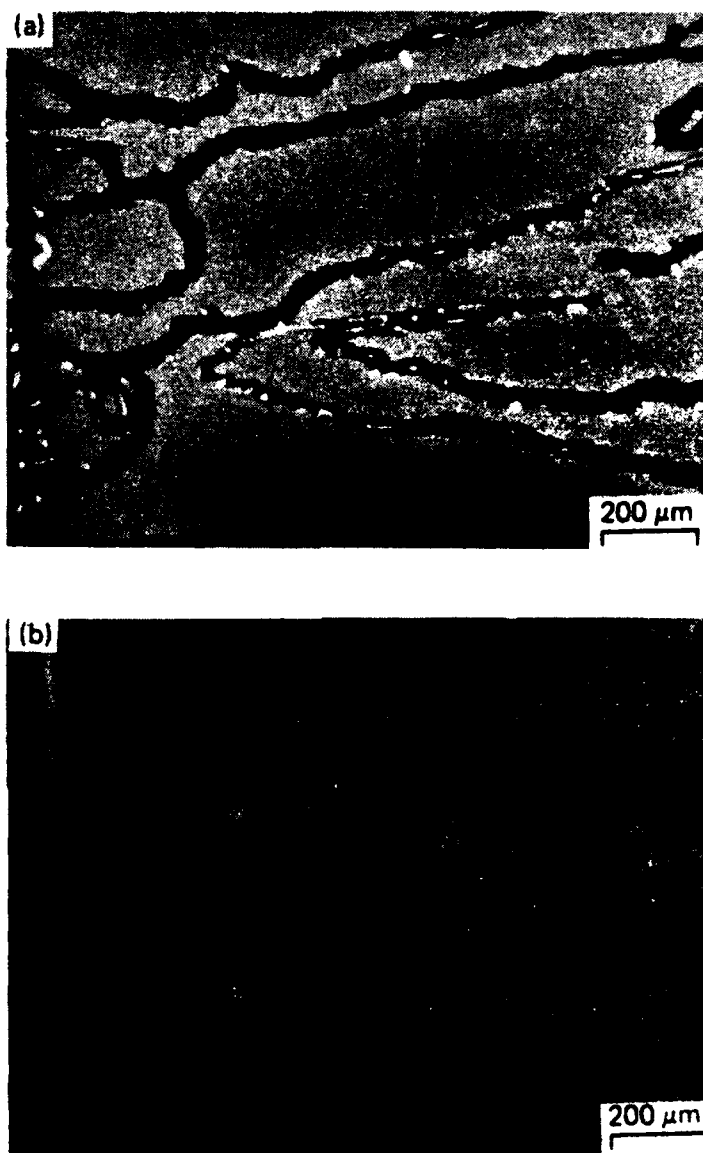
Figure 5.6: InP (a) and GaAs (b) samples encapsulated with SiO_2 and annealed at $750^{\circ}C$ for 30 min. These samples were encapsulated at $500^{\circ}C$ with a SiO_2 deposition rate of ~ 200 Å/min. An identical set of samples encapsulated in another CVD system at $400^{\circ}C$ and a SiO_2 deposition rate of ~ 1500 Å/min yielded similar results [110].

were cracked in both sets while the SiO_2 layers on GaAs were intact in both groups. Figure 5.6 compares for one such set of samples, the results of annealing at $750^\circ C$ for 30 min. These results together with our calculation of stress in these two systems indicate that the cracking observed in InP must be initiated by a mechanism other than thermal stress.

5.2.3. *Discussion*

We believe that the cracking phenomenon observed in the annealing of encapsulated InP is the result of an interaction between mechanical stress, chemical reactions, and possibly defects in the film itself (e.g., pinholes). In this section we will discuss the data in these terms.

The time evolution of the cracking as described in Section 5.2.1 suggests that there is a stress mechanism at work. This stress is presumably responsible for the 1.5 μm feature and the associated shearing of the SiO_2 seen in Figure 5.2. The fact that the 1.5 μm feature does not follow major crystalline directions, and the smooth but random transitions it makes across the surface indicate it is governed by forces other than those responsible for the 25 μm features. We investigated whether the 1.5 μm fracture could be caused by residual mechanical damage of the surface from polishing; however, we found that samples with newly exposed surfaces obtained with a 0.1% bromine-methanol etchant exhibited the same SiO_2 cracking as the unetched samples. It is also unlikely that the film shearing results from a P pressure buildup at the interface. This would more likely lead to film lift-off or peeling by adversely affecting film adhesion. Experience with Si_3N_4 encapsulated InP has shown that when phosphorus evaporates from an opening in the film it does not cause film cracking, but rather a rectangular etch pit which grows with time. Therefore, we conclude that the 1.5 μm feature represents the shearing of the SiO_2 film as a result of stress.

According to our stress calculations, thermally induced stress alone cannot explain the cracking observed. It appears most likely that the cracking is initiated by a local reaction of the SiO_2 film at the InP surface. Recently, Wager and Wilmsen have cataloged possible reactions between SiO_2 and InP [121]. They conclude that within the temperature range 25° - $350^{\circ}C$ no reaction is expected between SiO_2 and InP or its oxides. However, reactions of Si and SiO with the oxides of In and P are possible, as is a weak reaction of Si with InP. The lack of adequate entropy data prevented them from taking into account the temperature dependent entropy term in their calculations of the Gibbs free energy for the reactions. This term might be expected to become important at the temperatures considered here, possibly making a SiO_2-InP reaction feasible. Also the stoichiometry of our layers may not strictly be SiO_2, resulting in reactions between Si or SiO with the native oxide on the surface [122,123]. Recent profiles taken with ESCA indicate that there is a thick In_2O_3/P_2O_5 layer at the interface of samples with CVD-SiO_2 deposited at $450^{\circ}C$ [86,124]. It is presently uncertain if there also exists an interfacial layer of phospho-silicate glass [124]. The presence of such interface layers would invalidate our stress calculations, since a multi-layer system would have to be considered. Thermal expansion mismatch in such a multi-layered system could give rise to the stress needed to initiate the cracking. Alterna-tively, a reaction of Si or O with the substrate could lead to a mechani-cally weakened film, making cracking possible. Our Auger data indicates the possible depletion of O in the region I areas. Figure 5.7 also illus-trates this possibility. An oxygen-depleted fault to the left of the
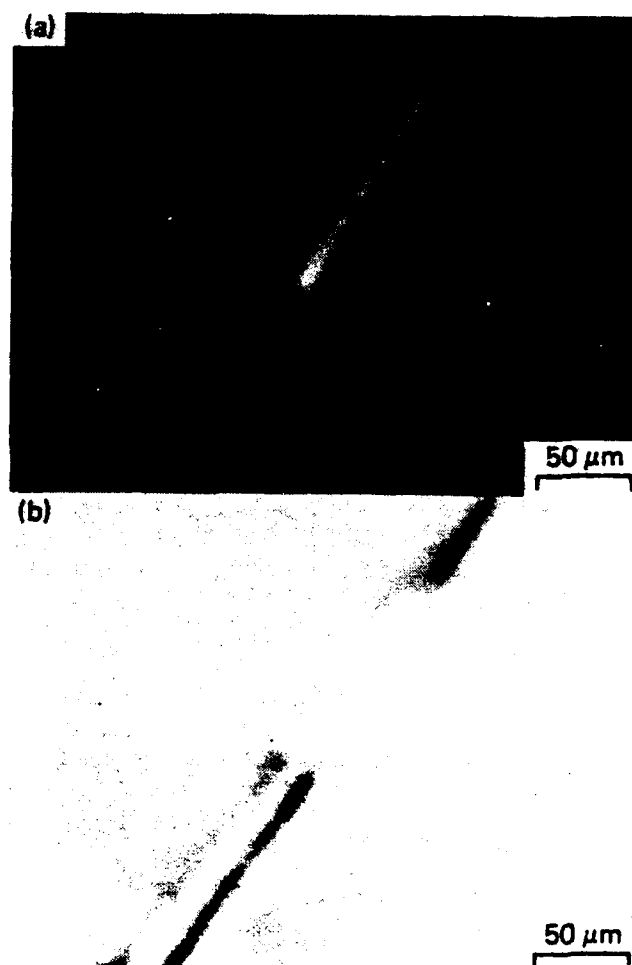
Figure 5.7: (a) Absorbed current image of a crack in a SiO_2 layer taken with the Auger microprobe. (x250) (b) Auger oxygen image of the same area seen in (a). (x250) [110]

major crack in Figure 5.7(b) is not visible in the absorbed current image of 5.7(a), and is presumably a crack in its formative stage. The question concerning possible Si reactions is presently unresolved.

Film defects such as pinholes may also contribute to the cracking phenomena observed, although they do not seem responsible for the initiation. It would be difficult to explain the time evolution behavior in terms of randomly distributed pinholes. It is observed, however, that the distribution of cracks across the surface is nonuniform. This may be correlated to the nonuniform distribution of pinholes we have observed with Cu-decoration of these films.

5.3 High Temperature Anneals with Si_3N_4 Caps

As mentioned earlier, our Si_3N_4 caps routinely survive 60 min anneals at 800°C without cracking; but another problem limits us to anneal temperatures T < 840°C. This temperature limit is the result of the volatile thermal etching characteristics of InP and may therefore similarly affect other caps annealed at high temperatures. Figure 5.8(a) is a schematic representation of a Si_3N_4 encapsulated InP sample prior to annealing. Microscopic examination of the cleaved edges of InP samples reveal that these edges are not smooth but consist of families of parallel faces along the cleavage plane. Depending upon the deposition technique, the layer thickness on these edges is generally less than that on the top or bottom surfaces by several hundred angstroms. Also, because of the rough edges, there are areas which have received only a very thin layer with poor adhesion or no layer at all. Such areas have a major effect on the encapsulated material during anneals above 800°C. At these elevated temperatures phosphorus vapor

(a)

(001)

Si₃N₄

(b)

(001)

InP
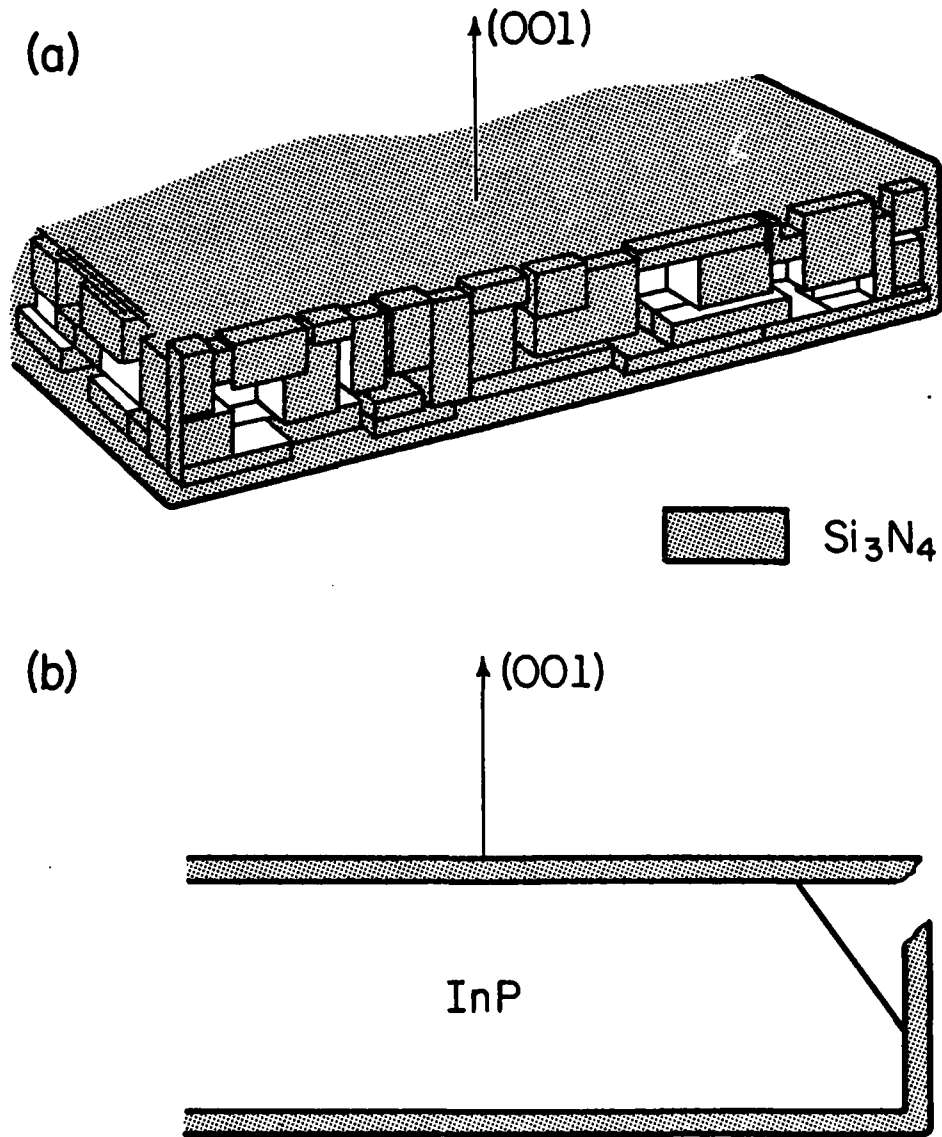
LP-2097

Figure 5.8: (a) Representation of the cleaved edges of a Si_3N_4 encapsulated InP sample prior to annealing. (b) Cut-away, side view representation of the same sample following a high temperature anneal $(T > 800^{o}C)$. Very rapid thermal etching due to preferential P vapor loss from an uncapped edge area has resulted in undercutting of an otherwise intact surface layer of Si_3N_4 [87].

escapes rapidly through thinnly capped or uncapped areas. This preferential
P evaporation initiates the formation and agglomeration of In droplets, lead-
ing to thermal etching [79-81]. This etching process of the In droplets trying
to maintain equilibrium saturation with phosphorus by reacting with the
underlying InP continues for the duration of the anneal. Of interest here
is the fact that once this thermal etching process is initiated at the edges,
it will continue to proceed regardless of the quality or integrity of the
surface encapsulating layer. For anneals performed above 800°C, intact sur-
face Si_3N_4 films have often been observed which are undercut by thermal
etching. This situation is shown schematically in Figure 5.8(b). The InP
surface not affected by this thermal etching appears to be of comparable
quality to surfaces annealed at lower temperatures. Therefore, the annealing
temperature limit for our Si_3N_4 caps, or any other cap capable of surviving
these elevated temperatures, depends largely on the sample size and on the
amount of material loss around the edges.

In an attempt to prevent edge losses at high temperatures, we have
examined double layered caps involving SiO_2/Si_3N_4 and PSG/Si_3N_4. Because of
the simplicity of the pyrolytic deposition method, these oxides proved to
be a convenient means of reducing edge loss by simply increasing the total
cap thickness. Our experience has been that the most inert encapsulant at
high temperatures (T > 800°C) resulting in the best InP surfaces is a double
layered cap of thick PSG over our standard Si_3N_4 encapsulant. Similar
advantages of multilayer encapsulation have been discussed by others for
GaAs [125] and InP [82,126].

6. PHOTOLUMINESCNECE STUDIES OF IMPLANTED InP

6.1 Introduction

Successful implantation processing of InP will require detailed information regarding the thermal annealing parameters of temperature and time necessary to reorder the crystalline lattice damaged by the atomic collisions associated with implantation and to activate implanted dopants. In this chapter, photoluminescence has been used to examine the optical spectra of semi-insulating InP processed under various conditions so as to characterize: (1) the extent of lattice reordering which occurs during ishochronal and isothermal anneals of InP damaged by an electrically inactive impurity (^{4}He); and, (2) the degree of lattice reordering and optical activation of the implanted impurity which occurs during isochronal and isothermal anneals of InP implanted with an acceptor impurity (^{9}Be).

6.2 PL Spectra of Virgin SI InP

Before discussing the spectra from implanted and annealed InP it would be useful at this point to briefly summarize the spectral character- istics of the virgin, semi-insulating InP (Fe) used in these studies. Approximately 65 samples from two neighboring slices of the same single crystal·boule were characterized prior to processing, and Figure 6.1 is typical of the observed spectra. The strongest peak in the spectra occurs at 1.414 eV; this is the near bandedge luminescence which contains a large number of unresolved emission lines. The constituent lines of this emission peak have been attributed to free excitons, excitons bound to neutral and ionized donors, and to excitons bound to neutral acceptors [127-129]. This emission at 1.414 eV has been observed in the spectra of InP prepared under almost all growth techniques [127-133] and is most often attributed to
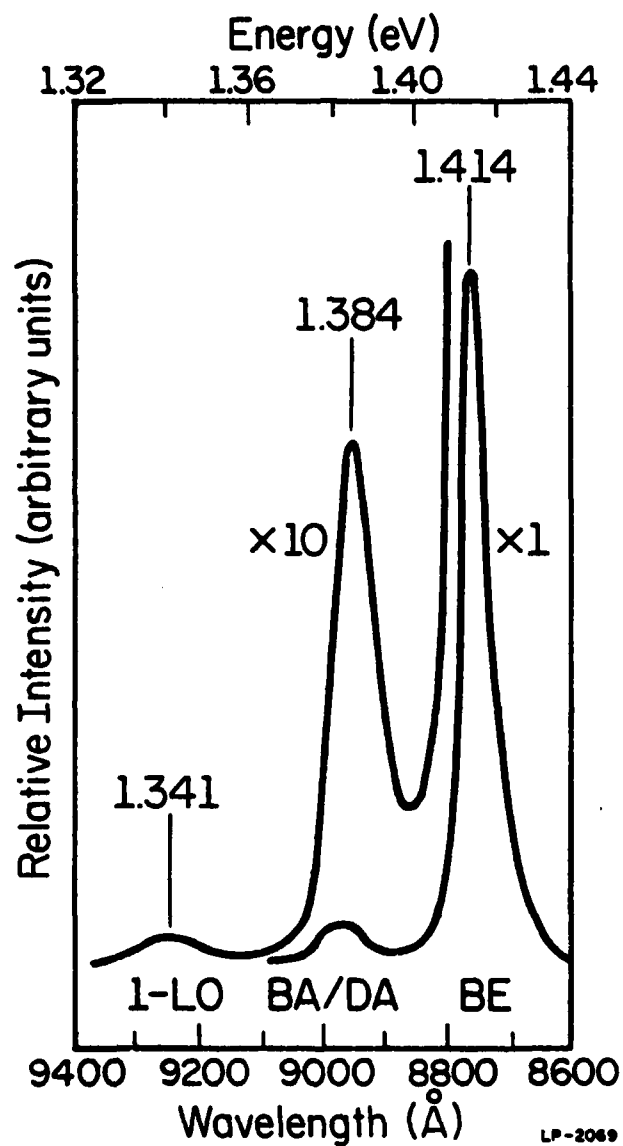
Figure 6.1: Photoluminescence spectra of virgin Fe-doped, semi-insulating (100) InP. Numerical factors are amplification relative to that used for the bandedge luminescence [75].

excitons bound to a neutral acceptor [109]. The width (FWHM) of this 1.414 eV band is 7.3 meV. For this band we find a standard deviation of ± 32% in the values of the peak intensity and of the integrated band intensity for the 65 samples studied. We shall refer to this band in the PL spectra of bulk, SI InP as the bandedge (BE) peak.

The second prominent feature in Figure 6.1 is located at 1.384 eV. Singlet or doublet emission lines have been noted in this energy range (1.380-1.384) from InP grown by various methods. These lines have been attributed either to a two-hole transition involving an exciton bound to the neutral acceptor responsible for the 1.414 eV transition [127] or to band to acceptor (BA) and donor-acceptor (DA) transitions [108,128,133]. Recent articles identify the acceptor involved in the 1.384 eV peak as carbon [130,133,134]. The width of this band in our samples is 14.9 meV. We find for this band, as with the BE band, a standard deviation of ± 33% in the values of the peak intensity and of the band integrated intensity. We shall refer to this second band feature in the PL spectra as the BA/DA band.

The third band in Figure 6.1 is located at 1.341 eV. This feature is separated by ~ 43 meV from the 1.384 eV band and therefore is attributed to the longitudinal optical phonon replica (1-LO) of the 1.384 eV band [131].

Pomrenke et al. [74] have noted that as a result of native defects and/or residual impurities the resolution of peaks in LEC InP(Fe) is limited to those separated by more than 6.5 meV. On the basis of the classical Rayleigh criteria and the width of the BE band observed here, we must agree with this observation. It should be noted, however, that shoulders or weak peaks superimposed on these bands which were separated by

only 3-4 meV were often observed. Due to the resolution limit and small variations in peak wavelengths, the identification of peak energies is confined to three significant figures.

6.3 PL Spectra of ^{4}He Implanted SI InP

In this section the lattice reordering in 51 keV, ^{4}He implanted SI InP as a function of implant fluence and anneal temperature and time is examined. Helium was chosen because it should remain electrically and chemically inactive in the crystal, thereby affecting the lattice mainly through the implantation damage it creates. For the energy and fluences examined here the implant energy deposition density ranges from ~4.6 x 10^{17} - 4.6 x 10^{19} keV cm^{-3}. Atomic profiles (SIMS) of the damage related re-distribution of ^{56}Fe in these samples are presented in Chapter 7. Photo-luminescnece is useful in characterizing lattice reordering, since in incompletely annealed samples nonradiative channels compete with radiative channels for electron-hole recombination thereby decreasing total sample luminosity, and also because the bandedge luminosity associated with excitons is extremely sensitive to lattice perfection.

Representative spectra are shown in Figure 6.2 for samples implanted with 51 keV, 10^{15} cm^{-2} ^{4}He and annealed for 30 min at the indicated temperatures. Several spectral features are related to annealing with a Si_3N_4 cap, as discussed in the Section 4.4.2. In Figure 6.2(b) the twin peaks at 1.381 eV and 1.378 eV which occurred in annealed unimplanted samples are again observed. Previously this pair was seen only in samples annealed below 650°C, and the 1.378 eV peak dominated the BA/DA band for samples annealed above 650°C. In this ^{4}He implanted series the existence of both peaks at slightly higher anneal temperatures probably results from the fact that a shorter anneal time (30 min) was used. As expected from the Si_3N_4 capping results, at 800°C the 1.378 eV line dominates the emission of

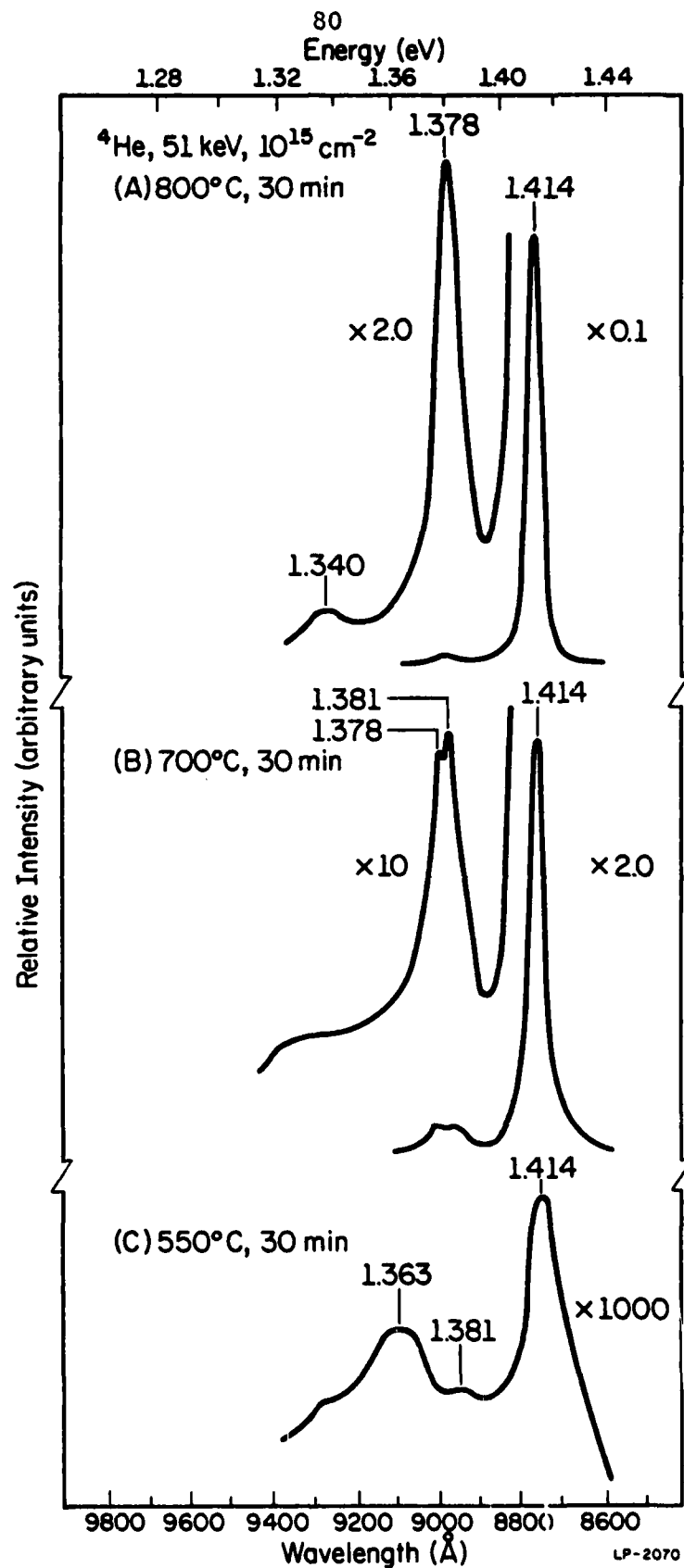**Figure 6.2:** Photoluminescence spectra of SI InP implanted with 10^{15} cm^{-2}, 51 keV ^{4}He and annealed for 30 min at (a) 800°C, (b) 700°C, and (c) 550°C. Numerical factors are amplification relative to bandedge luminescence of Figure 6.1 [75].

the BA/DA band in Figure 6.2(a). Although not shown here, the behavior of the BA/DA band in the 10^{13} cm^{-2} and 10^{14} cm^{-2} ^{4}He implanted and annealed samples is similar, i.e., for $T \leq 700^{\circ}$C the BA/DA band contains two peaks of comparable intensity at 1.381 eV and 1.378 eV and for $T > 700^{\circ}$C the band emission is dominated by the 1.378 eV line. In Figure 6.2(a) and 6.2(b) we can see the increased luminosity between the BA/DA and 1-LO bands which was already noted in Section 4.4.2. At 550°C [Figure 6.2(c)] a broad feature at 1.363 eV appears to be part of this increased luminescence between the BA/DA and 1-LO bands. Some of our results suggest this feature may be related to implant dose. From Figure 6.2 the recovery of the lattice from implantation damage can be seen in the return of the BE band width to preimplant values and also in the decreasing amplification required to observe signal emission as the anneal temperature increases.

To monitor this crystalline reordering as a function of implant dose and anneal temperature, we have plotted the integrated intensity of the BE band for a series of isochronal anneals in Figure 6.3. Annealing stages have been reported to exist in implanted InP at $\sim 200^{\circ}$C and $\sim 400^{\circ}$C on the basis of Hall measurements [18]. Using photoluminescence, we have not been able to study samples annealed much below 500°C because of low luminosities in the heavily damaged material. It is generally recognized, however, that in device fabrication, anneals in excess of 500°C are required to activate implanted impurities. Therefore, the measurements reported here span the anneal temperature range of primary interest. In agreement with reports by Davies, et al. [18,76], we note rapid recovery in BE band emission between 550°C and 650°C (Figure 6.3(a)). At 800°C, all doses shown BE integrated intensitites above unimplanted levels. As

(100) SI InP(Fe)
$2300 \text{ Å } Si_3N_4$ Cap
30 min Anneals

^{4}He Implants
51 keV
--- Unprocessed
..... 10^{15} cm^{-2}
— 10^{14} cm^{-2}
-- 10^{13} cm^{-2}

Relative Integrated Intensity

Anneal Temperature (°C)

LP-2063

Figure 6.3: Integrated BE band intensities for a series of isochronal (30 min) anneals of 51 keV, ^{4}He implanted SI InP [75].

(100) SI InP(Fe)
2300 Å Si_3N_4 Cap
30 min Anneals

Relative Integrated Intensity

^{4}He Implants
51 keV
--- Unprocessed
..... 10^{15} cm^{-2}
—— 10^{14} cm^{-2}
-- 10^{13} cm^{-2}
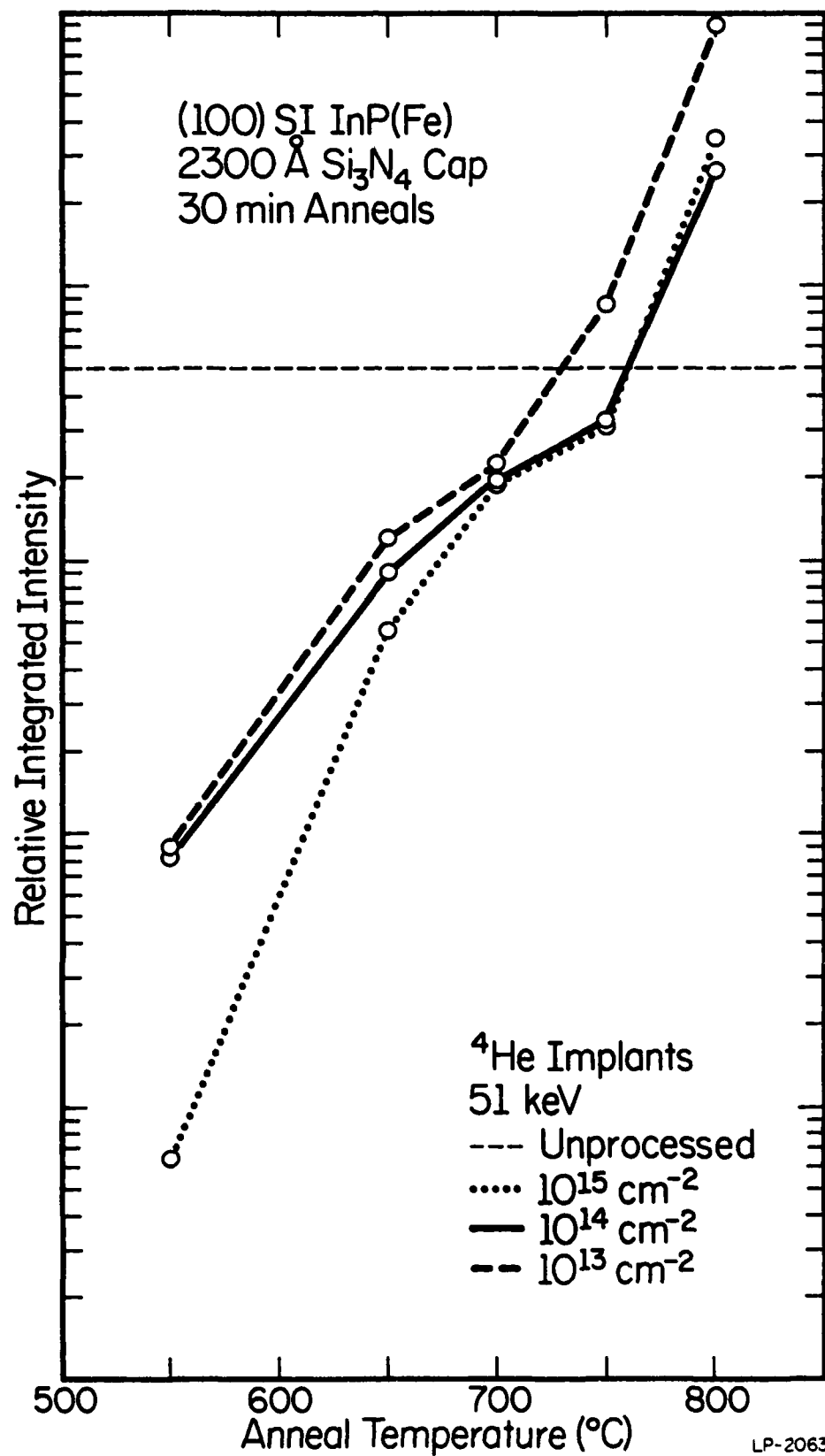
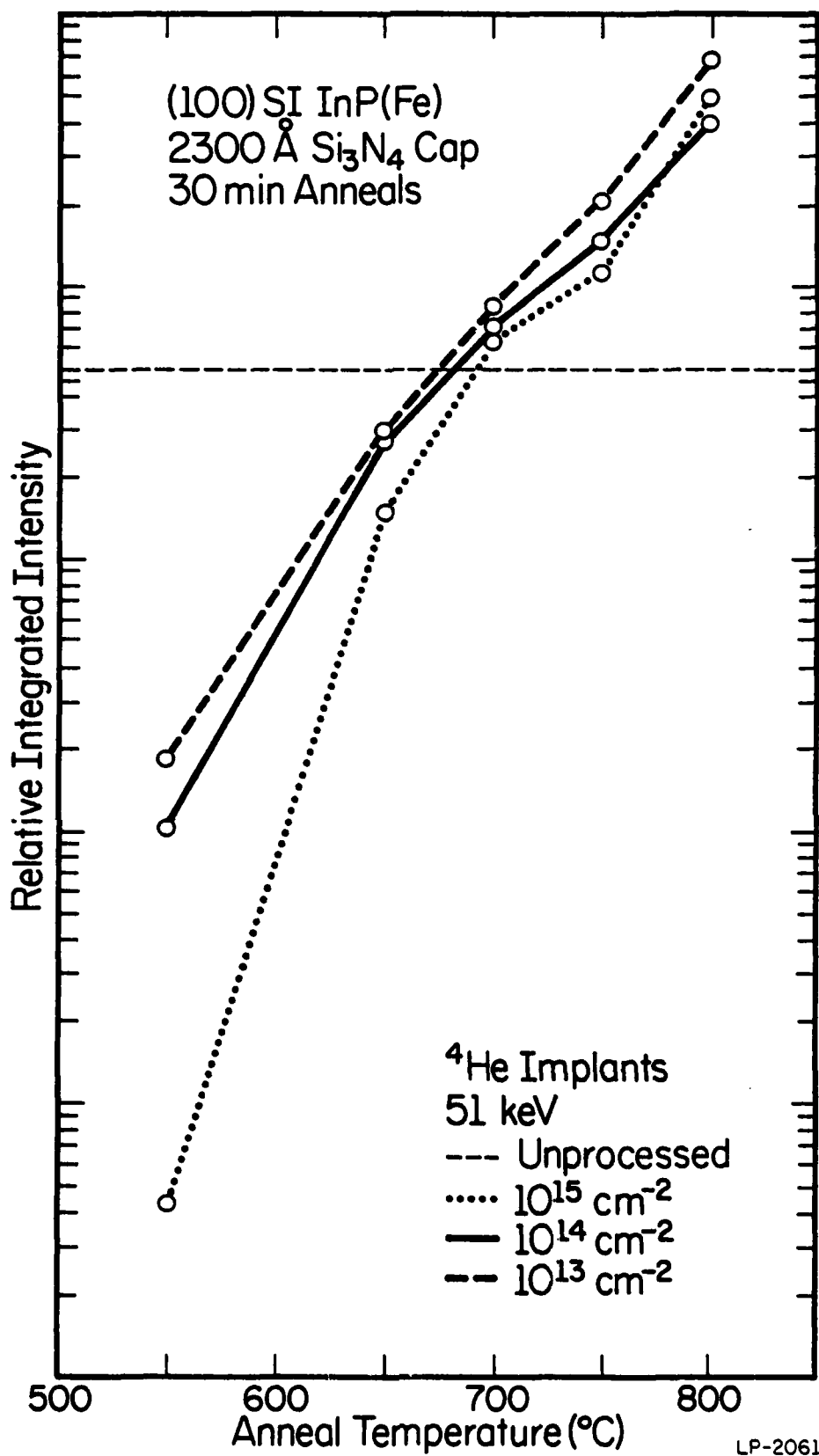Anneal Temperature (°C)

500   600   700   800

LP-2061

Figure 6.4: Integrated BA/DA band intensities for a series of isochronal (30 min) anneals of 51 keV, ^{4}He implanted SI InP [75].

discussed in Section 4.4.2, the increase in the BE band integrated intensity does not occur until the 1.378 eV line dominates the emission of the BA/DA band. An accurate assessment of the annealing process is hindered by the general rise in the intensities above preimplant levels. With this qualification in mind, our data indicate continuing lattice recovery from moderate implant damage to the highest temperature of $\sim 750^{\circ}$C.

For completeness, we exhibit in Figure 6.4 the isochronal annealing characteristics of the BA/DA band in these ^{4}He implanted samples. The effect of the tail of luminescence on the low energy side of the BA/DA band has not been included in the integration of this band's intensity. As was the case with the Si_3N_4 capping series of Section 4.4.2, the increase of the BA/DA band integrated intensity above virgin levels occur at a lower temperature than does the comparable increase in BE band intensity. At levels above those of unimplanted samples, the BA/DA band is dominated by emission at 1.378 eV. Because of the similarities of Figures 6.3 and 6.4 to Figure 4.8 and since ^{4}He is not expected to be optically active we may conclude that the high temperature anneals (T > 700°C) of this series are influenced by factors related to annealing with a Si_3N_4 cap.

The isothermal (750°C) annealing characteristics of 10^{15} cm^{-2}, ^{4}He implanted SI InP are shown in Figure 6.5 as a function of anneal time. It is clear that at this temperature the integrated intensity of the BA/DA band is above virgin levels for all t $\geq$ 15 min. In the 15 and 30 min anneals the band contains 1.381 eV and 1.378 eV lines of comparable intensities while the 1.378 eV line dominates in the 60 min and 120 min anneals. This observation supports our previous assumption that not only anneal temperature but also anneal time influences the point at which the

(A) (100) SI InP(Fe)
2300 Å Si_3N_4 Cap
750°C Isothermal Anneals
^{4}He Implant, 51 keV, 10^{15} cm^{-2}
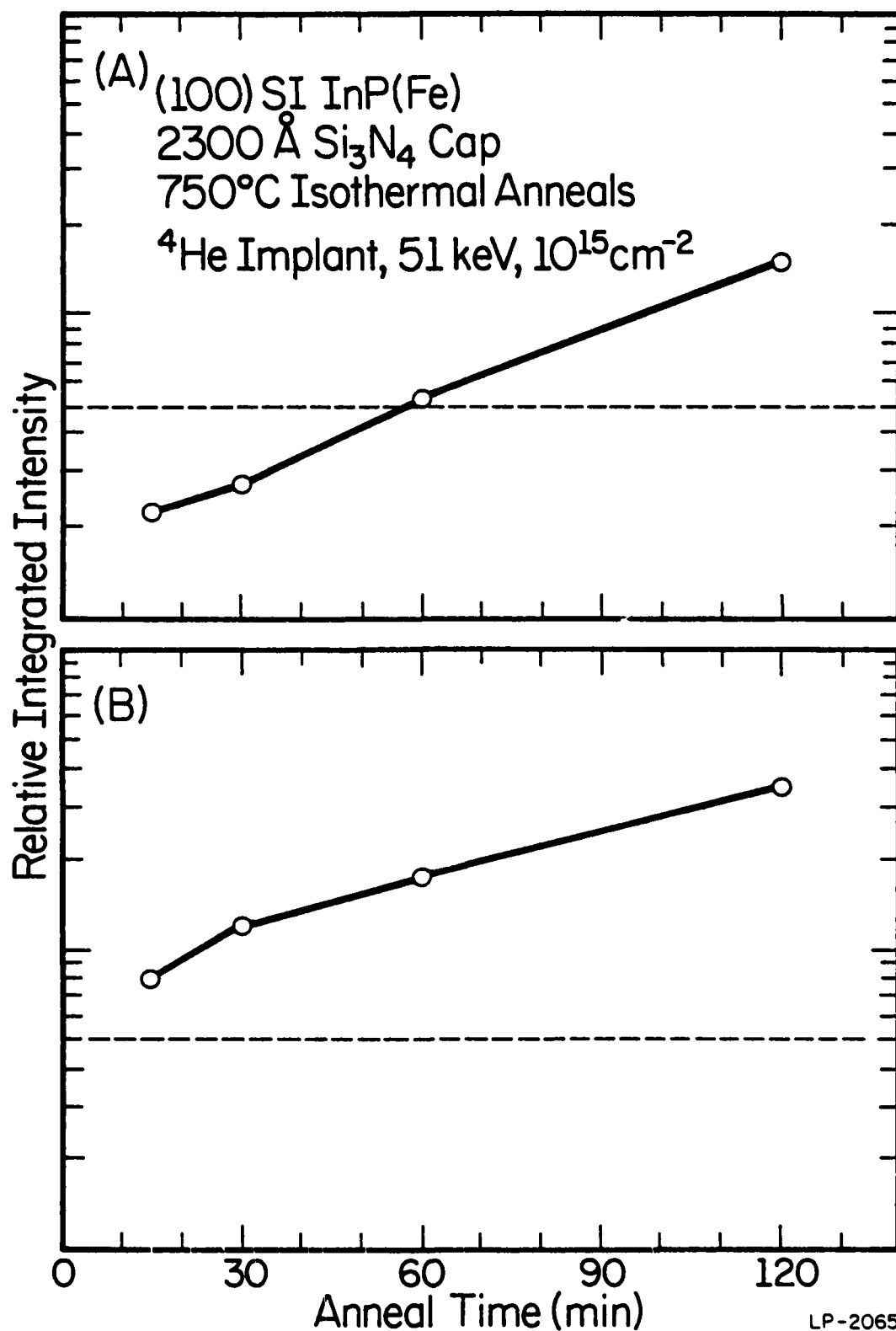
(B)

Relative Integrated Intensity

Anneal Time (min)

LP-2065

Figure 6.5: Integrated intensities of (a) the BE band and (b) the BA/DA band for a series of isothermal (750°C) anneals of 51 keV, 10^{15} cm^{-2} ^{4}He implanted SI InP [75].
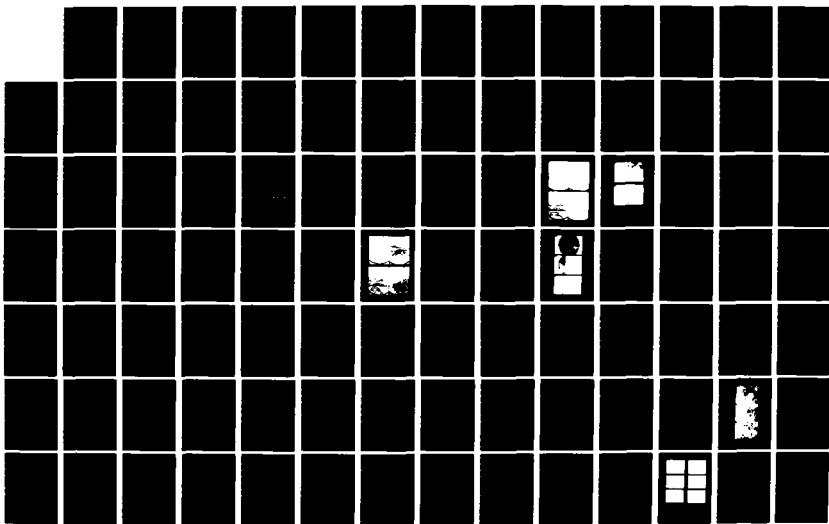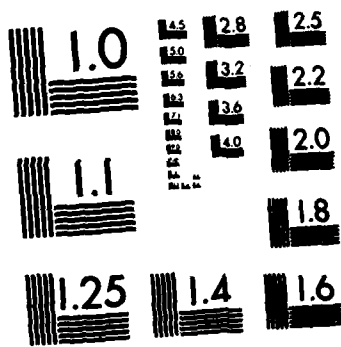
1.378 eV line dominates the BA/DA emission band. Comparing Figure 6.5(a) to 6.5(b) it becomes evident that the BE band intensity rises above virgin levels at later anneal times than does the BA/DA band. This result parallels the relationship of these two bands in regard to the temperature at which their integrated intensities exceed unimplanted levels. Figures 6.5(a) and 6.5(b) indicate no saturation of the integrated intensities with time; instead, the intensities of both band increase exponentially with anneal time. This result together with those of Section 4.4.2 suggest the diffusion of an optically active impurity into the analyzed region as a result of annealing with a Si_3N_4 cap.

6.4 PL Spectra of ^{9}Be Implanted SI InP

In this section, lattice reordering and impurity activation in SI InP implanted with 100 keV ^{9}Be is examined. Several potential InP device applications will require a controllable method of acceptor doping. ^{9}Be is an attractive implanted acceptor to investigate because its low mass results in less implant damage than with heavier ions. With the energy and doses examined here the implant energy deposition density ranges from $\sim 2 \times 10^{18} - 2 \times 10^{20}$ keV cm^{-3}. The atomic (SIMS) profiles of the Be and Fe redistribution in these samples are presented in Chapter 7.

Representative spectra from 10^{15} cm^{-2} and 10^{13} cm^{-2} ^{9}Be implanted samples are shown in Figure 6.6. Two new features appear which have not been seen in previous Si_3N_4 capped or ^{4}He implanted spectra. Comparing Figure 6.1 to Figure 6.6(a) it is evident that the peak of the BE band shifts to lower energies. This BE peak shift to lower energies increases with increasing implant dose. After an 800°C anneal the BE peak position for the fluences examined here is: 1.413 eV for 10^{13} cm^{-2}, 1.410 eV for 10^{14} cm^{-2}, and 1.408 eV for 10^{15} cm^{-2}. Since previously examined spectra showed
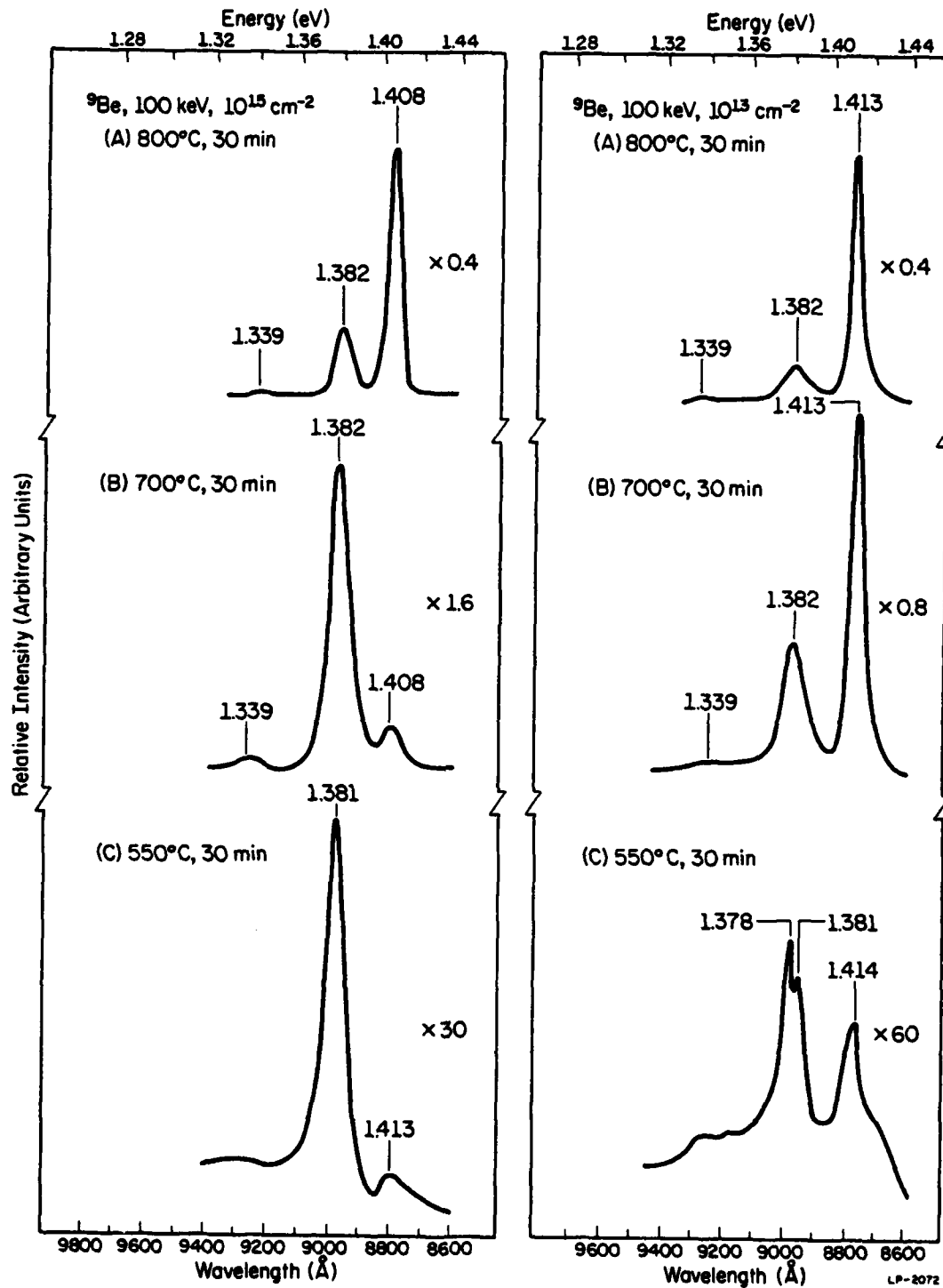
Figure 6.6: Photoluminescence spectra of SI InP implanted with 100 keV ^{9}Be to doses or 10^{15} cm^{-2} of 10^{13} cm^{-2} and annealed for 30 min at (a) 800°C, (b) 700°C, and (c) 550°C. Numerical factors are amplification relative to bandedge luminescence of Figure 6.1 [75].

no detectable shift in the BE peak position, this behavior cannot be
attributed to capping or damage effects. We believe that this dose
dependent peak shift in the BE band most probably results from inter-site
interactions (Stark interaction effects or impurity banding effects).
Such effects would be consistent with the dose and anneal temperature
dependence of the shift since they are related to the concentration of
activated Be acceptors. Considering the location of the new BE peaks in
the band gap of InP it would be likely that the peak transitions result
from exciton recombination at Be acceptors.

The other new feature in the spectra of these ^{9}Be implanted samples
is the peak position of the BA/DA band. Within our resolution limits the
position of this peak is 1.382 eV for all doses examined here. We have
surveyed a limited number of 10^{15} cm^{-2} ^{9}Be implants into undoped VPE InP
in which the peak resolution is much better than in the SI InP. These VPE
samples are characterized by a peak at 1.383 eV which is not present in
unimplanted material. Additionally, we have examined the spectra at various
depths extending from the surface to 0.75 µm in samples implanted with 10^{15}
cm^{-2} ^{9}Be and annealed at 750°C for 30 min. The resulting optical profile
of the BA/DA band emission at 1.382 eV shows some correlation to the atomic
^{9}Be profiles obtained with SIMS [138]. Also, from Figure 6.6 and other
spectra it is clear that the peak intensity of the 1.382 eV emission increases
with implant dose in the range from 10^{13} -10^{15} cm^{-2}. Therefore, we
believe that the 1.382 peak in ^{9}Be implanted SI InP is due to optically
active Be acceptors. An estimate of the Be acceptor ionization energy may
be obtained if we ignore possible inter-site effects and assume the 1.382
eV emission results from a band to acceptor transition. Using a band gap

energy E_g = 1.4233 eV (2^oK) [139] we estimate the Be acceptor ionization energy to be 41.3 $\pm$ 3 meV. This estimate is within the range of reported binding energies for other acceptors in InP [74,109,130,134].

Other features seen in Figure 6.6 were discussed above. At 550^oC the 10^{13} cm^{-2} ^{9}Be sample has a BA/DA band which contains two peaks, one of which (1.378 eV) has been shown to be associated with Si_3N_4 capping and annealing. The 10^{15} cm^{-2} ^{8}Be sample annealed at 550^oC does not show this 1.378 eV peak, presumably because of the competition from the emerging 1.382 eV peak associated with Be acceptors. From Figure 6.6(c) we can also see increased luminescence between the BA/DA band and the 1-LO phonon band as in previous spectra.

In Figure 6.7 we have plotted the integrated intensity of the BE band as a function of implant dose and anneal temperature. Note that the 10^{13} cm^{-2} series recovers more rapidly in the range from 550^oC - 650^oC than do either 10^{14} cm^{-2} or 10^{15} cm^{-2} dose samples. This variation in annealing behavior between the 10^{13} cm^{-2} dose and the higher doses seems to be much larger than might be expected from the results of Figure 6.3. There the plots showed nearly parallel curves that were predictably dependent on fluence. Our estimates of the energy deposition density indicate an overlap of this quantity for the 10^{13} cm^{-2} and 10^{14} cm^{-2} implants of ^{9}Be with the 10^{14} cm^{-2} and 10^{15} cm^{-2} implants of ^{4}He (2×10^{18} - 4.6×10^{19} keV cm^{-3}). Although the differences in annealing behavior for the ^{9}Be doses considered here are not presently understood, it seems that they do not result from different levels of implant damage density.

(100) SI InP(Fe)
2300 Å Si₃N₄ Cap
30 min Anneals

⁹Be Implants
100 keV
--- Unprocessed
..... 10^{15} cm⁻²
— 10^{14} cm⁻²
-- 10^{13} cm⁻²

Relative Integrated Intensity

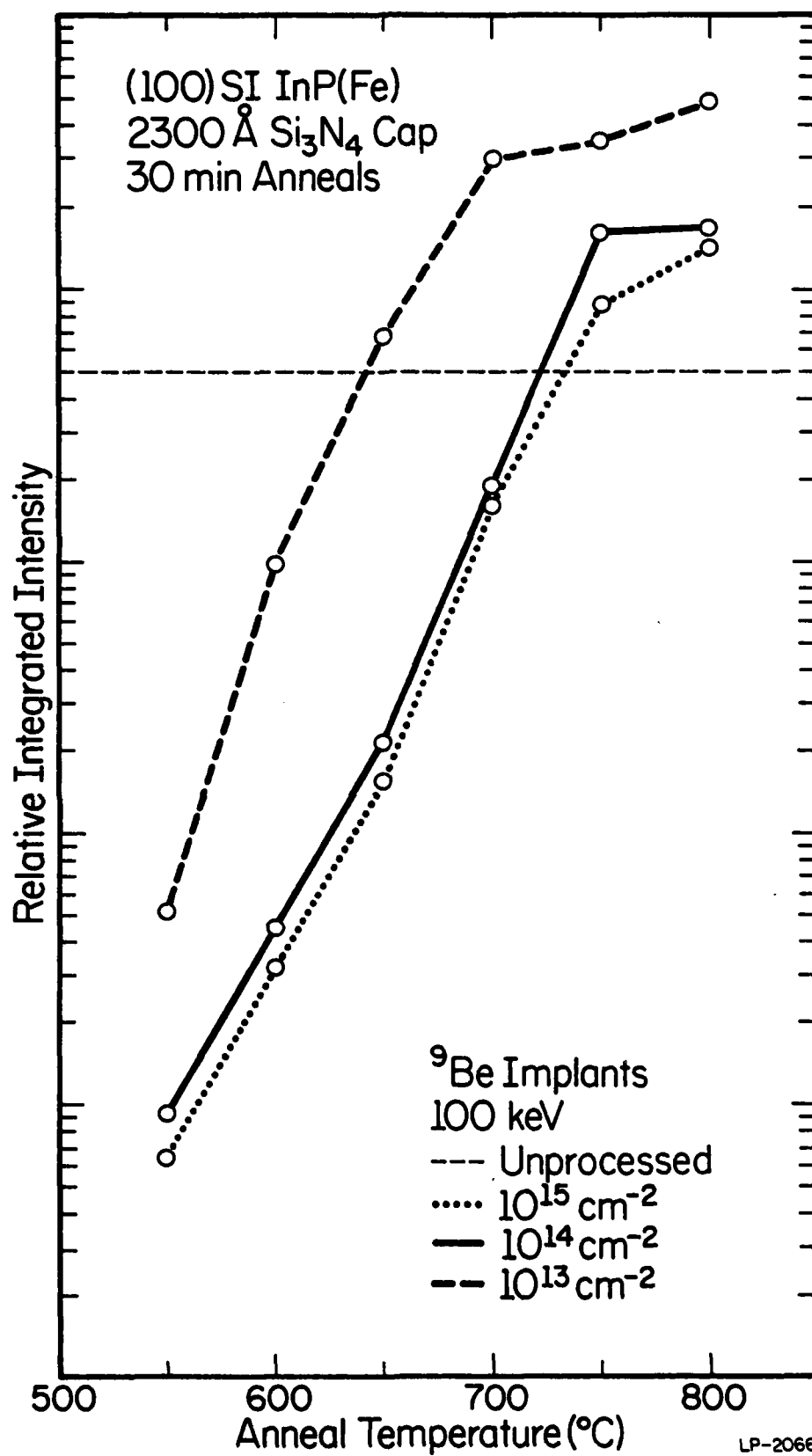Anneal Temperature (°C)

LP-2066

Figure 6.7: Integrated BE band intensities for a series of isochronal (30 min) anneals of 100 keV, ⁹Be implanted SI InP [75].

As might be expected from our previous isochronal anneal plots, for $T \geq 750^{\circ}C$ we find that the BE band emission is greater than in unimplanted samples. Because of the strong luminescence associated with Be acceptors at 1.382 eV, the 1.378 eV line does not dominate the BA/DA band in these samples as was the case in previous samples where the BE band intensity was above virgin levels. At low annealing temperatures, however, (before substantial concentrations of Be are activated) the 1.378 eV line can be observed (Figure 6.6(c)). As stated earlier, we believe that the emergence of the emission at 1.378 eV is related to the observation of integrated band intensitites greater than those in unprocessed material. In recent years articles have appeared which report unusual surface properties for InP with high luminosities associated with minimal surface band bending [140,141]. It is possible that the increased levels of BE band luminescence we consistently observe at high anneal temperatures result from a reduction in the surface space charge layer of SI InP due to the accumulation of the impurity/ defect involved in the 1.378 eV line. In our optical depth profiling of the Be acceptor emission we have observed that the BE band emission is above virgin levels at all depths examined from the surface to 7500 Å; therefore, the phenomena is not restricted to the near surface. Based on preliminary SIMS results this depth dependence may be related to the increased levels of ^{28}Si we have found in Si_3N_4 capped and annealed samples. Further work is being done to determine if such a relationship does exist. A complicating factor in the space charge layer explanation for increased luminosity levels is the finding that the compensating deep acceptor ^{56}Fe getters to the surface and into the implanted region above background levels [138]. Therefore, it is possible that the BE enhancement results from the annealing of native defects in bulk InP or from a gettered impurity with greater radiative ef-

ficiency than that of the other impurities in virgin material. Obviously more research will be required to ascertain the origin of the increased levels of luminosity in high temperature annealed SI InP.

Figure 6.8 presents the isochronal annealing behavior of the BA/DA band in these ^{9}Be implanted samples. Again, the increased luminescence on the low energy side of the BA/DA band has not been included in the integration of the band's intensity . For purposes of comparison to Figure 6.4 we have included the unimplanted reference level. Because the BA/DA band is now dominated by emission associated with Be acceptors, the curves of Figure 6.8 differ significantly from those of Figure 6.4 which we have proposed to be influenced by near surface gettering of an impurity during annealing. For low and moderate doses it appears from Figure 6.8 that saturation of the Be activation occurs in the range $700 \leq T \leq 750^\circ$C. For 10^{15} cm^{-2} doses, activation of Be appears to increase smoothly with temperature up to 750°C. Between 750°C and 800°C all three fluences exhibit a small decrease in Be related emission, which may result from Be migration away from the near surface region.

The isothermal (750°C) annealing characteristics of 10^{15} cm^{-2}, ^{9}Be implanted SI InP are shown in Figure 6.9. Unlike Figure 6.5(b) in which the BA/DA band integrated intensity increased exponentially with anneal time, it is clear from Figure 6.9(b) that the BA/DA band, now dominated by Be emission, shows saturation in the time range from 30-60 min. For anneal times t > 60 min a decrease in Be related emission is observed, which would be consistent with the assumption of Be migration away from the near surface region.
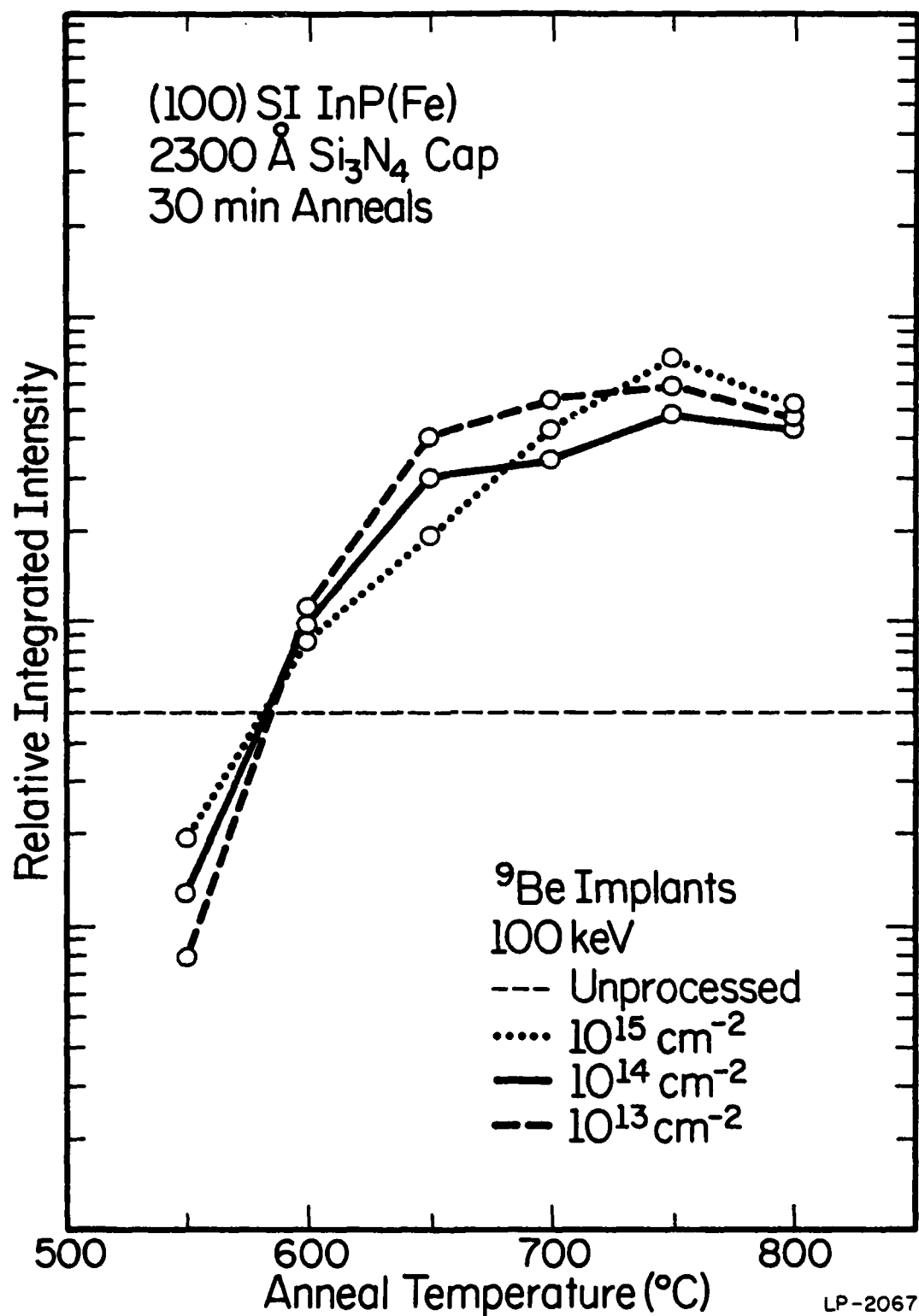
Figure 6.8: Integrated BA/DA band intensities for a series of isochronal (30 min) anneals of 100 keV, [9]Be implanted SI InP [75].
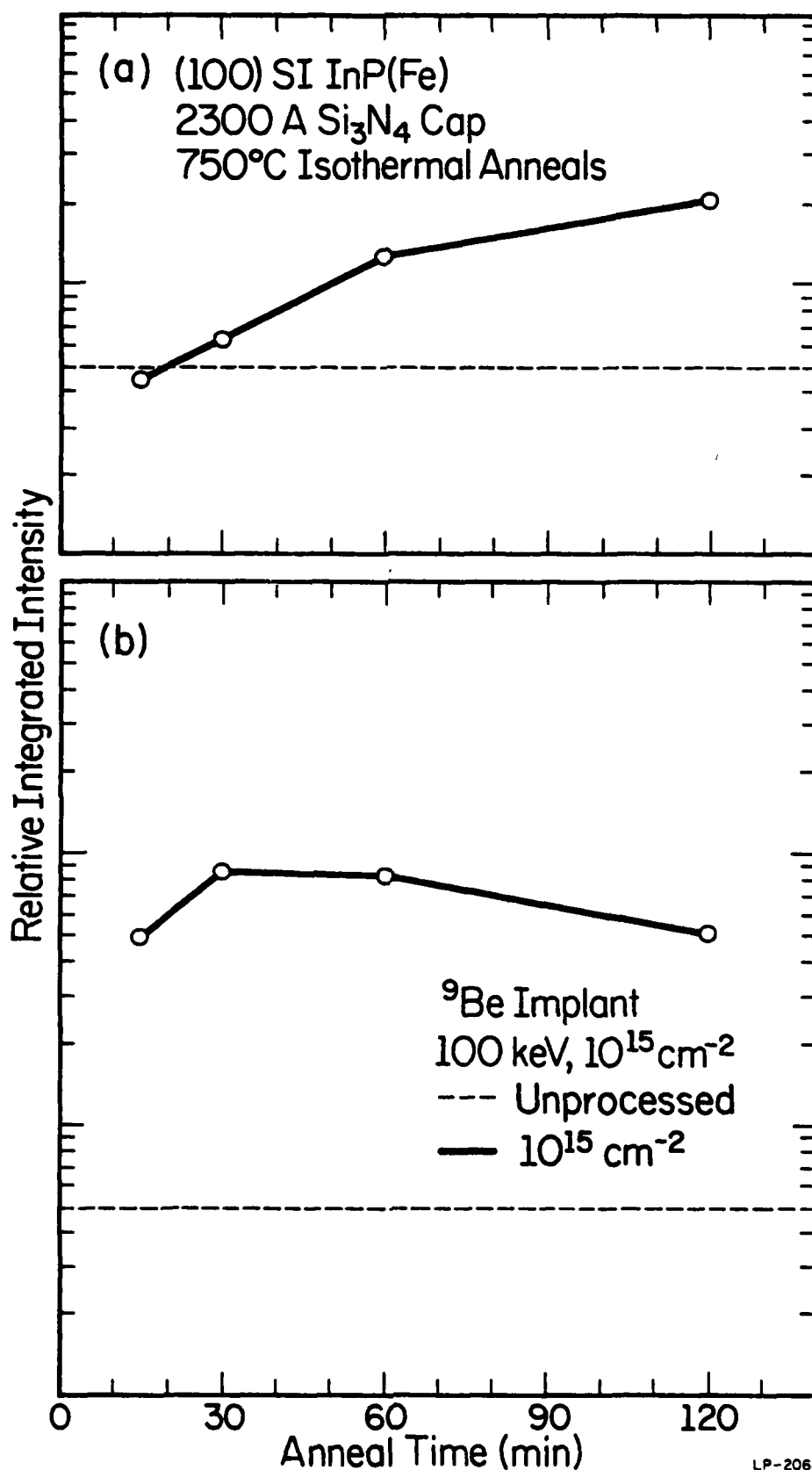
Figure 6.9: Integrated intensities of (a) the BE band and (b) the BA/DA band for a series of isothermal (750°C) anneals of 100 keV, 10^{15} cm^{-2} ^{9}Be implanted SI InP [75].

6.5 Summary

In this study of PL spectra from 1.44 - 1.30 eV we have observed the following:

(1) The virgin, (100) Fe-doped InP examined here is characterized by three luminescence bands at 1.414, 1.384, and 1.341 eV. These are attributed respectively to bandedge luminescence (BE), band to acceptor and donor to acceptor (BA/DA) luminescence, and luminescence from the 1-LO phonon replica of the BA/DA band. The widths (FWHM) of the BE and BA/DA bands are 7.3 and 14.9 meV respectively. For the ~ 65 samples taken from two neighboring slices of the same boule, variations of ~ ± 30% were noted in the peak intensity and integrated intensity of the BE and BA/DA bands.

(2) An increase in luminosity between the BA/DA and 1-LO band has been observed after annealing in both unimplanted and implanted samples. Weak structures at ~ 1.36 eV are often superimposed on this broad tail of luminescence. The origin of this luminescence is not presently understood, but possibilities were discussed previously in Section 4.4.2.

(3) High temperature (T > 700°C) anneals of unimplanted SI InP or material implanted with inactive impurities result in shifting of the BA/DA peak from 1.384 eV to 1.378 eV. Preliminary analysis using SIMS indicates that in the Si_3N_4 capped and 750°C annealed samples the ^{28}Si concentration level is above virgin levels to a depth of ~ 7000 Å. Besides Si in-diffusion from the cap, annealing-induced radiative defects or gettering of impurities from the bulk could cause the 1.378 eV peak.

(4) In all samples examined, high temperature (T > 750°C) anneals result in integrated BE band intensities greater than those in unimplanted samples. This phenomenon has been correlated to the presence of the 1.378 eV

peak. The luminosity increase may result from a reduction in the sur-
face space charge layer of SI InP due to the accumulation of the active
impurity involved in the 1.378 eV transition. It is also possible the
BE band enhancement results from the annealing of native defects in
bulk InP or from a gettered impurity with greater radiative efficiency
than that of the other impurities in virgin material.

(5) Isothermal (750°C) anneals of 51 keV, 10^{15} cm^{-2} ^{4}He implanted SI InP
exhibit exponential increases above virgin levels with anneal time
for both the BE and BA/DA band integrated intensities. No saturation
effects are observed for t $\leq$ 120 min. We believe this supports the
view of an active impurity diffusing into the analysis region. Fol-
lowing 51 keV, 10^{13} - 10^{15} cm^{-2} implants of ^{4}He, thirty-minute anneals
at 750°C appear sufficient to restore the lattice to approximately
preimplant levels of quality.

(6) 100 keV implants of ^{9}Be result in dose-dependent shifting of the BE
band peak from 1.414 eV in unimplanted samples to 1.408 eV in 10^{15} cm^{-2}
implanted InP. This shifting is probably due to inter-site interactions.
In the ^{9}Be implanted samples the BA/DA band is dominated by a new
emission peak at 1.382 eV which we show to be associated with Be. We
estimate the Be acceptor ionization energy to be 41.3 $\pm$ 3 meV. Maximum
Be activation appears to occur for all doses at $\sim$ 750°C for 30 min
anneals. At 750°C, 10^{15} cm^{-2} ^{9}Be implanted SI InP exhibits saturation
of Be activation between 30-60 min with decreasing Be associated emission
at 1.382 eV resulting from longer anneals.

7.   SIMS STUDIES OF ATOMIC REDISTRIBUTION IN ANNEALED InP

In this chapter the redistribution of intentionally present, compensating dopants (Fe or Cr) and of implanted impurities (Be, Mg, and Si) in annealed, semi-insulating InP has been studied using SIMS.

7.1   Fe and Cr Redistribution in SI InP

Semi-insulating InP is extremely important in the fabrication of devices because it can serve as a substrate for the subsequent growth of an epitaxial device layer, and it can provide device isolation when implantation directly into the material is employed. Whereas presently almost all available semi-insulating GaAs is chromium-doped, semi-insulating InP can be obtained by doping either with chromium or iron. Cr has a much lower solid solubility in InP than in GaAs, which necessitates the use of high purity starting material to achieve high resistivity [16]. Since such purity in InP is still not routinely obtained, Fe, which has a higher solid solubility in InP than does Cr, is being used as an alternative in the growth of semi-insulating InP [142,143]. Recently, a number of studies have shown the redistribution of Cr in annealed GaAs [144-146] and in implanted GaAs [58,147]. The redistribution of the bulk compensating dopants, Fe or Cr, in annealed and implanted semi-insulating InP is described in the following section.

7.1.1   *Redistribution Resulting from Annealing*

Figures 7.1 and 7.2 exhibit the profiles of Fe and Cr resulting from annealing the substrates with a Si_3N_4 cap. With the exception of a large Fe accumulation within the first 1200 Å of the surface, the Fe profile in the $550^{\circ}C$, 30 min anneal is otherwise indistinguishable from the unannealed profile. This is not true of the profile resulting after a $800^{\circ}C$, 30 min anneal. Again, an Fe accumulation region with a maximum concentration of
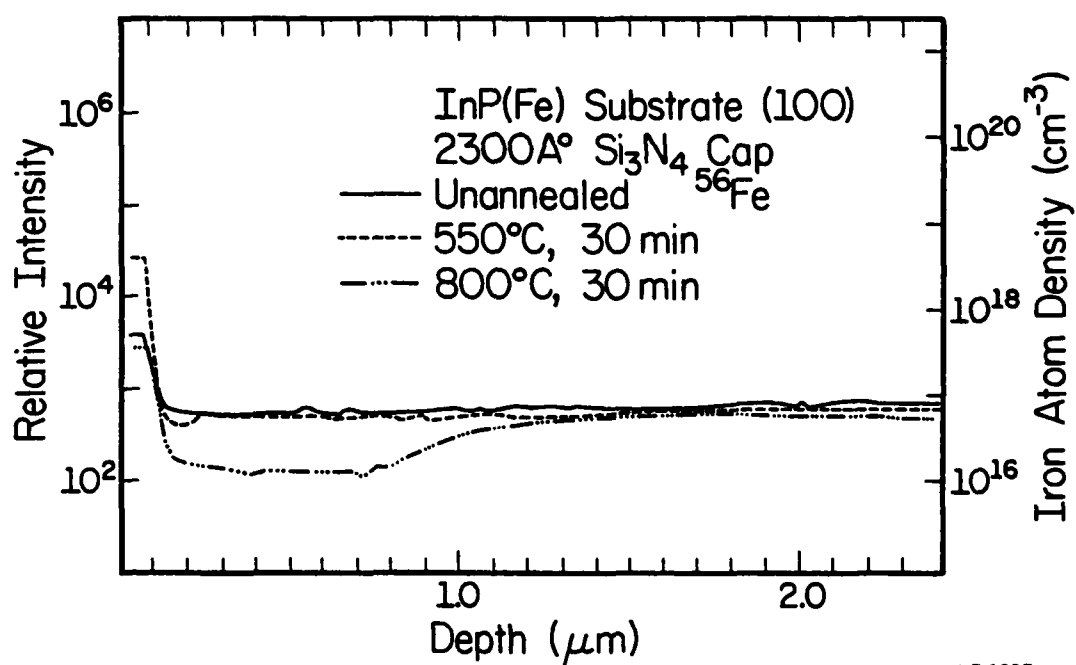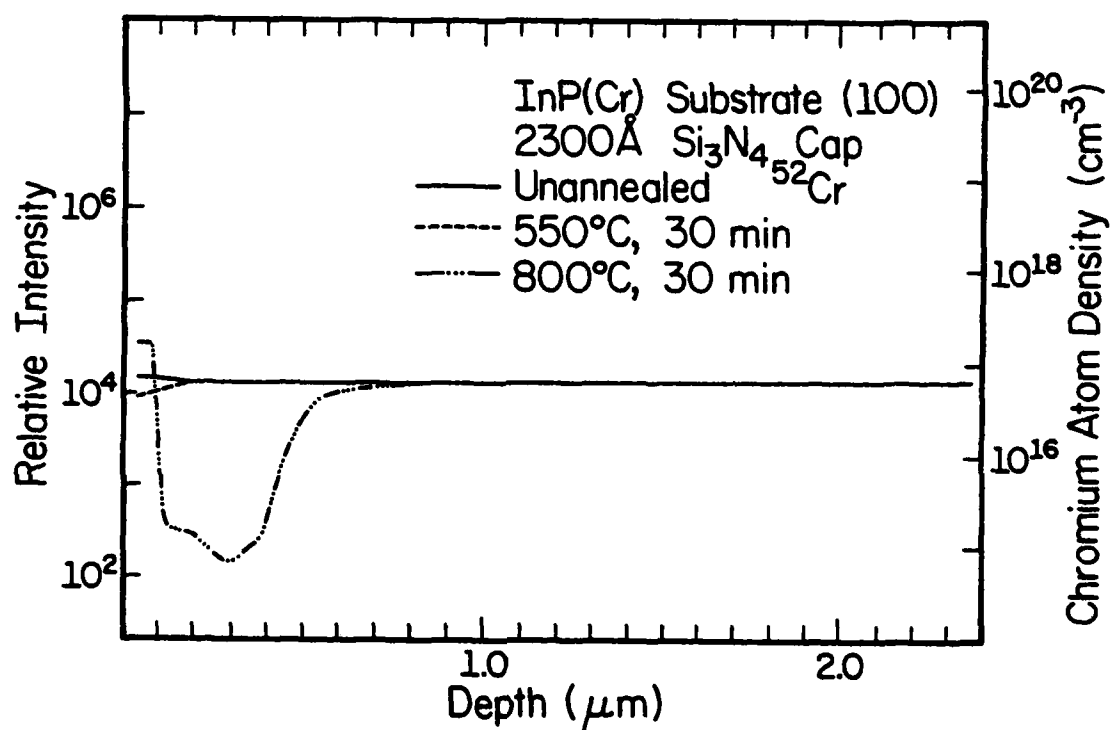
Figure 7.1: SIMS profiles of Fe in a semi-insulating InP substrate following 30 min. anneals at 550°C and 800°C with a Si_3N_4 encapsulant [21].

Figure 7.2: SIMS profiles of Cr in a semi-insulating InP substrate following 30 min. anneals at 550°C and 800°C with a Si_3N_4 encapsulant [21].

$\sim 4 \times 10^{17}$ cm^{-3} extends from the surface to a depth of ~ 1000 Å. However, following this zone is an Fe depletion region. This broad, flat-bottomed region originates within 1000 Å of the surface and returns to the normal background level at a depth of ~ 1.2 μm. The minimum Fe concentration within this region is $\sim 1.4 \times 10^{16}$ cm^{-3}.

The redistribution of Cr resulting from annealing differs significantly from that of Fe. As with Fe there is no evidence of major redistribution resulting from a 500°C, 30 min anneal. Qualitatively, the Cr profile after a 800°C, 30 min anneal is similar to that of Fe, in that a surface accumulation region and a depletion zone appear. The surface accumulation zone ends at a depth of ~ 1000 Å, while the Cr depletion region extends to a depth of ~ 8000 Å. The minimum Cr concentration within this region is $\sim 9.2 \times 10^{14}$ cm^{-3}. Although redistribution of Cr occurs over a region of ~ 8000 Å versus $\sim 12,000$ Å for Fe, Cr redistribution is more severe in the sense that the concentration of the compensating dopant is an order of magnitude lower in the depletion zone than in Fe-doped substrates.

The depletion regions observed in the Fe and Cr doped substrates are in keeping with reports of conductive surface layers following thermal annealing of InP substrates [19,76]. Additionally, the redistribution is very similar to recent reports of Cr migration in annealed GaAs substrates [58,144-146]. Originally, the accumulation and subsequent depletion regions of Cr in GaAs were speculated to be due to a strain-induced effect caused by the thermal mismatch between the encapsulant and the GaAs [147]. However, recent work by Vasudev et al.[58], indicates that Cr redistribution in GaAs is not significantly influenced by the encapsulant and is in fact larger under capless anneal conditions. Moreover, Kasahara and Watanabe [146] reported that Cr

redistribution in GaAs is controlled by the partial pressure of arsenic during the anneal, which confirms an early observation by Tuck et al. [144], concerning the role of As overpressure with relation to Cr redistribution. At present, therefore, the best explanation of Cr redistribution in GaAs appears to be that it results from the gettering of Cr to surface regions which have high concentrations of defects introduced either by annealing or by mechanical damage [148]. There is reason to believe that the same relationship between defects and compensating dopant also explains our results in InP. It is unclear at present what importance should be attached to the quantitative differences observed between Fe and Cr redistribution profiles in InP. Possibly the differences can be explained in terms of the surface solubility and original background density of the compensating dopant, as suggested by Vasudev et al. [58]. Furthermore, differences between Cr and Fe outdiffusion into the Si_3N_4 cap must be considered. Obviously further work is needed to determine if important differences do indeed exist between Fe and Cr redistribution in InP as our results suggest.

7.1.2 *Redistribution Resulting from the Implantation of Neutral Dopants*

Impurity gettering to damaged (i.e., vacancy-rich) regions produced by ion implantation is often observed in Si [149,150] and in GaAs [58,147,151]. In this section the gettering of Fe and Cr to damaged regions produced by the implantation of electrically neutral species in semi-insulating InP is discussed. Helium was chosen as one such species because it should remain electrically and chemically inactive in the crystal, thereby having no effect on the compensating dopants except form the damage it creates. It is possible for "gas bubbles" or voids to form by the diffusion of insoluble gas atoms to nucleation sites [28,152]. To rule out redistribution due to the possible
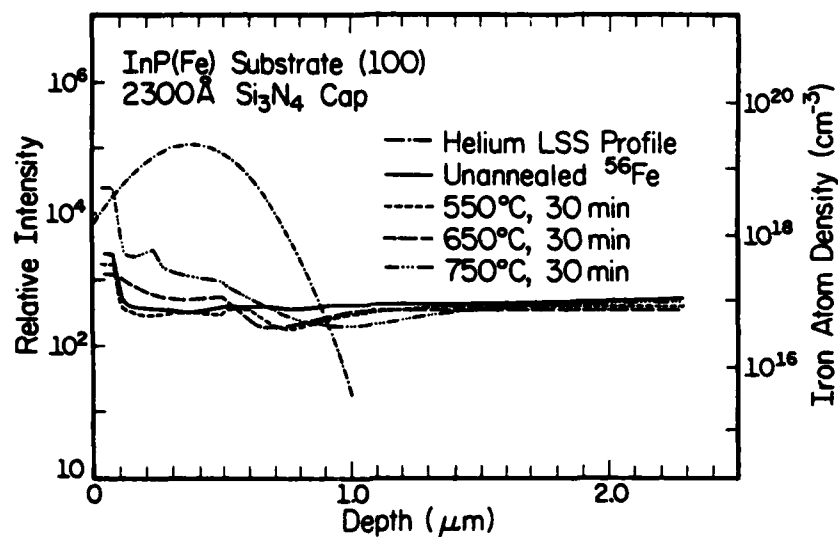
Figure 7.3: SIMS profiles of Fe in a semi-insulating InP substrate implanted with He (1.06×10^{15} cm^{-2}, 51 keV) and annealed for 30 min. at the indicated temperatures with a Si_3N_4 encapsulant [21].
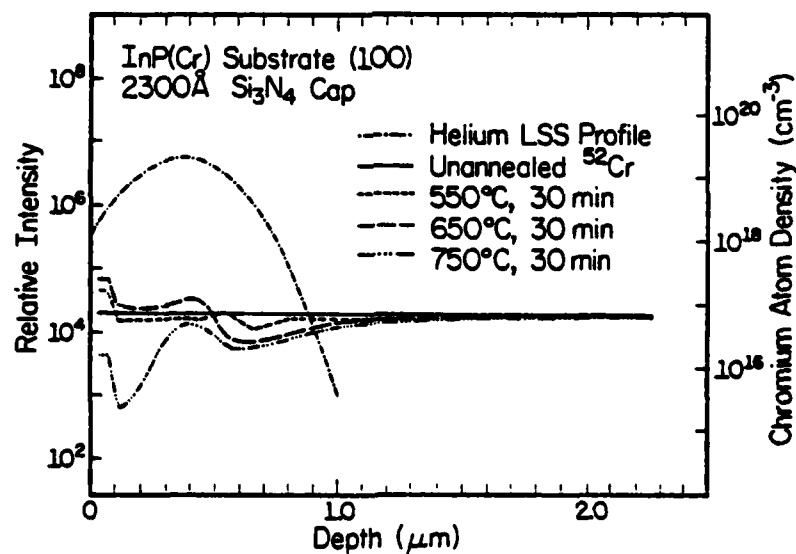
Figure 7.4: SIMS profiles of Cr in a semi-insulating InP substrate implanted with He (1.06×10^{15} cm^{-2}, 51 keV) and annealed for 30 min. at the indicated temperatures with a Si_3N_4 encapsulant [21].

presence of such voids, a non-gaseous element, boron, was also implanted. It is assumed that boron fills column III sites, and is therefore electrically inactive in the crystal (although the possibility of chemical activity cannot be completely ruled out).

A He fluence of 1.06×10^{15} cm^{-2} was implanted into the samples at 51 keV and 0.5 μA scanned current. Under these conditions the LSS projected range is 3640 Å with the profile of energy deposited into nuclear collisions peaking at $\sim$ 3200 Å (see Figure 2.2). Figures 7.3 and 7.4 show the Fe and Cr profiles, respectively, resulting from thirty minute anneals of this He-implanted InP. As in the previously discussed unimplanted samples, a surface accumulation zone exists within the first 1000 Å for both types of compensating dopants. Surface accumulation of Fe is much more pronounced than that of Cr, which is also consistent with the previous results. However, unlike the profiles in the unimplanted samples, we find in the He implanted samples an accumulation region followed by a depletion region rather than broad depletion regions extending to $\sim$ 1 μm. It is clear that both Fe and Cr accumulate in a region about the projected range of He. The 550°C, 30 min anneal profiles show little restructuring except for small depletion regions on the bulk side of the projected range peak. The 750°C, 30 min annealed Fe-doped sample has an accumulation zone with a concentration of $\sim$ 2.6 x 10^{17} cm^{-3} and a depletion zone with a concentration of $\sim$ 3.4 x 10^{16} cm^{-3}. The Cr-doped sample annealed under identical conditions shows even larger variations of concentration in the various regions.

Boron was implanted at 126 keV and 0.5 μA to a fluence of 6.8 x 10^{14} cm^{-2} in Fe-doped InP substrates. The LSS projected range is 3640 Å and the damage profile peaks at $\sim$ 2890 Å (see Figure 2.2). The as-implanted

Figure 7.5: SIMS profiles of Fe in a semi-insulating InP substrate implanted with B (6.8×10^{14} cm^{-2}, 126 keV) and annealed for 30 min. at the indicated temperatures with a Si$_3$N$_4$ encapsulant [21].
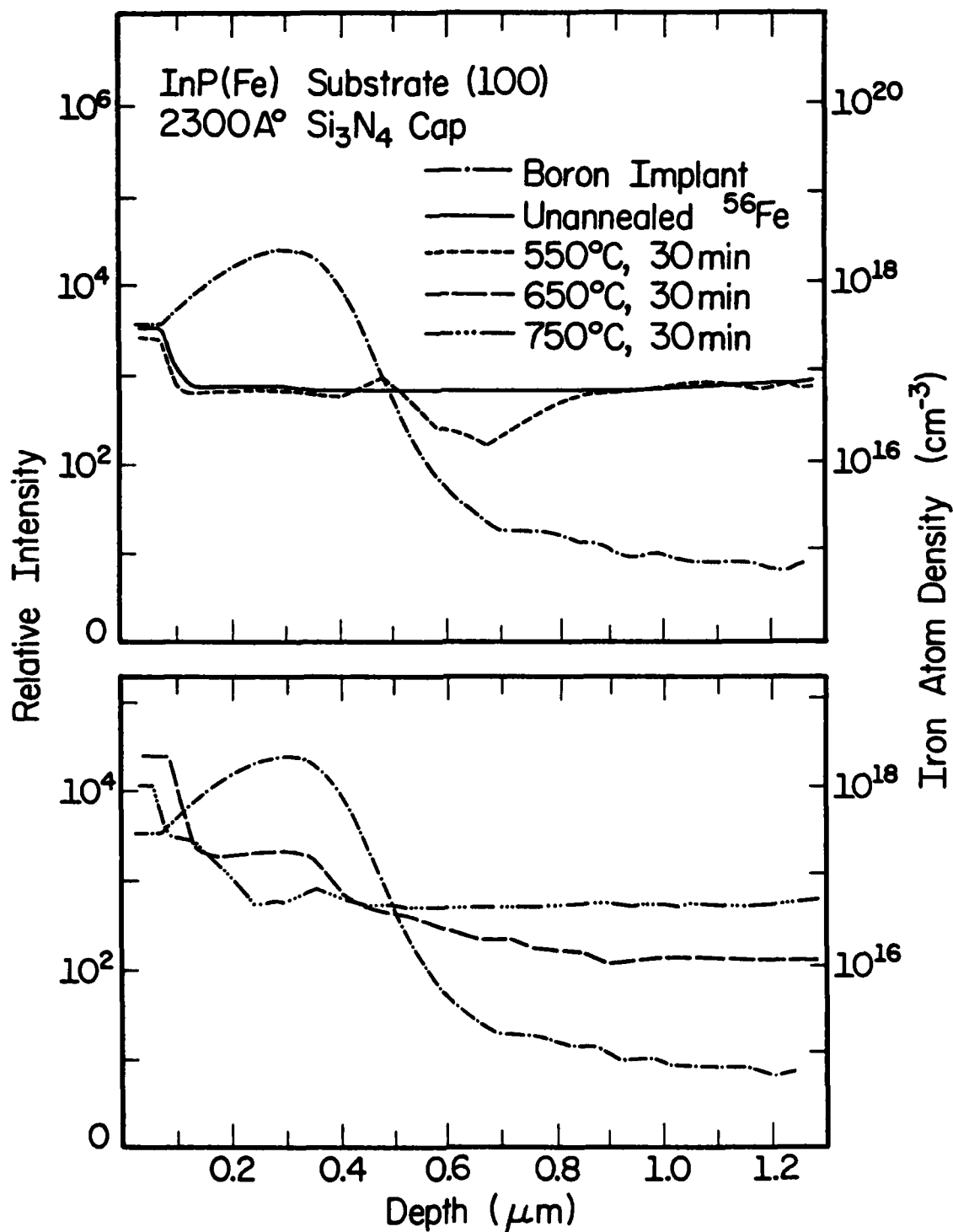
boron profile obtained by SIMS is shown in Figure 7.5. As in the 550°C profiles of He-implanted Fe-doped InP, an Fe depletion zone is formed on the bulk side of the projected range peak with a minimum Fe concentration of $\sim 1.6 \times 10^{16}$ cm^{-3}. Accumulation of Fe into the implant region and toward the surface is evident in the 650°C and 750°C anneals. The qualitative similarities between the redistribution of Fe in the He and B implanted samples appears to indicate that we are observing the gettering of the compensating dopant by implant related defects rather than diffusion due to gas voids or chemical effects.

7.2 Redistribution of Implanted ^{9}Be in SI InP

There exists a need for controllable acceptor doping of InP in several of the applications mentioned above. For example, InP p-type layers are used as confining layers in typical InGaAsP/InP double-heterostructure diode lasers. Low dark current avalanche photodiodes can be constructed from structures incorporating an InP p-n junction above a detecting InGaAsP layer [153]. It is also assumed that acceptor doping will play some part in the fabrication of logic circuits. To date Zn and Cd have been the dominant impurities used to obtain p-type InP by growth or diffusion techniques. It has been observed, however, that both impurities are rapid diffusants in InP and hence difficult to accurately control in the fabrication of p-n junctions [154-157]. Because of these difficulties the implantation of acceptors into InP has been considered as an alternative doping technique. ^{9}Be is a particularly appealing ion for such p-type implants. Due to its low mass, ^{9}Be can be implanted over a wide range of depths with conventional implanters, and creates less lattice damage than heavier p-type ions. Beryllium has already proven to be a useful implanted acceptor with good electrical activation in GaAs and GaAs$_{0.6}$P$_{0.4}$ [135-137,158]. More recently, ^{9}Be implantation

has been successfully employed to fabricate diodes in InP and in InGaAsP [159-162]. For these reasons the redistribution of implanted ^9Be resulting from furnace anneals was studied in semi-insulating InP.

7.2.1 Comments on Mass Interferences

On several occasions we have observed molecular interference with the ^{56}Fe signal in the implanted region. This interference was observed in the unannealed 10^{15} cm^{-2} ^9Be implant sample, and is a problem only for the high fluence implants. Since the mass 56 profile reflected the peak shape of the unannealed ^9Be implant, we presume this interference is from the molecule $^{56}(BeOP)^+$. System response to this molecule varied between sessions and may be attributable to aging in the system's electron multiplier. The annealed profiles of high fluence implants presented here were obtained when instrumental conditions were such that this molecular interference was not observed. Profiles taken during sessions when interference was observed contained ^{56}Fe profile peaks even after subtracting out the molecular interference. In addition, the reality of the structures observed in the ^{56}Fe profiles of high fluence implanted material is confirmed by similar structures in the ^{52}Cr profiles (which have no apparent molecular interference).

Another possible interference at mass 56 is the ^{28}Si dimer, $^{56}Si_2$. Mass 28 profiles taken from samples that were Si_3N_4 encapsulated and annealed at 800°C for 30 min contain a strong surface signal well above background, apparently resulting from Si in-diffusion from the encapsulant. Our analysis of dimer yield from crystalline Si indicates that the $^{56}Si_2^+$ yield is ~ 2.5 orders of magnitude lower than the $^{28}Si^+$ yield (or, ~ 0.4% of the parent ion). The yield of $^{56}Si_2^+$ from dilute ^{28}Si in InP should be even lower since dimer production is roughly proportional to the square of the parent concentration.

Taking this into account, $^{56}Si_2$ interference is possible only at the InP surface in the data presented here. Additional facts, however, suggest that even at the surface this possible dimer interference may not be significant. Depth profiles of the ^{54}Fe isotope show iron surface accumulation regions similar to those seen in ^{56}Fe profiles. Estimates of ^{56}Fe signal levels based on the isotopic abundance of ^{54}Fe predict ^{56}Fe signal levels comparable to those observed experimentally. Also, for the profiles exhibited here, the first channel of ^{56}Fe data was usually acquired at a depth where $^{56}Si_2^+$ interference is expected on the basis of our observations to be minimal.

7.2.1 *SIMS Profiles of Annealed ^9Be Implants*

Figure 7.6 shows the SIMS profiles resulting from implantation of 1×10^{13} cm^{-2} ^9Be into Fe-doped InP with subsequent 30 min anneals. At 550°C the ^9Be atomic profile exhibits little diffusion. The ^{56}Fe profile, however, has undergone some movement even at this relatively moderate annealing temperature. It is observed that the Fe concentration is higher than the original background level both at the surface and in an area to the left (surface) side of the implanted peak. As will be discussed later, this particular region coincides closely to the peak in the theoretical damage profile created by the implantation process. These accumulation regions are followed by an ^{56}Fe depletion region extending to ~ 1 μm before returning to the background level. At 650°C and 750°C rapid diffusion of the initial ^9Be profile toward the surface and the bulk is seen. In addition, significant movement of ^{56}Fe is observed, with the previously noted depletion zone in the 550°C anneal deepening and broadening. At 750°C the ^{56}Fe profile reaches a minimum concentration of ~ 1×10^{16} cm^{-3} and returns to the background doping level at a depth of ~ 2.0 - 2.5 μm.

Figure 7.6: SIMS unannealed and annealed profiles of Fe-doped InP implanted with 100 keV, 10^{13} cm^{-2} ^{9}Be. Thirty minute anneals were performed with a Si$_3$N$_4$ encapsulant [138].

In Figure 7.7 the results of implanting ^{9}Be to a fluence of 1 x 10^{14} cm^{-2} and subsequent 30 min annealing are shown. The ^{9}Be profile resulting from a 550°C, 30 min anneal differs markedly from that seen in Figure 7.6(b). Movement of ^{9}Be toward the surface and the bulk is seen in this case, with a shoulder appearing on the bulk side of the initial profile. An unusual feature of this profile is the flat, essentially constant concentration of ^{9}Be ranging from ~ 1-2 μm following by an abrupt drop to the ^{9}Be background detection level. It can also be noted that ^{56}Fe getters into the implanted region slightly above its background concentration. The ^{56}Fe depletion zone previously mentioned is seen to return rapidly to background in a region coinciding with the abrupt drop in the ^{9}Be atomic profile. The ^{9}Be profile resulting from a 650°C, 30 min anneal is similar to the 550°C anneal in that a peak is still observed about the implanted range, followed by a shoulder on the bulk side of the profile. However, the ^{9}Be profile appears to return to the background level more gradually in this case than for the 550°C anneal. At 750°C the ^{9}Be profile is essentially flat and featureless, exhibiting a very gradual drop to the background detection limit. The ^{56}Fe profile for this anneal consists of a surface accumulation region followed by an extremely broad, flat depletion zone. Although Figure 7.7(d) does not show ^{56}Fe returning to background, it has been observed in other profiles taken from this sample. This return takes place much more gradually than in any of the other profiles from this set however.

Figure 7.8 shows profiles of Fe-doped InP implanted with a fluence of 1 x 10^{15} cm^{-2} of ^{9}Be. As this figure illustrates, annealing this material at 550°C for 30 min results in gross restructuring of both the ^{9}Be and ^{56}Fe initial profiles. Referring to Figure 7.8(b), note that in addition to the

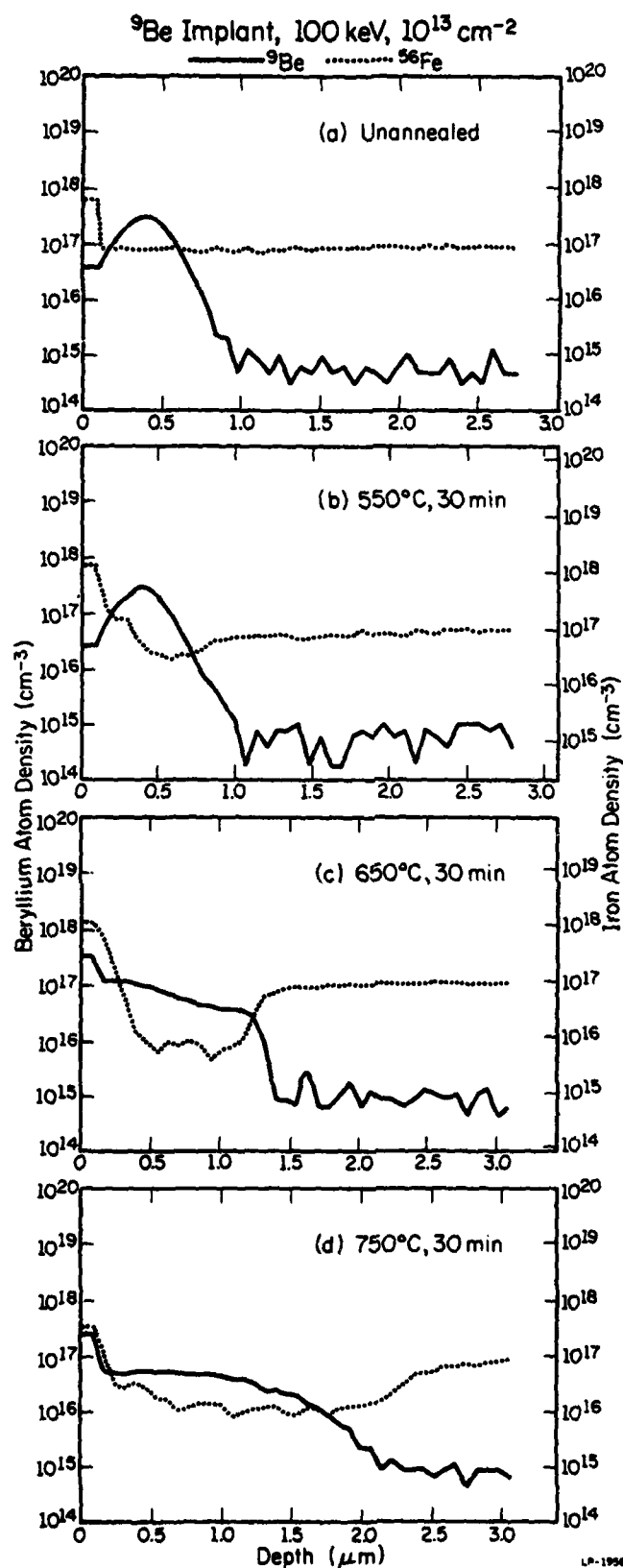**⁹Be Implant, 100 keV, 10¹⁴ cm^{−2}**

Figure 7.7: SIMS unannealed and annealed profiles of Fe-doped InP implanted with 100 keV, 10^{14} cm^{-2} ^{9}Be. Thirty minute anneals were performed with a Si$_3$N$_4$ encapsulant [138].

^{9}Be Implant, 100 keV, 10^{15} cm^{-2}
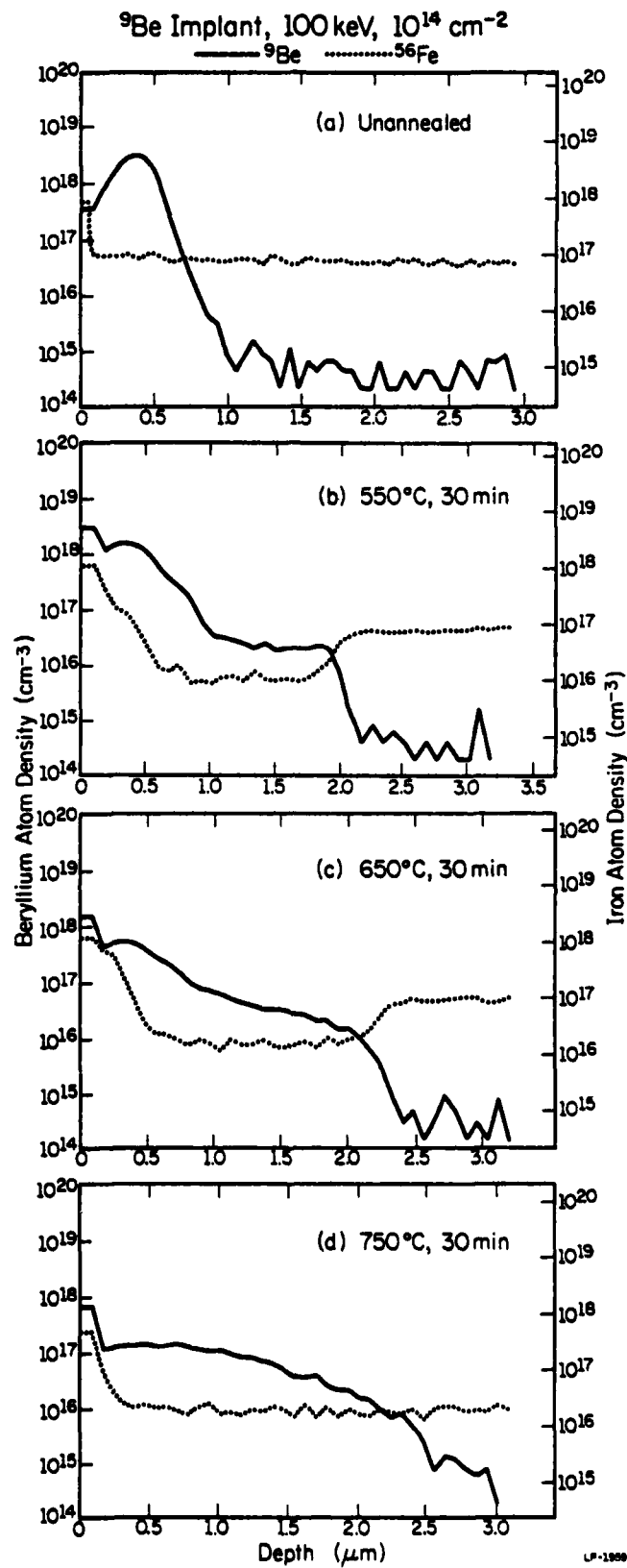
——— ^{9}Be   ··········· ^{56}Fe

Figure 7.8:   SIMS unannealed and annealed profiles of Fe-doped InP implanted with 100 keV, 10^{15} cm^{-2} ^{9}Be.   Thirty minute anneals were performed with a Si$_3$N$_4$ encapsulant [138].

^{9}Be peak in the implanted region, a large peak occurs on the surface side of the implanted peak with a smaller peak evident on the bulk side. The position of this smaller peak correlates well with the observed shoulders at this depth in the other implants. The most dramatic feature of this particular profile is the constant-concentration tail of ^{9}Be extending several microns into the bulk. ^{56}Fe redistribution appears to be correlated with the motion of ^{9}Be, with strong gettering occurring on the surface side and the bulk side of the initial ^{9}Be profile. Deeper profiles indicate that the constant-concentration tail of ^{9}Be extends to a depth of $\sim$ 4 μm before dropping abruptly to the background detection limit with a corresponding sudden return to the background doping level in the ^{56}Fe profile at this same depth. At 650°C, ^{56}Fe is observed to getter into the region to the right of the ^{9}Be peak and into the implanted peak area. The ^{9}Be profile at this temperature still exhibits a peak in the implanted region, a shoulder on the bulk side of the profile, and a constant-concentration tail extending from 1-2 μm in the bulk. The ^{9}Be profile resulting from a 30 min, 750°C anneal exhibits a peak with a concentration reduced by approximately one order of magnitude from the peak implant concentration. The ^{56}Fe profile of this anneal exhibits the previously observed surface accumulation and a deep depletion zone extending $\sim$ 2 μm into the bulk before returning to background. An unusual feature of these profiles is the retrograde motion of the abrupt drop in ^{9}Be (or of the rise in ^{56}Fe) as the annealing temperature is increased. Higher anneal temperatures result in shallower regions of impurity redistribution, which is contrary to simple diffusion mechanisms.

To date most reports on implantation of InP have employed annealing schedules of T $\geq$ 700°C for $\sim$ 10-15 min [18,19,76,78]. Therefore we examined the
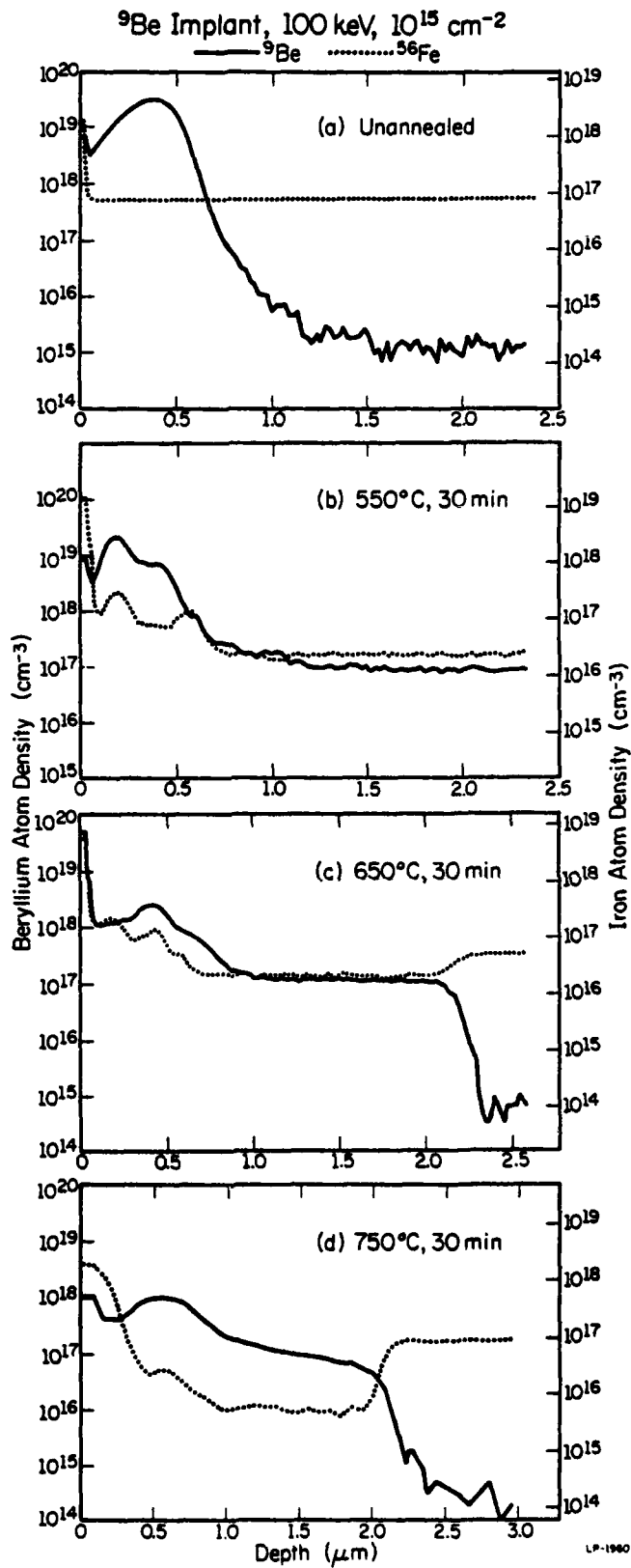
⁹Be Implant, 100 keV, 10¹⁵ cm⁻²

Figure 7.9: SIMS unannealed and annealed profiles of Fe-doped InP implanted with 100 keV, 10¹⁵ cm⁻² ⁹Be. Fifteen minute anneals were performed with a Si₃N₄ encapsulant [138].

effect of 15 min anneals on the restructuring of ^{9}Be and ^{56}Fe profiles in material implanted with a ^{9}Be fluence of 10^{15} cm^{-2}. From Figure 7.9 it can be seen that these profiles are qualitatively similar to those obtained with 30 min anneals. The redistribution of ^{9}Be and ^{56}Fe in 10^{15} cm^{-2} implants appears to be rapid, with significant structure and diffusion occurring within only 15 min of annealing.

Figure 7.10 contains impurity profiles after 30 min anneals of Cr-doped InP implanted with 1 x 10^{15} cm^{-2} fluence of ^{9}Be. The resultant ^{9}Be profiles are similar in most respects to correspondingly processed Fe-doped InP. Since molecular interference is not expected or seen at mass 52, the observed ^{52}Cr peaks in Figure 7.10 suggest that the ^{56}Fe peaks in Figures 7.8 and 7.9 are real and not entirely the result of molecular interference. Evidence of retrograde motion of the ^{9}Be redistribution front is again observed in these profiles [note the different depth scale in 7.10(b)]. Qualitatively, ^{52}Cr appears to redistribute much as ^{56}Fe but with several quantitative differences. Although near-surface SIMS data is suspect, it certainly appears that ^{52}Cr does not getter to the surface as strongly as does ^{56}Fe. In fact, the near-surface ^{52}Cr signals are comparable to the original ^{52}Cr background level. Another significant difference between ^{56}Fe and ^{52}Cr appears in the minimum concentration observed in the depletion zones. Whereas the ^{56}Fe concentration is observed to deplete approximately an order of magnitude in the depletion zones, ^{52}Cr depletes approximately two orders of magnitude in this depletion zone. These differences between ^{56}Fe are ^{52}Cr and consistent with the profiles discussed in Section 7.1.

In order to determine the role of the substrate in the observed ^{9}Be profiles, an undoped, 12 μm-thick vapor phase epitaxial (VPE) layer of InP
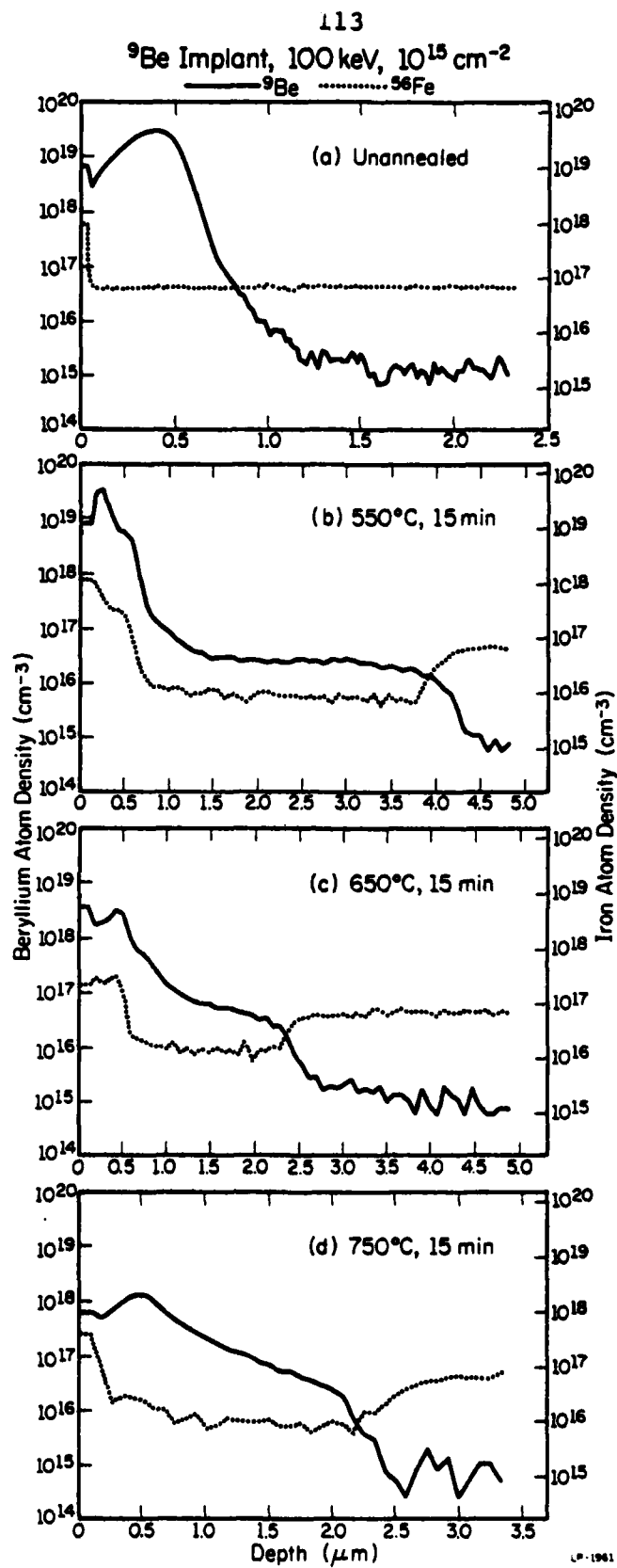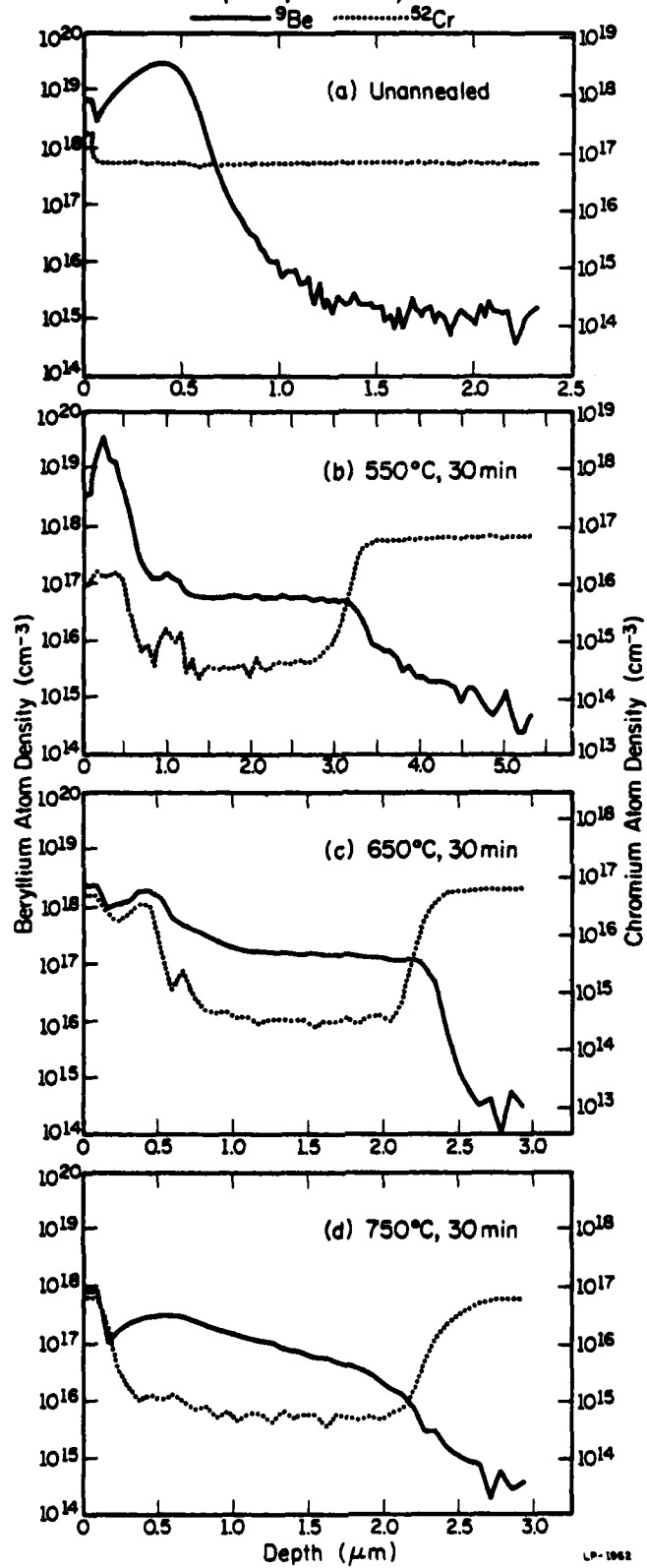
Figure 7.10: SIMS unannealed and annealed profiles of Cr-doped InP implanted with 100 keV, 10^{15} cm^{-2} ^{9}Be. Thirty minute anneals were performed with a Si_3N_4 encapsulant [138].

$$^9\text{Be Implant, } 100\,\text{keV, } 10^{15}\,\text{cm}^{-2}$$
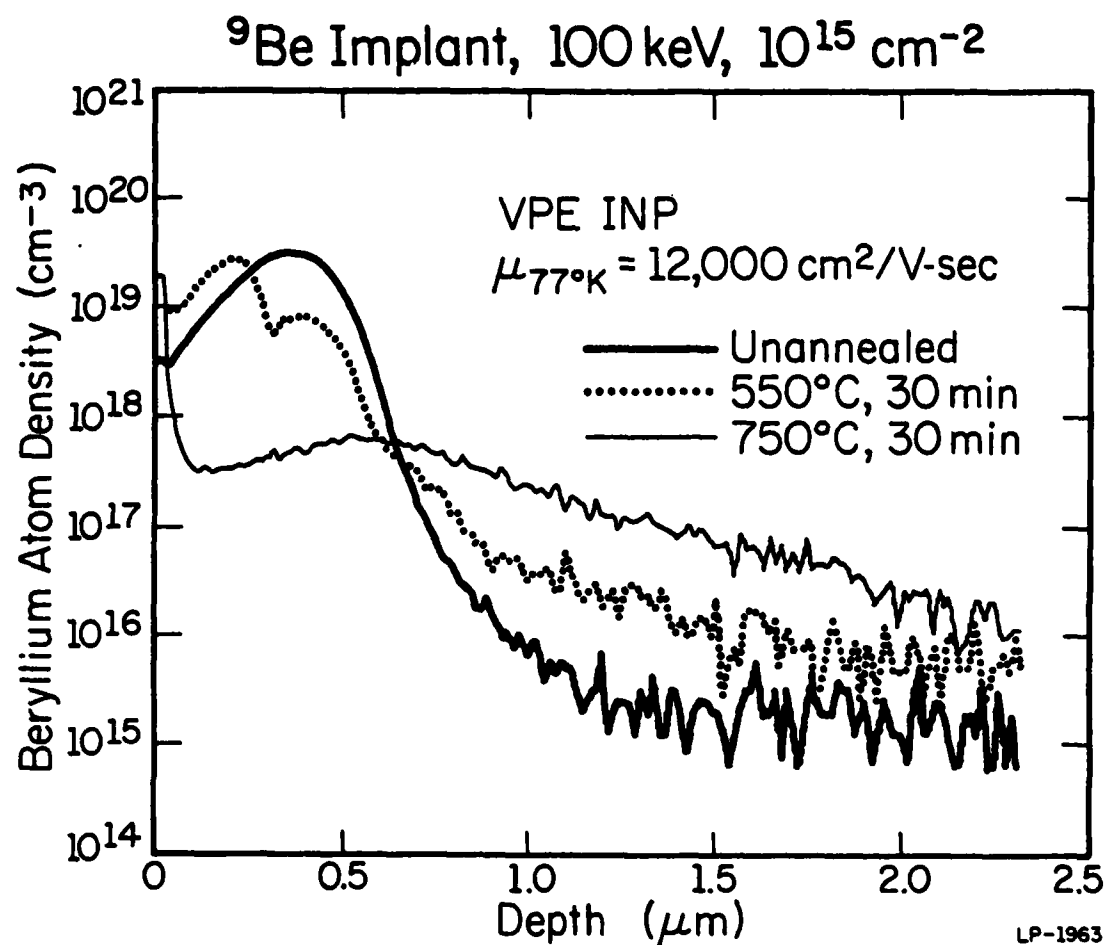
Figure 7.11: SIMS unannealed and annealed profiles of a 12 μm-thick, undoped VPE InP layer implanted with 100 keV, 10^{15} cm^{-2} ^{9}Be. Thirty minute anneals were performed with a Si$_3$N$_4$ encapsulant [138].

was implanted with ^{9}Be. The resultant profiles are shown in Figure 7.11. In most respects these profiles are similar to those observed in comparable anneals of Fe-doped or Cr-doped material. Note however in the 550°C anneal shown here the lack of the constant-concentration ^{9}Be tail observed in Figures 7.8(b) and 7.10(b).

7.2.3 Discussion: Surface Phenomena

As previously mentioned, one must be cautious in attaching too much quantitative importance to the initial surface signals obtained by SIMS. Surface oxides will enhance the yield of positive secondary ions within the first hundred angstroms [52,145]. Additionally, the sputtering rate and data acquisition time can smear this effect out over a larger distance. Quantitatively, the first channel of ^{56}Fe data may to some degree reflect ^{56}Si$_2$ interference as described earlier. However, although the exact surface concentrations are somewhat in doubt, it is apparent that in the majority of the anneal profiles ^{56}Fe exhibits strong gettering to the surface above the background doping concentration and that ^{9}Be also shows diffusion towards the surface, depending on fluence and annealing. It is interesting that the surface gettering of ^{52}Cr is not as strong as that of ^{56}Fe. The concentrations of ^{52}Cr in the annealed profiles shown in Figure 7.10 are either at the original doping level or slightly below this level. This behavior of ^{52}Cr and ^{56}Fe is consistent with previously observed effects in annealed-only samples and material implanted with "neutral" impurities (He, ^{10}B) [21].

Various mechanisms have been proposed to explain the observation of impurity redistribution at surfaces, including: (i) strain-induced redistribution resulting from thermal mismatch between the encapsulant and the substrate [147]; (ii) surface states and surface impurities giving rise to a near surface electric field [163,164]; (iii) surface defects resulting from

mechanical damage or annealing [148]. Recent work indicates that Cr redistribution in GaAs can occur without an encapsulating layer [58] and is in fact influenced by the partial pressure of As during the annealing of bare GaAs surfaces [144,146]. Differences in ^{52}Cr and ^{56}Fe accumulation may possibly be understood in terms of surface solubility effects and the original doping concentration of the compensating dopant [58]. For all three impurities, ^{9}Be, ^{52}Cr, and ^{56}Fe, diffusion into the Si_3N_4 must also be considered. Previous work done in our group using SIMS has shown that Be can be detected in the Si_3N_4 encapsulating layer after annealing Be-implanted GaAs at 900°C for 30 min [165].

7.2.4 Discussion: Near Surface Phenomena

The next region we wish to consider extends from $\sim$ 0.1 - 0.6 μm. Several aspects of the observed redistribution in this region may be understood on the basis of implantation-related damage. Shown in Figure 2.2 are the LSS Gaussian, the Gaussian theoretical damage profile, and the SIMS profile of the unannealed 10^{15} cm^{-2} ^{9}Be implant. The shape of the SIMS profile and its fit to four-moment distributions will be discussed in Chapter 8. The peak of the Gaussian damage profile occurs at $\sim$ 2900 Å while the LSS mean range for 100 keV ^{9}Be is $\sim$ 3640 Å (see Table 2.1).

At the fluences of 10^{13} and 10^{14} cm^{-2}, the position of the damage peak at 2900 Å agrees well with the position of an Fe peak just to the left of the implant peak [see for example Figures 7.6(b), 7.7(b), and 7.7(c)]. In the previous section we examined the ^{56}Fe profiles resulting from the implantation of He with the same scanned current, mean depth, and peak concentration as the 100 keV, 10^{15} cm^{-2} ^{9}Be implants discussed here. The ^{56}Fe profiles described there also showed gettering into the damage region which peaked at $\sim$ 3200 Å for 51 keV He. Those Fe profiles, however, resemble the

10^{13} cm^{-2} profiles shown in Figure 7.6 more than the Fe profiles of Figures

7.8 and 7.9 which result from 10^{15} cm^{-2} ^{9}Be implants. Although the peak

concentration of He was equal to that of a 100 keV, 10^{15} cm^{-2} ^{9}Be implant,

the lower mass of He results in much less energy deposition into the lattice.

For this reason the Fe profiles observed in the He implants of Section 7.1.2

resemble those resulting from low fluence ^{9}Be implants. Such gettering of

impurities to implantation-induced damage areas is frequently observed in

Si and in GaAs [149,166,167].

The redistribution of Be and the compensating dopants differ

markedly in the 10^{15} cm^{-2} implanted samples from the profiles observed in

the lower fluence implants. As can be seen in Figures 7.8(b), 7.9(b),

7.10(b), and 7.11, twin peak structures appear in the Be, Fe, and Cr profiles.

In all cases the drop between the impurity shoulders occurs in the approxi-

mate position of the damage peak at ~ 2900 Å. Such "up-hill" impurity flow

cannot be explained by damage enhanced diffusion, which should lead to

profile flattening rather than this type of redistribution [168]. There are

at least two possible models for this behavior.

Such two-peaked structures have sometimes been attributed to the

presence of an amorphous layer [58,169]. Electron channelling patterns obtained

from implanted, unannealed samples are shown in Figure 7.12. Comparing the

pattern of Figure 7.12(a) to the other patterns of Figure 7.12 indicates

that based on the loss of higher order Coates lines, the implanted samples

are heavily damaged as expected. The presence of the major Coates lines in

these samples however, indicates that the disordered material is not amorphous.

In view of these results, it appears that amorphization is not the cause of

the observed Be redistribution.

Figure 7.12: (a) Electron channelling patterns (ECP) from the surface of an unimplanted sample. ECP from samples implanted with 100 keV, 10^{15} cm^{-2} ^{9}Be at depths of: (b) surface, (c) $\sim$ 2900 Å below the surface, and (d) $\sim$ 3600 Å below the surface [138].
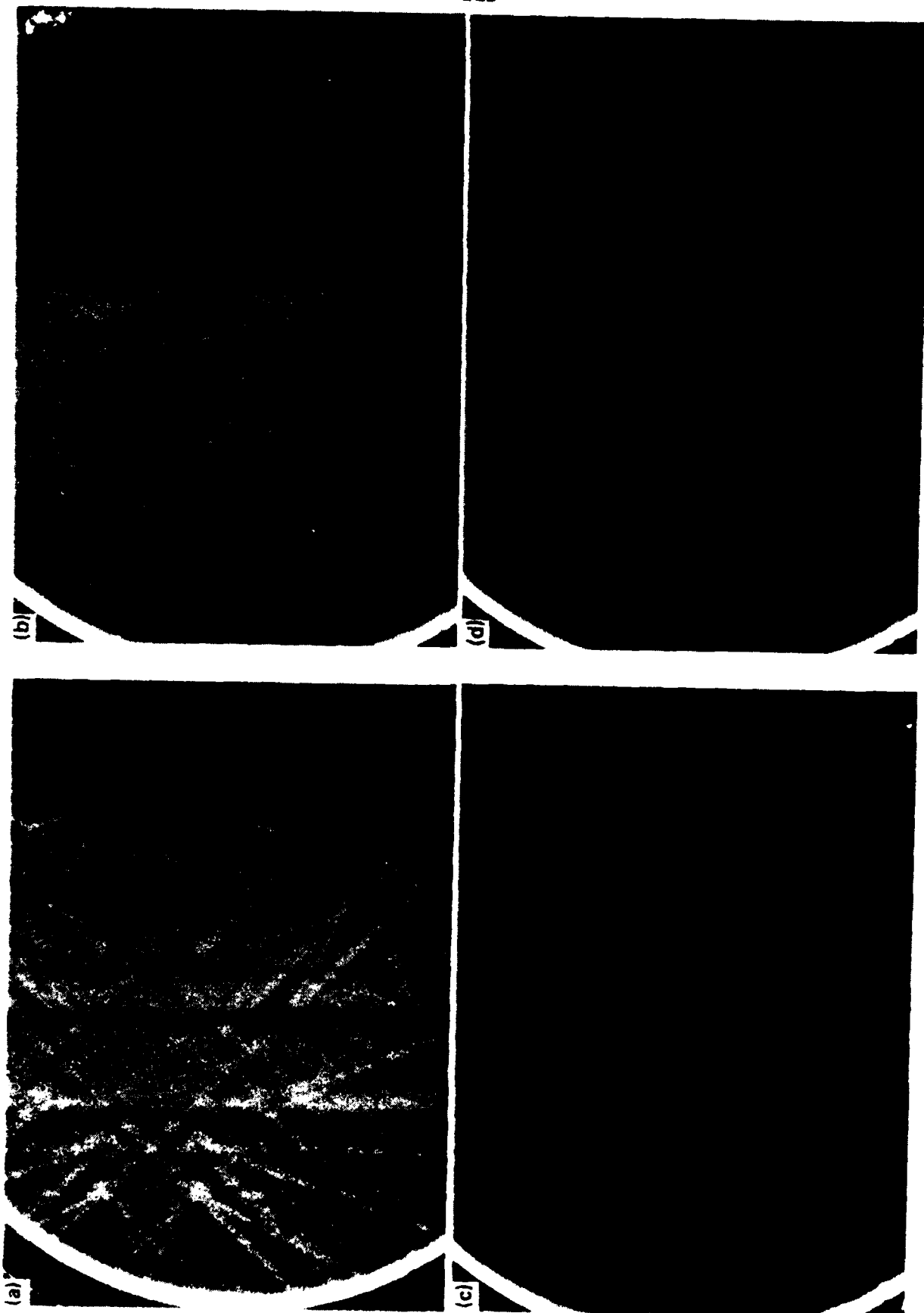
Figure 7.12
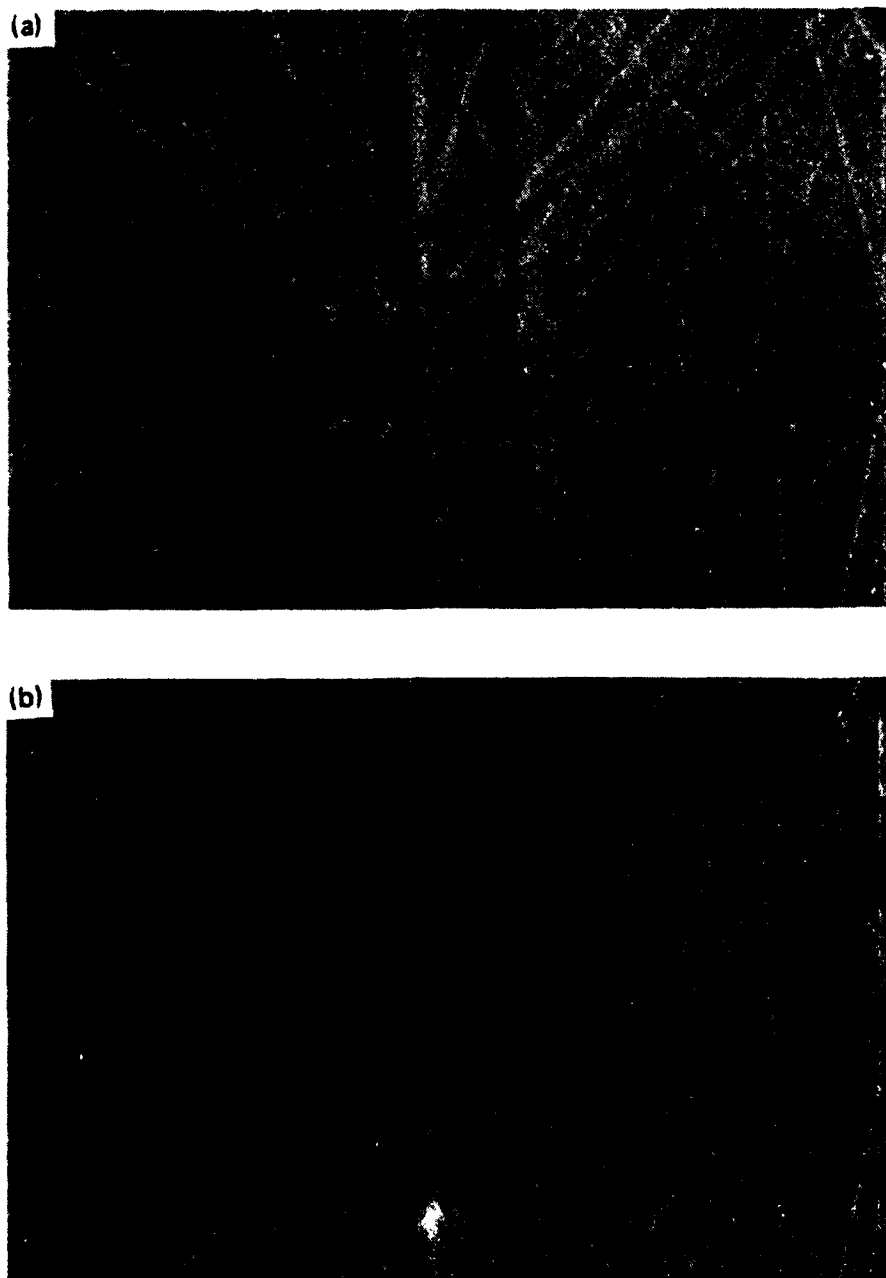
Figure 7.13: (a) Electron channeling pattern (ECP) from the surface of an unimplanted sample. (b) ECP at a depth of $\sim$ 3000 $\overset{o}{A}$ below the surface from a sample implanted with 100 keV, 10^{15} cm^{-2} ^{9}Be and annealed for 30 min at 550°C [138].

Another explanation of the double peak structures can be found in the models proposed by Baruch [168] and Akutagawa et al. [150], for similar structures in Si. According to these models, impurity shoulders with a central dip can result from: (1) distinct but interacting currents of defects and impurities with their own gradients and diffusivities; (2) impurity-defect pairs which diffuse rapidly away from the peak of the localized damage distribution. These explanations for the observed dip and shoulders are both consistent with the fact that this structure appears at the position of the theoretical damage peak.

In addition to the channelling patterns of unannealed material, we have examined the ECP from 550°C, 30 min anneals of 10^{15} cm^{-2} Be implanted InP. Channelling patterns at depths of $\sim$ 0, 1500, 3000, and 4500 $\overset{\circ}{A}$ have been analyzed and are virtually indistinguishable from unimplanted material. Only the pattern shown in Figure 7.13 at a depth of $\sim$ 3000 $\overset{\circ}{A}$ (near the theoretical damage peak) showed a barely perceptible loss of higher order Coates lines. It is obvious from Figure 7.12 and 7.13 that significant reordering of the lattice occurs at this low temperature, although electrical activation of the implanted impurity generally requires higher annealing temperatures.

7.2.5 Discussion: Bulk Phenomena

Several unusual profile features are evident in the bulk regions of the samples analyzed in this work. These are: (1) constant-concentration tails of ^{9}Be extending over distances on the order of microns; (2) constant-concentration depletion zones of the compensating impurity (^{52}Cr or ^{56}Fe) extending over similar distances; (3) correlation between the diffusion profile of the ^{9}Be and the compensating impurity (i.e., the depth at which the compensating impurity returns to its doping level coincides with the

depth at which the constant-concentration tail of ^{9}Be drops to the detection limit); and (4) retrograde motion of the ^{9}Be diffusion front (or of the compensating impurity depletion zone front) with higher annealing temperatures. Of these features, depletion of the compensating impurity on the bulk side of the implanted peak has previously been observed in annealed InP implanted with "neutral" elements (He, ^{10}B) as described in Section 7.1.2. To our knowledge, the other features reported here have not been previously observed in conjunction with implantation of InP or GaAs.

Perhaps the most striking features of the impurity redistribution are the long, essentially flat ^{9}Be tails and the accompanying Fe or Cr depletion zones. Such diffusion cannot result from normal Fickian (random walk) diffusion. Similarly, conventional field-enhanced diffusion [163,164,170] does not explain the correlation between the ^{9}Be and ^{52}Cr or ^{56}Fe profiles. To explain such correlations with field enhanced diffusion would require that ^{9}Be, ^{52}Cr, and ^{56}Fe all have the same effective diffusion coefficients.

When considering these bulk phenomena the following relevant factors emerge from this work: (1) the dose dependent location of the end of the ^{9}Be diffusion tail (or of the ^{52}Cr or ^{56}Fe depletion zone) at 550°C; (2) the retrograde motion of these features with elevated annealing temperature; (3) the more gradual sloping of the ^{9}Be diffusion front at 750°C versus the constant concentration tails seen at 550°C; and (4) the lack of constant-concentration tails of ^{9}Be in 10^{15} cm^{-2} implanted and annealed VPE material. The fact that the constant-concentration ^{9}Be tail does not appear in VPE InP indicates that either the compensating dopants (Fe or Cr) or other residual impurities and/or defects in semi-insulating, bulk InP are necessary in the creation of this tail. Formation of pair complexes of ^{9}Be with ^{52}Cr or ^{56}Fe

might explain the observed correlation between the ^{9}Be and the compensating impurity profiles. It is unclear if energy considerations prevent ^{9}Be from complexing with the deep level acceptors Fe (neutral state Fe_{In}^{+3}) [171,172] or Cr (neutral state Cr^{+2}) [171]. Based on the depletion of ^{56}Fe or ^{52}Cr in the regions of the ^{9}Be tail, it seems more likely that ^{9}Be participates with the compensating impurities in a cooperative diffusion mechanism. Such possible effects alone, however, cannot explain the retrograde behavior of the ^{9}Be tail and the accompanying end of the ^{52}Cr or ^{56}Fe depletion zone. Based on the temperature dependence of this phenomenon, a defect or defect complex with enhanced diffusion could be responsible for the deep diffusion at low temperatures (i.e., 550°C). The concentration of such defects or defect complexes is reduced at higher temperatures (i.e., 650-750°C), resulting in shallower redistribution of the impurities. Annealing effects of such a defect structure with enhanced diffusion can explain the more gradual diffusion front of ^{9}Be observed at 750°C versus the abrupt fronts seen at 550°C. Additionally, by assuming these defect structures to be implant damage related, it is possible to account for the observed dose dependent depth of the ^{9}Be diffusion front seen in the 550°C anneals. However, it is necessary to connect such defect structures with the presence of ^{52}Cr or ^{56}Fe or other impurities in bulk InP, without which the flat tails of ^{9}Be are not formed. Alternately the constant-concentration ^{9}Be may result from a low Be solubility in undamaged, semi-insulating InP (published results for Be-doped LPE layers[173] indicate no saturation of carrier concentration up to ~ 6×10^{18} cm^{-3}) with the rate-limiting step of the process being the release of Be from the damaged layer. If it is further assumed that the Be solubility increases with temperature it is possible to understand the shallower ^{9}Be profiles at

TABLE 7.1

Pauling covalent tetrahedral radius[176], r_{PA}, Phillips covalent tetrahedral radius[177], r_{PH}, Pauling electronegativity [176], ϵ_{PA}, and Phillips electronegativity[177], ϵ_{PH}

Ion	r_{PA} (Å)	r_{PH} (Å)	ϵ_{PA}	ϵ_{PH}
In	1.44	1.405	1.7	0.99
P	1.10	1.128	2.1	1.64
Fe	----	-----	1.8	----
Cr	----	-----	1.6	----
Be	1.06	0.975	1.5	1.5
B	0.88	0.853	2.0	2.0
Mg	1.40	1.3C1	1.2	0.95
Si	1.17	1.173	1.8	1.41

higher temperatures. Solubility effects, however, do not explain the correlation of the ^{9}Be profile to that of the ^{52}Cr or ^{56}Fe profile in semi-insulating InP, so that this solubility model also seems to require cooperative diffusion between ^{9}Be and the compensating impurities.

It has been observed that an ideal substitutional impurity should possess: (1) a covalent tetrahedral radius close to the host atom it replaces; (2) small electronegativity difference with the host; and, (3) valence close to the host[174]. A recent review of redistribution effects in III-V compounds has stressed the importance of electronegativity and size effects in determining diffusion behavior[175]. We have tabulated the values of electronegativity and the covalent tetrahedral radii for relevant atoms as calculated by Pauling[176] and Phillips[177] in Table 7.1. From this table it is clear that ^{10}B is farther from In in both size and electronegativity than is ^{9}Be. As described in Section 7.1.2, ^{10}Be implants of 126 keV and 6.79×10^{14} cm^{-2} dose were performed to simulate the damage resulting from a 100 keV, 10^{15} cm^{-2} ^{9}Be implant (energy deposition of 2×10^{20} keV cm^{-3}). The resulting ^{10}B atomic profiles show very little diffusion after 750°C, 30 min anneals, in contrast to identical anneals of any ^{9}Be dose considered here[178]. Electronegativity and size considerations alone are therefore not sufficient to explain the rapid diffusion of ^{9}Be.

7.3 Redistribution of Implanted Mg in SI InP

The need for a well behaved (i.e., high activation, low diffusivity) implanted acceptor in InP has already been described in the preceding section. The examination of high dose Mg implants in InP resulted from the findings of the poor annealing characteristics for high dose Be implants in InP. In terms of atomic mass, Mg is more appropriate for implantation than other acceptors of heavier mass such as Zn or Cd. The lower mass of Mg should

result in less damage and afford greater variation in the location of the projected range than with heavier ions. From the Phillips values for covalent tetrahedral radii and electronegativity given in Table 7.1, Mg should be a better substitutional impurity for In than is Be. To study implanted Mg, the isochronal annealing characteristics of 250 keV, 10^{15} cm^{-2} implants of ^{26}Mg have been examined in this work using SIMS. This isotope of Mg was chosen because it readily provides the low ion current required in this study to prevent beam heating of the sample. Implantation took place at room temperature using a Mg current density of ~ 0.1 μA cm^{-2} (see Table 2.1).

Shown in Figure 2.3 are the SIMS atomic profiles of the as-implanted ^{26}Mg and the theoretical profiles for the impurity and the accompanying damage. To facilitate comparisons with our Be implant work, the Mg peak concentration is roughly comparable to that of Be in the 10^{15} cm^{-2} implant discussed in the preceding section. The mode of the LSS Gaussian for Mg occurs at 2994 Å and the mode of the Gaussian damage profiles is located at ~ 1630 Å (see Table 2.1). The fit of four moment distributions to the experimental SIMS profile will be discussed in Chapter 8.

Shown in Figure 7.14 are the SIMS profiles for 30 min anneals from 550-750°C. Redistribution of the implanted Mg is seen to occur at 550°C. This anneal results in a flat profile of ~ 1.3 x 10^{19} cm^{-3} of Mg extending from the surface to a depth of approximately 4000 Å. At higher annealing temperatures this region is increasingly depleted of Mg, resulting in a minimum concentration of ~ 3.7 x 10^{16} cm^{-3} at 750°C. Comparing Figures 2.3 and 7.14(d), we observe that the Mg depletion zone occurs in the region of maximum implant damage. Along with this depletion zone, an accumulation region of Mg occurs on the bulk side of the initial Mg profile. As Mg is

^{26}Mg Implant, 250 keV, 10^{15} cm^{-2}

—— ^{26}Mg ·········· ^{56}Fe

(a) Unannealed

(b) 550°C, 30min

(c) 650°C, 30min

(d) 750°C, 30min

Magnesium Atom Density (cm^{-3})

Iron Atom Density (cm^{-3})

Depth (μm)
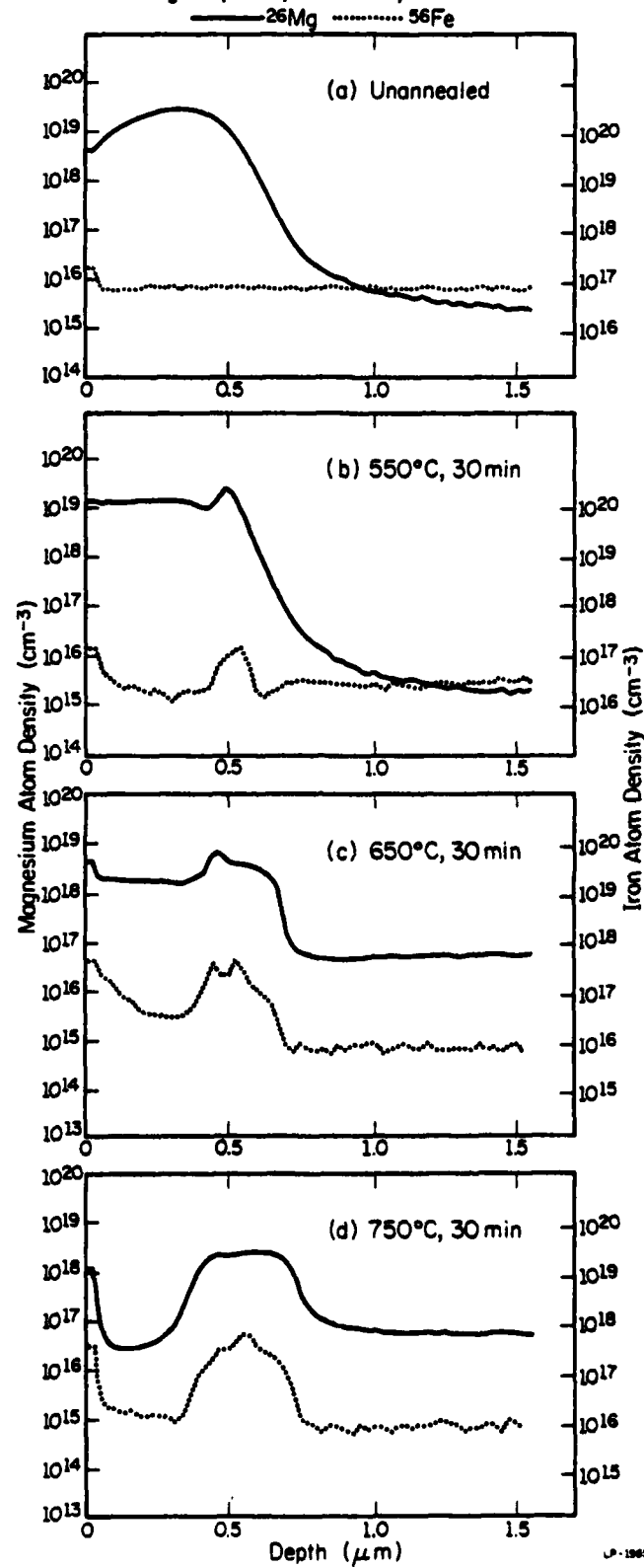
Figure 7.14: SIMS unannealed and annealed profiles of Fe-doped InP implanted with 250 keV, 10^{15} cm^{-2} Mg, following 30 min anneals with a Si$_3$N$_4$ encapsulant [188].

depleted from the near surface region with increased annealing, the width
of the Mg accumulation region increases. This suggests that Mg is gettering
into the region just below the maximum implant damage. The compensating Fe
dopant also getters into the same region as the annealing proceeds. This
Fe accumulation zone increases in width with increasing annealing tempera-
ture, essentially matching the Mg profile shape. This redistribution of
Fe to closely reflect the profile of the implanted acceptor was also observed
in our Be implant studies.

The observed depletion and accumulation zones of Mg appear to be
related to the presence of an amorphous surface layer and an accompanying
damaged crystalline region below the amorphous layers. For a Mg dose of
1×10^{15} cm^{-2} implanted at 250 keV, the energy deposition density is calcu-
lated to be $^\sim 1.7 \times 10^{21}$ keV cm^{-3} (approximated from the product of the
dose and the nuclear energy loss per unit length). Assuming the validity
of the energy deposition density model [23,179], this is from 3-6 times the
critical energy deposition density necessary for the amorphization of InP,
as calculated for the cases of Ar and Si at room temperature [180,181]. Electron
channelling patterns (ECP) for as-implanted InP were obtained from the surface
and from a depth of $^\sim$ 1600 Å. Both surfaces were devoid of Coates lines,
indicating an amorphous implanted region. The material was re-examined a
year after implantation and was still found to be amorphous, supporting a
similar observation by Kennedy[181]. This amorphous surface layer is located
in the same region where Mg depletion zones are formed during annealing,
suggesting a causal relationship. Figure 2.3 illustrates that in the region
of gettering (5500 - 6500 Å) the energy deposition is approximately two
orders of magnitude less than at the peak of the damage profile. Presumably

Figure 7.15: (a) Electron channelling pattern (ECP) from an unimplanted InP surface. (b-d) ECP at depths of: (b) surface; (c) $\sim$ 1600 Å below the surface; and (d) $\sim$ 3900 Å below the surface. These samples were implanted with 250 keV, 10^{15} cm^{-2} Mg and annealed for 30 min at $550^{\circ}C$ [188].
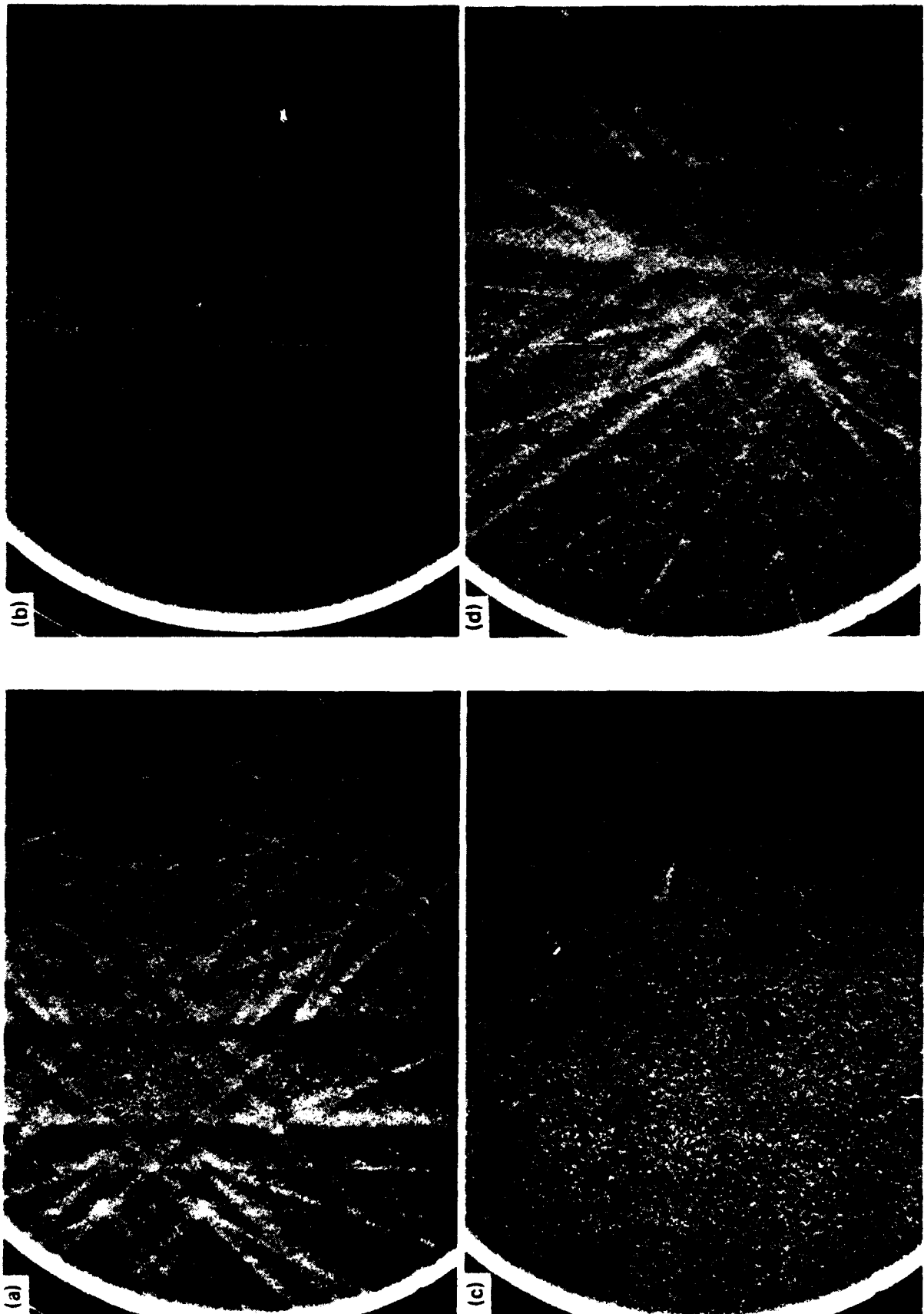
Figure 7.15

this region, although damaged, is not driven amorphous. Impurity accumulation into the damaged crystalline region below an amorphous implanted layer has been previously observed in Si and attributed to gettering by residual defects[182]. A similar mechanism apparently causes Mg and Fe gettering into the damaged crystalline region in InP.

Although an extensive study of channelling patterns from these samples has not been done, some channelling patterns from annealed material have been obtained. Figure 7.15 exhibits channelling patterns from material annealed for 30 min at 550°C. The lack of contrast and of any Coates lines suggest than an amorphous layer still exists in the near surface region following this anneal. The results from material annealed for 30 min at 650°C are similar to those shown in Figure 7.15. ECP obtained from 30 min and 60 min anneals at 750°C are shown in Figures 7.16(b) and 7.16(c). In these photographs the backscattered electron signal was not differentiated as in Figure 7.15 because the weak bands visible in 7.16(b) and 7.16(c) were too low in contrast to yield a visible pattern in the differentiated signal mode. The surfaces of both the 30 and 60 min, 750°C annealed material revealed no observable channelling patterns. The faint channelling patterns of 7.16(b) and 7.16(c) were obtained at depths near the mode of the Gaussian damage profile. Although some recrystallization has apparently occurred at 750°C, the patterns are of very poor quality when compared to those from unimplanted material. These results seem to be inconsistent with other published results [180,181] which indicate that major reordering of amorphous InP occurs in the range from 450-500°C. It has been reported that, in addition to the degree of crystallinity, factors such as lattice strain of a few percent can result in loss of resolution or contrast in electron channelling patterns

134

Figure 7.16: (a) Electron channelling pattern (ECP) from an unimplanted InP
surface. (b) ECP at a depth of ~ 1600 Å below the surface of Mg implanted
sample annealed for 30 min at 750°C. (c) ECP at a depth of ~ 1900 Å below
the surface of Mg implanted sample annealed for 60 min at 750°C. The
backscattered electron signal has not been differentiated as was the case
in Figure 7.15 [188].
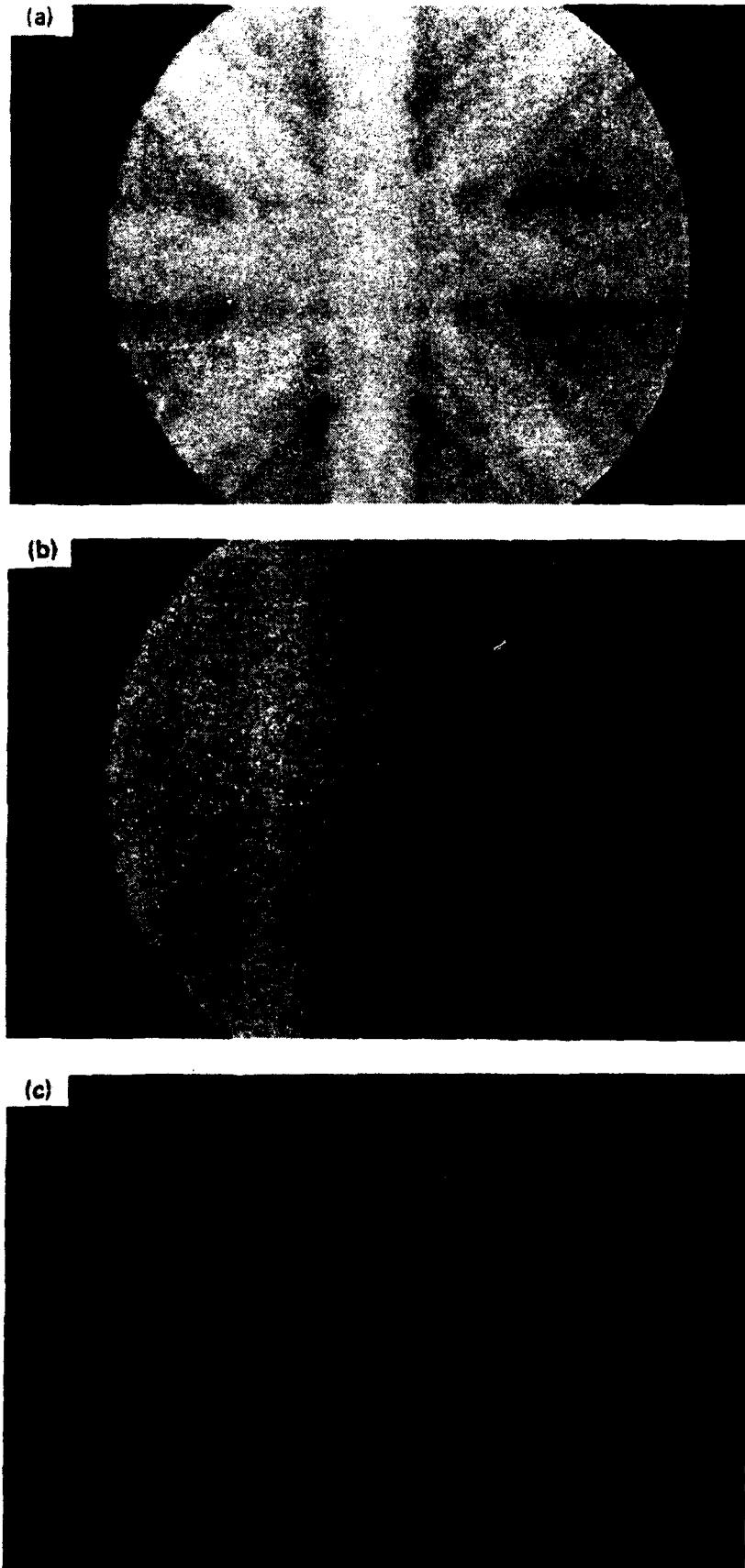
Figure 7.16
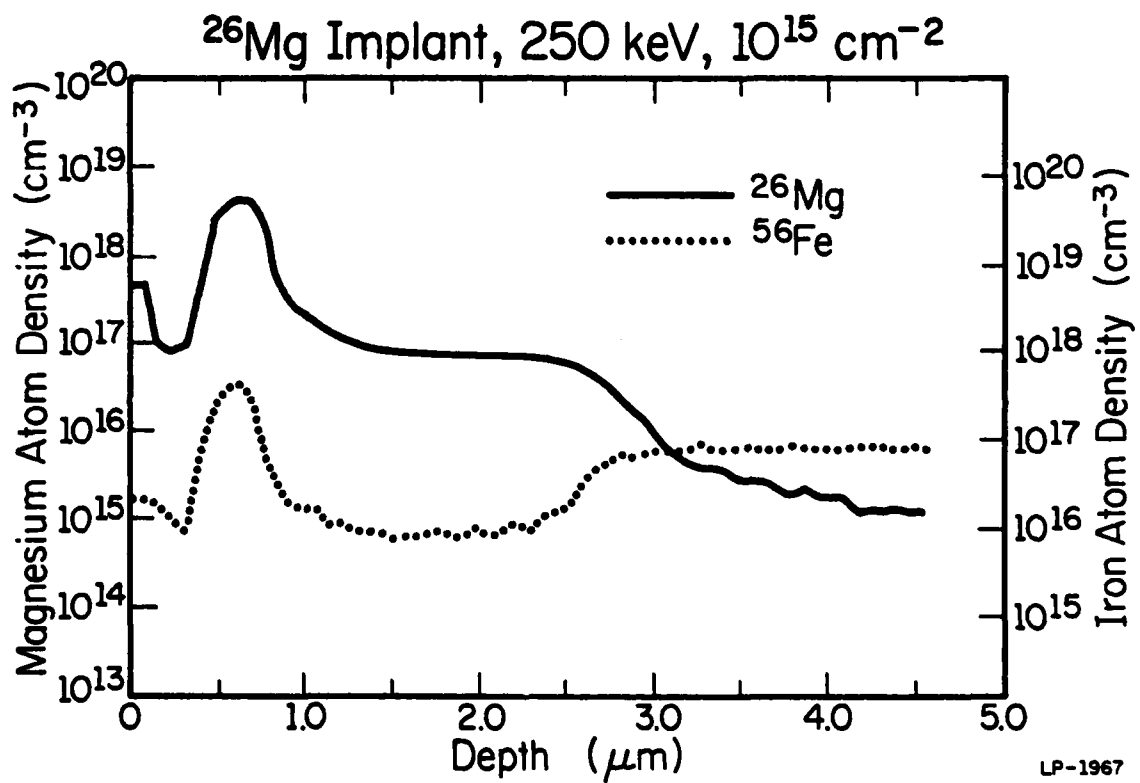
^{26}Mg Implant, 250 keV, 10^{15} cm^{-2}

Figure 7.17: SIMS profile of Fe-doped InP implanted with 250 keV, 10^{15} cm^{-2} Mg and annealed for 30 min at 750°C with a Si$_3$N$_4$ encapsulant [188].

[183]. For the Mg implants discussed here, lattice strain may be significant and could therefore be responsible for the discrepancy between our results and those of others regarding the recrystallization temperature for amorphous InP.

The annealing characteristics of Mg-amorphized InP shown in Figure 7.14 may explain the electrical characteristics of Mg-implanted InP reported by Donnelly and Hurwitz [184]. For room temperature implants of 150 keV of Mg fluence above 10^{14} cm^{-2} they find a drastic reduction in sheet hole concentration. Our calculations indicate that a 10^{14} cm^{-2} dose of 150 keV Mg yields a deposited energy density of ~ 2×10^{20} keV cm^{-3}, which is roughly the threshold for amorphization of InP, assuming the validity of this amorphization model. Therefore the reduction in sheet hole concentration for fluences above 10^{14} cm^{-2} could be the result of amorphization and depletion from the amorphous layer as observed here. This assumption is consistent with the fact that sheet concentration increases with dose up to 10^{15} cm^{-2} for implants performed at 150°C [184], because this elevated target temperature is reportedly sufficient to prevent amorphization of InP [180,181].

Figure 7.17 is a deeper profile taken from a sample annealed at 750°C. A flat, constant-concentration tail of Mg and an accompanying depletion of Fe extend over a considerable distance in the bulk, similar to that observed in the Be implant work. Because the Be implants did not amorphize the InP, it can be assumed that this feature is not related to amorphization effects. Possible explanations for this flat tail feature have been discussed in the preceding section. As was the case for Be, the correlation between the flat Mg tail and the Fe depletion zone is striking.

7.4 SIMS Profiles of ^{28}Si Implants in SI InP

Because of the strongly anomalous redistribution of both Be and Mg, Si implants were performed to determine if this donor behaves similarly.

Si implantation in InP is of considerable interest because of its use in the formation of n-channels in InP field effect transistors (FET) [126]. It has generally been observed that Si implants result in good donor activation [19, 76, 98]. Based on values for the covalent tetrahedral radius and electronegativity given in Table 7.1, Si appears to be a reasonably suitable substitutional impurity for the In lattice atom.

Using SIMS we have analyzed the annealing behavior of 240 keV, 5×10^{14} cm^{-2} ^{28}Si implanted into Fe-doped InP. Figure 2.3 contains the as-implanted ^{28}Si atomic profile together with the LSS Gaussian approximation and the theoretical damage profile. The mode for the LSS Gaussian occurs at 2464 Å while the mode of the energy deposition profile occurs at ~ 1562 Å (see Table 2.1).

Shown in Figure 7.18 are the ^{28}Si profiles resulting from implantation and annealing for 30 min at 750°C. Unfortunately, the ^{28}Si profiles suffer from a rather large background signal (corresponding to ~ 10^{17} cm^{-3}), due to molecular interference. Mass spectra from the surface and bulk of uniplanted samples yield a strong peak at mass 27 and a weaker peak at mass 28. This suggests the interference observed at mass 28 is dominated by the hydride of the mass 27 background impurity (presumably ^{27}Al) rather than by residual ^{28}Si content. Recent studies of liquid encapsulated Czochralski grown InP using spark source mass spectrometry reveal, however, that the Si content of such single crystals is greater than the residual Al concentration (~ 0.1 ppma vs. ~ 0.03 ppma) [185, 186]. It appears most likely that the mass 27 background results from a "memory effect" in the SIMS system's immersion lens caused by the sputtering of an Al grid used in aligning the system optics prior to sample profiling.
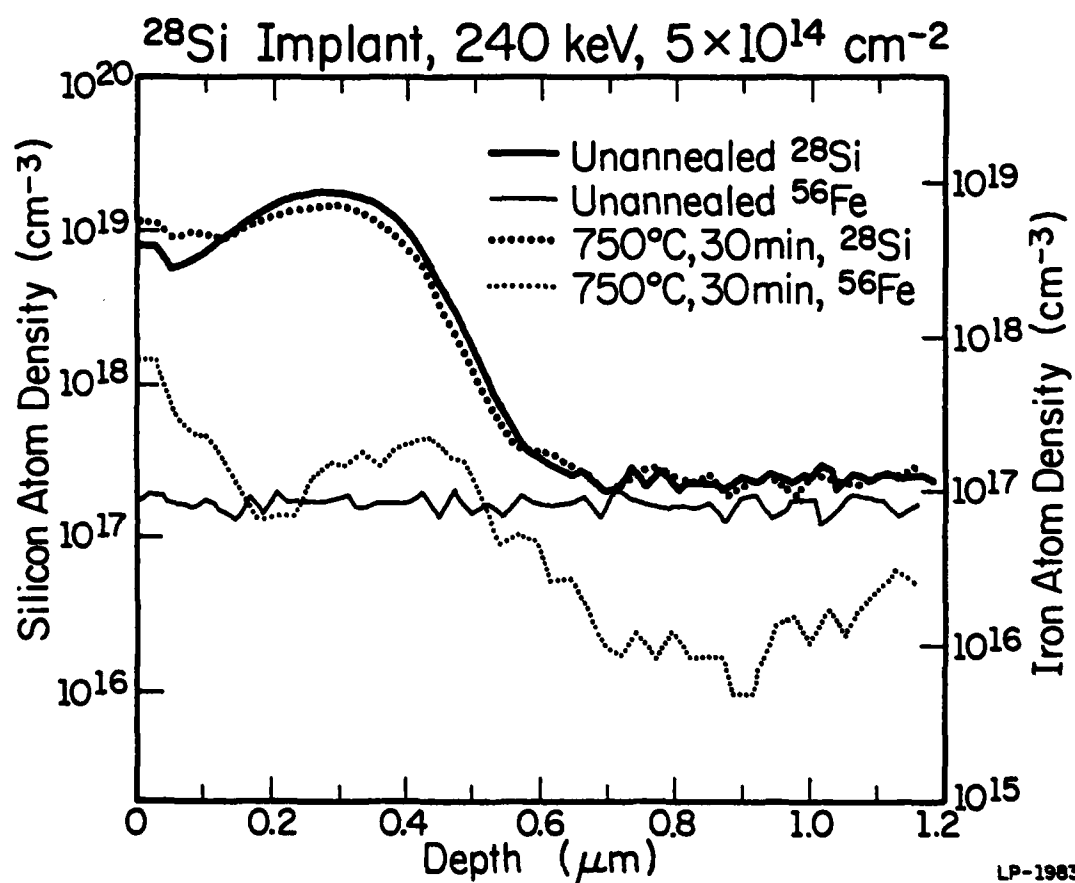
Figure 7.18: SIMS unannealed and annealed profiles of Fe-doped InP implanted with 240 keV, 5×10^{14} cm^{-2} Si. 30 min anneals were performed with a Si$_3$N$_4$ encapsulant [188].

In spite of the background interference, the results in Figure 7.18 indicate that little atomic redistribution of the implanted ^{28}Si occurs for 750°C, 30 min anneals. The lack of major redistribution for ^{28}Si observed here appears consistent with Hall profiling measurements made by Donnelly and Hurwitz on Fe-doped InP implanted at room temperature with 10^{15} cm^{-2} of Si at 400 keV [19]. Significant movement of Fe is detected, however. An Fe accumulation zone followed by a depletion zone is formed on the bulk side of the implanted ^{28}Si peak. With the exception of the large, near surface depletion zone seen in Figure 7.14, this Fe behavior parallels that observed in the Mg implant series.

The lack of major ^{28}Si redistribution in these anneals is significant when compared to the annealing characteristics of high dose Mg or Be implants. Kennedy has found via channelling measurements that a fluence of 10^{14} cm^{-2} of 200 keV ^{28}Si is sufficient to produce an amorphous InP layer at room temperature [181]. Based on this measurement it is assumed that the 5×10^{14} cm^{-2}, 240 keV implant of ^{28}Si has amorphized the InP examined here. In fact, the energy deposition density calculated for this implant (1.1×10^{21} keV cm^{-3}) is comparable to that of the ^{26}Mg implant (1.7×10^{21} keV cm^{-3}). Despite this similarity, there are significant differences between the annealing characteristics of Si and Mg.

The implanted Si examined here results in far less redistribution than is seen in lower fluence ^{9}Be implants with much less implant related damage. The redistribution behavior of the implanted acceptors Mg and Be seems to parallel the rapid diffusion exhibited by Zn and Cd during growth [155-157]. It has previously been observed that donor implants result in higher electrical activations than acceptor implants in InP [184]. It seems that the redistribution behavior of acceptors in InP may be a fundamental

limitation leading to low activations.

It is clear from these results that more information is needed on the amorphization and the kinetics of recrystallization of amorphous InP. This is particularly true since the measured average displacement energy of the lattice atoms in InP is less than that of GaAs or Si (7.7 eV compared with 9.4 and 15.8 eV for GaAS and Si, respectively) [187]. As a result, amorphization effects may be encountered more frequently during normal processing in InP than has been the case with GaAs or Si.

7.5 Summary

The main results of the SIMS studies may be summarized as follows:

(1) High temperature anneals with a Si_3N_4 cap result in the formation of Fe accumulation regions within the first 1000 Å of the surface of Fe-doped, SI InP. Comparable anneals of Cr-doped SI InP indicate that Cr does not exhibit such strong surface gettering.

(2) In Si_3N_4 capped SI InP, depletion zones of the compensating impurity are formed following high temperature anneals. Cr exhibits larger concentration gradients in these zones than does Fe.

(3) In samples implanted with electrically and chemically inactive impurities (^{4}He, ^{10}B), Fe and Cr exhibit accumulation into the implant damage region on the surface side of the projected range peak. This occurs in addition to the features noted in (1) and (2) which are associated with the use of Si_3N_4 cap.

(4) Under typical annealing conditions for InP (T $\geq$ 700°C, t ≈ 15-30 min), implanted ^{9}Be is a rapid diffusant even for fluences as low as 1×10^{13} cm^{-2}.

(5) Short (15 min) anneals of high fluence ^{9}Be implants result in substantial diffusion and redistribution, comparable to that for 30 min anneals.

(6) Electronegativity and size considerations alone are not sufficient to explain the rapid diffusion of ^{9}Be in InP.

(7) Two peaked structures of Be, Cr, and Fe appear in the 550°C anneals of 10^{15} cm^{-2} implanted material. Such structures may result from rapid defect diffusion away from the damaged region. Electron channelling patterns and comparisons with ^{10}B implants appear to rule out an amorphous layer as the cause of such twin peaked structures.

(8) Correlations are observed between ^{9}Be and compensating impurity profiles in annealed high fluence implanted samples. The compensating impurities return to the background doping level in the same region that the ^{9}Be drops to background detection limits.

(9) Flat, constant-concentration tails of ^{9}Be extending over distances on the order of microns are observed in semi-insulating InP. This anomalous diffusion is not observed in undoped VPE InP. It is possible that either the compensating dopant (Fe or Cr) or other residual impurities and/or defects in semi-insulating InP play a role in the formation of such tails. Alternatively, these constant-concentration ^{9}Be tails may result from a low Be solubility in undamaged, semi-insulating InP with the rate-limiting step of the process being the release of Be from the damaged layer.

(10) Implantation of 10^{15} cm^{-2}, 250 keV Mg at room temperature results in amorphization of InP. Electron channelling patterns from samples

annealed for 30 min at 550°C and 650°C exhibit no patterns at the surface or at depths near the region of maximum implant induced damage. Weak channelling patterns are observed at depths near the damage peak in material annealed at 750°C for 30 and 60 min.

(11) Drastic redistribution of Mg and Fe occurs during 30 min anneals of such implanted material. Depletion zones are formed in the region of maximum implant damage, followed by accumulation zones on the bulk side of the initial Mg profile. The widths of the accumulation zones increase with temperature, suggesting gettering of impurities from the surface into this bulk region. As in the Be implant studies, the motion of Fe observed here closely reflects the profile of the implanted Mg acceptor.

(12) Flat, constant-concentration tails of Mg extending over distances of 1 μm or more are observed in the bulk after annealing. The depth at which Fe returns to its background level and its concentration gradient at this point are closely correlated to the Mg profile. These features have been observed also in the Be study. Since the Be implants did not amorphize InP, it may be assumed that these features are not related to amorphization effects.

(13) Little redistribution of ^{28}Si occurs for 30 min, 750°C anneals of 240 keV, 5×10^{14} cm^{-2} ^{28}Si implants. Based upon calculations and available experimental data, this implant schedule should result in amorphous InP. This behavior of ^{28}Si differs significantly from that of Mg in amorphous InP. Redistribution of Fe does occur in these Si implanted samples, however, resulting in an accumulation region followed by a depletion zone on the bulk side of the implanted ^{28}Si peak.

8. THEORETICAL AND EMPIRICAL DISTRIBUTIONS FOR InP ION IMPLANTATION PROFILES

8.1 Introduction

In the course of the implantation studies in InP the shortcomings of the LSS Gaussian approximation became apparent for light mass projectile implantations dominated by electronic stopping. Although the theoetical LSS projected ranges agreed adequately with experiment, profile shapes were encountered which differed significantly from the LSS Gaussian. There has been substantial interest [189-191] in finding analytical distributions which when combined with the appropriate parameters will predict the shape of ion implanted profiles with greater sophistication than the common Gaussian approximation using the penetration theory of Lindhard, Scharff, and Schiott (LSS) [31]. Distributions such as the joined half-Gaussian [192], the Edgeworth [37], the Gram-Charlier [35], and the Pearson system [35,190,191] have been proposed to fit asymmetrical implant profiles. The Pearson IV distribution in particular has been shown capable of excellent fits to experimental implant profiles in Si [190,191].

In this chapter, four implantation profiles involving ^{9}Be, ^{10}B, ^{26}Mg and ^{28}Si are considered in the intermediate energy range $3 < \epsilon < 7$ (where ϵ is the LSS dimensionless energy parameter [31,37]). The purpose of this chapter is to examine the fit to experimental profiles from distribution functions which employ four moments rather than only two moments as with the Gaussian.

8.2 Experimental and Gaussian Profiles

Qualitatively the experimental (SIMS) profile shapes shown in Figures 8.1 - 8.4 can be understood on the basis of electronic stopping and the mass ratio (μ) of the average target mass to the projectile mass. Electronic stopping begins to dominate over nuclear stopping [24] in the region

Figure 8.1: SIMS profile of [9]Be implant (100 keV, 1 x 10^{15} cm^{-2}) in (100) InP and theoretical profiles [195].

Figure 8.2: SIMS profiles of ^{10}B implant (126 keV, 6.79 x 10^{14} cm^{-2}) in (100) InP and theoretical profiles [195].

Figure 8.3: SIMS profile of ^{26}Mg implant (250 keV, 1 x 10^{15} cm^{-2}) in (100) InP and theoretical profiles [195].
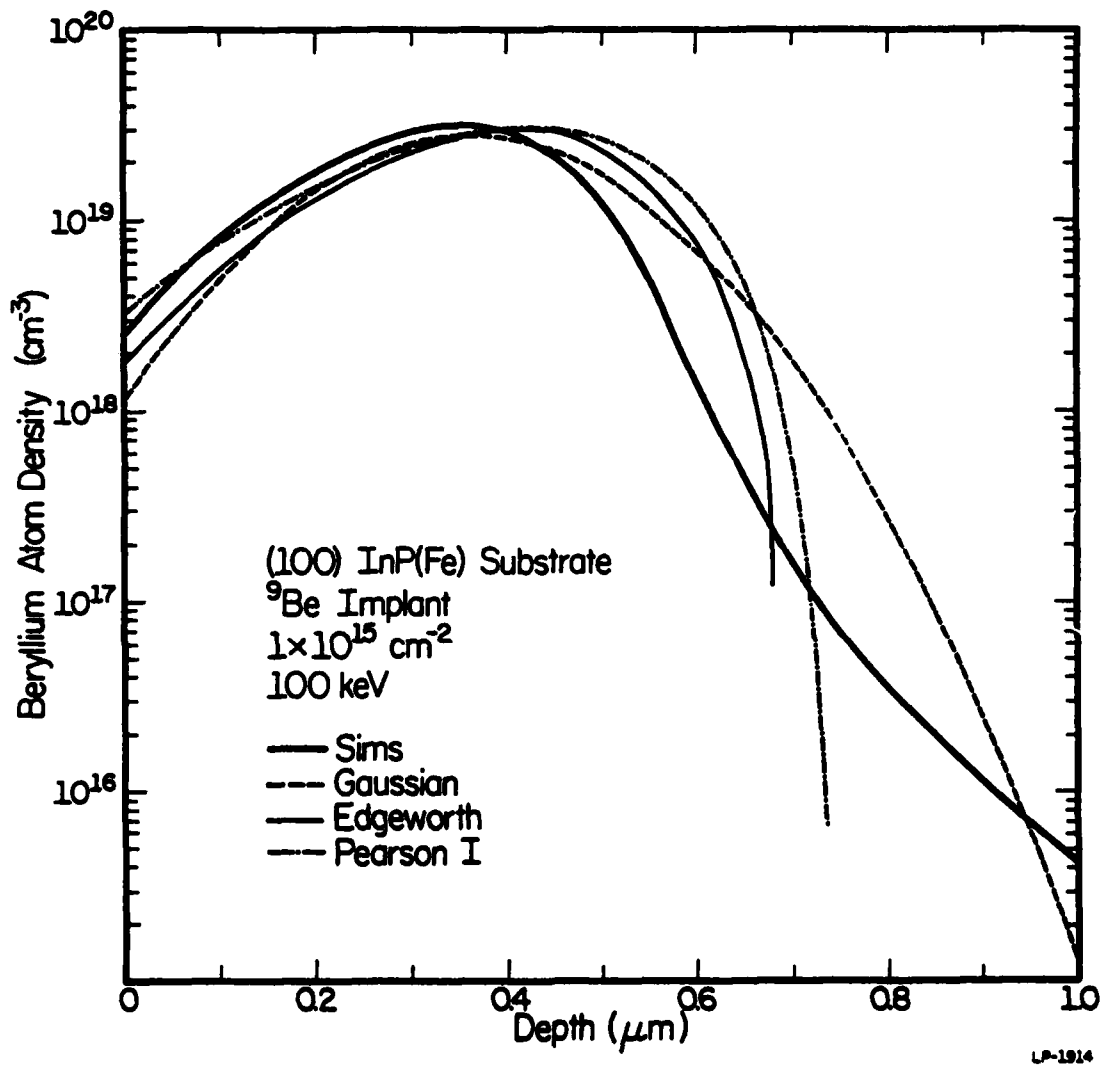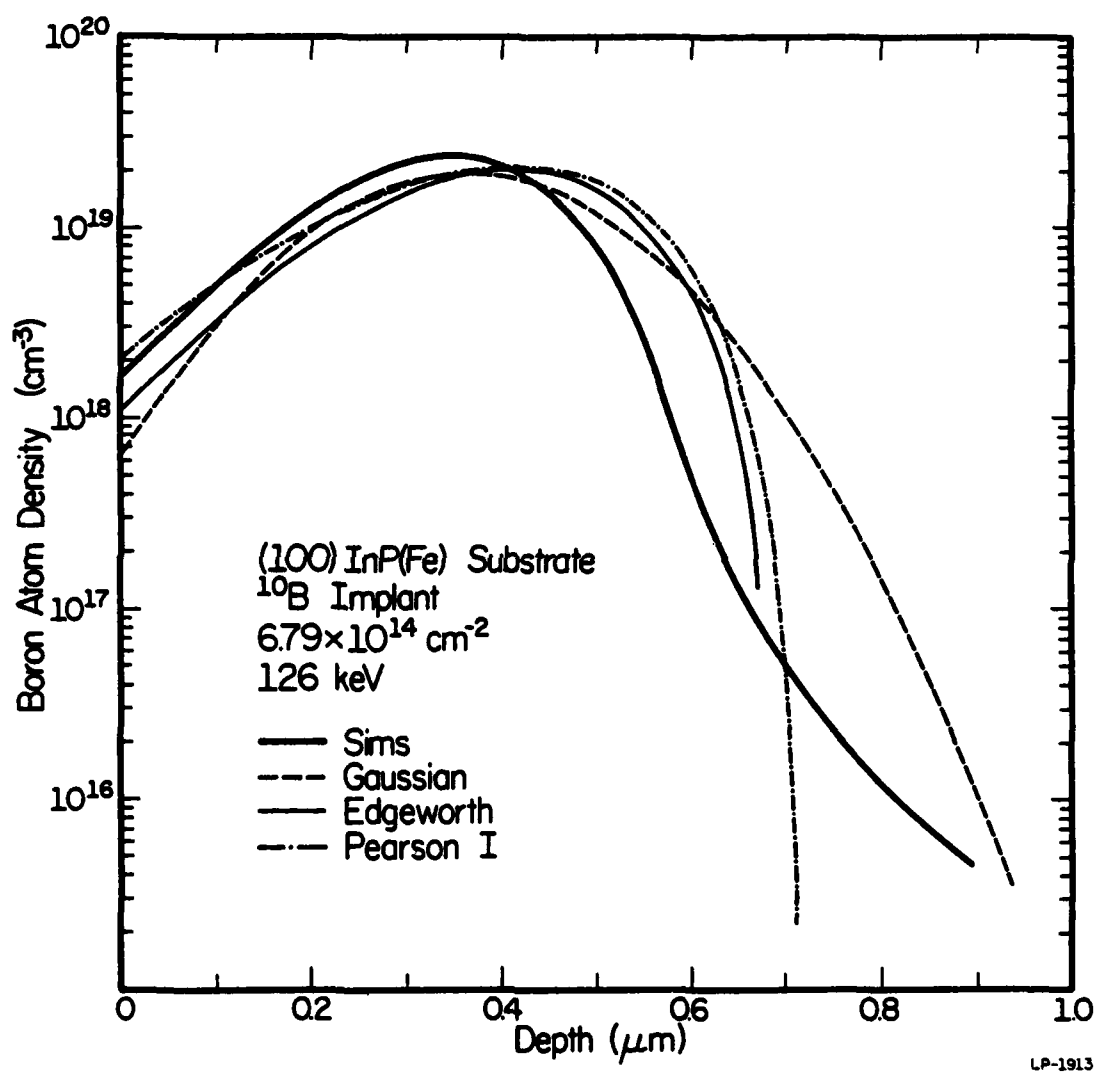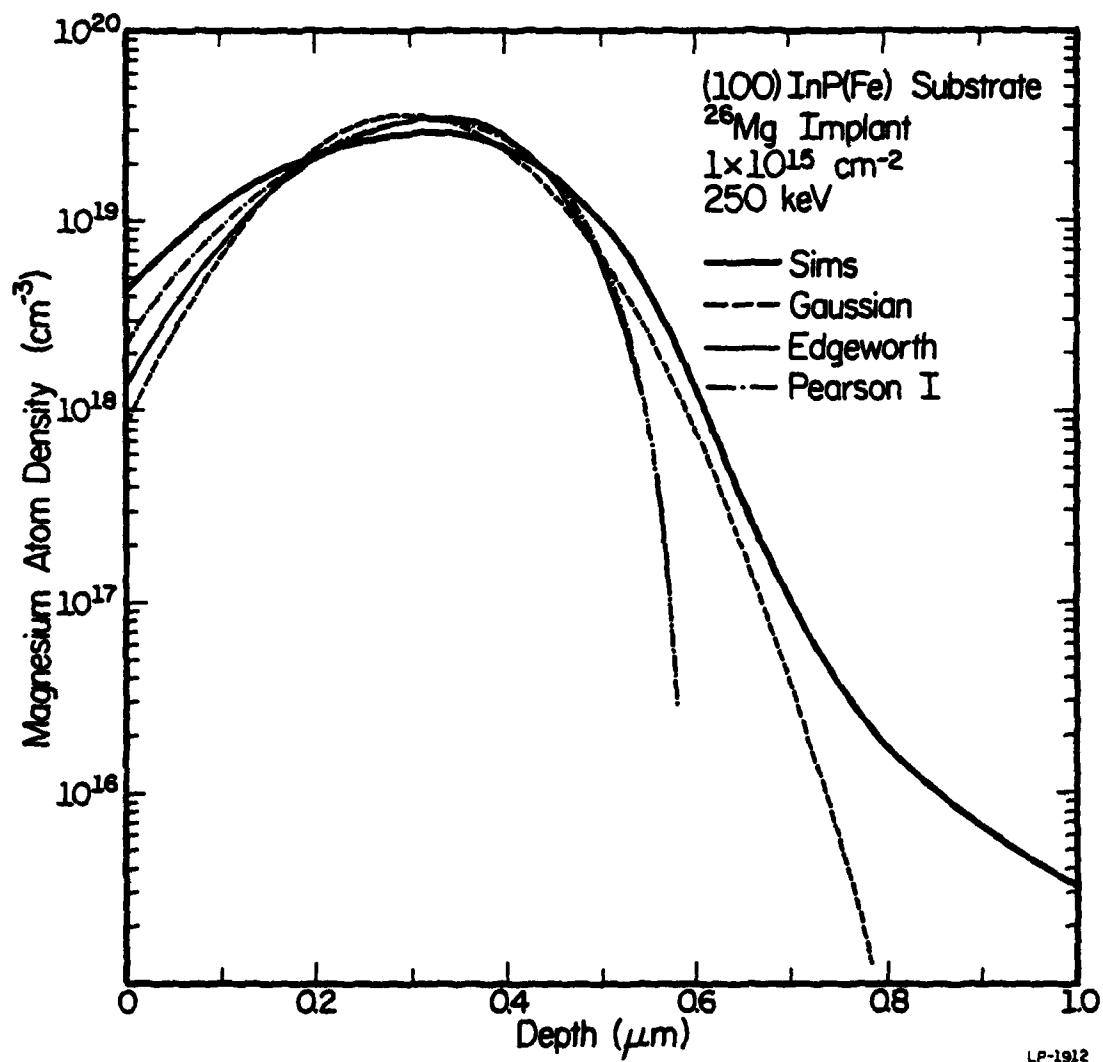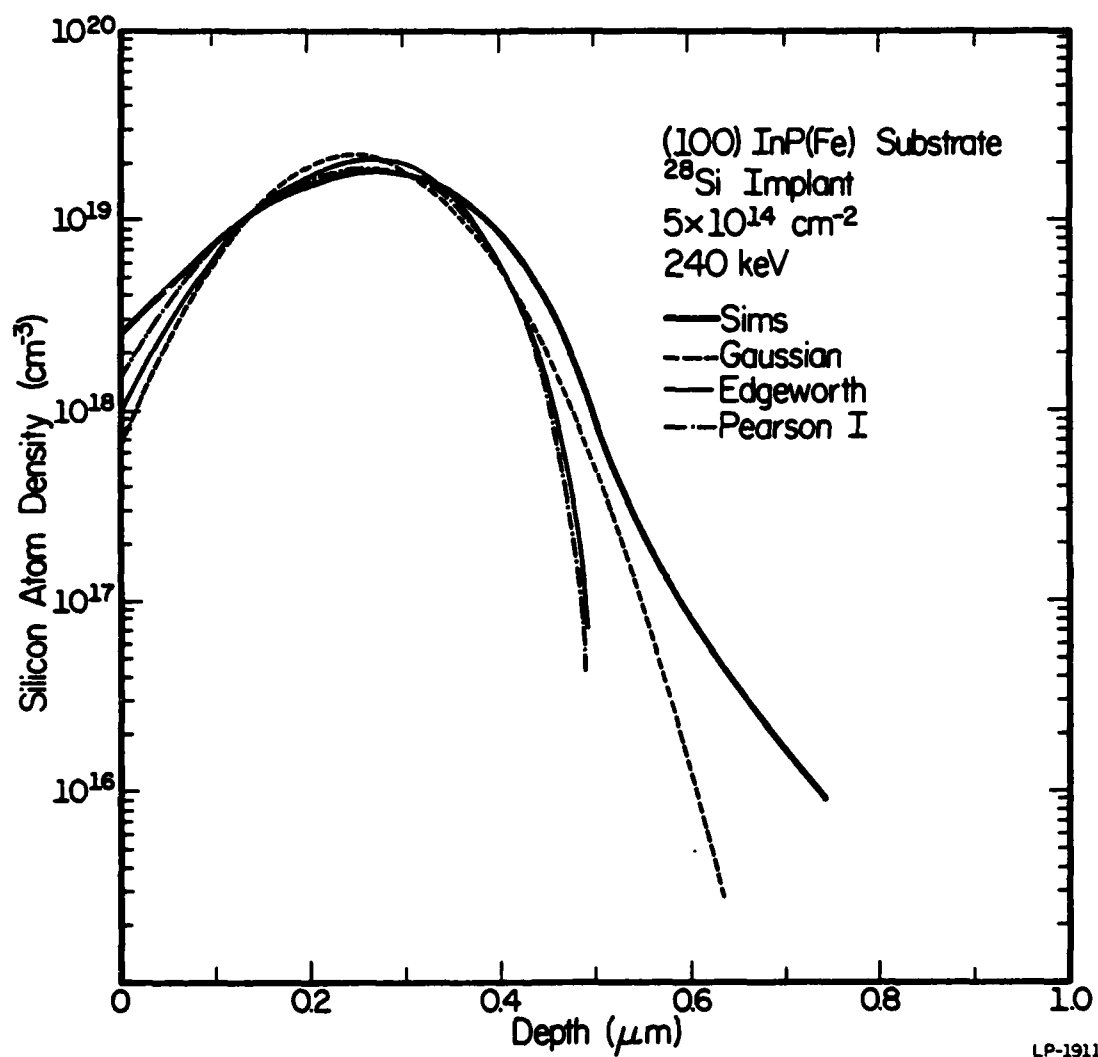
Figure 8.4: SIMS profile of ^{28}Si implant (240 keV, 5×10^{14} cm^{-2}) in (100) InP and theoretical profiles [195].

$\epsilon \approx 3$. This fact, the values of ϵ, and the fractional energy loss to electronic stopping given in Table 8.1 indicate that electronic stopping dominates over nuclear stopping in all the implantations discussed here, except for possibly the ^{28}Si implant. Winterbon has noted that implants dominated by nuclear stopping result in profiles containing a tail extending to large depths, whereas in implants dominated by electronic stopping this tail is cut off and the profile is skewed toward the surface [35]. The sign and magnitude of the third moment (skewness) γ_1, shown in Table 8.2 therefore indicates the role of electronic stopping in these implants and correctly predicts the skewing of the profiles toward the surface. Another factor relevant in the case of low mass projectiles (high μ) such as ^{9}Be and ^{10}B is backscattering from target atoms, which should skew the distributions even more toward the surface. These observations are borne out by our experimental profiles, particularly in the case of the ^{9}Be and ^{10}B implantations.

Shown in Figures 8.1 - 8.4 are the theoretical LSS Gaussian distributions for the implants considered. The mean range, <x>, along the projected range path and the standard deviation along the projected range path, σ, were obtained from a computer program utilizing the Gibbons, Johnson, and Mylroie formulation of the LSS theory [37]. Table 8.2 lists these LSS theorectical values as $<x>_G$ and σ_G. From Figure 8.1 - 8.4 it can be seen that the experimental modal depths are within $\sim \pm$ 10% of the LSS mean range values. However, it appears from Figure 8.1 and 8.2 that the LSS value of σ can differ significantly from experimental values. It has been noted by others[24,35,190] that based on experimental results the uncertainty in the LSS electronic stopping power is $\sim$ 20-30% (due to approximations of linear energy loss with velocity and in an associated proportionality constant [31,35]). In particular,

TABLE 8.1

LSS dimensionless energy ε, LSS fraction of energy loss to electronic stopping $(\frac{\eta}{E})$, and the ratio of average target mass to incident ion mass μ.

Ion	ε	$(\frac{\eta}{E})$	μ
^{9}Be	6.37	~ 90%	8.1
^{10}B	6.24	~ 88%	7.3
^{26}Mg	4.05	~ 72%	3.0
^{28}Si	3.15	~ 65%	2.6

TABLE 8.2

Gibbons' mean range $<x>_G$, Winterbon's mean range $<x>_W$, Gibbons' standard deviation σ_G, Winterbon's standard deviation σ_W, skewness γ_1, kurtosis β_2.

Ion	ENERGY (keV)	$<x>_G$ (Å)	$<x>_W$ (Å)	σ_W (Å)	σ_G (Å)	γ_1	β_2
^{9}Be	100	3643	3562	1429	1512	-0.76	3.65
^{10}B	126	3643	3496	1382	1437	-0.77	3.69
^{26}Mg	250	2994	2865	1081	1126	-0.50	3.04
^{28}Si	240	2464	2338	921	986	-0.37	2.86

Schiott [193] has shown that, due to such underestimation of the magnitude of electronic stopping for some projectile-target combinations, LSS can overestimate experimental values of σ by 20-30%. As a result, the large deviations of the LSS Gaussian from the experimental profiles might be expected because of the dominant role electronic stopping plays in the ^{9}Be and ^{10}B implants. Yet, a comparison of the theoretical values of σ in Table 8.2 to the empirical values of σ in Table 8.3 reveals the differences to be less in the cases of ^{9}Be and ^{10}B than in the ^{26}Mg and ^{28}Si cases. Therefore, the differences between the LSS Gaussian and the experimental profiles in Figures 8.1 and 8.2 do not result from an overestimation of σ. Rather, these differences in the cases of the ^{9}Be and ^{10}B implants seem more simply to be due to the large values of the third and fourth moments (Table 8.3). Such large values of γ_1 and β_2 result in highly asymmetric profiles which the symmetric Gaussian is incapable of adequately representing.

8.3 Edgeworth and Pearson I Distributions

Motivated by these deficiencies of the LSS Gaussian approximation for the ^{9}Be and ^{10}B profiles, we have examined the fits obtained with Edgeworth and Pearson distributions using four moments based on theoretical results. Mathematical definitions of these first four moments of a distribution are listed here for completeness [190]:

$$<x> \text{ (mean)} = \int_{-\infty}^{\infty} x f(x) \, dx$$

$$\sigma \text{ (standard deviation)} = \left(\int_{-\infty}^{\infty} (x - <x>)^2 \, f(x) \, dx \right)^{\frac{1}{2}}$$

$$\gamma_1 \text{ (skewness)} = \frac{\int_{-\infty}^{\infty} (x-\langle x\rangle)^3 f(x) \; dx}{\sigma^3}$$

$$\beta_2 \text{ (kurtosis)} = \frac{\int_{-\infty}^{\infty} (x-\langle x\rangle)^4 f(x) \; dx}{\sigma^4}$$

A computer program was written which utilizes the quantities listed in Table 8.2 to generate the Edgeworth and Pearson I distribution solutions.

A comment concerning the definition of $\langle x\rangle_G$ and $\langle x\rangle_W$ in Table 8.2 must be made at this point. The first moment as obtained from either the Gibbons [37] or Winterbon [35] tables is the average or mean range of the distribution along the projected range path. This moment has often been referred to as the "projected range". The experimentally relevant quantity, however, is the mode or peak of the distribution $f(x)$, which occurs at the point where $df(x)/dx = 0$. The mean and modal values are equal only when the distribution is symmetrical, as in the case of the Gaussian [190]. The approximate position of the modal range can be obtained from the first four moments of the distribution by use of the Pearson approximation given in reference 194 as equation (3.87):

$$x_{mode} = \langle x\rangle + a$$

where

$$a = - \frac{\sigma\gamma_1(\beta_2 + 3)}{10\beta_2 - 12\gamma_1^2 - 18} = - \frac{\sigma\gamma_1(\beta_2 + 3)}{A}$$

The quantities a and A are defined by Hofker et al. [190]. As can be seen

from this equation, for distributions with negative values of skewness γ_1, the modal range is deeper than the mean range and vice-versa for distributions with positive γ_1.

The values of $<x>$ and σ_G listed in Table 8.2 are the mean range and standard deviation along the projected range path obtained from our computer program utilizing the Gibbons, Johnson, and Mylroie formulation of the LSS theory[37]. The moments $<x>_W$, σ_W, γ_1, and β_2 listed in Table 8.2 have been calculated from Winterbon's tables of data [35] with the assumption of mass scaling and the substitution of the compound target with a monatomic target of average charge and mass.

8.31   *Edgeworth Distribution*

The Edgeworth distribution is a series expansion in which the series terms are related to successively higher order moments [36,194]. This distribution may be expressed as the product of a Gaussian function, $g(x)$, and a polynomial, $p(x)$:

$$f(x) = p(x) \, g(x)$$

with the polynomial terminated to include the highest order moment desired. In this work the following expression for the polynomial, terminated to include all moments up to the fourth, has been used[37].

$$p(x) = 1 + \frac{\gamma_1}{6} (x^3 - 3x) + \frac{\gamma_1^2}{72} (x^6 - 15x^4 + 45x^2 - 15)$$

$$+ \frac{\beta_2 - 3}{24} (x^4 - 6x^2 + 3)$$

The calculated Edgeworth distributions are shown in Figures 8.1 - 8.4. These particular curves have been constructed using the moments $<x>_G$,

σ_g, γ_1, and β_2. In all four cases the curve is terminated at the point where the distribution function begins to exhibit oscillations. Such oscillations have been previously encountered and attributed to the termination of the polynomial p(x) [37]. In all cases the Edgeworth series peaks at a deeper point than the LSS Gaussian. This type of behavior has been previously reported in conjunction with the Edgeworth series [36] and should be expected since we are modifying a Gaussian to take into account the predicted distribution skewness. Since the theoretical values of γ_1 in Table 8.2 are all negative, the Edgeworth modal range is deeper than the mode of the LSS Gaussian which, due to the Gaussian's symmetry, is also the mean range <x>. In addition, because the magnitude of the skewness is greatest in the [9]Be and [10]B implants, the largest difference between mean and modal ranges is seen in Figures 8.1 and 8.2.

8.3.2 *Pearson I Distribution*

The Pearson distributions are a family of frequency functions based on the solutions of the differential equation:

$$\frac{df(x)}{dx} = \frac{(x - a)\, f(x)}{b_o + b_1 x + b_2 x^2}$$

where f(x) is the frequency function [190,194]. The expressions for a, b_o, b_1, and b_2 are [190,194]:

$$a = -\frac{\sigma \gamma_1 (\beta_2 + 3)}{A}$$

$$b_o = -\frac{\sigma^2 (4\beta_2 - 3\gamma_1^2)}{A}$$

$$b_1 = a$$

$$b_2 = -\frac{(2\beta_2 - 3\gamma_1^2 - 6)}{A}$$

where

$$A = 10\beta_2 - 12\gamma_1^2 - 18$$

In contrast to series expansion distributions such as the Edgeworth, the Pearson distributions are determined entirely by the first four moments. The particular Pearson distribution which is the solution of the differential equation is determined by the nature of the roots [194] of the denominator $(b_o + b_1 x + b_2 x^2)$. The nature of the moments $\langle x \rangle_W$, σ_W, γ_1, and β_2 were such as to yield real roots of opposite sign for the characteristic equation. Because the Pearson IV distribution is valid only when the roots of $(b_o + b_1 x + b_2 x^2)$ are imaginary, we were excluded from using this particular Pearson distribution with the theoretical moments considered here. The nature of these roots demanded a Pearson I distribution. The expression for $f(x)$ that we have employed in our computer program is given in reference 194 as equation (6.12):

$$f(x) = \frac{a_1^{m_1} a_2^{m_2}}{(a_1 + a_2)^{m_1 + m_2 + 1} B(m_1 + 1, m_2 + 1)} \left(1 + \frac{x}{a_1}\right)^{m_1} \left(1 - \frac{x}{a_2}\right)^{m_2}$$

where x is measured from the mode. The constants in this equation are defined as:

$$B(m_1 + 1, m_2 + 1) = \frac{\Gamma(m_1 + 1) \Gamma(m_2 + 1)}{\Gamma(m_1 + m_2 + 2)}$$

$$m_1 = \frac{a_1}{b_2(a_1 + a_2)}$$

$$m_2 = \frac{a_2}{b_2(a_1 + a_2)}$$

where a_1, a_2 satisfy the relations

$$a_1, a_2 > 0$$

$$b_o + b_1 x + b_2 x^2 = b_2(x + a_1)(x - a_2)$$

The range of the distribution is $-a_1 < x < a_2$ where again x is measured from the mode. This is in contrast to the Pearson IV distribution which has unlimited range in both directions.

The calculated Pearson I distributions are shown in Figures 8.1 - 8.4. In all four cases the Pearson I distribution yields a slightly improved fit over the LSS Gaussian approximation in the near surface region. The rapid drop-off of the curves beyond the mode is characteristic of the distribution as it approaches the range validity limit [194]. In the case of the ^{26}Mg and ^{28}Si implants, the Pearson I mode coincides quite closely to the experimental mode. However, in the profiles of primary concern (^9Be and ^{10}B implants) the Pearson I is similar to the Edgeworth in that the distribution mode is several hundred angstroms deeper than the experimental mode. The experimental mode for the ^9Be and ^{10}B implantations is in fact closer to the theoretical range value <x> than to the expected modal range, which is fortuitous for the Gaussian approximation.

Therefore, with the exception of a slight improvement in fit in the near surface region, it can be seen that Edgeworth and Pearson I distributions constructed with four moments derived from theoretical values are not significantly better representations of implant profiles in InP than is

the standard LSS Gaussian. Based on these results it appears that for certain implants in InP accurate prediction of the implant profile using moments derived from theory (with the substitution of a monatomic target) will be difficult.

8.4 Pearson IV Distribution and Emprically Determined Moments

In collaboration with R. G. Wilson of Hughes Research Laboratory, the first four moments of the implants considered here have been emprically determined by iteratively fitting the Pearson IV distribution solution to the experimental profile [191]. The Pearson IV distribution is employed for these empirical curves, rather than other four moment distributions such as the Edgeworth, because of its established success in describing implant profiles in Si and in GaAs [190,191]. The moments obtained with this procedure are σ, γ_1, and β_2. The first moment <x> is obtained by using the Pearson approximation [194] given above, together with the experimental mode and the other empirically derived moments. These first four moments are given in Table 8.3. It can be noted by comparing the theoretical four moments in Table 8.2 to the empirical four moments in Table 8.3 that the largest discrepancies occur in the values of skewness, γ_1, and of kurtosis, β_2. A similar result concerning calculated and experimental moments has also been reported by Hofker et al. [190]. It is not the intent here to determine the cause of these discrepancies between the theoretical and empirical moments; however, Hofker et al. [190] have found that when larger values of the electronic stopping coefficient are used in their theoretical calculations the resulting theoretical moments correspond reasonably well to the experimental moments. Also note that, as expected with Pearson IV distributions, the moments in Table 8.3 yield imaginary roots for the characteristic equation mentioned above. The resulting

TABLE 8.3

Empirically determined Pearson IV moments: The mean range <x>, the standard
deviation σ, skewness γ_1, and kurtosis β_2

Ion	ENERGY (keV)	<x> (Å)	σ (Å)	γ_1	β_2
^9Be	100	3210	1555	−1.34	8.33
^{10}B	126	3011	1420	−1.22	7.20
^{26}Mg	250	2709	1660	−0.96	5.51
^{28}Si	240	2417	1220	−0.53	3.63

(100) InP(Fe) Substrate
^{9}Be Implant
$1 \times 10^{15} cm^{-2}$
100 keV

— Pearson IV

Beryllium Atom Density (cm^{-3})

Depth (μm)

LP-1907

Figure 8.5: SIMS experimental points for ^{9}Be implant (100 keV, 1 x1 10^{15} cm^{-2}) and empirically derived Pearson IV distribution [195].

Figure 8.6: SIMS experimental points for ^{10}B implant (126 keV, 6.79 x 10^{14} cm^{-2}) and empirically derived Pearson IV distribution [195].
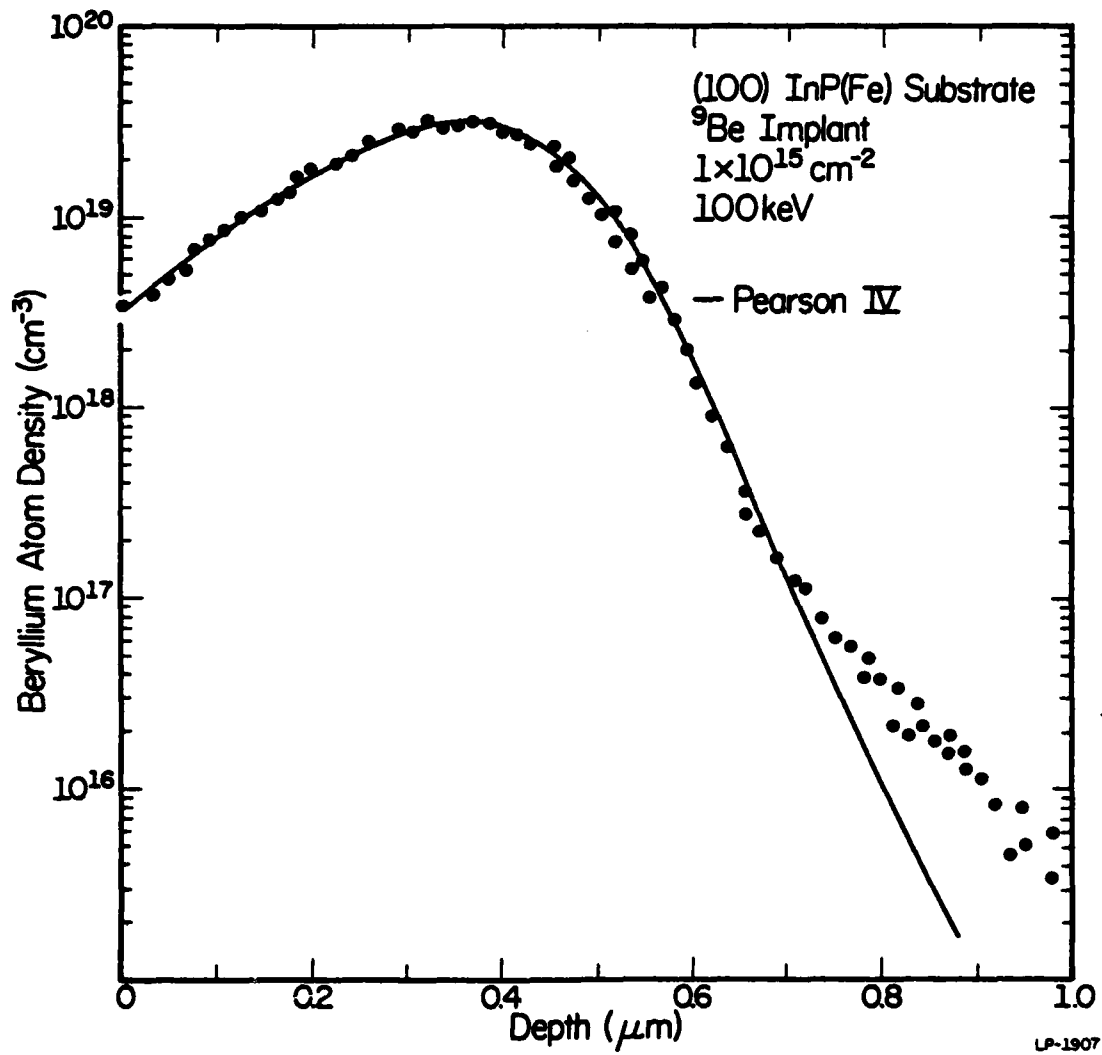
Figure 8.7: SIMS experimental points for ^{26}Mg implant (250 keV, 1 x 10^{15} cm^{-2}) and empirically derived Pearson IV distribution [195].
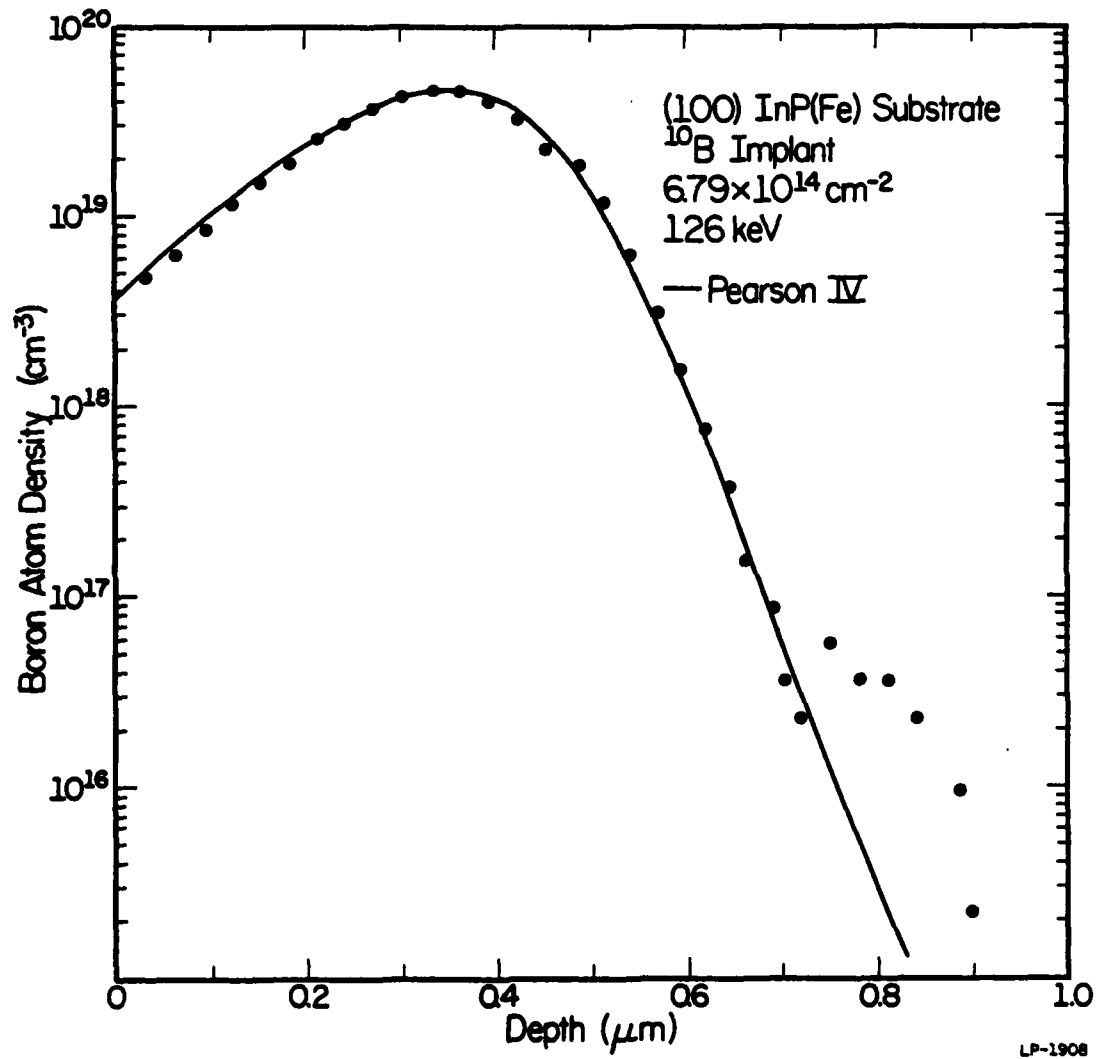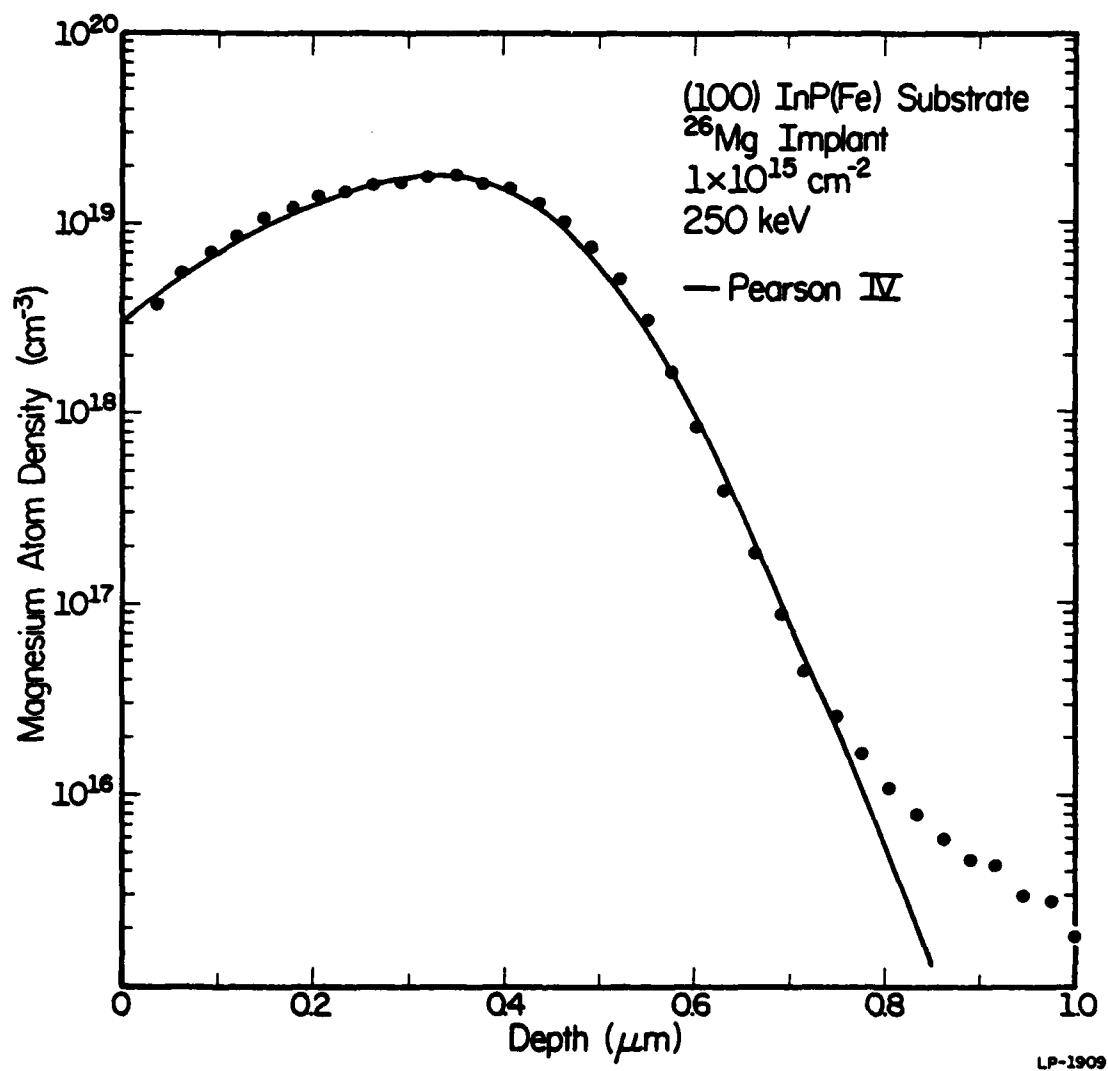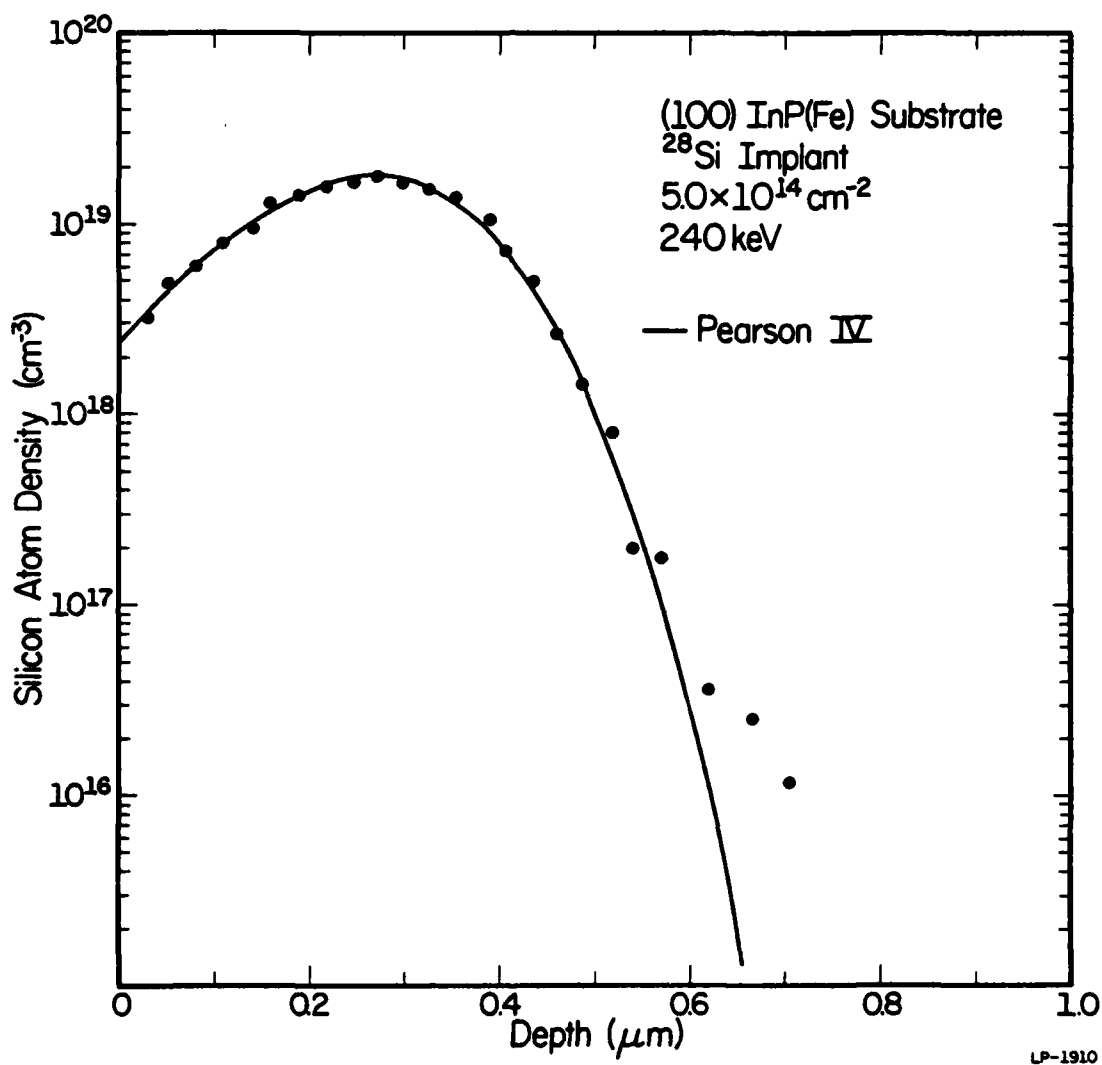
Figure 8.8: SIMS experimental points for ^{28}Si implant (240 keV, 5 x 10^{14} cm^{-2}) and empirically derived Pearson IV distribution [195].

Pearson IV distributions and their fit to experimental points are shown in Figures 8.5 - 8.8. As with Si [190] and GaAs [191], these empirically derived Pearson IV distributions excellently fit the implantation profiles in InP over at least two orders of magnitude. Figures 8.5 - 8.8 illustrate that if the appropriate set of four moments is employed the Pearson IV distribution is quite capable of describing implantation profiles in InP.

8.5 Summary

We have observed in InP that light mass projectile implantations highly dominated by electronic stopping cannot be accurately represented by standard LSS Gaussian profiles. With the intention of obtaining better predictions of implantation profiles, we have examined profiles obtained with statistical distributions which require higher order moments. The moments for these distributions have been calculated from Winterbon's tables of data [35], which are based on theoretical considerations. In deriving these moments we have substituted for the compound target a monatomic target of average charge and mass, and we have assumed the validity of mass scaling[35].

Using theoretical values for the first four moments, profiles have been constructed using the Edgeworth and Pearson I distribution functions. The Pearson IV distribution would be preferable to the Pearson I because of its reported success in describing implantation profiles in Si and in GaAs; however, the values of the theoretical moments in our implants are such as to preclude the Pearson IV and require the Pearson I solution of the Pearson family differential equation. It is found that Edgeworth and Pearson I distributions constructed with four moments derived from theoretical values are not significant improvements over the standard LSS Gaussian representation of implant profiles in InP.

As noted, the theoretical values for the first four moments have been obtained by substituting the compound target with a monatomic target of average charge and mass. Such an approximation may be appropriate for GaAs, in which the ratio of target masses is ~ 1:1 but in InP this ratio is ~ 3.7:1. In this regard the backscattering of ^{9}Be in InP should differ from that in the almost equivalent monatomic target, Ge. Winterbon has observed that for 4:1 target mass ratios the moments derived with the monatomic target approximation differ from those derived without this assumption [35]. It remains to be determined whether more accurate profiles could be constructed from the Edgeworth or Pearson I distribution using theoretical moments derived without the substitution of an equivalent monatomic target.

We have empirically determined the four moments of the experimental implantation profiles. The values of these moments are such as to permit the use of the Pearson IV distribution. These empirically determined moments together with the Pearson IV distribution provide excellent fits to the experimental profiles over at least two orders of magnitude. If the appropriate set of four moments is obtained, the Pearson IV distribution is capable of accurately describing implantation profiles in InP.

In light of these results it appears that a priori predictions of implantation profiles in InP based on theoretical moments will not be a trivial matter. At the present, accurate descriptions of implantation profiles in InP will best be obtained using the Pearson IV distribution with tables of empirically determined four moments.

9. LUMINESCENCE ASSOCIATED WITH DAMAGED
InP SURFACES

9.1 Introduction

During the photoluminescence studies discussed in Chapter 6, a radiative transition was observed in the PL spectra of damaged InP surfaces which was not seen in the spectra of InP with polished surfaces. Several publications have drawn attention to the unique surface properties of InP in comparison with other III-V compounds. Capacitance-voltage studies on metal-insulator-semiconductor (MIS) n-type InP capacitors report (almost independently of the dielectric employed) interface state densities from $2 - 5 \times 10^{11}$ cm^{-2} eV^{-1} [13-15, 196]. This density is lower than that for n-type GaAs ($\sim 2 \times 10^{12}$ cm^{-2} eV^{-1}) and makes n-type InP an attractive material for integrated logic circuits employing normally-off devices [11,12,197]. Additionally, several articles have focused interest on the surface-related optical properties of InP. Of particular interest is the report of a low surface recombination velocity for n-type InP of $\sim 10^3$ cm sec^{-1} (versus $\sim 10^7$ cm sec^{-1} in GaAs) and a photoluminescence (PL) intensity $\sim$ 100 times greater than that obtained from GaAs of similar free electron concentration [140]. In this chapter another unusual optical feature of the InP surface is discussed.

9.2 Experimental Results

Three types of surfaces have been investigated and these are shown in Figure 9.1. Figure 9.1(c) shows the surface of a sample prior to any polishing. This surface is the result of the sawing operation used to obtain (100) oriented wafers from the single crystal boule. Such surfaces will be referred to here as "as-sawn". Figure 9.1(a) shows the results of chemically polishing an "as-sawn" surface with a 1% bromine-methanol solution
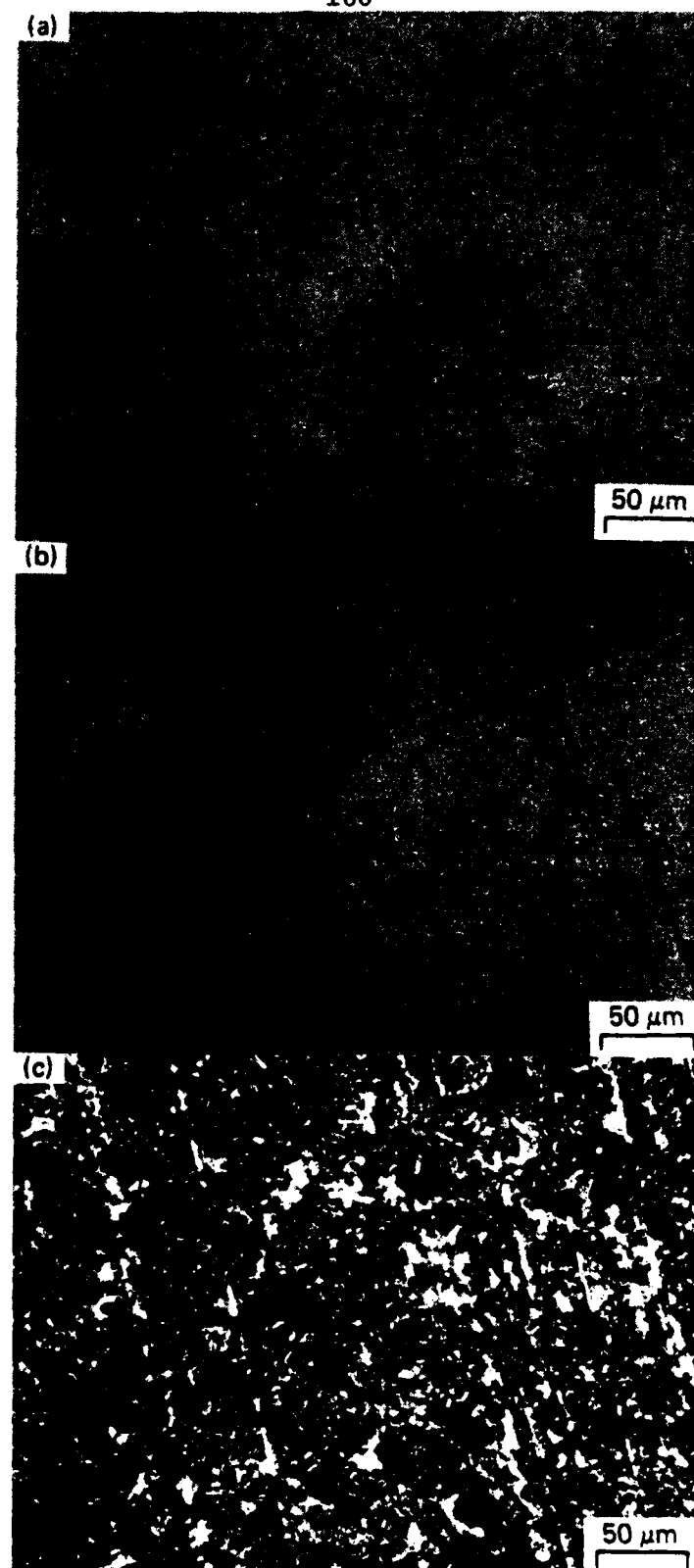
Figure 9.1: Optical micrographs of the three surfaces discussed:
(a) "polished", (b) "semi-polished", (c) "as-sawn" [211].

and a rotating polishing pad. The results of this operation are monitored
with an optical microscope and the polishing is continued until scratches,
digs, or pits are no longer visible on the surface. The mirror-like surface
of Figure 9.1(a) is referred to here as "polished". The surface displayed
in Figure 9.1(b) results from chemical polishing similar to that employed
for "polished" surfaces, but in this case the polishing is terminated
before a perfect mirror surface is obtained. The scratches visible in
Figure 9.1(b) are the result of incomplete polishing of "as-sawn" surfaces.
Surfaces similar to that in Figure 9.1(b) are referred to here as "semi-
polished".

Figure 9.2 displays the photoluminescence spectra obtained from the
three surfaces described above. Referring to Figure 9.2(a) the spectral
features characteristic of standard Fe-doped InP are seen. The origins of
these features have already been discussed in Section 6.2.

An expected result of this work is the observation of a decrease in
luminescence intensity when the surface is less than perfectly polished.
The effects of polishing damage on the PL intensity of GaAs have been
reported in the past [198-200]. These studies indicate that surface damage
can decrease the radiative efficiency by at least an order of magnitude from
that obtained from the best surface. A similar result is observed here for
InP surfaces. Comparing the integrated intensitites of the "semi-polished"
and "as-sawn" spectra to that of the "polished" spectra we obtain 20% and
40% respectively. Presumably such decreases in luminosity can be attributed
to surface damage on a macroscopic scale (e.g., scratches) and on a micro-
scopic scale (e.g., dislocations, vacancy-complexes) which introduce non-
radiative recombination channels [201]. The difference in luminosity be-
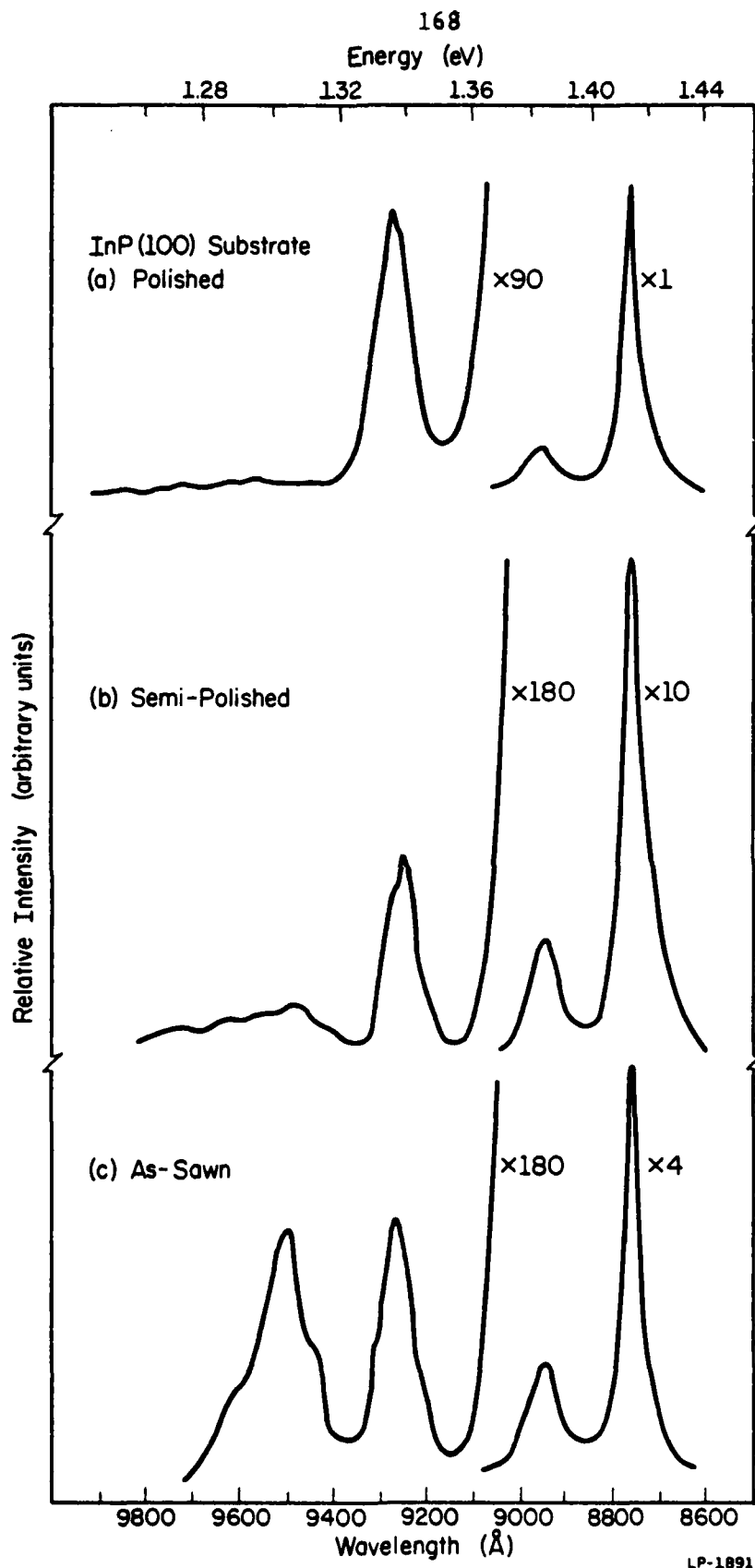tween "semi-polished" and "as-sawn" surfaces may appear contradictory;

Figure 9.2: Typical photoluminescence spectra from the three surfaces shown in Figure 9.1. The sample temperature for these measurements was 5°K [211].

however, the majority of this effect can be explained in terms of the latter surface having a much larger absorption of the incident radiation. Crude measurements of the reflected power from the surfaces of Figure 9.1 have been made. "Polished" and "semi-polished" surfaces yield comparable reflection while the reflected power from "as-sawn" surfaces is ~ 20-40 times weaker. These measurements, together with the equation for luminescent intensity given in reference 140, suggest that absorption effects are the predominant cause of the observed luminosity differences seen in Figures 9.2(b) and 9.2(c). Several publications have shown that the PL intensity from InP is strongly affected by surface band-bending effects leading to a space charge layer and an optically dead layer [202-204]. Differences in surface band-bending between "as-sawn" and "semi-polished" surfaces may also play a role in the observed luminosity differences.

An unusual result of this work is the appearance of a new spectral feature at 1.30(6) eV. As can be seen from Figure 9.2(a) "polished" surfaces exhibit no PL peaks in this energy range, whereas spectra obtained from "semi-polished" surfaces exhibit a weak luminescence in this region. Greater damage to the surface in the "as-sawn" case results in the strongest 1.30(6) eV feature. Figure 9.2 suggests that the evolution of this transition is related to the degree of mechanical surface damage. This transition has also been observed under other circumstances which further support this view of its origin. "Polished" surfaces degraded by exposure to concentrated HCl exhibit weak spectral features in the 1.30(6) eV region which were not present in the spectra prior to the HCl treatment. This 1.30(6) eV feature has also been observed when the excitation beam is incident on an isolated pit of an otherwise perfect "polished" surface. These results support the surface damage origin of this transition proposed

by Street et al. who were to our knowledge the first to observe this
feature [204]. They observed this PL band from samples which cleaved poorly
under vacuum and resulted in surfaces with a very large density of surface
steps. It should be pointed out that our material and processing techniques
differ in several respects: (1) Street et al. performed experiments on
(110) InP while ours were on (100) InP; (2) their crystals were lightly
doped n and p-type while ours are semi-insulating; (3) their samples were
cleaved and examined in ultrahigh vacuum while ours have been exposed to
air. Despite these differences we observe the identical transition reported
by Street et al.

In a publication following their initial report of the 1.3 eV
transition, Street and Williams [205] reported observing a decay in the
radiative luminescence of the transition as a result of room temperature
annealing in a period of days. They stated that this may explain why this
feature is not routinely observed in the PL spectra of InP. Although we
made no effort to examine such annealing effects, we have observed the
transition in "as-sawn" surfaces months after the sawing operation. This
may be the result of the much greater damage of these surfaces in comparison
to those examined by Street and Williams.

9.3 Summary

Surface studies performed in the last few years indicate that no
intrinsic surface states exist in the fundamental gap of vacuum cleaved
GaAs or InP (110) surfaces [206,207]. It is now believed that previous
reports of Fermi level pinning were due to extrinsic states. In light of
these findings and considering the extent of damage to our surfaces (together
with their exposure to air), it is believed that transitions due to intrinsic
surface states can be ruled out. Using a value of 1.423 eV for the bandgap

energy at 5°K [139] would place the observed transition at 117 meV from the bulk conduction band edge; however, the exact location of this level with respect to the surface conduction band is unknown due to probable band bending at the surface. In this regard the 1.30(6) eV feature may be a transition to an effectively shallow level (bent band edge to surface defect state) or a 117 meV transition to an optically deep level. The detailed nature of the defects giving rise to the observed transition is not known. In this regard the influence of the anion should not be overlooked, since it appears to affect Schottky barrier heights and the surface recombination velocity in other multicomponent semiconductors [208-210]. Experimental evidence suggests that chemical adsorption of oxygen on InP directly affects the P surface atoms but not the In surface atoms [206]. The chemical volatility of the phosphorus component of InP would appear to make phosphorus-related defects likely candidates for understanding the detailed nature of the 1.30(6) eV transition.

10. BORON CONTAMINATION AND PRECIPITATION
IN LEC GROWN InP

In this chapter, polycrystalline InP and single crystal, liquid encapsulated Czochralski (LEC) grown InP have been examined for evidence of unintentional boron contamination due to growth procedures. Precipitates of boron or a boron compound have been found in InP grown by the LEC method with ooric oxide (B_2O_3) encapsulation and pyrolitic boron nitride (pBN) crucibles.

10.1 LEC Growth Technique

The single-crystal InP substrates analyzed here are the result of two separate growth steps, each of which may introduce unintentional impurities. The first growth procedure is the synthesis or compounding of indium and phosphorus to obtain the polycrystalline InP charge used in the subsequent single crystal growth [20,212,213]. During synthesis a boat containing an In-rich melt is located within a furnace zone at $\sim$ 1060-1100°C and is in contact with phosphorus vapor from solid phosphorus situated in a cooler furnace zone ($\sim$ 400-500°C). Synthesis is accomplished by slowly pulling the In-rich melt through a temperature profile leading to directional solidification of the melt.

The second step involves the growth of single crystal InP from the synthesized polycrystalline ingot. Crystalline InP has been prepared by a number of techniques including zone melting, gradient freeze, horizontal Bridgman, and liquid encapsulated Czochralski (LEC) pulling [16,20,117,212-215]. As a result of the large, round boules ($\sim$ 100-300 g, $\sim$ 1.5" diameter) obtainable by the LEC method, this presently appears to be the most practical technique for growing device-grade InP. In the LEC technique the crucible containing the melt is housed in a high pressure chamber which has been

evacuated and backfilled with an inert gas (e.g., N_2 or Ar) [216,217].

A liquid encapsulant (usually boric oxide, B_2O_3) covers the melt in the

crucible. The encapsulant ideally serves as a liquid seal preventing vapor

loss of volatile elements if the pressure of the inert gas above the

encapsulant is greater than the dissociation pressure of the melt. As

the crystal emerges from the melt and the liquid encapsulant layer, a

film of encapsulant adheres to the outside of the boule, thereby preventing

loss of volatile components from the growing crystal. Upon completion of

pulling, this B_2O_3 layer is removed with hot water.

The possible sources of contamination in this growth process are:

(i) the boat containing the In melt during synthesis; (ii) the encapsulating

layer used during LEC pulling; (iii) the crucible containing the melt

during LEC pulling. B_2O_3 is used almost universally as the liquid encapsulant

in LEC growth of various III-V compounds because of its chemical stability,

density, low melting point, viscosity, and transparency [216-218]. The

composition of the synthesis boat and of the melt crucible varies from lab

to lab, but the most common materials are silica or pyrolytic boron nitride

(pBN). It has been reported that silica crucibles introduce silicon

impurities in LEC crystals due to dissolution of the crucible by

B_2O_3 [185,219-221]. Additionally, silica crucibles containing B_2O_3 tend

to fracture when cooled to room temperature [20,217]. To avoid these problems,

the use of pBN crucibles has become common.

10.2 Experimental Results

Tables 10.1 and 10.2 summarize our study of boron contamination

in the growth of InP. Impurity concentrations were measured by secondary-

ion mass spectrometry (SIMS) using a CAMECA IMS-3f ion microprobe.

Table 10.1

SIMS boron analysis of polycrystalline InP synthesized
in indicated growth ware

SAMPLE	SYNTHESIS BOAT	^{11}B CONCENTRATION (atoms/cm^3)	PRECIPITATION (?)
NRL Synthesis – 49 Slice – ?	SiO$_2$	$(4.3 \pm 2.9) \times 10^{15}$	No
NRL Synthesis – 52 Slice – 1	SiO$_2$	$(1.9 \pm 1.3) \times 10^{15}$	No
NRL Synthesis – 52 Slice – 3	SiO$_2$	$(2.0 \pm 1.4) \times 10^{15}$	Nc
NRL Synthesis – 27 Slice – ?	pBN	$(5.2 \pm 3.8) \times 10^{15}$	No
NRL Synthesis – 33 Slice – 1	pBN	$(1.8 \pm 1.2) \times 10^{15}$	No
NRL Synthesis – 33 Slice – 3	pBN	$(1.9 \pm 1.3) \times 10^{15}$	No

Table 10.2

SIMS boron analysis of single crystal InP
obtained with indicated growth ware

SAMPLE	SYNTHESIS BOAT	LEC CRUCIBLE	^{11}B CONCENTRATIONS (atoms/cm^3)	PRECIPITATION
Metals Res. Corp Boule - ? Slice - ?	SiO$_2$	SiO$_2$	$(3.2 \pm 1.6) \times 10^{15}$	No
Crys. Comm. Inc. Boule - 136 (CCIPS) Slice - Top	SiO$_2$	SiO$_2$	$(11.0 \pm 4.7) \times 10^{15}$	No
Crys. Comm. Inc. Boule - 136 (CCIPS) Slice - Bottom	SiO$_2$	SiO$_2$	$(5.3 \pm 3.9) \times 10^{15}$	No
NRL Boule - 2-25(H) Slice - 1	SiO$_2$	pBN	$(3.8 \pm 2.1) \times 10^{15}$	No
NRL Boule - 2-25(H) Slice - 55	SiO$_2$	pBN	$\sim 3 \times 10^{18}$	Yes
NRL Boule - 2-10(H) Slice - Bottom 1/3	pBN	pBN	$\sim 1 \times 10^{18}$	Yes

The results of our analysis of various NRL (Naval Research Laboratory) polycrystalline samples are shown in Table 10.1. Our results are in general agreement with earlier reports of boron concentrations measured in polycrystalline ingots from other labs [17,185]. We have examined samples from both ends of polycrystalline ingots synthesized in silica and in pBN boats. No variation of boron concentration along the length of a polycrystalline ingot is seen in ingots grown with either silica or pBN boats. Additionally, from Table 10.1, no significant differences in the B levels can be detected between silica boat ingots and ingots synthesized in pBN. Our data indicate that within detection limits, pBN boats have little influence on boron contamination of the melt.

Several single crystals of semi-insulating InP were examined, and the results are summarized in Table 10.2. Except in samples where precipitation was detected, the measured boron concentrations are comparable to those reported by other groups for LEC grown InP [185,216,217,222,223]. Three samples shown in Table 10.2 were synthesized and pulled exclusively from silica ware, and employed a B_2O_3 encapsulant during pulling. The average level of boron present in these samples is slightly higher than that found in the polycrystalline samples of Table 10.1, however, within the experimental uncertainty of the SIMS technique, the concentrations still overlap. From these results we conclude that, at most, the B_2O_3 employed in LEC pulling contributes only a small amount of boron to the crystal. Hopkins et al. [224] have recently reported the same result for LEC grown GaAs.

This study was initiated because of the discovery of boron-rich regions or precipitates while depth profiling boron implants in single crystals from NRL boule 2-10(H). In the course of depth profiling to 2.5 μm,
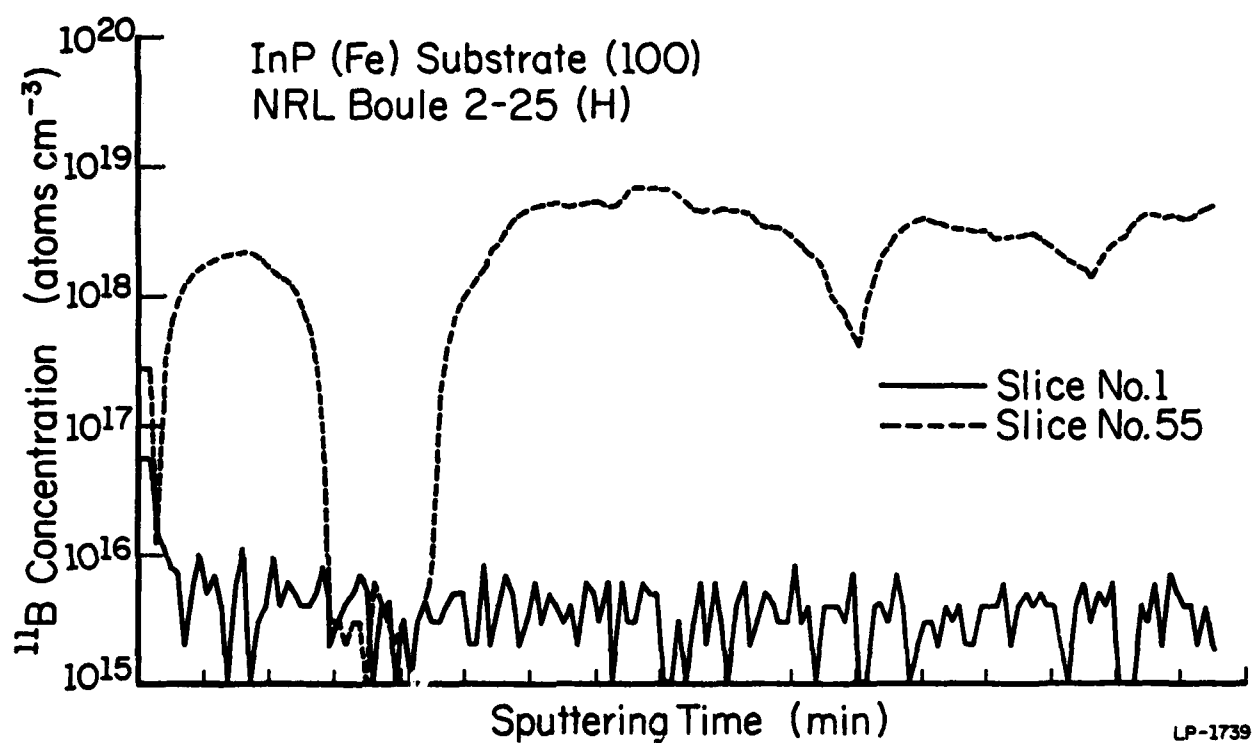
Figure 10.1: ^{11}B concentration SIMS profiles for slices from top (slice 1) and bottom (slice 55) of NRL boule 2-25(H) [178].

approximately 2-3 precipitates of varying size would be encountered. Between

precipitates the boron background in these samples is comparable to samples

listed in Table 10.2 which did not contain precipitates. Boule 2-10(H)

was synthesized and pulled entirely in pBN growth ware with the analyzed

slices taken from the botton (last-to-freeze) third of the boule.

Two slices of semi-insulating InP from different portions of the

same NRL boule (2-25(H)) were analyzed. To isolate possible sources of

boron contamination, the polycrystalline InP charge for this boule was

synthesized in silica. Subsequently,the single crystal ingot was pulled

from a pBN crucible. Comparison of the SIMS B profiles for these two

slices is shown in Figure 10.1. Slice 1, which is from the top (first-to-

freeze) end of the boule, has a boron concentration comparable to other

nc -precipitate containing samples as seen from Table 10.2. No large

precipitates are observed in slice 1. Slice 55 is taken from the bottom of

boule 2-25(H). As seen from Figure 10.1 the boron concentration in this sample

differs drastically both in nature and concentration from that of slice 1.

Whereas slice 1 has an essentially uniform level of boron contamination,

slice 55 contains large, distinct precipitates with boron concentrations

2-3 orders of magnitude higher than the boron level in slice 1. This pre-

cipitation phenomenon can be more clearly observed in a series of photo-

graphs (Figure 10.2) taken at successive depths using the ^{11}B ion image

from the CAMECA IMS-3f. In these photographs, clusters containing high

concentrations of boron appear and are then replaced by other clusters as

the sputtering proceeds. A first order estimate of the precipitate

density indicates $\sim 1 \times 10^{18}$ precipitates cm^{-3} in slice 55. Averaging

the boron signal over the precipitate fluctuations gives a boron concentra-

tion of $\sim 3 \times 10^{18}$ cm^{-3}, in sharp contrast with the $\sim 4 \times 10^{15}$ cm^{-3} observed
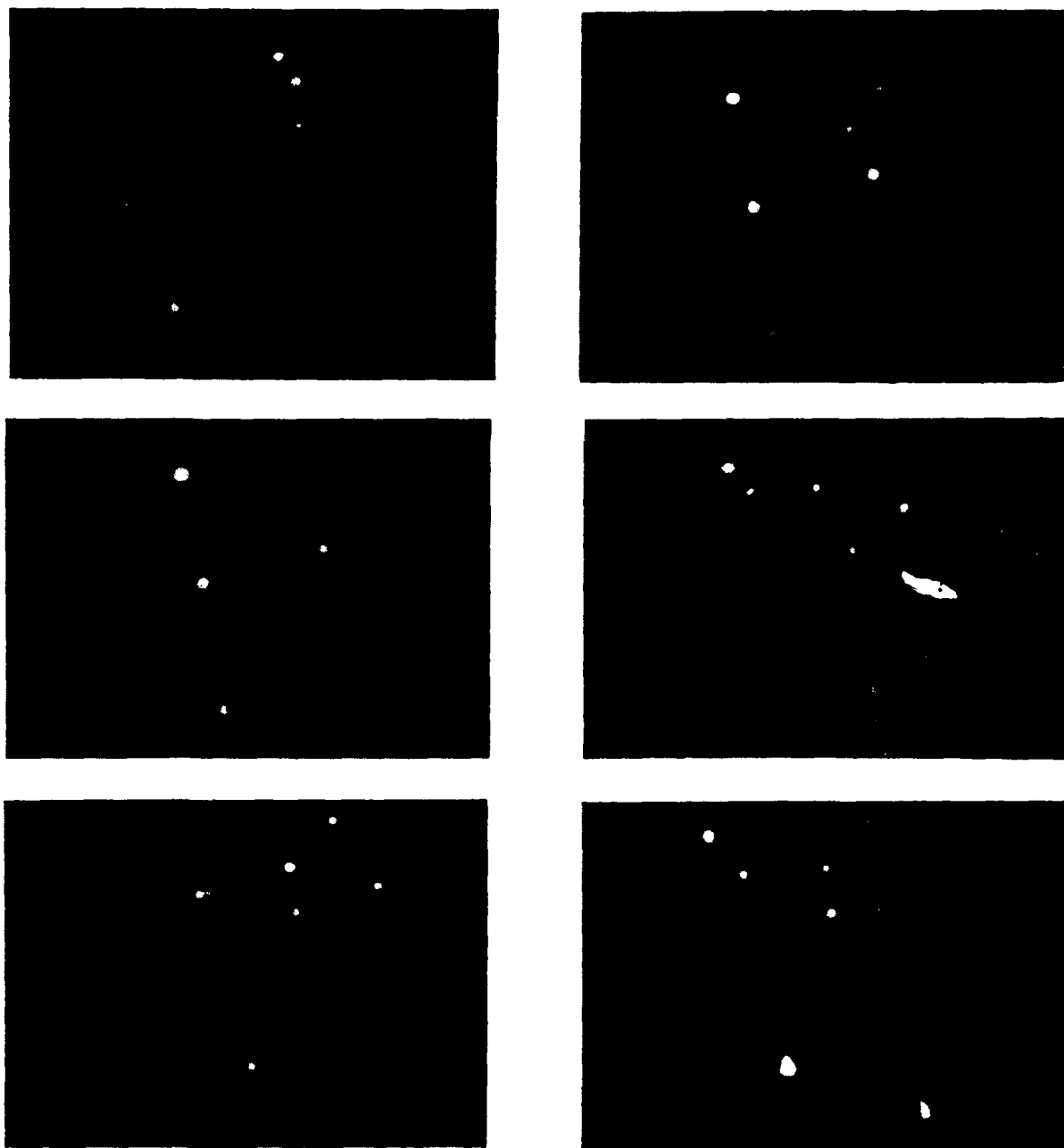
Figure 10.2: Successive depth photographs of ^{11}B ion images taken while sputtering slice 55 of NRL boule 2-25(H) [178].

for slice 1 from the same boule. We have observed in various samples that the number of precipitates encountered during a profile depends on the sample's location in the boule with the density of precipitates increasing towards the bottom (last-to-freeze) end of the boule.

The exact chemical composition of the observed boron clusters is not known. Profiles have been taken monitoring ^{27}Al, ^{28}Si, ^{52}Cr, and ^{56}Fe simultaneoulsy with ^{11}B. No correlation of boron precipitates with any of these impurities has been observed. Components of the precipitates such as ^{14}N, ^{16}O, or ^{31}P still remain possible due to poor detection capability and background masking effects.

It has been reported by Mullin et al. [17] that a peak at 1.32 eV is found in the photoluminescence spectra of pulled crystals only and never in the spectra of polycrystalline starting material. They noted that this peak is clearly associated with B_2O_3 liquid encapsulated growth. It was not determined if the peak is directly due to elemental boron or due to an interaction of B_2O_3 with other contaminants [17,222]. We have analyzed the photoluminescence spectra of the sample shown in Tables 10.1 and 10.2. With the samples held at 5°K, spectra were obtained for the energy range from 1.42 - 1.15 eV using a system resolution of 1 meV. No strong peak in the region about 1.32 eV is detected in either slice 55 or slice 1, and their spectra in this region are comparable to those obtained from the polycrystalline samples of Table 10.1. Comparison of the spectra from slice 55 to that from slice 1 yielded no significant differences. It appears that boron does not produce any luminescence lines in the range from 1.42 - 1.15 eV, supporting a similar observation by Williams et al. [102].

10.3 Discussion

Our work to date has not unambigously established the source of boron contamination and precipitation in LEC grown InP. We have observed, however, that pBN in the absence of B_2O_3 does not cause detectable boron contamination above what is normally measured in samples grown in silica. The polycrystalline ingots analyzed here were each grown over approximately two week periods while the NRL single crystals were grown in 1-2 days. The temperatures involved for the synthesis and LEC growth of the analyzed samples are comparable. LEC growth proceeds at the melting point ($1062^{\circ}C$) while the synthesis boat for the NRL polycrystalline samples sits in a linearly ramped temperature zone of $1060-1100^{\circ}C$. If pBN were the source of boron contamination then taking into account the times and temperatures involved, one would conclude that boron contamination similar to that seen in pBN crucible grown single crystals should certainly be present in pBN boat synthesized ingots. Our results indicate, however, that the boron levels at either end of pBN synthesized polycrystalline ingots are comparable to those synthesized in silica boats. On the other hand, we observe that B_2O_3 in the absence of a pBN crucible does not lead to precipitation. Although the average level of boron present in silica crucible grown samples is slightly higher than that found in the polycrystalline samples, the concentrations are clustered in a range of less than an order of magnitude. No precipitates have been observed in B_2O_3, silica crucible grown single crystals. These results lead us to postulate that the source of boron contamination most consistent with our observations is the result of interaction between B_2O_3 and pBN.
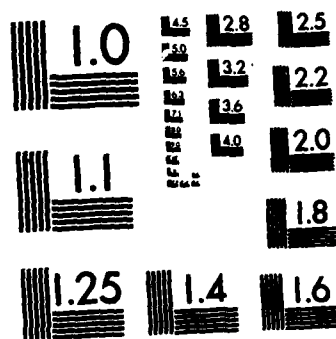
MICROCOPY RESOLUTION TEST CHART

NATIONAL BUREAU OF STANDARDS-1963-A

To study the diffusivity of boron in InP we have examined the boron atomic profiles resulting from thirty minute of ^{10}B implanted InP encapsulated with 2300 Å of Si_3N_4. Very little diffusion of boron could be detected in material annealed at $750^{\circ}C$. Computer simulation of profiles resulting from various diffusion coefficients has allowed us to determine the upper limit for the boron coefficient in InP to be $D(750^{\circ}C) < 1 \times 10^{-14} cm^2 sec^{-1}$.

To our knowledge no literature exists on the electrical properties of boron in InP, although it is commonly assumed to be electrically inactive since it is isoelectronic with In [216]. Aside from the question of elemental boron's electrical activity in InP, the boron precipitates can be expected to cause problems in devices fabricated on such substrates. Lattice distortion in precipitate regions could affect epitaxial growth and could also change the "effective" dielectric constant of the material which, upon application of an external field, would lead to local inhomogeneities of electric field. Such precipitates may also create localized space-charge regions which will influence carrier mobility [225]. These effects will have serious consequences on the performance of devices fabricated in InP substrates rich in boron precipitates.

10.4 Summary

We have discovered precipitates of boron or a boron compound in single crystal InP grown by the LEC method with B_2O_3 and pBN crucibles. The density of precipitates depends on the sample's location in the boule, with the number of precipitates increasing towards the last-to-freeze end of the boule. The boron background concentrations in polycrystalline InP and in B_2O_3 encapsulated, silica crucible, LEC grown InP single crystals

lie in the range from $10^{15} - 10^{16}$ cm^{-3}. We have observed that pBN in the absence of B_2O_3 does not lead to detectable boron contamination above what is normally seen in samples grown in silica. There are indications that B_2O_3 may be responsible for possibly higher boron concentrations than those normally found in polycrystalline samples, but the increase is less than an order of magnitude. B_2O_3 in the absence of a pBN crucible has not been observed to lead to boron precipitation. We postulate that the likely source of boron contamination in crystals with boron precipitates is the result of an interaction of B_2O_3 and pBN.

Photoluminescence spectra were obtained for the SIMS analyzed polycrystalline and single crystal samples. On the basis of photoluminescence spectra it was not possible to distinguish between single crystals with precipitates and those without. Boron does not appear to produce any luminescence in the energy range of 1.42 - 1.15 eV.

On the basis of boron atomic profiles resulting from thirty minute, 750°C anneals of ^{10}B implanted InP, a diffusion coefficient of D(750°C) < 10^{-14} cm^2 sec^{-1} has been determined for boron in InP.

11. SUMMARY

If ion implantation is to become a standard doping technique in InP
it will be necessary to develop reliable annealing procedures. Yet because
of the relatively limited research effort expended to date on implantation
studies of InP a large number of basic issues remain to be examined. Three
such topics have been addressed in this work. These are: Which of the
commonly employed encapsulants (SiO_2, PSG, or Si_3N_4) but suppresses In or P
outdiffusion from the InP surface during high temperature anneals? What
are the anneal time and temperature required for lattice recovery from im-
plant damage and for activation of implanted impurities? What are the
redistribution characteristics of implanted and other intentionally present
impurities during such anneals?

Encapsulation studies described here indicate that a PSG cap with
~ 5 at.% P is superior to either a SiO_2 cap or a Si_3N_4 cap for annealing InP
in the temperature range from 450°-800°C. Using photoluminescence, P vacancy-
related luminescence has been observed in the spectra of SiO_2 capped and
annealed InP, indicating P outdiffusion through SiO_2 encapsulants of InP.
SIMS analysis indicates that 600°C, 60 min anneals with a SiO_2 cap result in
Si levels in the InP above those found in unprocessed InP to depths of ~ 1 μm.
In addition, the usefulness of SiO_2 as an InP cap is limited since it has
been found to crack when annealed in the temperature range from 650-750°C.
It has been concluded from Auger studies that factors other than thermal
expansion mismatch (e.g., chemical interactions) play a role in this SiO_2
cracking phenomenon. On the basis of PL measurements it appears that little,
if any, P outdiffusion occurs through a Si_3N_4 cap. It has been observed with

PL that high temperature anneals with a Si_3N_4 cap result in luminosity levels greater than those associated with unprocessed material and in the emergence of a new spectral feature of 1.378 eV. Indium has been detected by both AES and SIMS on the surfaces of Si_3N_4 caps following 30 min and 60 min, 750°C anneals. SIMS measurements of samples annealed for 60 min at 750°C with Si_3N_4 indicate Si levels above those found in unprocessed InP to depths of ~ 0.75 μm. No such Si contamination of InP has been observed following anneals with a PSG cap. PL measurements indicate that in comparison to SiO_2 or Si_3N_4 caps, PSG encapsulation least affects the luminosity levels or spectral features of the capped InP. Some SIMS results suggest that In is outdiffusing through the PSG caps, but further work is required on this point before reaching a definite conclusion. On the basis of the results discussed here it is concluded that PSG encapsulation with ~ 5 at.% P is better than either SiO_2 or Si_3N_4 in preserving the characteristics of encapsulated InP during furnace anneals in the range from 450-750°C.

PL measurements of the integrated bandege luminescence from annealed samples following 51 keV, 10^{13} - 10^{15} cm^{-2} implants of ^{4}He indicate that 30 min anneals at 750°C are sufficient for the lattice to recover from implant damage and to restore pre-implant levels of optical quality. Identical conclusions are obtained from PL examination of the integrated bandedge luminescence of annealed samples implanted with 100 keV, 10^{13} - 10^{15} cm^{-2} ^{9}Be. From these studies it is estimated that the Be acceptor ionization energy in InP is 41.3 ± 3 meV. Maximum Be optical activation occurs for 30-60 min anneals at 750°C.

Using SIMS, depletion zones of the compensating impurity, Cr or Fe, have been observed in Si_3N_4 capped and 800°C annealed SI InP. Cr exhibits larger concentration gradients in these depletion zones than does Fe. Under typical annealing conditions for InP (T ≥ 700°C, t = 15-30 min) it is found from SIMS analysis that implanted ^9Be is a rapid diffusant in SI InP. High dose (10^{15} cm^{-2}), 100 keV implants of ^9Be into Si InP result in structured and correlated Be and Cr or Fe atomic profiles. Flat tails of ^9Be extending over distances of a few microns are observed in high dose implanted SI InP but not in comparably processed VPE InP. Also, ^9Be is found to diffuse deeper (~ 3.5 μm) at annealing temperatures of 550°C than in 750°C anneals (~ 2.3 μm) of 10^{15} cm^{-2} implanted SI InP. SIMS studies of 10^{15} cm^{-2}, 250 keV Mg implanted SI InP show drastic redistribution of Mg and Fe during 30 min anneals for temperatures from 550-750°C. As in the Be implant studies, the redistribution of Fe is correlated with the diffusion profile of the implanted Mg. In contrast to ^9Be or ^{26}Mg, little redistribution of ^{28}Si is seen following 750°C, 30 min anneals of SI InP implanted with 240 keV, 5 x 10^{14} cm^{-2} ^{28}Si.

Although the present results answer the basic questions raised here, important new questions have arisen regarding InP implantation. Most importantly, further work is required to understand the physics governing the redistribution behavior of implanted impurities in SI InP. The behavior of Be and Mg seen here seems to parallel the rapid diffusion shown by Zn and Cd during diffusion doping of InP [155,157]. Furthermore, others have pointed out that donor implants result in higher electrical activations than acceptor impants in InP [184]. Is the redistribution behavior of acceptors in InP a fundamental limitation leading to low activations? This question

is important not only from a scientific viewpoint but also technologically since it will severely limit the applicability of acceptor implantation in InP. Furthermore, the frequency of unusual or unexpected results in this work (i.e., Chapters 8-10) illustrates the current limited understanding of InP properties. In conclusion, the results presented here clearly indicate the need for further studies before ion implantation of InP is a well understood technique.

REFERENCES

1. J. J. Gallagher, Proceedings of the 1980 NATO Sponsored InP Workshop, Rome Air Development Center, Hanscom Air Force Base, MA (Technical Memorandum #RADC-TM-80-07) 1.

2. J. E. Stich and P. N. Robson, IEEE Trans. Electron Devices ED-23, 1086 (1976).

3. F. B. Fank, J. D. Crowley, and J. J. Berenz, Microwave Journ., 86 (June 1979).

4. L. Wandinger, Microwave Journ., 71 (March 1981).

5. C. Hilsum and H. D. Rees, Electron. Lett. 6, 277 (1970).

6. H. T. Lam and G. A. Acket, Electron. Lett. 7, 723 (1971).

7. W. Fawcett and D. C. Herbert, Electron. Lett. 9, 308 (1973).

8. A. G. Foyt, Proceedings of the 1980 NATO Sponsored InP Workshop, Rome Air Development Center, Hanscom Air Force Base, MA (Technical Memorandum #RADC-TM-80-07) 21.

9. T. Miya, Y. Terunuma, T. Hosaka and T. Miyashita, Electron. Lett. 15, 106 (1979).

10. L. G. Cohen and C. Lin, Appl. Optics 16, 3136 (1977).

11. D. L. Lile and D. A. Collins, Thin Solid Films 56, 225 (1979).

12. L. Messick, IEEE Trans. Electron Devices ED-28, 218 (1981).

13. L. Messick, J. Appl. Phys. 47, 4949 (1976).

14. D. L. Lile and D. A. Collins, Appl. Phys. Lett. 28, 554 (1976).

15. G. G. Roberts, K. P. Pande, and W. A. Barlow, Electron. Lett. 13, 581 (1977).

16. J. B. Mullin, A. Royle, and B. W. Straughan, International Symposium on GaAs and Related Compounds, 1970, Inst. of Physics Conf. Ser. No. 9, London, 1971, 41.

17. J. B. Mullin, A. Royle, B. W. Straughan, P. J. Tufton, and E. W. Williams, J. Crystal Growth 13/14, 640 (1972).

18. D. E. Davies, J. P. Lorenzo, and M. L. Deane, Appl. Phys. Lett. 31, 256 (1977).

19. J. P. Donnelly and C. E. Hurwitz, Appl. Phys. Lett. 31, 418 (1977).

20. R. L. Henry and E. M. Swiggard, <u>International Symposium on GaAs and Related Compounds, 1976</u>, Inst. of Physics Conf. Ser. no. 33b, London, 1977, 28.

21. J. D. Oberstar, B. G. Streetman, J. E. Baker, and Peter Williams, J. Electrochem. Soc. <u>128</u>, 1814 (1981).

22. J. F. Gibbons, Proc. IEEE <u>56</u>, 295 (1968).

23. J. F. Gibbons, Proc. IEEE <u>60</u>, 1062 (1972).

24. J. W. Mayer, L. Erickson, and J. A. Davies, <u>Ion Implantation in Semiconductors</u>, Academic Press, New York, 1970.

25. F. H. Eisen, Rad. Effects <u>47</u>, 99 (1980).

26. J. P. Donnelly, Nucl. Instrum. Methods <u>182/182</u>, 553 (1981).

27. B. G. Streetman, IEEE Trans. Nucl. Sci. <u>NS-28</u>, 1742 (1981).

28. P. D. Townsend, J. C. Kelly, and N. E. W. Hartley, <u>Ion Implantation, Sputtering, and their Applications</u>, Academic Press, New York, 1976.

29. S. Datz, <u>Structure and Collisions of Ions and Atoms</u>, I. A. Sellin (ed.), Springer-Verlag, New York, 1978, 309.

30. J. Lindhard and M. Scharff, Phys. Rev. <u>124</u>, 128 (1961).

31. J. Lindhard, M. Scharff, and H. E. Schiott, Kgl. Danske Videnskab Selskab. Mat. Fys. Medd. <u>33</u>, no. 14 (1963).

32. H. E. Schiott, Kgl. Danske Videnskab Selskab. Mat. Fys. Medd. <u>35</u>, no. 9 (1966).

33. H. E. Schiott, Rad. Effects <u>6</u>, 107 (1970).

34. D. K. Brice, <u>Ion Implantation Range and Energy Deposition Distributions</u>, Vol. 1, IFI/Plenum Publishing Corp., New York, 1975.

35. K. B. Winterbon, <u>Ion Implantation Range and Energy Deposition Distributions</u>, Vol. 2, IFI/Plenum Publishing Corp., New York, 1975.

36. K. B. Winterbon, Peter Sigmund, and J. B. Sanders, Kgl. Danske Videnskab Selskab. Mat. Fys. Medd. <u>37</u>, no. 14 (1970).

37. J. F. Gibbons, W. S. Johnson, and S. W. Mylroie, <u>Projected Range Statistics Semiconductors and Related Materials</u>, 2nd ed., Dowden, Hutchinson and Ross, Inc., PA, 1975.

38. W. J. Shannon, RCA Rev. <u>31</u>, 431 (1970).

190

39. M. J. Helix, K. V. Vaidyanathan, B. G. Streetman, H. B. Dietrich, and P. K. Chatterjee, Thin Solid Films 55, 143 (1978).

40. M. J. Helix, Ph.D. dissertation, University of Illinois at Urbana-Champaign, 1979. Also Coordinated Science Laboratory Report R-858, UILU-ENG 78-2251.

41. K. V. Vaidyanathan, M. J. Helix, D. J. Wolford, B. G. Streetman, R. J. Blattner, and C. A. Evans, J. Electrochem. Soc. 124, 1781 (1977).

42. Physical Electronics Industries, Technical Information, 1975.

43. T. A. Carlson, Photoelectron and Auger Spectroscopy, Plenum Press, New York, 1975.

44. Richard E. Honig, Thin Solid Films 31, 89 (1976).

45. Charles A. Evans, Jr., Anal. Chem. 47, 855 (1975).

46. R. Castaing and J. F. Hennequin, Advances in Mass Spectrometry, Vol. V, A. Quayle (ed.), Institute of Petroleum, London, 1971, 419.

47. C. A. Anderson, Int. J. Mass Spectrom. Ion Phys. 2, 61 (1969).

48. C. A. Anderson, Int. J. Mass Spectrom. Ion Phys. 3, 413 (1970).

49. A. Benninghoven, Z. Naturforsch. 22a, 841 (1967).

50. C. A. Evans, Jr., Thin Solid Films 19, 11 (1973).

51. M. L. Yu, Phys. Rev. Lett. 40, 574 (1978).

52. Peter Williams, Surf. Sci. 90, 588 (1979).

53. Cameca Instruments Inc., Technical Information, 1979.

54. R. Castaing and G. Slodzian, J. Micros. 1, 395 (1962).

55. R. C. Barber, R. L. Bishop, H. E. Duckworth, J. O. Meredith, F. C. G. Southon, P. Van Rookhuyzen, and P. Williams, Rev. Sci. Instrum. 42, 1 (1971).

56. Peter Williams and H. E. Duckworth, Sci. Prog. 60, 319 (1972).

57. W. K. Hofker, H. W. Werner, D. P. Oosthoek, and H. A. M. DeGrefte, Rad. Effects 17, 83 (1973).

58. P. K. Vasudev, R. G. Wilson, C. A. Evans, Jr., Appl. Phys. Lett. 36, 837 (1980).

59. Conilee G. Kirkpatrick, Ph.D. dissertation, University of Illinois at Urbana-Champaign, 1974. Also Coordinated Science Laboratory Report R-662, UILU-ENG 74-2228.

60. Albert J. Rosa, Ph.D. dissertation, University of Illinois at Urbana-Champaign, 1975. Also Coordinated Science Laboratory Report R-685, UILU-ENG 75-2220.

61. Richard E. Anderson, Ph.D. dissertation, University of Illinois at Urbana-Champaign, 1974. Also Coordinated Science Laboratory Report R-660, UILU-ENG 74-2226.

62. Donald J. Wolford, Ph.D. dissertation, University of Illinois at Urbana-Champaign, 1979. Also Coordinated Science Laboratory Report R-862, UILU-ENG 78-2255.

63. Pallab K. Chatterjee, Ph.D. dissertation, University of Illinois at Urbana-Champaign, 1976. Also Coordinated Science Laboratory Report R-721, UILU-ENG 76-2209.

64. B. O. Seraphin and H. E. Bennett, Semiconductors and Semimetals, Vol. 3, R. K. Willardson and A. C. Beer (eds.), Academic Press, New York, 1968, 499.

65. D. G. Coates, Phil. Mag. 16, 1179 (1967).

66. D. S. Gemmell, Rev. Mod. Phys. 46, 129 (1974).

67. J. P. Spencer, C. J. Humphreys, and P. B. Hirsch, Phil. Mag. 26, 193 (1972).

68. C. R. Bayliss and D. L. Kirk, Thin Solid Films 29, 97 (1975).

69. C. R. Bayliss and D. L. Kirk, J. Phys. D 9, 233 (1976).

70. W. Y. Lum and A. R. Clawson, J. Appl. Phys. 50, 5296 (1979).

71. N. N. Sirota, Semiconductors and Semimetals, Vol. 4, R. K. Willardson and A. C. Beer (eds.), Academic Press, New York, 1968, 80.

72. R. F. C. Farrow, J. Phys. D 7, 2436 (1974).

73. S. Guha and F. Hasegawa, Solid-State Electron. 20, 27 (1977).

74. Gernot S. Pomrenke, Y. S. Park and Robert L. Hengehold, J. Appl. Phys. 52, 969 (1981).

75. J. D. Oberstar and B. G. Streetman, J. Appl. Phys., to be published.

76. D. Eirug Davies, J. P. Lorenzo and T. G. Ryan, Solid-State Electron. 21, 981 (1978).

77. J. P. Donnelly and C. A. Armiento, Appl. Phys. Lett. 34, 96 (1979).

78. D. Eirug Davies, W. D. Potter and J. P. Lorenzo, J. Electrochem. Soc. 125, 1845 (1978).

79. G. A. Antypas, Appl. Phys. Lett. 37, 64 (1980).

80. A. R. Clawson, W. Y. Lum and G. E. McWilliams, J. Crystal Growth 46, 300 (1979).

81. B. Molnar, Appl. Phys. Lett. 36, 927 (1980).

82. J. Kasahara, J. F. Gibbons, T. J. Magee and J. Peng, J. Appl. Phys. 51, 4119 (1980).

83. K. V. Vaidyanathan, C. L. Anderson, H. L. Dunlap and D. E. Holmes, Nucl. Instrum. Methods 182/183, 631 (1981).

84. S. Singh, W. A. Bonner, I. Camlibel, W. H. Grodkiewicz, T. R. Kyle, G. Pasteur, L. G. VanUitert and R. S. Williams, Appl. Phys. Lett. 38, 349 (1981).

85. Takashi Nishioka and Yoshiro Ohmachi, J. Appl. Phys. 51, 5789 (1980).

86. C. W. Wilmsen, J. F. Wager and J. Stannard, Inst. Phys. Conf. Ser. 50, London, 1980, 251.

87. J. D. Oberstar, B. G. Streetman, J. E. Baker, N. L. Finnegan, E. A. Sammann, Peter Williams, Thin Solid Films, to be published.

88. G. Queirolo and G. U. Pignatel, J. Electrochem. Soc. 127, 2438 (1980).

89. E. A. Sammann and J. D. Oberstar, unpublished.

90. I. S. T. Tsong, M. D. Monkowski, J. R. Monkowski, P. D. Miller, C. D. Moak, B. R. Appleton and A. L. Wintenberg, Physics of MOS Insulators, G. Luckovsky, S. T. Pantelides and F. L. Galeneer (eds.), Pergamon Press, New York, 1980, 321.

91. N. M. Johnson, D. K. Biegelsen, M. D. Moyer, V. R. Deline and C. A. Evans, Jr., Appl. Phys. Lett. 38, 995 (1981).

92. J. C. Mikkelsen, Jr., Appl. Phys. Lett. 39, 601 (1981).

93. D. V. McCaughn and R. A. Kushner, Characterization of Solid Surfaces, R. F. Kane and G. B. Larrabee (eds.), Plenum, New York, 1974, 627.

94. H. W. Werner and A. E. Morgan, J. Appl. Phys. 47, 1232 (1976).

95. K. Wittmaack, J. Appl. Phys. 50, 493 (1979).

96. W. Reuter, M. L. Yu, M. A. Frisch and M. B. Small, J. Appl. Phys. 51, 850 (1980).

97. G. Slodzian, Ann. Phys. $\underline{9}$, 591 (1964).

98. J. P. Donnelly and G. A. Ferrante, Solid-St. Electron. $\underline{23}$, 1151 (1980).

99. K. J. Bachmann and E. Buehler, J. Electrochem. Soc. $\underline{121}$, 835 (1974).

100. G. G. Baumann, K. W. Benz and M. H. Pilkuhn, J. Electrochem. Soc. $\underline{123}$, 1232 (1976).

101. J. D. Oberstar and B. G. Streetman, Thin Solid Films, to be published.

102. E. W. Williams, W. Elder, M. G. Astles, M. Webb, J. B. Mullin, B. Straughan and P. J. Tufton, J. Electrochem. Soc. $\underline{120}$, 1741 (1973).

103. Yoshimitsu Yamazoe, Yoichi Sasai, Taneo Nishino and Yoshihiro Hamakawa, Jpn. J. Appl. Phys. $\underline{20}$, 347 (1981).

104. J. U. Fischbach, G. Benz, N. Stath and M. H. Pilkuhn, Solid-State Comm. $\underline{11}$, 725 (1972).

105. Kotaru Tsubaki and Koichi Sugiyama, Jpn. J. Appl. Phys. $\underline{19}$, 1185 (1980).

106. B. V. Shanabrook, P. B. Klein, P. G. Siebenmann, H. B. Dietrich and S. G. Bishop, Extended Abstracts of the Electrochemical Society Fall Meeting, Denver, 1981, 841.

107. W. H. Koschel, S. G. Bishop, B. D. McCombe, W. Y. Lum and H. H. Wieder, Int. Symp. on GaAs and Related Compounds, 1976, Inst. Phys. Conf. Ser. 33a, London, 1977, 98.

108. U. Heim, Solid State Commun. $\underline{7}$, 445 (1969).

109. A. M. White, P. J. Dean, K. M. Fairhurst, W. Bardsley, E. W. Williams, and B. Day, Solid State Commun. $\underline{11}$, 1099 (1972).

110. J. D. Oberstar, B. G. Streetman, and E. A. Sammann, Thin Solid Films, $\underline{81}$, 347 (1981).

111. K. V. Vaidyanathan, private communication.

112. A. K. Sinha, H. J. Levinstein and T. E. Smith, J. Appl. Phys. $\underline{49}$, 2433 (1978).

113. Hideo Sunami, Yokichi Itoh and Kikuji Sato, J. Appl. Phys. $\underline{41}$, 5115 (1970).

114. Yoshihiro Tsunoda, Jpn. J. Appl. Phys. $\underline{16}$, 1869 (1977).

115. Takashi Tokuyama, Yasuhiro Fujii, Yoshimitsu Sugita and Seigou Kishino, Jpn. J. Appl. Phys. $\underline{6}$, 1252 (1967).

116. Leonard Bernstein and Robert J. Beals, J. Appl. Phys. 32, 122 (1961).

117. K. J. Bachmann, E. Buehler, J. L. Shay, and D. L. Malm, Proc. 5th Int. Symp. on GaAs and Related Compounds, 1974, Inst. of Phys., London, 1975, 121.

118. I. Kudman and R. J. Paff, J. Appl. Phys. 43, 3760 (1972).

119. Thermophysical Properties of Matter, Vol. 13, Y. S. Touloukian and C. Y. Ho (eds.), Plenum, New York, 748 (1977).

120. E. D. Pierron, D. L. Parker and J. B. McNeely, J. Appl. Phys. 34, 4669 (1967).

121. J. F. Wager and C. W. Wilmsen, J. Vac. Sci. Technol. 17, 800 (1980).

122. W. E. Spicer, I. Lindau, P. Pianetta, P. W. Chye and C. M. Garner, Thin Solid Films 56, 1 (1979).

123. R. H. Williams and I. T. McGovern, Surf. Sci. 51, 14 (1975).

124. C. W. Wilmsen, R. W. Kee, J. F. Wager, J. Stannard and L. Messick, Thin Solid Films 64, 49 (1979).

125. A. Lidow, J. F. Gibbons, T. Magee, and J. Peng, J. Appl. Phys. 49, 5213 (1978).

126. K. R. Gleason, H. B. Dietrich, R. L. Henry, E. D. Cohen, and M. L. Bark, Appl. Phys. Lett. 32, 578 (1978).

127. A. M. White, P. J. Dean, L. L. Taylor, R. C. Clarke, D. J. Ashen, and J. B. Mullin, J. Phys. C: Solid State Phys. 5, 1727 (1972).

128. J. U. Fishbach, G. Benz, N. Stath, M. H. Pilkuhn, and K. W. Benz, Solid State Commun. 11, 721 (1972).

129. D. C. Reynolds, C. W. Litton, R. J. Almassy, S. B. Nam, P. J. Dean, and R. C. Clarke, Phys. Rev. B 13, 2507 (1976).

130. K. Hess, N. Stath, and K. W. Benz, J. Electrochem. Soc. 121, 1208 (1974).

131. O. Roder, U. Heim, and M. H. Pilkuhn, J. Phys. Chem. Solids 31, 2625 (1970).

132. D. Barthruff, K. W. Benz, and G. A. Antypas, J. Electron. Mat. 8, 485 (1979).

133. H. Temkin and W. A. Bonner, J. Appl. Phys. 52, 397 (1981).

134. P. J. Dean, D. J. Robbins, and S. G. Bishop, J. Phys. C: Solid State Phys. 12, 5567 (1979).

135. R. G. Hunsberger, R. G. Wilson, and D. M. Jamba, J. Appl. Phys. 43, 1318 (1972).

136. P. K. Chatterjee, W. V. McLevige, and B. G. Streetman, Solid St. Electron. 19, 961 (1976).

137. W. V. McLevige, M. J. Helix, K. V. Vaidyanathan, and B. G. Streetman, J. Appl. Phys. 48, 3342 (1977).

138. J. D. Oberstar, B. G. Streetman, J. E. Baker, and Peter Williams, J. Electrochem. Soc. 129, 1312 (1982).

139. S. B. Nam, D. C. Reynolds, C. W. Litton, T. C. Collins, P. J. Dean, and R. C. Clarke, Phys. Rev. B 13, 1643 (1976).

140. H. C. Casey, Jr. and E. Buehler, Appl. Phys. Lett. 30, 247 (1977).

141. Koushi Ando, Akio Yamamoto, and Masafumi Yamaguchi, J. Appl. Phys. 51, 6432 (1980).

142. O. Nizuno and H. Watanbe, Electron. Lett. 11, 118 (1975).

143. Hadis Morkoc, James T. Andrews, and Syed B. Hyder, Electron. Lett. 14, 715 (1978).

144. B. Tuck, G. A. Adegboyega, P. R. Jay, and M. J. Cardwell, Int. Symp. on GaAs and Related Compounds, 1978, Inst. Phys. Conf. Ser. 45, London, 1979, 114.

145. A. M. Huber, G. Morillot, N. T. Linh, P. N. Favennec, B. Deveaud, and B. Toulouse, Appl. Phys. Lett. 34, 858 (1979).

146. Jiro Kasahara and Naozo Watanabe, Jpn. J. Appl. Phys. 19, L151 (1980).

147. C. A. Evans, Jr., V. R. Deline, T. W. Sigmon, and A. Lidow, Appl. Phys. Lett. 35, 291 (1979).

148. T. J. Magee, J. Peng, J. D. Hong, C. A. Evans, Jr., V. R. Deline, R. M. Malbon, Appl. Phys. Lett. 35, 277 (1979).

149. T. E. Seidel, R. L. Meek, and A. G. Cullis, J. Appl. Phys. 46, 600 (1975).

150. W. Akutagawa, H. L. Dunlap, R. Hart, and O. J. Marsh, Journ. Appl. Phys. 50, 777 (1979).

151. H. B. Dietrich and J. Comas, Ion Implantation in Semiconductors, 1976, Plenum Press, New York, 1977, 735.

152. A. G. Cullis, T. E. Seidel, and R. L. Meek, J. Appl. Phys. 49, 5188 (1978).

153. K. Nishida, K. Taguichi, and Y. Matsumoto, Appl. Phys. Lett. 35, 251 (1979).

154. A. Hooper, B. Tuck, and A. J. Baker, Solid-St. Electron. 17, 531 (1974).

155. A. Hooper and B. Tuck, Solid-St Electron. 19, 513 (1976).

156. E. A. Rezek, P. D. Wright, and N. Holonyak, Jr., Solid-St. Electron. 21, 325 (1978).

157. P. K. Tien and B. I. Miller, Appl. Phys. Lett. 34, 701 (1979).

158. J. P. Donnelly, F. J. Leonberger, and C. O. Bozler, Appl. Phys. Lett. 28, 706 (1976).

159. W. T. Devlin, K. T. Ip, D. P. Leta, L. F. Eastman, G. H. Morrison, and J. Comas, Int. Symp. on GaAs and Related Compounds, 1978, Inst. Phys Conf. Ser. 45, London, 1979, 510.

160. C. A. Armiento, J. P. Donnelly, and S. H. Groves, Appl. Phys. Lett. 34, 299 (1979).

161. M. Feng, J. D. Oberstar, T. H. Windhorn, L. Cook, G. E. Stillman, and B. G. Streetman, Appl. Phys. Lett. 34, 591 (1979).

162. J. P. Donnelly, C. A. Armiento, V. Diadiuk, and S. H. Groves, Appl. Phys. Lett 35, 75 (1979).

163. C. M. Wolfe and K. H. Nichols, Appl. Phys. Lett. 31, 356 (1977).

164. K. H. Nichols, R. E. Goldwasser, and C. M. Wolfe, Appl. Phys. Lett. 36, 601 (1980).

165. W. V. McLevige, Ph.D. dissertation, University of Illinois at Urbana-Champaign. Also, Coordinated Science Laboratory Report R-802, also available from NTIS, Springfield, VA 22161 (Report #AD-A057 645/4G1).

166. C. O. Bozler, J. P. Donnelly, W. T. Lindley, and R. A. Reynolds, Appl. Phys. Lett. 29, 698 (1976).

167. M. Y. Tsai, Ph.D. dissertation, University of Illinois at Urbana-Champaign, Coordinated Science Laboratory Report R-824, also available from NTIS, Springfield, VA 22161 (Report #AD-A069 779/7GA).

168. P. Baruch, Radiation Effects in Semiconductors, 1976, Inst. Phys. Conf. Ser. 31, London, 1977, 126.

169. H. B. Dietrich, W. H. Wiesenberg, and J. Comas, Appl. Phys. Lett. 28, 182 (1976).

170. S. K. Ghandi, The Theory and Practice of Microelectronics, John Wiley and Sons, Inc., New York, 1969, 68.

171. G. H. Strauss, J. J. Krebs, and R. L. Henry, Phys. Rev. B 16, 974 (1977).

172. S. Fung, R. J. Nicholas, and R. A. Stradling, J. Phys. C: Solid State Phys. 12, 5145 (1979).

173. E. B. Abrams, S. Sumski, W. A. Bonner, and J. J. Coleman, J. Appl. Phys. 50, 4469 (1979).

174. L. C. Kimerling and J. M. Poate, Lattice Defects in Semiconductors, 1974, Inst. Phys. Conf. Ser. 23, London, 1975, 126.

175. M. N. Yoder, "Complexes and Their Effects on III-V Compounds," presented at the Semi-Insulating III-V Materials Conference (Nottingham, 1980).

176. L. Pauling, The Nature of the Chemical Bond, Cornell University Press, 3rd ed., 1960.

177. J. C. Phillips, Bonds and Bands in Semiconductors, Academic Press, New York, 1973.

178. J. D. Oberstar, B. G. Streetman, J. E. Baker, P. Williams, R. L. Henry, and E. M. Swiggard, J. Crystal Growth 54, 443 (1981).

179. H. J. Stein, F. L. Vook, D. K. Brice, J. A. Borders, and S. T. Picraux, Proc. 1st Int. Conf. on Ion Implantation, L. Chadderton and F. Eisen, (eds.), Gordon and Breach, New York, 1971, 17.

180. W. Rothemund and C. R. Fritzsche, J. Vac. Sci. Technol. 16, 968 (1979).

181. E. F. Kennedy, Appl. Phys. Lett. 38, 375 (1981).

182. M. Y. Tsai, D. S. Day, B. G. Streetman, P. Williams and C. A. Evans, Jr., J. Appl. Phys. 50, 188 (1979).

183. D. C. Joy, Journ. of Microscopy 103, 14 (1975).

184. J. P. Donnelly and C. E. Hurwitz, Solid St. Electron. 23, 943 (1980).

185. B. Cockayne, W. R. MacEwan, and G. T. Brown, Proceedings of the 1980 NATO Sponsored InP Workshop, Rome Air Development Center, Hanscom Air Force Base, MA, (Technical Memorandum #RADC-TM-80-07), 29.

186. D. Rumsby, R. M. Ware, and M. Whittaker, ibid., 77.

187. R. Bauerlein, Z. Physik 176, 498 (1963).

188. J. D. Oberstar, B. G. Streetman, J. E. Baker, and Peter Williams, J. Electrochem. Soc. 129, 1320 (1982).

189. W. K. Hofker, Philips Research Reports Supplements, No. 8, 41 (1975).

190. W. K. Hofker, D. P. Oosthoek, N. J. Koeman and H. A. M. DeGrefte, Rad. Effects 24, 223 (1975).

191. Robert G. Wilson, Rad. Effects 46, 414 (1980).

192. J. F. Gibbons and S. Mylroie, Appl. Phys. Lett. 22, 568 (1973).

193. Hans E. Schiott, Can. Journ. of Phys. 46, 449 (1968).

194. Maurice G. Kendall and Alan Stuart, The Advanced Theory of Statistics, Vol. I, 4th ed., Macmillan Publishing Co., New York, 1977.

195. J. D. Oberstar, H. Shichijo, M. Keever, B. G. Streetman, J. E. Baker, and Peter Williams, Rad. Effects, 61, 109 (1982).

196. C. W. Wilmsen, Crit. Rev. Solid State Sci. 5, 313 (1975).

197. D. L. Lile, A. R. Clawson and D. A. Collins, Appl. Phys. Lett. 29, 207 (1976).

198. B. Tuck, Phys. Stat. Sol. 36, 285 (1969).

199. V. A. Zuev, V. G. Litovchenko, G. A. Sukach and D. V. Korbutyak, Phys. Stat. Sol. 17, 353 (1973).

200. A. Karpel and B. Pratt, Sol. State Comm. 12, 325 (1973).

201. J. I. Pankove, Optical Processes in Semiconductors, Dover Publications, Inc., New York, 1971, 164.

202. Koushi Ando, Akio Yamamote and Masafumi Yamaguchi, J. Appl. Phys. 51, 6432 (1981).

203. D. B. Witty and D. F. Kyser, J. Appl. Phys. 38, 375 (1967).

204. R. A. Street, R. H. Williams and R. S. Bauer, J. Vac. Sci. Technol. 17, 1001 (1980).

205. R. A. Street and R. H. Williams, J. Appl. Phys. 52, 402 (1981).

206. W. E. Spicer, I. Lindau, P. E. Gregory, C. M. Garner, P. Pianetta and P. W. Chye, J. Vac. Sci. Technol. 13, 780 (1976).

207. A. McKinley, C. P. Srivastava and R. H. Williams, J. Phys. C: Solid St. Phys. 13, 1581 (1980).

208. J. O. McCaldin, T. C. McGill and C. A. Mead, Phys. Rev. Lett. 36, 56 (1976).

209. D. R. Schifres, N. Holonyak, Jr., R. D. Burnham, H. R. Zwicker, D. L. Keune, W. O. Groves, M. G. Crawford and J. W. Burd, Solid-St. Electron. 14, 949 (1971).

210. Murray S. Daw and D. L. Smith, Appl. Phys. Lett. __36__, 690 (1980).

211. J. D. Oberstar and B. G. Streetman, Surf. Sci. __108__, L470 (1981).

212. G. A. Antypas, Int. Symp. on GaAs and Related Compounds, 1976, Inst. Phys. Conf. Ser. 33b, London, 1977, 55.

213. G. W. Iseler, Proceedings of the 1980 NATO Sponsored InP Workshop, Rome Air Development Center, Hanscom Air Force Base, MA (Technical Memorandum #RADC-TM-80-07), 9.

214. O. G. Folberth and H. Weiss, Z. Naturforsch. __10__, 615 (1955).

215. G. A. Antypas, J. Crystal Growth __33__, 174 (1976).

216. J. B. Mullin, R. J. Heritage, C. H. Holliday and B. W. Straughan, J. Crystal Growth __3/4__, 281 (1968).

217. J. B. Mullin, Crystal Growth and Characterization, Japan, 1974, North Holland Publishing Co., Amsterdam, 1975, 75.

218. A. G. Fischer, J. Electrochem. Soc. __117__, 41C (1970).

219. M. E. Weiner, D. T. Lassota and B. Schwartz, J. Electrochem. Soc. __118__, 301 (1971).

220. G. M. Blom and W. K. Zwicker, Acta Electron. __16__, 315 (1973).

221. M. L. Young and S. J. Bass, J. Phys. D: Appl. Phys. __4__, 995 (1971)

222. J. B. Mullin, A. Royle, B. W. Straughan, P. J. Tufton and E. W. Williams, Int. Symp. on GaAs and Related Compounds, 1972, Inst. of Physics, London, 1973, 118.

223. R. C. Newman, F. Thompson, J. B. Mullin and B. W. Straughan, Phys. Letters __33A__, 113 (1970).

224. C. G. Hopkins, V. R. Deline, R. J. Blattner, C. A. Evans, Jr. and T. J. Magee, Appl. Phys. Lett. __36__, 989 (1980).

225. Leonard R. Weisberg, J. Appl. Phys. __33__, 1817 (1962).

APPENDIX 1:

Projected Range Statistics for

^{9}Be, ^{26}Mg, and ^{28}Si in InP.

LSS RANGE STATISTICS FOR   BE

IN   P

SUBSTRATE PARAMETERS-

	IN	P
Z	49	15
M	114.828	30.978
N	.1977E+23	.1977E+23
RHO/R	.2318E+01	.1104E+02
EPS/E	.3859E-01	.1433E+00
CHSF	.4832E+01	.7571E+01
MU	12.758	3.441
GAMMA	.2696	.6979
SHO	.4473E+02	

ION-   BE

| Z | 4 |
| M | 9.000 |

CROSS SECTION SUB. E= 3.00

ELECTRONIC CROSS SECTIONS OF
LINDHARD,SCHARFF,SCHIOTT

ENERGY (KEV)	PROJECTED RANGE (MICRONS)	PROJECTED STANDARD DEVIATION (MICRONS)	RANGE (MICRONS)	STANDARD DEVIATION (MICRONS)	NUCLEAR ENERGY LOSS (KEV/MICRON)	ELECTRONIC ENERGY LOSS (KEV/MICRON)
10	0.0363	0.0077	0.1100	0.0223	0.4443E+02	0.5503E+02
20	0.0720	0.0402	0.2079	0.0336	0.4157E+02	0.7783E+02
30	0.1000	0.0653	0.2876	0.0414	0.3558E+02	0.9532E+02
40	0.1467	0.0891	0.3618	0.0473	0.3155E+02	0.1101E+03
50	0.1838	0.0933	0.4242	0.0519	0.2453E+02	0.1231E+03
60	0.2203	0.1052	0.4932	0.0555	0.2549E+02	0.1340E+03
70	0.2568	0.1168	0.5534	0.0585	0.2259E+02	0.1454E+03
80	0.2930	0.1259	0.6188	0.0610	0.2126E+02	0.1557E+03
90	0.3291	0.1347	0.6657	0.0632	0.2018E+02	0.1651E+03
100	0.3643	0.1429	0.7188	0.0652	0.1921E+02	0.1740E+03
110	0.3988	0.1508	0.8174	0.0666	0.1449E+02	0.1825E+03
120	0.4326	0.1575	0.8644	0.0681	0.1797E+02	0.1904E+03
130	0.4658	0.1641	0.9099	0.0696	0.1703E+02	0.1984E+03
140	0.4983	0.1703	0.9564	0.0708	0.1623E+02	0.2059E+03
150	0.5325	0.1758	0.9976	0.0719	0.1540E+02	0.2131E+03
160	0.5659	0.1810	1.0396	0.0729	0.1458E+02	0.2201E+03
170	0.5987	0.1858	1.0806	0.0739	0.1411E+02	0.2269E+03
180	0.6309	0.1938	1.1206	0.0747	0.1367E+02	0.2335E+03
190	0.6625	0.1947	1.1596	0.0755	0.1327E+02	0.2399E+03
200	0.6936	0.1966	1.1996	0.0763	0.1299E+02	0.2461E+03
220	0.7542	0.2064	1.2352	0.0774	0.1227E+02	0.2581E+03
240	0.8130	0.2130	1.3077	0.0787	0.1178E+02	0.2696E+03
260	0.8702	0.2194	1.3778	0.0798	0.1142E+02	0.2806E+03
280	0.9250	0.2257	1.4447	0.0807	0.1119E+02	0.2912E+03
300	0.9801	0.2312	1.5098	0.0815	0.1075E+02	0.3014E+03
320	1.0333	0.2363	1.5729	0.0822	0.1033E+02	0.3113E+03
340	1.0853	0.2411	1.6342	0.0829	0.9981E+01	0.3209E+03
360	1.1363	0.2455	1.6910	0.0835	0.9571E+01	0.3302E+03
380	1.1865	0.2496	1.7528	0.0841	0.9721E+01	0.3392E+03
400	1.2357	0.2535	1.8087	0.0846	0.8899E+01	0.3481E+03
420	1.2841	0.2571	1.8641	0.0851	0.8575E+01	0.3567E+03
440	1.3318	0.2606	1.9182	0.0855	0.8776E+01	0.3650E+03
460	1.3787	0.2638	1.9712	0.0859	0.7991E+01	0.3732E+03
480	1.4249	0.2668	2.0232	0.0863	0.7721E+01	0.3813E+03
500	1.4705	0.2696	2.0741	0.0867	0.7463E+01	0.3891E+03
550	1.5817	0.2761	2.1973	0.0874	0.6873E+01	0.4081E+03
600	1.6893	0.2817	2.3153	0.0883	0.6354E+01	0.4263E+03
650	1.7936	0.2866	2.4286	0.0888	0.5901E+01	0.4437E+03
700	1.8950	0.2910	2.5379	0.0888	0.5509E+01	0.4604E+03
750	1.9935	0.2948	2.6434	0.0900	0.5176E+01	0.4766E+03
800	2.0898	0.2983	2.7455	0.0905	0.4988E+01	0.4922E+03
850	2.1828	0.3015	2.8446	0.0909	0.4400E+01	

LSS RANGE STATISTICS FOR   MG
IN   IN   P

SUBSTRATE PARAMETERS-

	IN	P
Z	49	15
M	114.820	30.974
N	.1977E+23	.1977E+23
RHU/W	.4405E+01	.1195E+02
EPS/E	.1085E-01	.2920E-01
CNSE	.1645E+02	.1863E+02
MU	4.416	1.191
GAMMA	.0022	.9924
SNU	.2711E+03	

	MG
ION-	
Z	12
M	26.900

CROSS SECTION SUB. E= 0.20
ELECTRONIC CROSS SECTIONS OF
LINDHARD,SCHARFF,SCHIOTT

ENERGY (KEV)	PROJECTED RANGE (MICRONS)	PROJECTED STANDARD DEVIATION (MICRONS)	RANGE (MICRONS)	STANDARD DEVIATION (MICRONS)	NUCLEAR ENERGY LOSS (KEV/MICRON)	ELECTRONIC ENERGY LOSS (KEV/MICRON)
10	0.0138	0.0102	0.0314	0.0092	0.3336E+03	0.8561E+02
20	0.0255	0.0147	0.0542	0.0156	0.3331E+03	0.1211E+03
30	0.0370	0.0199	0.0757	0.0213	0.3233E+03	0.1483E+03
40	0.0485	0.0251	0.0967	0.0265	0.3106E+03	0.1712E+03
50	0.0602	0.0302	0.1173	0.0313	0.2986E+03	0.1914E+03
60	0.0719	0.0351	0.1375	0.0359	0.2873E+03	0.2097E+03
70	0.0837	0.0399	0.1575	0.0401	0.2767E+03	0.2265E+03
80	0.0956	0.0447	0.1773	0.0442	0.2670E+03	0.2421E+03
90	0.1075	0.0492	0.1968	0.0480	0.2579E+03	0.2568E+03
100	0.1195	0.0536	0.2161	0.0516	0.2496E+03	0.2707E+03
110	0.1315	0.0578	0.2352	0.0550	0.2420E+03	0.2839E+03
120	0.1434	0.0619	0.2542	0.0582	0.2350E+03	0.2965E+03
130	0.1554	0.0659	0.2729	0.0613	0.2288E+03	0.3087E+03
140	0.1675	0.0700	0.2914	0.0642	0.2195E+03	0.3203E+03
150	0.1798	0.0742	0.3098	0.0671	0.2137E+03	0.3315E+03
160	0.1921	0.0781	0.3281	0.0699	0.2081E+03	0.3424E+03
170	0.2043	0.0819	0.3462	0.0725	0.2028E+03	0.3530E+03
180	0.2165	0.0855	0.3641	0.0750	0.1977E+03	0.3632E+03
190	0.2286	0.0890	0.3818	0.0774	0.1929E+03	0.3731E+03
200	0.2407	0.0923	0.3994	0.0797	0.1882E+03	0.3828E+03
220	0.2649	0.0990	0.4341	0.0844	0.1798E+03	0.4015E+03
240	0.2889	0.1051	0.4682	0.0881	0.1722E+03	0.4194E+03
260	0.3128	0.1111	0.5018	0.0918	0.1656E+03	0.4365E+03
280	0.3366	0.1169	0.5347	0.0952	0.1600E+03	0.4530E+03
300	0.3602	0.1224	0.5670	0.0984	0.1553E+03	0.4689E+03
320	0.3836	0.1277	0.5988	0.1014	0.1516E+03	0.4843E+03
340	0.4068	0.1328	0.6300	0.1042	0.1466E+03	0.4992E+03
360	0.4300	0.1377	0.6606	0.1069	0.1422E+03	0.5136E+03
380	0.4531	0.1425	0.6909	0.1093	0.1383E+03	0.5277E+03
400	0.4760	0.1470	0.7207	0.1117	0.1345E+03	0.5414E+03
420	0.4986	0.1514	0.7501	0.1139	0.1316E+03	0.5548E+03
440	0.5211	0.1556	0.7791	0.1160	0.1276E+03	0.5678E+03
460	0.5433	0.1597	0.8076	0.1180	0.1245E+03	0.5806E+03
480	0.5654	0.1636	0.8358	0.1200	0.1215E+03	0.5931E+03
500	0.5874	0.1674	0.8636	0.1218	0.1187E+03	0.6053E+03
550	0.6414	0.1765	0.9316	0.1268	0.1126E+03	0.6349E+03
600	0.6945	0.1848	0.9974	0.1297	0.1077E+03	0.6631E+03
650	0.7465	0.1926	1.0613	0.1331	0.1040E+03	0.6902E+03
700	0.7980	0.1999	1.1235	0.1362	0.9930E+02	0.7162E+03
750	0.8497	0.2068	1.1845	0.1391	0.8991E+02	0.7414E+03
800	0.9003	0.2132	1.2439	0.1417	0.8671E+02	0.7657E+03
850	0.9500	0.2192	1.3018	0.1441	0.8372E+02	0.7892E+03
900	0.9967	0.2248	1.3585	0.1464	0.8092E+02	0.8121E+03
950	1.0466	0.2301	1.4138	0.1485	0.7833E+02	0.8344E+03
1000	1.0937	0.2351	1.4681	0.1504	0.7595E+02	0.8561E+03

LSS RANGE STATISTICS FOR   SI

IN   IN   P

SUBSTRATE PARAMETERS-

	IN	P
Z	49	15
M	114.820	30.974
N	.1977E+23	.1977E+23
NMU/N	.4476E+01	.1143E+02
EPS/E	.0792E-02	.2508E-01
CNSE	.1813E+02	.1139E+02
NU	4.101	1.106
GAMMA	.0305	.9975
SNU	.5268E+03	

	SI
ION-	
Z	14
M	28.000

ELECTRONIC CROSS SECTIONS OF
LINDHARD,SCHARFF,SCHIOTT

ENERGY (KEV)	PROJECTED RANGE (MICRONS)	PROJECTED STANDARD DEVIATION (MICRONS)	RANGE (MICRONS)	STANDARD DEVIATION (MICRONS)	NUCLEAR ENERGY LOSS (KEV/MICRON)	ELECTRONIC ENERGY LOSS (KEV/MICRON)
10	0.0124	0.0067	0.0276	0.0061	0.4084E+03	0.9337E+02
20	0.0224	0.0129	0.0470	0.0137	0.4023E+03	0.1320E+03
30	0.0323	0.0173	0.0652	0.0187	0.3971E+03	0.1617E+03
40	0.0422	0.0218	0.0829	0.0233	0.3849E+03	0.1867E+03
50	0.0521	0.0261	0.1002	0.0276	0.3728E+03	0.2086E+03
60	0.0620	0.0303	0.1173	0.0317	0.3610E+03	0.2287E+03
70	0.0720	0.0344	0.1341	0.0355	0.3499E+03	0.2470E+03
80	0.0828	0.0383	0.1508	0.0392	0.3394E+03	0.2641E+03
90	0.0922	0.0424	0.1673	0.0427	0.3293E+03	0.2801E+03
100	0.1023	0.0463	0.1836	0.0460	0.3199E+03	0.2952E+03
110	0.1125	0.0500	0.1998	0.0492	0.3110E+03	0.3097E+03
120	0.1227	0.0536	0.2159	0.0522	0.3028E+03	0.3234E+03
130	0.1329	0.0571	0.2318	0.0551	0.2958E+03	0.3366E+03
140	0.1431	0.0606	0.2475	0.0579	0.2876E+03	0.3493E+03
150	0.1533	0.0639	0.2631	0.0606	0.2812E+03	0.3616E+03
160	0.1635	0.0672	0.2786	0.0631	0.2751E+03	0.3735E+03
170	0.1736	0.0704	0.2940	0.0655	0.2695E+03	0.3850E+03
180	0.1841	0.0739	0.3093	0.0680	0.2598E+03	0.3961E+03
190	0.1945	0.0773	0.3245	0.0700	0.2542E+03	0.4074E+03
200	0.2049	0.0804	0.3395	0.0726	0.2489E+03	0.4175E+03
220	0.2255	0.0864	0.3693	0.0769	0.2387E+03	0.4379E+03
240	0.2468	0.0921	0.3987	0.0809	0.2292E+03	0.4574E+03
260	0.2665	0.0975	0.4276	0.0846	0.2205E+03	0.4761E+03
280	0.2869	0.1027	0.4561	0.0881	0.2126E+03	0.4940E+03
300	0.3072	0.1078	0.4842	0.0913	0.2054E+03	0.5114E+03
320	0.3274	0.1126	0.5119	0.0944	0.1990E+03	0.5282E+03
340	0.3475	0.1173	0.5392	0.0973	0.1932E+03	0.5444E+03
360	0.3675	0.1219	0.5661	0.1001	0.1883E+03	0.5602E+03
380	0.3875	0.1263	0.5926	0.1027	0.1841E+03	0.5755E+03
400	0.4074	0.1305	0.6188	0.1051	0.1846E+03	0.5905E+03
420	0.4266	0.1346	0.6445	0.1074	0.1779E+03	0.6193E+03
440	0.4461	0.1386	0.6699	0.1096	0.1717E+03	0.6332E+03
460	0.4656	0.1424	0.6951	0.1117	0.1678E+03	0.6469E+03
480	0.4848	0.1462	0.7199	0.1137	0.1641E+03	0.6602E+03
500	0.5040	0.1498	0.7444	0.1156	0.1605E+03	0.6924E+03
550	0.5512	0.1583	0.8045	0.1201	0.1522E+03	0.7232E+03
600	0.5977	0.1663	0.8628	0.1241	0.1448E+03	0.7527E+03
650	0.6434	0.1738	0.9197	0.1277	0.1383E+03	0.7811E+03
700	0.6884	0.1808	0.9751	0.1310	0.1327E+03	0.8086E+03
750	0.7326	0.1874	1.0291	0.1341	0.1261E+03	0.8351E+03
800	0.7762	0.1935	1.0819	0.1368	0.1245E+03	0.8551E+03
850	0.8191	0.1994	1.1334	0.1394	0.1216E+03	0.8808E+03
900	0.8625	0.2051	1.1841	0.1419	0.1897E+03	0.8857E+03
950	0.9052	0.2104	1.2339	0.1442	0.1865E+03	0.9148E+03
1000	0.9471	0.2154	1.2825	0.1463	0.1834E+03	0.9337E+03

VITA

John David Oberstar was born on June 2, 1952 in Waukegan, Illinois.
He has been attending the University of Illinois at Urbana-Champaign since
September, 1971. In May, 1975 he received a Bachelor of Science degree
in Physics with high distinction in the curriculum. He received a Master
of Science degree in Physics in May, 1977. While in the Physics Department
he served as a teaching assistant and was often cited by students for ex-
cellence in undergraduate teaching. He transferred to the Electrical
Engineering Department in 1977 and has been a research assistant in the
Coordinated Science Laboratory since the fall of 1978. In 1979 he was
awarded an IBM Pre-Doctoral Fellowship. Mr. Oberstar is a member of the
American Physical Society, the Electrochemical Society, the Institute of
Electrical and Electronics Engineers, and the Optical Society of America.
He is currently a candidate for the degree of Doctor of Philosophy from
the University of Illinois.

END